

**Enhanced Osseointegration of  
Endoprostheses Using Selective Laser  
Sintered Porous Titanium Alloy Combined  
With Solution Deposited Coatings**

---

**Aadil Sarfaraz Mumith**

Submitted for the degree of Doctor of Philosophy

**Biomedical Engineering**

John Scales Centre for Biomedical Engineering  
Institute of Orthopaedics and Musculoskeletal Science  
Division of Surgery and Interventional Science  
University College London (UCL)  
Royal National Orthopaedic Hospital  
Stanmore  
HA7 4LP  
United Kingdom

I, Aadil Sarfaraz Mumith, confirm that the work presented in this thesis is my own. Where information has been derived from other sources, I confirm that this has been indicated in the thesis.

## Thesis Abstract

Massive endoprostheses are used for the reconstruction of bone defects following removal of malignant bone tumours. Aseptic loosening is a major cause of failure of endoprostheses and accounts for 25% of revisions. The main hypothesis of this thesis was that a novel porous selective laser sintered (SLS) Ti<sub>6</sub>Al<sub>4</sub>V collar augmented with electrochemically deposited hydroxyapatite coatings will enhance osseointegration.

A radiological study that evaluated the effect of chemotherapy on the osseointegration of massive endoprostheses in bone tumour patients showed significantly increased loosening at 3 years in patients who received chemotherapy and that osseointegration to the implant collar was protective against signs of radiographic loosening. This study highlighted the importance of increasing osseointegration of these implants.

An experimental study investigated the osseointegration of SLS Ti<sub>6</sub>Al<sub>4</sub>V collars in an ovine midshaft implant over a 6 month period. SLS porous collars provided a greater area for bone contact ( $p < 0.001$ ) and greater osseointegration ( $p < 0.001$ ), with bone directly permeating into the porous structure.

Electrochemically deposited hydroxyapatite (EHA), silicate-substituted hydroxyapatite (ESiHA) and strontium-substituted hydroxyapatite (ESrHA) were developed enabling the inner pores of SLS structure to be coated. ESiHA (1.63 Si wt%) and ESrHA (4.08 Sr wt%) coatings were optimised and both crystalline and amorphous phases were found with significant dissolution of Si from ESiHA ( $p = 0.002$ ). No significant differences were found when stem cell proliferation and osteogenic differentiation were compared between coatings.

In an ovine defect model, investigation of these coatings on SLS implants of two different pore sizes (1125 $\mu$ m and 550 $\mu$ m) showed increased osseointegration with electrochemically coated implants ( $p < 0.001$ ). Osseointegration was greatest with the EHA coating on the smaller pore size ( $p < 0.05$ ).

In conclusion, the hypothesis can be accepted and novel electrochemically coated laser sintered porous collars may provide a viable alternative ingrowth region to enhance the osseointegration of massive bone tumour endoprotheses.

## **Acknowledgements**

The work presented in this thesis could not be completed without all the staff and students at the John Scales Centre for Biomedical Engineering, UCL, RNOH, Stanmore. It has been an absolute pleasure to work with them all and I would like to thank all of them, especially the members of SLW. I would like to acknowledge the Royal College of Surgeons of England, Orthopaedic Research UK and the Skeletal Cancer Action Trust for funding this work.

Guiding orthopaedic surgeons through academia, I am sure, is quite the challenge although Dr Melanie Coathup is too polite to ever confess this. Her supervision and encouragement helped drive the work in this thesis. I wish her all the best with her new role in the future in which she will undoubtedly thrive.

I owe my deepest gratitude to Professor Gordon Blunn for this opportunity. His inspiration, guidance and mentoring has allowed me to achieve beyond my expectations. His commitment to his students is unparalleled and I hope to continue sharing ideas and anecdotes with him for the years to come. Generations of orthopods have walked through the corridors of BME; quite simply, 'Prof' is the reason why.

To my daughter, Mariam, at 6 months she had already attended more international conferences than most junior doctors. As she grew older, all she knew was that she missed her dad due to his busy commitments. Hopefully this part-time father will manage to find a better balance in the years to come.

A special thank you to my sister, my parents and my in-laws for all their support and motivation, enabling me to complete this body of work.

I dedicate this thesis to my wife Arma for her immeasurable patience, unwavering support and belief in me. She has made sacrifices and has been my pillar throughout my career, for which I am eternally grateful.

All that I have achieved is credit to my family and their guidance.

## Table of contents

Thesis Abstract .....	1
Acknowledgements.....	3
Table of contents .....	4
Table of tables .....	10
Table of figures .....	13
Table of equations .....	22
Abbreviations .....	23
Chapter 1. Introduction .....	25
1.1 Bone structure .....	28
1.2 Bone formation .....	30
1.2.1 Osseinduction, osseoconduction and osseointegration .....	30
1.2.2 Mesenchymal stem cells (MSCs) .....	31
1.2.3 Osteoblasts .....	31
1.2.4 Osteocytes .....	33
1.2.5 Osteoclasts .....	33
1.2.6 Intramembranous ossification .....	35
1.2.7 Endochondral ossification .....	36
1.2.8 Strain related bone remodelling .....	37
1.2.9 Bone matrix .....	37
1.2.10 Bone mineral.....	38
1.3 Bone Tumours .....	38
1.3.1 Overview .....	38
1.3.2 Epidemiology.....	39
1.4 Allograft reconstruction .....	40
1.5 Rotationplasty .....	41
1.6 Endoprostheses.....	42

1.6.1	Evolution of the endoprosthesis .....	42
1.6.2	Aseptic loosening of endoprostheses.....	43
1.6.3	Extracortical bone bridging and hydroxyapatite collar .....	44
1.6.4	Porous metals and pore size.....	49
1.6.5	Implant materials.....	52
1.7	Additive layer manufacturing.....	53
1.7.1	What is it? .....	53
1.7.2	Additive manufacturing in orthopaedics.....	56
1.7.3	Other production considerations with additive manufacturing .....	62
1.7.4	Future perspectives.....	62
1.8	Surface modification to enhance bioactivity .....	63
1.9	Hydroxyapatite.....	63
1.9.1	Substituted Hydroxyapatites.....	65
1.9.2	Silicon.....	66
1.9.3	Strontium.....	66
1.10	Coating techniques.....	67
1.10.1	Plasma spray .....	67
1.10.2	Hot isostatic pressing (HIP).....	69
1.10.3	Thermal spray coating.....	69
1.10.4	Pulsed laser deposition .....	70
1.10.5	Wet-chemical coating techniques .....	70
1.10.6	Dip coating.....	71
1.10.7	Ion beam assisted deposition (IBAD).....	71
1.10.8	Sputter coating.....	71
1.10.9	Electrochemical deposition .....	72
	Aims and Hypotheses of thesis.....	76
	Chapter 2. Early Radiographic Loosening of Distal Femoral Replacements in Patients Undergoing Chemotherapy .....	78

2.1	Introduction.....	79
2.2	Patients and methods.....	82
2.2.1	Radiographic analysis.....	84
2.2.2	Statistics.....	86
2.3	Results.....	87
2.3.1	Extracortical bone growth.....	87
2.3.2	Osseointegration.....	87
2.3.3	Gap.....	88
2.3.4	Radiolucent Line (RLL) Score.....	88
2.3.5	Correlation analysis.....	88
2.4	Discussion.....	90
2.5	Conclusion.....	93
Chapter 3. Augmenting Osseointegration of Endoprostheses using Laser Sintered Porous Collars.....		94
3.1	Introduction.....	95
3.2	Materials and Methods.....	98
3.2.1	Manufacture of collars.....	98
3.2.2	EC deposition of HA onto SP porous collars.....	99
3.2.3	Surgery.....	100
3.2.4	Analgesia.....	100
3.2.5	Insertion of diaphyseal implants.....	101
3.2.6	Radiological analysis.....	102
3.2.7	Histomorphometry.....	103
3.2.8	Statistics.....	104
3.3	Results.....	105
3.3.1	Evaluation of coating.....	105
3.3.2	Radiological analysis of extracortical bone growth.....	106

3.3.3	Histomorphometric analysis of collar surface size and pore content .	108
3.3.4	Histological appearance of bone ingrowth into the collars.....	110
3.4	Discussion .....	113
3.5	Conclusion.....	118
Chapter 4.	Development, Characterization and Evaluation of the Bioactivity of Silicate and Strontium Substituted Hydroxyapatite Coatings .....	119
4.1	Introduction .....	120
4.2	Methods.....	125
4.2.1	Sample preparation.....	125
4.2.2	Disc holder, surface area and current density .....	126
4.2.3	Electrochemical deposition of HA coating (EHA) .....	126
4.2.4	Electrochemical deposition of SiHA coating (ESiHA) .....	127
4.2.5	Electrochemical deposition of SrHA coating (ESrHA) .....	127
4.2.6	Analysis of surface morphology and thickness of EC coatings ...	128
4.2.7	Characterisation of coating.....	129
4.2.8	Cell culture and maintenance.....	129
4.2.9	Characterisation of human mesenchymal stem cells (hMSCs) using tri-lineage differentiation .....	131
4.2.10	Culture of hMSCs on EHA, ESiHA and ESrHA coatings.....	132
4.2.11	SEM.....	134
4.2.12	Statistical analysis.....	134
4.3	Results.....	135
4.3.1	EC coatings.....	135
4.3.2	Characterisation of hMSCs .....	153
4.3.3	Cell proliferation and differentiation on EHA, ESiHA and ESrHA coatings .....	154
4.4	Discussion .....	161
4.5	Conclusion.....	168

Chapter 5. Development, Refinement, Characterisation and Evaluation of the Bioactivity of Silicate and Strontium Substituted Hydroxyapatite Coatings .....	169
5.1 Introduction .....	170
5.2 Methods .....	173
5.2.1 Sample preparation .....	173
5.2.2 Electrochemical deposition of HA coating .....	173
5.2.3 Electrochemical deposition of SiHA coating (ESiHAlI) .....	173
5.2.4 Electrochemical deposition of SrHA coating (ESrHAlI) .....	174
5.2.5 Surface morphology and thickness of EC coatings .....	174
5.2.6 Coating Characterisation .....	174
5.2.7 Cell culture and maintenance .....	175
5.2.8 Characterisation of ovine MSCs using tri-lineage differentiation .	176
5.2.9 Culture of oMSCs on EHA, ESiHAlI and ESrHAlI coatings .....	176
5.2.10 SEM .....	178
5.2.11 Statistical analysis .....	178
5.3 Results .....	179
5.3.1 Light microscopy .....	179
5.3.2 Surface morphology – Scanning Electron Microscopy (SEM) .....	181
5.3.3 Coating thickness .....	183
5.3.4 EDS .....	185
5.3.5 Crystallinity .....	187
5.3.6 Profilometry .....	188
5.3.7 Characterisation of ovine MSCs .....	192
5.3.8 Culture of ovine MSCs on EHA, ESiHAlI and ESrHAlI coatings .	193
5.4 Discussion .....	203
5.5 Conclusion .....	210

Chapter 6. Evaluating Osseointegration of Laser Sintered $Ti_6Al_4V$ Electrochemically Coated Scaffolds Using an Ovine Femoral Condyle Defect Model.....	211
6.1 Introduction .....	212
6.2 Materials and Methods.....	213
6.2.1 Manufacture of implants .....	213
6.2.2 EHA coating of implant.....	214
6.2.3 ESiHAlI coating of implant.....	214
6.2.4 ESrHAlI coating of implant .....	215
6.2.5 In vivo study design.....	215
6.2.6 Surgery.....	217
6.2.7 Analgesia .....	217
6.2.8 Insertion of implants into femoral condyle defects.....	217
6.2.9 Histomorphometry .....	219
6.2.10 Statistics.....	220
6.3 Results.....	222
6.3.1 Histological appearance of bone ingrowth into implants.....	222
6.3.2 Histomorphometric analysis of collar surface size and pore content .....	226
6.4 Discussion .....	229
6.5 Conclusion .....	234
Chapter 7. General Discussion and Conclusion.....	235
7.1 General Discussion.....	236
7.2 General Conclusions.....	250
7.3 Future Work .....	252
Chapter 8. Bibliography .....	254

## Table of tables

Table 1-1 Molecules for osteoblast differentiation and function. Modified from Ralston, 2005.....	32
Table 1-2 Peak age for bone lesions. ....	39
Table 1-3 Classification of bone tumours. Revised WHO classification. ....	39
Table 1-4 ASTM standard terminology for AM technologies.....	53
Table 1-5 Reported impact of operative time with AM application, negative average time values correspond to shorter operative times, modified from (Tack et al., 2016).....	58
Table 1-6 The ideal characteristics of a calcium phosphate coating, modified from Surmenev et al (Surmenev et al., 2014). ....	64
Table 1-7 adapted from Yang et al (Yang et al., 2005) for alternative methods of coating with HA. ....	74
Table 2-1 comparisons of demographic data across chemotherapy and non-chemotherapy groups. <sup>a</sup> Mann-Whitney U test, <sup>b</sup> $\chi^2$ test. ....	82
Table 2-2 Patients included in chemotherapy group with chemotherapy regimen. <sup>a</sup> 5 of 12 cycles of methotrexate omitted due to complications. <sup>b</sup> Randomised to VAI as part of Euro-Ewing 99 study. <sup>c</sup> Randomised to VAC as part of Euro-Ewing 99 study. <sup>d</sup> Methotrexate and cisplatin stopped at later cycles due to complications. ....	84
Table 2-3 Summary of data (median, IQR) for variables throughout the 1 <sup>st</sup> , 2 <sup>nd</sup> and 3 <sup>rd</sup> post-operative year radiographs between the non-chemotherapy and chemotherapy groups. <sup>abcd</sup> p<0.05.....	87
Table 2-4 Correlation analysis between variables with Pearson correlation coefficients and p-values. *p<0.05.....	88
Table 3-1 Preparation protocol for the production of thin sections. IMS, industrial methylated spirit.....	104
Table 3-2 Results of measurements of ECBB around each collar type with medians (IQR) shown. <sup>a</sup> Kruskal-Wallis test. ....	108
Table 3-3 Median (IQR) histomorphometric measurements quantifying areas of bone, soft tissue and cement found within collar thin sections together with p-values. <sup>a</sup> Mann-Whitney U test: comparing the amount of bone/soft	

tissue/cement between the collars. <sup>b</sup> Kruskal-Wallis test: comparing the amount of bone/soft tissue/cement content within each collar. ....	110
Table 4-1 Current densities and deposition times used to produce EHA, ESiHA and ESrHA coatings on Ti alloy discs. n=6 for each combination. ....	128
Table 4-2 Summary of the thickness of all coatings produced using varying current densities and deposition times. ....	141
Table 4-3 p-values for pair-wise comparisons of thickness of coating with different current density/deposition time combinations. p<0.05 is considered to be significant and are identified in italics. ....	147
Table 4-4 p-values for pair-wise comparisons of thickness of coating with different current density/deposition time combinations. p<0.05 is considered to be significant and are identified in italics. ....	148
Table 4-5 p-values for pair-wise comparisons of thickness of coating with different current density/deposition time combinations. p<0.05 is considered to be significant and are identified in italics. ....	149
Table 4-6 Summary of coating Ca:P ratios and levels of elemental substitution. ....	150
Table 4-7 AlamarBlue® assay result (mean±SD) for coatings per timepoint (day). ....	155
Table 4-8 Significant pair-wise comparisons over timepoints, p-values as shown. ....	155
Table 4-9 p-values for pair-wise comparisons of normalised AlamarBlue® assay results of various coatings at day 3. p<0.05 is considered to be significant and are identified in italics. ....	155
Table 4-10 p-values for pair-wise comparisons of normalised AlamarBlue® assay results of various coatings at day 7. p<0.05 is considered to be significant and are identified in italics. ....	155
Table 4-11 Normalised ALP assay result (mean±SD) for coatings per timepoint (day). ....	157
Table 4-12 p-values for pair-wise comparisons of normalised ALP assay results of various coatings at day 3. p<0.05 is considered to be significant and are identified in italics. ....	157

Table 4-13 p-values for pair-wise comparisons of normalised ALP assay results of various coatings at day 7. $p < 0.05$ is considered to be significant and are identified in italics.....	157
Table 4-14 p-values for pair-wise comparisons of normalised ALP assay results of various coatings at day 14. $p < 0.05$ is considered to be significant and are identified in italics.....	157
Table 5-1 Summary of thicknesses of ESiHAlI and ESrHAlI coatings produced with varying parameters.....	183
Table 5-2 EDS results for both phase I and phase II coatings. Ratios are presented as Ca:(P+Si) and (Ca+Sr):P for the appropriate coatings. ....	185
Table 5-3 Summary of Ra (nm) values for each coating in ascending order ..	189
Table 5-4 p-values for pair wise comparisons using ANOVA with bonferroni correction for Ra values of coatings. $p < 0.05$ is considered to be significant and are identified in italics.....	189
Table 5-5 Summary of AlamarBlue® assay results for all coatings at all timepoints. ....	194
Table 5-6 p-values for pair-wise comparisons of normalised AlamarBlue® assay results of varying coatings at day 3. $p < 0.05$ is considered to be significant and are identified in italics.....	194
Table 5-7 Summary of ALP assay results (mean±SD) for all coatings at all timepoints. ....	195
Table 6-1 Plug position and orientation within condyle defects. U, uncoated; PS, plasma sprayed; EHA, electrochemical HA; ESiHAlI, electrochemical SiHA 2 <sup>nd</sup> phase; ESrHAlI, electrochemical SrHA 2 <sup>nd</sup> phase. *SP orientated inwards. ...	216
Table 6-2 Preparation protocol for the production of thin sections.....	221
Table 6-3 Significant p-values and percentage integration (IQR) for significant findings between various scaffold designs. U, uncoated; PS, plasma sprayed HA; EHA, electrochemical HA; ESiHAlI, electrochemical SiHA; ESrHA, electrochemical SrHA; SP, small pore; LP, large pore.....	227

## Table of figures

Figure 1-1: The trabecular and cortical structure of bone. The cortical structure of bone consists of the Haversian system that is made up of a central canal of blood vessels surrounded by the concentric collagen lamellae (Ralston, 2005). .....	28
Figure 1-2 A list of differentiation markers for MSCs, pre-osteoblasts and osteocytes during MSC differentiation to osteoblasts and osteocytes. (Miron and Zhang, 2012).....	31
Figure 1-3 Schematic representation of the influence of pathways upon bone remodelling (Bose et al., 2013). .....	35
Figure 1-4 Stages of endochondral ossification. (A) Cartilage model. (B) Formation of primary centre of ossification. (C) Established primary centre, angiogenesis in remaining cartilage model. (D) Development of secondary centres of ossification responsible for longitudinal growth. (E) Adult bone where the growth plate has fused. From Mackie et al (Mackie et al., 2008). .....	36
Figure 1-5 Percent of new cases of malignant bone tumours by age group (Howlader et al., 1975-2013). .....	40
Figure 1-6 Distal femoral endoprosthesis with HA coated collar. ....	45
Figure 1-7 Extracortical bony bridging onto a grooved HA coated collar as part of a distal femoral endoprosthesis. ....	46
Figure 1-8 Radiograph of fractured proximal tibial replacement stem with no evidence of osseointegration (Fromme et al., 2017). ....	46
Figure 1-9 Contour plot of stress distribution (von Mises) in FE model (bone and implant): (a) no growth, scale 0-500MPa, (b) no growth, (c) 25% growth, (d) 50% growth, (e) 75% growth, (f) 100% growth (Fromme et al., 2017). ....	47
Figure 1-10 AdHAesio HA Collar from Stanmore Implants .....	48
Figure 1-11 Schematic representation of AM principles using different materials (Zhai et al., 2014), computer-aided design (CAD).....	54
Figure 1-12 Schematics of (a) vat polymerization, (b) fused filament fabrication, (c) selective laser sintering and (d) inkjet printing (Gu et al., 2016). ....	55
Figure 1-13 Typical thickness of coatings obtained by different process methods, showing the versatility of EPD in that it can produce a wide range of thicknesses of relevance for orthopaedic applications (Sridhar et al., 2002). ...	75

Figure 2-1 CONSORT flow diagram. ....	82
Figure 2-2 AP (right) and lateral (left) radiographs of DFR intramedullary stem showing the zones used for the RLL score together with length, thickness and gap distances measured around HA collar. Radiolucent lines are evident in all zones in the lateral radiograph giving a maximum score of 12. ....	85
Figure 2-3 Boxplot of radiolucent line scores (RLL) for non-chemotherapy and chemotherapy groups over time. *p<0.05. ....	89
Figure 3-1 Custom diaphyseal implant with a proximal and distal grooved collar. ....	98
Figure 3-2 Exploded view of custom diaphyseal implant without collars showing halving joint and screw location. ....	98
Figure 3-3 Pictures of grooved (left), small pore (middle) and large pore (right) collar designs. ....	99
Figure 3-4 (Left) 5cm resected mid-diaphyseal segment, (middle) prepared proximal femoral intramedullary canal, (right) proximal half of diaphyseal implant with grooved collar cemented in place. ....	102
Figure 3-5 ML radiograph of ovine tibia with midshaft implant in situ showing measurements taken for radiographic analysis; (a) surface area of bone pedicle from shoulder of implant, (b) maximal thickness of bone pedicle from shoulder of implant, (c) maximal length of pedicle from shoulder of implant. ....	103
Figure 3-6 X-ray diffraction spectra of EC coating identifying peaks for hydroxyapatite (HA) and titanium (Ti). ....	105
Figure 3-7 Backscattered scanning electron microscope image of SP collar cross-section showing electrochemical deposited CaP coating on strut surface. Scale bar shown, x130 magnification. R; resin, CaP; EC deposited CaP coating, C; Titanium alloy collar. ....	106
Figure 3-8 Boxplot showing length of pedicle growth observed radiographically from shoulder of each collar design. *small pore Vs grooved p=0.004, **large pore Vs grooved p=0.001. ....	107
Figure 3-9 Boxplot showing thickness of pedicle growth observed radiographically over each collar design. *small pore Vs grooved p<0.001, **large pore Vs grooved p<0.001. ....	107

Figure 3-10 Boxplot showing surface area of pedicle growth observed radiographically over each collar design. \*small pore Vs grooved  $p=0.005$ , \*\*large pore Vs grooved  $p=0.002$ ..... 108

Figure 3-11 Boxplot showing histomorphometric results for total surface of collar available for integration together with actual osseointegration for each of the collar types. Significant p-values of pair-wise comparisons are <sup>a</sup>0.016, <sup>b</sup><0.001, <sup>c</sup><0.001, <sup>d</sup><0.001. .... 109

Figure 3-12 Boxplot showing histomorphometric results for inner pore contents of SLS collars. Significant p-values of pair-wise comparisons are <sup>a</sup>0.003, <sup>b</sup><0.001, <sup>c</sup><0.001, <sup>d</sup>0.015. .... 110

Figure 3-13 (Left) radiograph of SP collar in situ, (Right) Light microscope image showing interface between porous collar and transection site. x2.5 magnification. Toluidine blue and Paragon stain used. B; Bone (pink), ST; Soft tissue (purple), C; Collar (black). Scale bar shown. .... 111

Figure 3-14 Light microscope image of inner pores of SP collar. Scale bar 200 $\mu$ m, x2.5 magnification, stained with Toluidine blue and Paragon. Bone (B, pink) and collar (C, black). .... 112

Figure 4-1 Surface profile shown with the mean line (M), the peaks (P) and troughs (T) of the asperities together with the Ra. .... 124

Figure 4-2 Apparatus setup for EC coating of EHA, ESiHA and ESrHA. (A): cathode 4 disc holder with 4 Ti alloy discs in situ; (B): beaker with electrolyte solution; (C): anode with platinum ring for EHA and platinum wire for ESiHA and ESrHA; (D): multimeter; (E): power supply; and (F): heat-stirrer..... 125

Figure 4-3 (Left) Roughened Ti<sub>6</sub>Al<sub>4</sub>V disc from above, scale bar shown equivalent to 2.5mm. (Right) Roughened surface of disc, scale bar shown equivalent to 1mm..... 135

Figure 4-4 Light microscopy images of EHA coatings with oblique light source. Scale bar shown is equivalent to 1mm. A) 10mA/cm<sup>2</sup> over 5 minutes, B) 20mA/cm<sup>2</sup> over 5 minutes, C) 30mA/cm<sup>2</sup> over 5 minutes, D) 10mA/cm<sup>2</sup> over 10 minutes, E) 20mA/cm<sup>2</sup> over 10 minutes and F) 10mA/cm<sup>2</sup> over 15 minutes... 136

Figure 4-5 Light microscopy images of ESrHA coatings with oblique light source. Scale bar shown is equivalent to 1mm. A) 15mA/cm<sup>2</sup> over 20 minutes, B) 15mA/cm<sup>2</sup> over 40 minutes, C) 20mA/cm<sup>2</sup> over 20 minutes, D) 20mA/cm<sup>2</sup>

over 40 minutes, E) 25mA/cm <sup>2</sup> over 20 minutes and F) 25mA/cm <sup>2</sup> over 40 minutes. ....	137
Figure 4-6 Light microscopy images of ESiHA coating with oblique light source. Scale bar shown equivalent to 1mm. A) 5mA/cm <sup>2</sup> over 30 minutes and B) 10mA/cm <sup>2</sup> over 60 minutes. ....	138
Figure 4-7 SEM images of an uncoated roughened Ti <sub>6</sub> Al <sub>4</sub> V disc surface. Scale bar and magnification as shown. ....	138
Figure 4-8 SEM images showing surfaces and crystal morphologies of EHA coatings produced from (A-C) 10mA/cm <sup>2</sup> , (D-F) 20mA/cm <sup>2</sup> and (G-I) 30mA/cm <sup>2</sup> current densities. Magnification and scale bars as shown. ....	139
Figure 4-9 SEM images of the surface of the ESiHA coating. Magnification and scale bars are as shown. ....	140
Figure 4-10 SEM images of ESrHA surface. Magnification and scale bars as shown. ....	140
Figure 4-11 Cross section of 30mA/cm <sup>2</sup> , 5 minute EHA coating showing typical appearance of crystal 'flare' (arrow). Magnification and scale bar as shown. D, disc; EHA; electrochemical HA coating; R, resin. ....	142
Figure 4-12 SEM images of cross sections of discs (D) embedded in resin (R) showing the thickness of the coating (EHA). (A) 10mA/cm <sup>2</sup> over 5 minutes, (B) 10mA/cm <sup>2</sup> over 10 minutes, (C) 10mA/cm <sup>2</sup> over 15 minutes, (D) 20mA/cm <sup>2</sup> over 5 minutes, (E) 20mA/cm <sup>2</sup> over 10 minutes and (F) 30mA/cm <sup>2</sup> over 5 minutes. ....	144
Figure 4-13 SEM images of ESiHA (white arrow) coated disc (D) cross sections embedded in resin (R). (A) 5mA/cm <sup>2</sup> over 5 minutes, (B) 5mA/cm <sup>2</sup> over 10 minutes, (C) 5mA/cm <sup>2</sup> over 15 minutes, (D) 10mA/cm <sup>2</sup> over 5 minutes, (E) 10mA/cm <sup>2</sup> over 10 minutes and (F) 10mA/cm <sup>2</sup> over 15 minutes. ....	145
Figure 4-14 SEM images of ESrHA coated disc (Ti) cross sections embedded in resin (R). (A) 15mA/cm <sup>2</sup> over 20 minutes, (B) 15mA/cm <sup>2</sup> over 40 minutes, (C) 20mA/cm <sup>2</sup> over 20 minutes, (D) 20mA/cm <sup>2</sup> over 40 minutes, (E) 25mA/cm <sup>2</sup> over 20 minutes and (F) 25mA/cm <sup>2</sup> over 40 minutes. ....	146
Figure 4-15 Boxplot of thickness of EHA coating (µm) produced by different current densities (mA/cm <sup>2</sup> ) over varying deposition times (minutes).....	147
Figure 4-16 Boxplot of thickness of ESiHA coating (µm) produced by different current densities (mA/cm <sup>2</sup> ) over varying deposition times (minutes).....	148

Figure 4-17 Boxplot of thickness of ESrHA coating ( $\mu\text{m}$ ) produced by different current densities ( $\text{mA}/\text{cm}^2$ ) over varying deposition times (minutes).....	149
Figure 4-18 EDS spectra of coatings. Ca, calcium; O, Oxygen; Ti, titanium; V, vanadium; Al, aluminium; Si, silicon; Sr, strontium; Na, sodium. x-axis = Energy (keV) .....	151
Figure 4-19 XRD spectra of all coatings as labelled. * denotes HA peaks with Si and Sr referring to the silicon or strontium present within the coating. Ti peaks are identified due to the underlying disc.....	152
Figure 4-20 (A) control culture of hMSCs in DMEM+. (B) Red stained calcium deposits from osteoblasts with Alizarin Red stain. (C) Red stained lipid within adipocytes with Oil Red O stain. (D) Blue pellet confirming presence of chondrocytes with Alcian Blue stain.....	153
Figure 4-21 Boxplot showing the AlamarBlue® activity for each of the coatings at each time-point. ....	154
Figure 4-22 Boxplot showing the normalised ALP assay result for each of the coatings at each timepoint. ....	156
Figure 4-23 Scanning electron micrographs of coating surfaces at different timepoints (days 3 (D3), 7 (D7), 14 (D14) and 28 (D28)). U, Uncoated; PS, Plasma spray; EHA, EC HA. White arrows identify cells. Scale bar and magnification as shown.....	159
Figure 4-24 Scanning electron micrographs of coating surfaces at different timepoints (days 3 (D3), 7 (D7), 14 (D14) and 28 (D28)). ESiHA, EC silicate-substituted HA; ESrHA, EC strontium-substituted HA. White arrows identify cells. Scale bar and magnification as shown. ....	160
Figure 4-25 Current efficiency as a function of current density for different total amounts of charge passed, derived from Redepenning et al. (Redepenning et al., 1996).....	161
Figure 5-1 $\text{Ti}_6\text{Al}_4\text{V}$ discs with (A) ESiHAlI and (B) ESiHA coatings. Scale bar equivalent to 2.5mm.....	179
Figure 5-2 $\text{Ti}_6\text{Al}_4\text{V}$ disc surface following deposition of an ESiHAlI coating. Scale bar shown equivalent to 1mm. ....	179
Figure 5-3 $\text{Ti}_6\text{Al}_4\text{V}$ with (A) ESrHAlI and (B) ESrHA coatings. Scale bar equivalent to 2.5mm.....	180

Figure 5-4 Ti<sub>6</sub>Al<sub>4</sub>V disc surface following deposition of ESrHAlI coating. Scale bar shown equivalent to 1mm. .... 180

Figure 5-5 Surface morphology of control roughened acid etched Ti<sub>6</sub>Al<sub>4</sub>V disc, micro-pits on the surface can be seen. Magnification and scale bar as shown ..... 181

Figure 5-6 Surface morphology of plasma sprayed HA coated Ti<sub>6</sub>Al<sub>4</sub>V discs. Magnification and scale bar as shown. .... 181

Figure 5-7 Surface morphology of EHA coated Ti<sub>6</sub>Al<sub>4</sub>V disc. Magnification and scale bar as shown. .... 181

Figure 5-8 Surface morphology of ESiHAlI coated Ti<sub>6</sub>Al<sub>4</sub>V disc. Magnification and scale bar as shown. .... 182

Figure 5-9 Low magnification of ESiHAlI coating showing heterogeneous shaped crystals. Magnification and scale bar as shown. .... 182

Figure 5-10 Surface morphology of ESrHAlI coated Ti<sub>6</sub>Al<sub>4</sub>V disc. Magnification and scale bar as shown. .... 182

Figure 5-11 SEM images of ESiHAlI coated disc cross sections in resin. (A) 0.8mA/cm<sup>2</sup> over 30 minutes, (B) 0.8mA/cm<sup>2</sup> over 45 minutes. Magnification and scale bar as shown. .... 183

Figure 5-12 SEM images of ESrHAlI coated disc (Di) cross sections in resin (R). (A) 7.5mA/cm<sup>2</sup> over 2.5 minutes, (B) 7.5mA/cm<sup>2</sup> over 5 minutes, (C) 15mA/cm<sup>2</sup> over 2.5 minutes and (D) 15mA/cm<sup>2</sup> over 5 minutes. Magnification and scale bars as shown. White arrows identify coating. .... 184

Figure 5-13 Boxplot of thickness of ESrHAlI coating (µm) produced by different current densities (mA/cm<sup>2</sup>) over varying deposition times (minutes). \*p<0.001 ..... 185

Figure 5-14 EDS spectra of ESiHA (top) and ESiHAlI (bottom). Ca, calcium; O, oxygen; P, phosphorous; Si, silicon. x-axis = Energy (keV) ..... 186

Figure 5-15 EDS spectra of ESrHA (top) and ESrHAlI (bottom). Ca, calcium; O, oxygen; P, phosphorous; Sr, strontium. x-axis = Energy (keV)..... 186

Figure 5-16 Proportion of element remaining in the coating at each timepoint as determined using EDS analysis. Error bars denote 95% confidence intervals. .... 187

Figure 5-17 XRD spectra of all coatings as labelled. \* denotes HA peaks with Si and Sr referring to the silicon or strontium present within the coating..... 188

Figure 5-18 Ra for each of the coatings in ascending order. ....	189
Figure 5-19 3D profile of uncoated disc surface. Scale bar with relative height shown on right.....	190
Figure 5-20 3D profile of PS HA disc surface. Scale bar with relative height shown on right.....	190
Figure 5-21 3D profile of ESrHAII disc surface. Scale bar with relative height shown on right.....	190
Figure 5-22 3D profile of EHA disc surface. Scale bar with relative height shown on right. ....	191
Figure 5-23 3D profile of ESiHAII disc surface. Scale bar with relative height shown on right.....	191
Figure 5-24 (A) Red stained calcium deposits from osteoblasts with Alizarin Red stain. (B) Red stained lipid within adipocytes with Oil Red O stain. (C) Blue pellet confirming presence of chondrocytes with Alcian Blue stain. ....	192
Figure 5-25 AlamarBlue® assay for each coating at 3, 7 and 14 days. ....	193
Figure 5-26 ALP assay for each coating at 3, 7 and 14 days.....	195
Figure 5-27 Scanning electron micrographs of coating surfaces at different timepoints (days 3 (D3), 7 (D7), 14 (D14) and 28 (D28)). U, Uncoated; PS, Plasma spray; EHA, EC HA. Red arrows identify cells. Scale bar and magnification as shown.....	198
Figure 5-28 Scanning electron micrographs of coating surfaces at different timepoints (days 3 (D3), 7 (D7), 14 (D14) and 28 (D28)). ESiHAII, EC silicate substituted HA; ESrHAII, EC strontium substituted HA. Red arrows identify cells. Scale bar and magnification as shown. ....	199
Figure 5-29 Crystal emerging from cell on uncoated disc. Magnification and scale bar as shown. ....	200
Figure 5-30 Filopodial and nanopodial interaction of cells to both large plate like crystals and needle shaped crystals on ESiHAII coating. Magnification and scale bar as shown. ....	200
Figure 5-31 Attachment of cell to ESrHAII crystals. Magnification and scale bar as shown.....	201
Figure 5-32 Single crystals and crystal clusters emerging from cells on ESrHAII coating. Magnification and scale bar as shown.....	201

Figure 5-33 Identical EDS spectra of single crystals (top) and crystal clusters (bottom) observed on coatings. Ca, calcium; O, oxygen; P, phosphorous. x-axis = Energy (keV).....202

Figure 6-1 3D models of selective laser sintered Ti<sub>6</sub>Al<sub>4</sub>V plugs measuring 8x15mm. Small pore (SP) and large pore (LP) regions shown. ....213

Figure 6-2 Diagrammatic representation of implant and defect positions within femoral condyle. ....216

Figure 6-3 Anteroposterior (above) and mediolateral (below) radiographs of retrieved femoral condyles with implants in situ. ....216

Figure 6-4 Operative stages of inserting implant into defects. Starting from surgical site preparation (a) followed by incision and exposure of condyle (b). Drilling and sequential insertion of each implant is performed (c-g) followed by closure of the wound (h). ....219

Figure 6-5 Light microscope image of implant within femoral condyle defect. x2.5 magnification. Toluidine blue and Paragon stain used. Bone, pink; Soft tissue, purple; Implant, black. Scale bar shown equivalent to 1mm. (a) uncoated, (b) plasma sprayed, (c) EHA, (d) ESiHAII and (e) ESrHAII.....224

Figure 6-6 Backscattered scanning electron microscopy (SEM) images of plug cross-sections showing direct attachment of bone to EC coatings. Top, EHA (x100). Middle, ESiHAII (x200). Bottom, ESrHAII (x120). Scale bars as shown (100µm). Yellow arrows identify coating, blue arrows show Haversian canals, red arrows identify lacuna. P, plug strut. R, resin. B, bone. ....225

Figure 6-7 Percentage integration of various experimental groups; U, uncoated; PS, plasma sprayed HA; EHA, electrochemical HA; ESiHAII, electrochemical SiHA; ESrHAII, electrochemical SrHA; SP, small pore; LP, large pore. Error bars represent 95% confidence intervals. \*\*<sup>#</sup>p<0.05.....227

Figure 6-8 Proportion of the porous space with bone and soft tissue growth between different coating/pore size combinations at 6 weeks. Error bars represent 95% confidence intervals. U, uncoated; PS, plasma sprayed HA; EHA, electrochemical HA; ESiHAII, electrochemical SiHA; ESrHAII, electrochemical SrHA; SP, small pore; LP, large pore. \*<sup>+</sup>p=0.047 .....228

Figure 7-1 SLS Ti<sub>6</sub>Al<sub>4</sub>V proximal femoral replacement. Assembled (left) and exploded (right) implant views shown with (a) intramedullary stem, (b) ingrowth

collar and (c) proximal femur with ingrowth regions for soft tissue attachments.  
.....253

## Table of equations

Equation 1 EC reaction where the current passing through the solution can control the pH. ....	96
Equation 2 Acid base reaction, determined by pH .....	96
Equation 3 Precipitation reaction, influenced by the concentration of $\text{HPO}_4^{2-}$ ...	96
Equation 4 Conversion of brushite into HA by immersion in NaOH for 72hrs. ...	96
Equation 5 Silicate substitution within HA lattice.....	120
Equation 6 Calculating current density using current and surface area. ....	126
Equation 7 The relationship between electrophoretic velocity ( $v$ ), charge of particle ( $Q$ ), radius of particle ( $r$ ), voltage used to produce electric field ( $E$ ) and $\eta$ can be considered as a constant as the concentration of HA particles in solution is usually low (Mondragon-Cortez and Vargas-Gutierrez, 2004). ....	163
Equation 8 Serial reactions leading to the formation of $\text{CaSiO}_3$ .....	204

## Abbreviations

Ø.....	Diameter
3D.....	Three-dimensional
AL.....	Aseptic loosening
ALP.....	Alkaline phosphatase
AM.....	Additive manufacturing
ANOVA.....	Analysis of variance
at%.....	Atomic percentage
CT.....	Computed tomography
CaP.....	Calcium phosphate
Ca:P.....	Calcium to phosphate ratio
DFR.....	Distal femoral replacement
<sup>d</sup> H <sub>2</sub> O.....	Distilled water
DMEM.....	Dubelcco's modified eagles medium
DNA.....	Deoxyribonucleic acid
EC.....	Electrochemical
ECBB.....	Extracortical bone bridging
ECG.....	Electrocardiogram
EDS.....	Energy dispersive spectroscopy
EHA.....	Electrochemical hydroxyapatite
ESiHA.....	Electrochemical silicate-substituted hydroxyapatite
ESiHAlI.....	Electrochemical silicate-substituted hydroxyapatite phase 2 (chapter 5)
ESrHA.....	Electrochemical strontium-substituted hydroxyapatite
ESrHAlI.....	Electrochemical strontium-substituted hydroxyapatite phase 2 (chapter 5)
FCS.....	Fetal calf serum
FEA.....	Finite element analysis
G.....	Grooved collar
HA.....	Hydroxyapatite
HIP.....	Hot isostatic pressing
hMSC.....	Human mesenchymal stem cells
ICPMS.....	Inductively coupled plasma mass spectroscopy
IMS.....	Industrial methylated spirit
IQR.....	Interquartile range
LP.....	Large pore collar
mA.....	Milliamps
mol%.....	Molar percentage
MRI.....	Magnetic resonance imaging
MSC.....	Mesenchymal stem cells
oMSC.....	Ovine mesenchymal stem cells
OPG.....	Osteoprotegerin
PBS.....	Phosphate buffered saline
PEEK.....	Polyetheretherketone
PLD.....	Pulsed laser deposition
PS.....	Plasma spray

PTH.....	Parathyroid hormone
RANK.....	Receptor activator of nuclear factor $\kappa$ B
RANKL.....	Receptor activator of nuclear factor $\kappa$ B ligand
RLL.....	Radiolucent line
SD.....	Standard deviation
SEM.....	Scanning electron microscopy
Si.....	Silicon
SiHA.....	Silicate-substituted hydroxyapatite
SLS.....	Selective laser sintering
SP.....	Small pore collar
Sr.....	Strontium
SrHA.....	Strontium-substituted hydroxyapatite
Ti.....	Titanium
Ti <sub>6</sub> Al <sub>4</sub> V.....	Titanium alloy (6% aluminium 4% vanadium)
TKA.....	Total knee arthroplasty
U.....	Uncoated
wt%.....	Weight percentage
XRD.....	X-ray diffraction

## **Chapter 1. Introduction**

Bone and soft tissue sarcomas are uncommon diagnoses and have been associated with high rates of mortality and morbidity. Advances in medicine and medical technology have improved rates of mortality although a significant morbidity remains. The gold standard treatment is chemotherapy, tumour resection and limb salvage with the use of endoprostheses.

When successful, the endoprosthesis allows for the patient to regain excellent function even after a significant resection. Unfortunately these endoprostheses have high rates of failure and patients undergo multiple operations as a result. The most common reason for failure is loosening of the implant. HA collars have been used as an ingrowth region to improve rates of loosening and implant survivorship, which they have done. Literature has shown that endoprostheses are subjected to high stresses that may lead to catastrophic failure as well as confirming that greater osseointegration of the implant offloads these stresses.

Orthopaedic implant technology is ever-evolving and this thesis aims to further the design of the HA collar to maximise its potential for osseointegration by utilising novel technologies such as 3D printing combined with electrochemically deposited coatings.

In the following introduction section, the biology of bone and the pathways involved in its turnover are described. Types of bone tumours are reported, as patients with these tumours ultimately undergo reconstruction and limb salvage using endoprostheses. The design evolution of orthopaedic implants including endoprostheses is discussed and the notion of 3-dimensional printing in the context of orthopaedics is reviewed. Finally, the techniques used to improve bioactivity of these implants are discussed together with coating techniques.



## 1.1 Bone structure

Bone is a highly specialised tissue with unique properties that allow for its central role as a structural support, source of haematopoiesis and as a mineral reservoir. It supports muscle and connective tissue to form the musculoskeletal system enabling motion (Taichman, 2005). Its anisotropic properties allow it to withstand ever changing biomechanical forces and undergo remodelling to improve bone strength in areas of load bearing and in fracture repair.

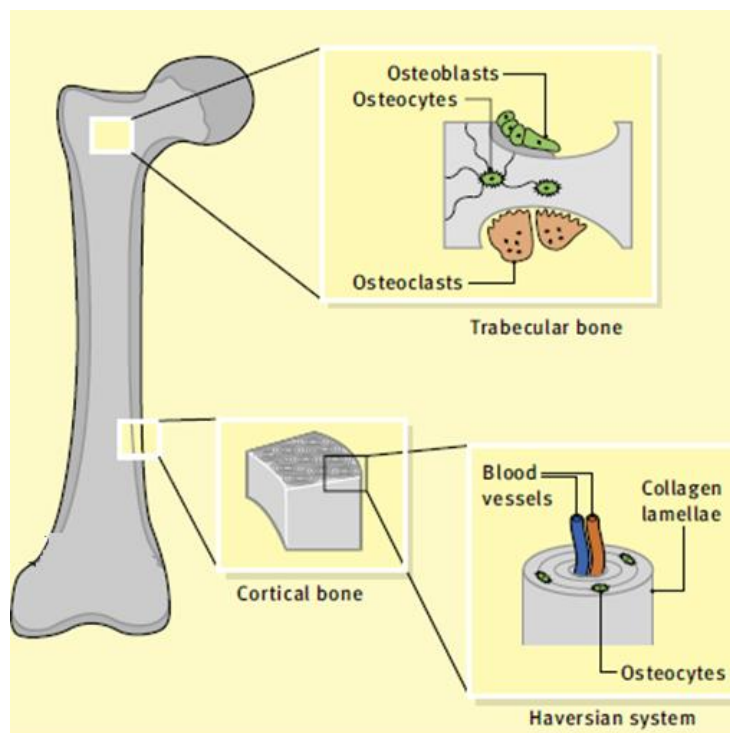


**Figure 1-1: The trabecular and cortical structure of bone. The cortical structure of bone consists of the Haversian system that is made up of a central canal of blood vessels surrounded by the concentric collagen lamellae (Ralston, 2005).**

There are two main variations of bone type; cortical and cancellous (or trabecular) (Figure 1-1). Cortical bone is dense, macroscopically solid and surrounds the marrow space with an external periosteal surface and an internal endosteal surface. The periosteal layer or periosteum envelops the cortical bone except at the joint surfaces. It is a fibrous connective tissue which provides a blood supply and nerve innervation, as well as containing osteoblasts and osteoclasts. Periosteum protects bone and provides nutrients for survival and has a central role in appositional growth of bone (Dwek, 2010). The endosteum is a membrane covering the inner surface of the cortical bone, the blood vessel canals (Volkmann's canals) within the cortical bone as well as

the network of cancellous bone (Davis et al., 1975). The periosteum comprises of an outer fibrous layer that consists of fibroblasts, collagen and elastin together with a neurovascular supply, altogether which provides structural support. The inner cambium layer is a cellular layer that provides the source of adult mesenchymal skeletal progenitor cells, osteoblasts and fibroblasts and therefore has a key role in bone growth, healing and remodelling (Allen et al., 2004). It is this layer that plays a key role in allowing for bone growth onto the ingrowth regions on orthopaedic implants such as hydroxyapatite collars that will be discussed later in this chapter.

Trabecular or cancellous bone has a honeycomb-like open porous structure composed of plates and rods forming trabeculae with spaces between them that are filled with bone marrow. The distribution of cortical and cancellous bone throughout the skeleton differs although the majority consists of cortical bone. Cancellous bone has a higher surface area when compared with cortical bone and remodels more rapidly (Ralston, 2005).

If categorising bone based on the organisation of collagen within it, two groups are identified. Woven bone is characterised by a haphazard organisation of collagen fibres whereas lamellar bone is identified by regular parallel alignment of its collagen fibres into sheets (Haversian lamellae with a central Haversian canal containing blood vessels). As a result, lamellar bone is far stronger than its woven counterpart. Woven bone is produced when there is rapid production of non-mineral matrix composed of collagen and non-collagen proteins by osteoblasts, classically in fracture healing (callus). Over time this woven bone undergoes remodelling to become lamellar bone which forms the most abundant type of bone in a mature adult.

The gross anatomy of a long bone consists of a central tubular shaft known as the diaphysis which comprises mainly of cortical bone surrounding a medullary cavity with bone marrow and little cancellous bone. The wider section proximally and distally to the diaphysis is known as the epiphysis, the walls of which consist of cortical bone but the intramedullary area consists of a higher proportion of cancellous bone to bone marrow. The region where the diaphysis meets the epiphysis is known as the metaphysis.

## 1.2 Bone formation

Bone is composed of three distinct cell types; osteoblasts, osteoclasts and osteocytes (Rodan, 1992) combined with osteoid and inorganic salts deposited within the matrix. Bone undergoes continual turnover and changes during one's lifetime that include radial and longitudinal growth, reshaping and remodelling (Clarke, 2008). This remodelling is associated with the activity of these three different types of bone cells.

Osteogenesis is the process by which new bone is formed by osteoblasts. These cells are responsible for the regulation and differentiation of osteoclasts and formation of bone matrix (Mackie, 2003).

### 1.2.1 Osseinduction, osseoconduction and osseointegration

Osseinduction was historically defined as 'the mechanism of cellular differentiation toward bone of one tissue due to the physicochemical effect or contact with another tissue' (Urist et al., 1967). Over the last 50 years the definition of osseinduction has evolved due to the vast improvements in behavioural cell analysis. As a result, osseinduction is now seen as the process whereby primitive, undifferentiated, pluripotent cells are stimulated to start differentiating down an osteogenic cell line (Albrektsson and Johansson, 2001). It can be divided into three main steps; stem cell recruitment, promotion of stem cell differentiation to osteoblasts and finally production of ectopic bone *in vivo* (Miron and Zhang, 2012).

Osseoconduction is the growth of bone onto a surface. This surface permits growth onto it, down into channels or its pores (Albrektsson and Johansson, 2001). In the case of implants, bone growth into them will only occur if full vascularisation is permitted. Locally acting factors are therefore mitogenic as well as angiogenic (Trippel et al., 1996). Osseoconductivity of an implant or surface can be further improved by coatings, surface topography and porosity, this will be described later in this chapter.

Osseointegration was described by Branemark et al (Branemark, 1977) and defined by Albrektsson et al (Albrektsson et al., 1981) as direct contact of living

bone with an implant seen under light microscopy. Biomechanical definition describes osseointegration as ‘a process whereby clinically asymptomatic rigid fixation of alloplastic materials is achieved, and maintained, in bone during functional loading’ (Zarb and Albrektsson, 1991).

### 1.2.2 Mesenchymal stem cells (MSCs)

First reported by Friedenstein (Friedenstein et al., 1970), MSCs were isolated from bone marrow and formed multipotent fibroblast-like colonies that can differentiate into adipocytes, chondrocytes, osteoblasts and myoblasts. Horwitz et al (Horwitz et al., 2005) defined MSCs by an array of phenotypic markers and ability for multipotential differentiation. Mechanisms dictating MSC migration is not fully understood (Méndez-Ferrer et al., 2010) although bone morphogenic proteins and platelet derived growth factors have been shown to play a role in rapidly recruiting MSCs to sites of injury (Ai-Aql et al., 2008, Miron and Zhang, 2012).

### 1.2.3 Osteoblasts

Osteoblasts originate from MSCs that can give rise to myoblasts, adipocytes and chondrocytes (Ducy et al., 2000). The key factors involved are shown in Table 1-1. Expression of Runt-related transcription factor 2 (Runx2) (Banerjee et al., 1997) and osterix (Nakashima et al., 2002) are essential in the process whereby MSCs differentiate into osteoblasts (Figure 1-2).

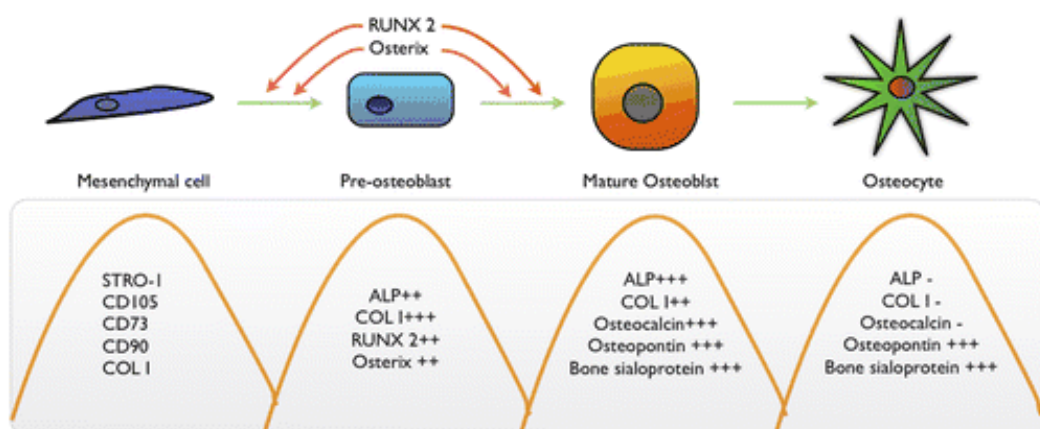


Figure 1-2 A list of differentiation markers for MSCs, pre-osteoblasts and osteocytes during MSC differentiation to osteoblasts and osteocytes. (Miron and Zhang, 2012)

Runx2 stimulates the production of collagen I, providing a structural framework for bone formation (Boskey et al., 1999). MSCs then differentiate into pre-osteoblast cells and these are characterised by alkaline phosphatase expression (ALP), an early marker of osteogenic differentiation (Tenenbaum, 1987). Once the pre-osteoblasts have developed into osteoblasts there is elevated expression of bone sialoprotein and osteocalcin. Bone sialoprotein has a role within the initial production of hydroxyapatite and hence in the mineralisation of bone (Tye et al., 2005). Osteocalcin is the most abundant non-collagenous protein in bone and also plays a role in bone growth and turnover as well as being a later marker of osteogenic differentiation (Miron and Zhang, 2012). Ligand-receptor-protein 5 (LRP5) is a further key regulator of bone formation and is activated by the Wnt family of proteins. Antagonistic to this is sclerostin, which is produced by osteocytes and inhibits bone formation by keeping the osteoblast in a quiescent state.

<b>Factor</b>	<b>Function</b>
Runx2	Transcription factor
Osterix	Transcription factor
Sclerostin	Inhibits bone formation, antagonistic with Wnt binding to LRP5
LRP5	Receptor
Wnt	Ligands to LRP5
Beta-catenin	Transcription factor

**Table 1-1 Molecules for osteoblast differentiation and function. Modified from Ralston, 2005.**

These mononuclear cells are not terminally differentiated. When active, a large Golgi apparatus and abundant rough endoplasmic reticulum is visible. Osteoblasts form tight junctions with neighbouring osteoblasts to allow for the development of a specialised plasma membrane allowing for vesicular trafficking and secretion (Caetano-Lopes et al., 2007). When quiescent, osteoblasts form bone-lining cells that cover the bone surfaces where neither bone resorption nor does bone formation occur. These cells are flat in nature with some of them showing processes extending into the canaliculi, with gap junctions being seen between the bone lining cells and osteocytes as well as between bone lining cells themselves. Although these cells are not actively producing osteoid, when it is required they are able to re-acquire their secretory activity, hypertrophy and become cuboidal in shape (Florencio-Silva et al., 2015).

The Wnt pathway and associated proteins are required for mesenchymal cells to commit down an osteoblastic lineage (Logan and Nusse, 2004). As they differentiate they begin to secrete uncalcified bone matrix (osteoid) which subsequently becomes calcified to form mineralised bone. Some osteoblasts become trapped within this osteoid and become known as osteocytes which are the most abundant cell type in bone. Their role is of a mechanosensor, instructing osteoblasts and osteoclasts to form and resorb bone respectively (Boron and Boulpaep, 2003, Manolagas, 2000). Hormones, growth factors, physical activity amongst other stimuli act through osteoblasts to effect bone formation (Harada and Rodan, 2003).

#### **1.2.4 Osteocytes**

The terminal form of a differentiated osteoblast is an osteocyte. These make up for over 95% of bone cells (Knothe Tate et al., 2004). They are a major signal sensor, integrator and transducer of the skeleton. Once embedded in the bone matrix they remain connected to each other, the bone surface, osteoblasts and the bone marrow (Kamioka et al., 2001, Palumbo et al., 1990) with a dendritic network via gap junctions which are composed of connexin (Bonewald, 1999, Plotkin et al., 2002) that run through the canaliculi. Osteocytes undergo apoptosis as suggested by the presence of empty lacunae that once were occupied by them. Oestrogen deficiency and chronic steroid treatment is harmful to bone structure. The use of hormone replacement, bisphosphonate therapy and physiological loading of bone may prevent osteocyte and osteoblast apoptosis (Plotkin et al., 2002) and in turn osteoporosis.

#### **1.2.5 Osteoclasts**

Osteoclasts are multinucleated cells that are involved in the resorption of mineralised bone at sites called Howship's Lacunae (Sommerfeldt and Rubin, 2001, Teitelbaum, 2000, Ralston, 2005). They are derived from myeloid/monocyte lineage, which circulate in blood vessels once they have been formed in the bone marrow. Once in circulation they are attracted to sites on bone surfaces. Multiple pre-cursor cells fuse to form a single multinucleated

cell with the ability to absorb calcified bone. Osteoclast formation, under normal circumstances is mainly controlled by osteoblastic cells.

Once formed mature osteoclasts form a tight sealing zone in order to attach to the bone surface demarcated by an actin ring that forms round the cell periphery. Hydrochloric acid as well as proteolytic enzymes are secreted into a space beneath the cell via a specialised membrane known as the ruffled border. The HCl creates an acidic environment at around pH 4 that dissolves the bone mineral. This hostile environment enables the removal of the organic phase of bone with cathepsin K, a matrix metalloproteinase and one of the most important proteases secreted by osteoclasts, allowing the breakdown of collagen (Ralston, 2013). The dual action of cathepsin k and hydrochloric acid causes a localised pit to form on the bone surface referred to as Howship's lacunae.

The RANK-RANKL pathway is essential for the differentiation of mature osteoclasts and ultimately bone resorption (Figure 1-3). Osteoblasts produce receptor activator nuclear factor kappa beta ligand (RANKL) which stimulates osteoclastogenesis as well as osteoprotegerin (OPG) which acts as a competitive blocker and binds to RANKL also decreasing the development of osteoclasts and bone resorption. RANKL interacts with a membrane bound receptor on the osteoclast precursor cell called RANK which when bound to RANKL induces the osteoclast precursor cells to differentiate. OPG is a soluble factor whereas both RANK and RANKL are membrane bound and so for an osteoclast to form the osteoclast precursor cells have to make contact with one another. Bone resorption is therefore partially controlled by these two proteins and their interaction with OPG. Another factor that is necessary for osteoclasts to form is a soluble cytokine produced by osteoblasts called macrophage colony stimulating factor.

There is therefore tight control of bone remodelling through complex interactions between cells and proteins. For remodelling to occur, appropriate cell signalling occurs to trigger osteoclasts to resorb the surface of the bone, followed by deposition of bone by osteoblasts. Together, the cells in any given particular region of the bone surface that are responsible for bone remodelling are known

as the basic multicellular unit, and it is the average lifespan of the basic multicellular unit that is referred to as the remodelling period. The size of a basic multicellular unit is roughly 200µm in diameter. The rate of remodelling is regulated by a wide variety of calciotropic hormones (PTH, thyroid hormone, sex steroids etc.). Bone remodelling is believed to proceed in a specialized vascular structure called the bone remodelling compartment that encloses the surface of the bone.

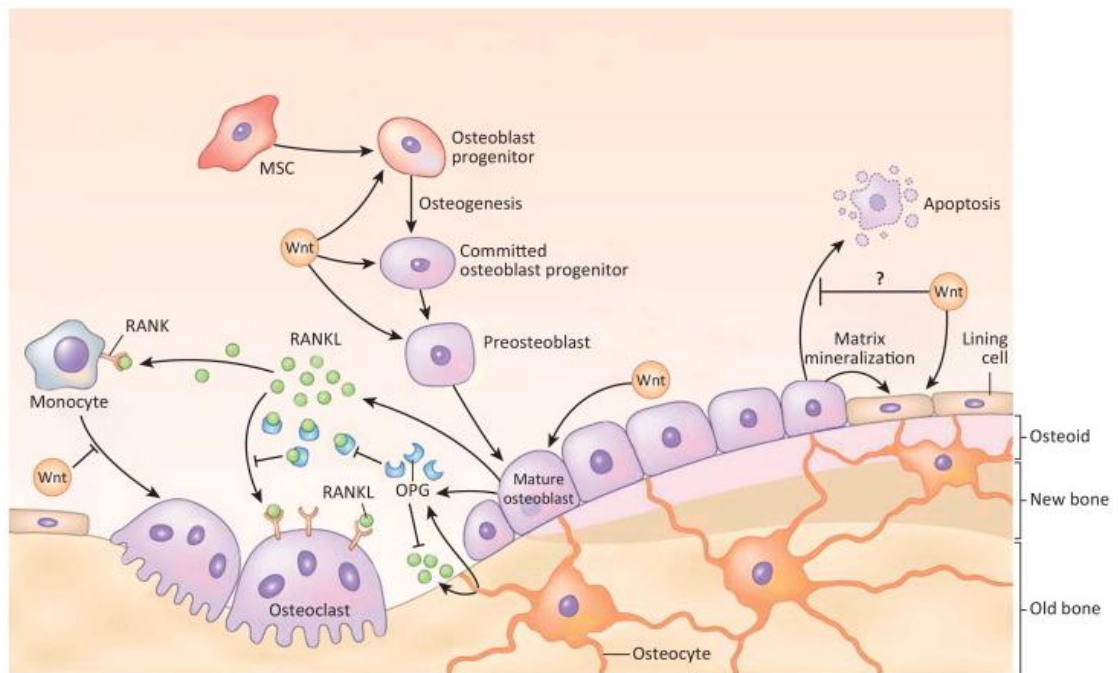


**Figure 1-3 Schematic representation of the influence of pathways upon bone remodelling (Bose et al., 2013).**

### 1.2.6 Intramembranous ossification

This form of bone development is what has already been described in the sections above. Mesenchymal cells proliferate and condense to form nodules. These differentiate into osteoblasts that start secreting osteoid with some of them getting trapped within forming osteocytes. As the calcification proceeds, bony spicules radiate out from the original area of ossification. The entire region of calcification also becomes surrounded by mesenchymal cells to form the periosteum with the inner surface cells becoming osteoblasts. These cells deposit further osteoid parallel to the existing spicules and as a result, layers of bone are formed (Gilbert, 2000) without any preceding cartilage.

### 1.2.7 Endochondral ossification

Most bones develop through endochondral ossification. This involves the formation of cartilage tissue from mesenchymal cells followed by the subsequent replacement of this by bone.

Mesenchymal stem cells migrate to form groups which subsequently differentiate into chondrocytes. These cells then produce a cartilage extracellular matrix. Once this basic cartilage model of the bone is produced, it is invaded by cells in its centre and at the ends forming primary and secondary ossification centres respectively. The cartilage is then replaced by bone starting from the ossification centres until skeletal maturity at which point the whole cartilaginous structure has been replaced by bone tissue apart from the cartilage layer forming the joints (Mackie et al., 2008).

The growth and behaviour of these chondrocytes are controlled by local (Indian hedgehog, parathyroid related peptide, fibroblast growth factors and cartilage extracellular matrix) and systemic factors (growth hormone, thyroid hormone). Transcription factors that control gene expression dictating cellular phenotype include Runx2, Sox9 and myocyte enhancer factor-2C (Mackie et al., 2008).

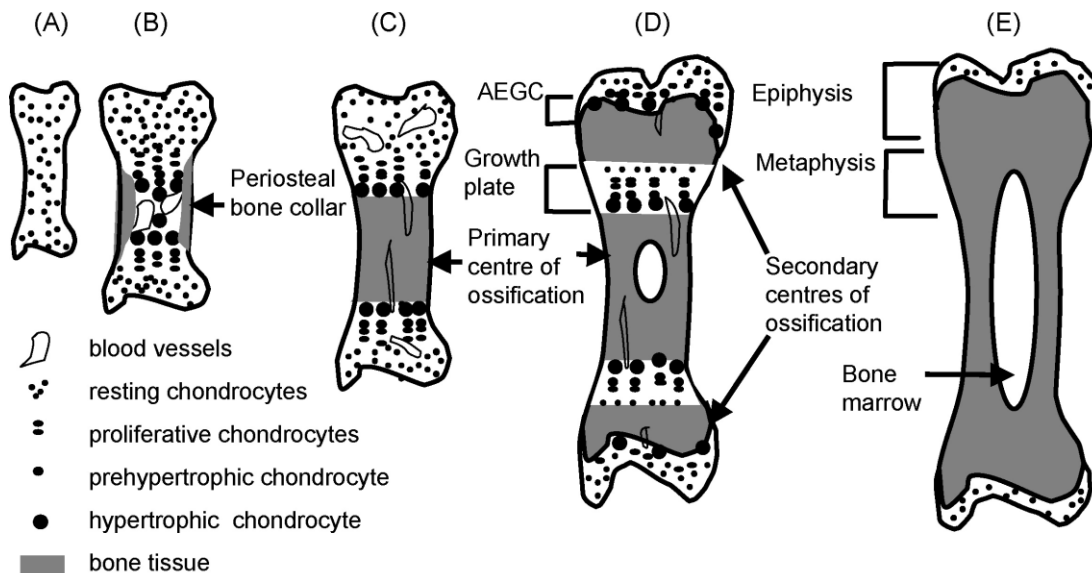


**Figure 1-4 Stages of endochondral ossification. (A) Cartilage model. (B) Formation of primary centre of ossification. (C) Established primary centre, angiogenesis in remaining cartilage model. (D) Development of secondary centres of ossification responsible for longitudinal growth. (E) Adult bone where the growth plate has fused. From Mackie et al (Mackie et al., 2008).**

### **1.2.8 Strain related bone remodelling**

Wolff proposed that a relationship ('Wolff's Law') between bone structure and the mechanical load it was subjected to existed with subsequent studies showing that the orientation of the trabecular structure within the proximal femur was the same direction as the stress trajectories. This allows for maximal strength with minimal weight (Hazenberg et al., 2006).

Mechanically induced bone remodelling is caused by strain magnitude, stress, cycle number, strain history and strain rate amongst others. Other studies have based their models on fatigue characteristics such as frequency of cracks and length of these cracks in the bone. If strain levels within the bone are above or below a certain critical level, cellular processes locally would then shift the equilibrium between bone resorption and bone production appropriately. It has become apparent that cellular responses in bone can be initiated by mechanotransduction. This process alters gene expression and protein synthesis. Osteocytes embedded within the bone are thought to provide feedback as a result of load-induced fluid flow and shear stresses that are detected via the lacuna-canalicular system (Hazenberg et al., 2006).

### **1.2.9 Bone matrix**

Bone constitutes an inorganic component (70%) of which 99% is hydroxyapatite and an organic component (25%) of which 90% is collagen type 1. 5% is made up of water. Hydroxyapatite is a complex of calcium and phosphate and gives bone its hardness and rigidity.

Osteoblasts synthesise and lay down precursors of collagen type 1 (Brodsky and Persikov, 2005). Osteoblasts also produce osteocalcin, the most abundant non-collagenous protein in bone matrix and proteoglycans. In rapidly forming bone, collagen 1 is deposited in organised parallel concentric layers forming lamellar bone whereas in instances where there is rapid deposition of collagen (e.g. fracture healing) it is organised in a basket like weave resulting in woven bone.

There are a number of non-collagenous proteins also synthesised and secreted by osteoblasts. The main being ALP, which aids in extracellular mineralisation (Orimo, 2010).

### **1.2.10 Bone mineral**

The most abundant mineral component of bone is crystalline hydroxyapatite (HA). Crystals are deposited along and are closely related to bone collagen fibrils seen under scanning electron microscopy. Inorganic phosphate (phosphorous) and calcium are sourced from nutrition. Calcium phosphate undergoes many maturation stages before forming HA. As a consequence of the deposition of minerals on a collagen fibril, bone is a highly organised tissue with structural integrity allowing for load bearing and mechanical function. Mineral deposition is dictated by calcium regulation, which in turn is controlled by important endocrine pathways involving Vitamin D metabolites and parathyroid hormone (Quarles, 2008).

## **1.3 Bone Tumours**

### **1.3.1 Overview**

The term bone tumour encompasses a very broad spectrum of conditions that include both benign and malignant pathologies. These tumours affect patients of all ages, however there is a predilection for certain age groups allowing the tumours to be classified (Table 1-2), furthermore bone tumours can be classified based on the dominant tissue within the lesion (Table 1-3), which enables clinicians to treat the tumour appropriately.

Age (years)	Benign	Malignant
<20	Fibrous cortical defect, nonossifying fibroma, simple bone cyst, chondroblastoma, Langerhans cell histiocytosis, osteoblastoma, osteofibrous dysplasia, chondromyxoid fibroma, fibrous dysplasia, enchondroma	Leukemia, Ewing's sarcoma, osteosarcomas, metastatic disease, neuroblastoma, retinoblastoma, rhabdomyosarcoma, Hodgkin's lymphoma
20-40	Enchondroma, giant cell tumour, osteoblastoma, osteoid osteoma, chondromyxoid fibroma, fibrous dysplasia	Osteosarcoma, adamantinoma
>40	Fibrous dysplasia, Paget's disease, non-Hodgkin lymphoma, chondrosarcoma, malignant fibrous histiocytoma, osteosarcomas (secondary to Paget's and radiation)	Metastatic disease (most common), myeloma

**Table 1-2 Peak age for bone lesions.**

Predominant Tissue	Benign	Malignant
<b>Bone forming</b>	Osteoma Osteoid osteoma Osteoblastoma	Osteosarcoma: Central Peripheral Parosteal
<b>Cartilage forming</b>	Chondroma Osteochondroma Chondroblastoma ?Chondromyxoid fibroma	Chondrosarcoma: Central Peripheral Juxtacortical Clear-cell Mesenchymal
<b>Fibrous tissue</b>	Fibroma Fibromatosis	Fibrosarcoma
<b>Mixed</b>	Chondromyxoid fibroma	
<b>Giant-cell tumours</b>	Benign osteoclastoma	Malignant osteoclastoma
<b>Marrow tumours</b>		Ewing's tumour Myeloma
<b>Vascular tissue</b>	Haemangioma Haemangiopericytoma Haemangioendothelioma	Angiosarcoma Malignant haemangiopericytoma
<b>Other connective tissue</b>	Fibroma Fibrous histiocytoma Lipoma	Fibrosarcoma Malignant fibrous histiocytoma Liposarcoma
<b>Other tumours</b>	Neurofibroma Neurolemmoma	Adamantinoma Chordoma

**Table 1-3 Classification of bone tumours. Revised WHO classification.**

### 1.3.2 Epidemiology

Sarcomas are malignant tumours of connective tissues with bone sarcomas being tumours of the skeleton and soft tissue sarcomas arising from mesenchymal tissue such as muscle, fat and blood vessels to name a few (Fletcher et al., 2002). They represent 1% of all adult cancers, 8% of adolescent cancers and 10% of cancers in children. Despite its rarity, these sarcomas

contribute to a large number of years of life lost given the relatively young demographic diagnosed with it (Amankwah et al., 2013).

According to the Surveillance, Epidemiology, and End Results (SEER) program there would have been 3,300 new cases, accompanied by 1,490 deaths (Howlader et al., 1975-2013) in the USA during 2016 alone. This type of cancer is most frequently diagnosed in those aged less than 20 years with 27% of new diagnosis belonging to that age group (Figure 1-5).

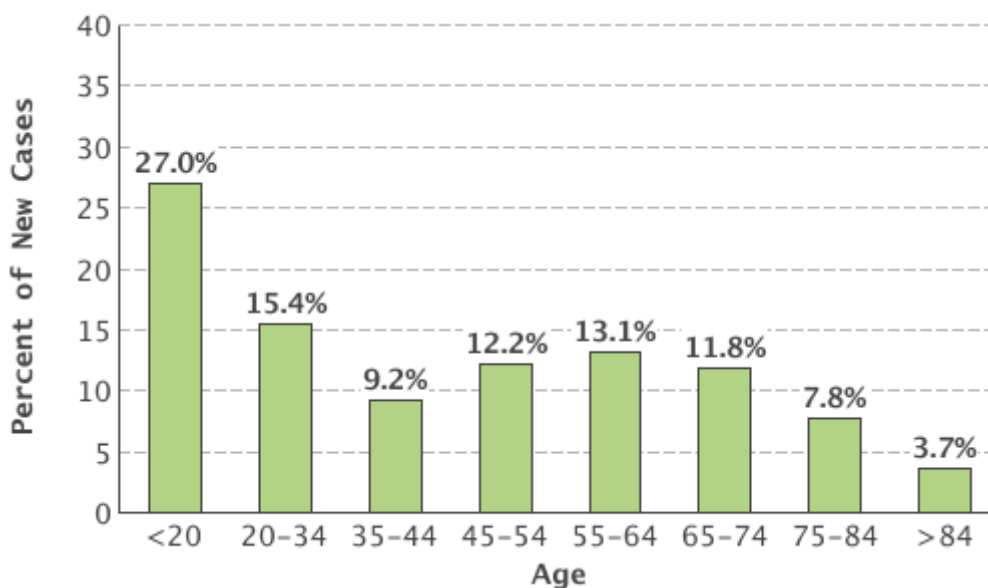


**Figure 1-5 Percent of new cases of malignant bone tumours by age group (Howlader et al., 1975-2013).**

Nearly 90% of patients with extremity bone tumours are candidates for limb-salvage surgery. The ability to reconstruct bone defects as a result of the tumour excision is made possible by the greater understanding of biological reconstructions using allografts as well as the advancement of endoprosthetic design.

#### **1.4 Allograft reconstruction**

Massive allografts can be used to reconstruct osseo-articular defects left after bone tumour resection. A common location for a primary bone tumour is around the knee and therefore resection of the tumour would involve loss of major tendon and ligamentous structures as well as some, if not, the whole joint. Allograft reconstruction allows for this defect to be filled with part of a joint and bone from a donor.

There are several advantages with the use of biological reconstruction with improved tendon-to-tendon healing as the allograft has preserved soft tissue attachments where the host tendons can be attached to. Allografts avoid the need for massive segmental stemmed implants that may have to cross growth plates and therefore affect limb development. The successful incorporation of an allograft with the host skeleton also increases the bone stock at the site of the initial resection, which can later be used in further reconstructions (Levin et al., 2017).

There are however disadvantages with the use of allografts. There is a significant shortage in the supply of appropriate massive allografts available for reconstructions in young patients which is an obvious problem given the incidence of bone tumours in this cohort. These allografts cannot be lengthened and therefore for skeletally immature patients they are left with limb length discrepancies and will have to undergo further procedures. There is also a high rate of mechanical failure and fracture with autografts coupled with high rates of infection, which is potentially devastating. Grafts may not incorporate with the host bone and therefore fail to produce significant structural integrity (Levin et al., 2017). As stabilising ligamentous structures are also removed in certain resections, instability has been observed in 72% of patients with proximal tibial allografts together with joint collapse from cartilage necrosis (Muscolo et al., 2010).

### **1.5 Rotationplasty**

Initially described by Borggreve et al (Borggreve, 1930) for patients left with limb deformities as a sequelae of tuberculosis, its popularity has diminished with the advent of improving implant designs. It still has a role as an option for failed limb salvage procedures. It involves the use of the lower leg below the knee as a surrogate for the distal femur with the foot rotated around to face the opposite direction and hence the ankle is used to replace the knee joint. This allows for less energy expenditure during ambulation compared with above knee amputations (van der Windt et al., 1992). This procedure avoids phantom limb pain, the need for further limb lengthening procedures, revision surgery for failed prostheses and loosening (Levin et al., 2017).

Complications of rotationplasty include delayed healing and infection. Vascular compromise has been reported being as high as 12% which would lead to amputation. Rotationplasty is an option which exists for those cases where limb salvage is not possible or has failed with amputation being the only other remaining option (Levin et al., 2017).

## **1.6 Endoprostheses**

### **1.6.1 Evolution of the endoprosthesis**

Austin-Moore created the first metallic endoprosthesis using an alloy known as Vitallium (Moore, 1952) to reconstruct a proximal femur following resection of a giant cell tumour. Radiographs at one year showed extracortical bone formation around the shaft of the implant. Following this success, the development of endoprosthesis had been started using Vitallium as well as other materials (Brav et al., 1958, Horwitz, 1955, Loomis, 1950, Macausland, 1954, Moore, 1957, Seddon and Scales, 1949, Venable, 1952). However success was still limited and at this time, amputation remained the gold standard in managing bone tumours.

Due to technological advances in various medical fields and improvements in the life expectancy of musculoskeletal tumour patients, advances in the development and manufacture of orthopaedic tumour implants grew rapidly in the 1970s. The advent of the modern tumour endoprosthesis had started with clinicians using pre-operative chemotherapy in conjunction with endoprosthetic reconstruction allowing improved survival rates together with limb salvage (Huvos et al., 1977, Rosen et al., 1976, Sinks and Mindell, 1975). Neo-adjuvant and adjuvant chemotherapy is currently the most common form of chemotherapy used in musculoskeletal oncology.

Developments in material science in producing titanium (Ti) alloys, most notably  $Ti_6Al_4V$ , paved the way for an improvement in endoprosthesis performance in resisting corrosion (Golish and Mihalko, 2011) and silver coating in reducing rates of infection (Ghani et al., 2012).

This has led endoprostheses to be the main choice in limb reconstruction for patients provided the tumour had been resected with satisfactory margins. This allows for successful functional rehabilitation with local recurrence rates being similar to amputation (Grimer et al., 2002) making endoprosthetic reconstruction and limb salvage the gold standard in the management of primary bone tumours.

The use of endoprostheses was popularised in the 1990s. These endoprostheses were either cemented or uncemented. John Charnley popularised the use of bone cement in the 1970s (Charnley, 1970) and his principles were applied to the fixation of endoprostheses, which comprised of an intramedullary stem continuous with the implant being cemented into the canal of the remaining bone. It became apparent that these cemented implants were becoming loose at the cement-implant interface leading to osteolysis of the surrounding bone. Cortical bone loss is seen initially at the point of direct contact between the bone and the shoulder of the implant. This is followed by worsening osteolysis thought to be induced by wear debris from the polymethylmethacrylate cement, which is commonly used for the initial fixation of the implant (Ward et al., 1997).

Loosening then led to implant failure although that it was not the sole cause. Wirganowicz et al (Wirganowicz et al., 1999) first described the causes of endoprosthetic failure and categorised them into mechanical and non-mechanical causes. Henderson et al further developed upon this to classify endoprosthetic failure into 5 different modalities; soft tissue failure (type I), aseptic loosening (type II), structural failure (type III), infection (type IV) and tumour progression (type V) (Henderson et al., 2011).

### **1.6.2 Aseptic loosening of endoprostheses**

Aseptic loosening (AL) in the context of cemented endoprostheses is the failure of the cement-bone interface surrounding the intramedullary stem of the implant. This occurs due to lack of osseointegration of the implant leading to excessive forces passing through the stem.

AL is one of the major causes of failure of endoprostheses and accounted for 25% of revisions in a series of 661 (Jeys et al., 2008). This study included both upper and lower limb cases. Distal femoral and proximal tibial replacements performed the worst in respect to AL with rates of 31% and 37% respectively. This was further supported by Unwin et al (Unwin et al., 1996), whose results were even worse in younger patients who placed increased mechanical demands on the implant leading to accelerated AL and earlier failure.

This stimulated the development of alternative designs in an attempt to reduce the rates of AL. Uncemented endoprostheses were subsequently developed however these were found to have higher rates of AL compared with the cemented implants due to poor initial intra-operative fixation (Batta et al., 2014). Cemented implants have therefore undergone further design changes in order to address issues of long-term survivorship and AL. Uncemented implants are also evolving with the development of the Compress® Compliant Pre-Stress Implant (Biomet, Warsaw, IN) which is an intramedullary device and provides continuous self adjusting compression of the implant onto the bone at the transection site that is thought to stimulate bone growth. Results however do not show any difference in survival rate at 5 years between the Compress implant and the standard uncemented type (Farfalli et al., 2009).

### **1.6.3 Extracortical bone bridging and hydroxyapatite collar**

Modifications to the endoprosthetic design have been made in order to prevent the migration of wear particles down the bone-implant interface by improving osseointegration and promoting the formation of a 'seal' (Ward et al., 1997). Encouraging extracortical bone-bridging (ECBB) and osseointegration of an implant also has favourable effects upon stress transfer through the implant and cement mantle which is thought to further reduce AL (Chao et al., 2004, Chao and Sim, 1990, Chao and Sim, 1992, Blunn and Wait, 1991, Sim and Chao, 1979, Taylor et al., 1997).

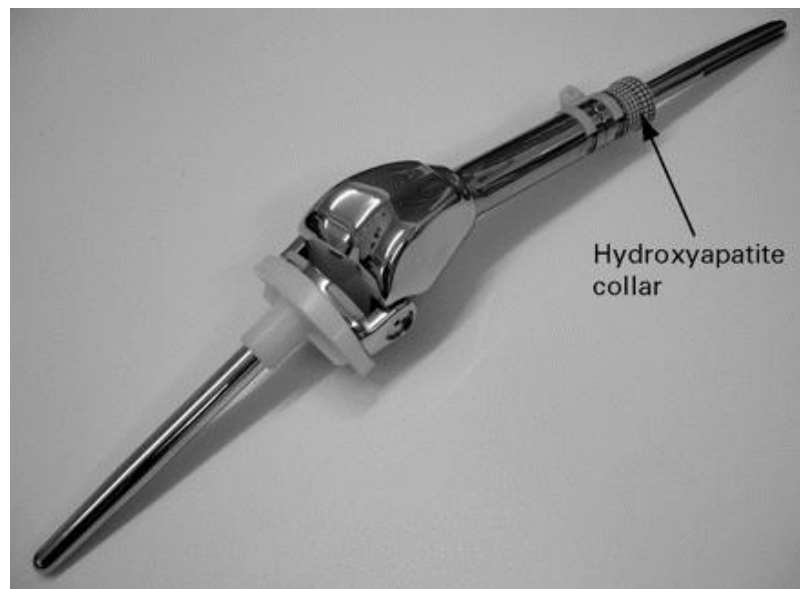


**Figure 1-6 Distal femoral endoprosthesis with HA coated collar.**

ECBB comprises of a pedicle of bone that forms adjacent to the implant shaft and has been observed frequently in endoprostheses on the medial-posterior aspect, corresponding to the areas of compressive load. Over time this pedicle increases in size. In vivo and clinical studies have shown ECBB to occur at the shoulder of endoprostheses. Histologically, direct bone implant contact of the pedicle was observed by Coathup et al (Coathup et al., 2013b). 66% of patients had evidence of osseointegration of the HA coated collar, an ingrowth region devised to encourage ECBB at the shoulder of the implant. In these patients endoprostheses survivorship was 98% at 18 years with non-osseointegrated implants showing only a 75% survivorship over the same period. Osseointegration of the extracortical bone has only been shown where a HA coating is used (Figure 1-7). In other designs with porous ingrowth regions, osseointegration is not seen although large amounts of bone formation at the shoulder are reported.



**Figure 1-7 Extracortical bony bridging onto a grooved HA coated collar as part of a distal femoral endoprosthesis.**

For adolescent patients undergoing endoprosthetic limb reconstruction, osseointegration at the implant shoulder is even more important. The implant becomes undersized as the bone grows. The stem as a result may become loose within the expanding intramedullary cavity. The undersized implant is also under increasing loads as the patient grows in size. These factors lead to high stresses passing through the implant and may eventually lead fracture of the implant at its shoulder (Figure 1-8).



**Figure 1-8 Radiograph of fractured proximal tibial replacement stem with no evidence of osseointegration (Fromme et al., 2017).**

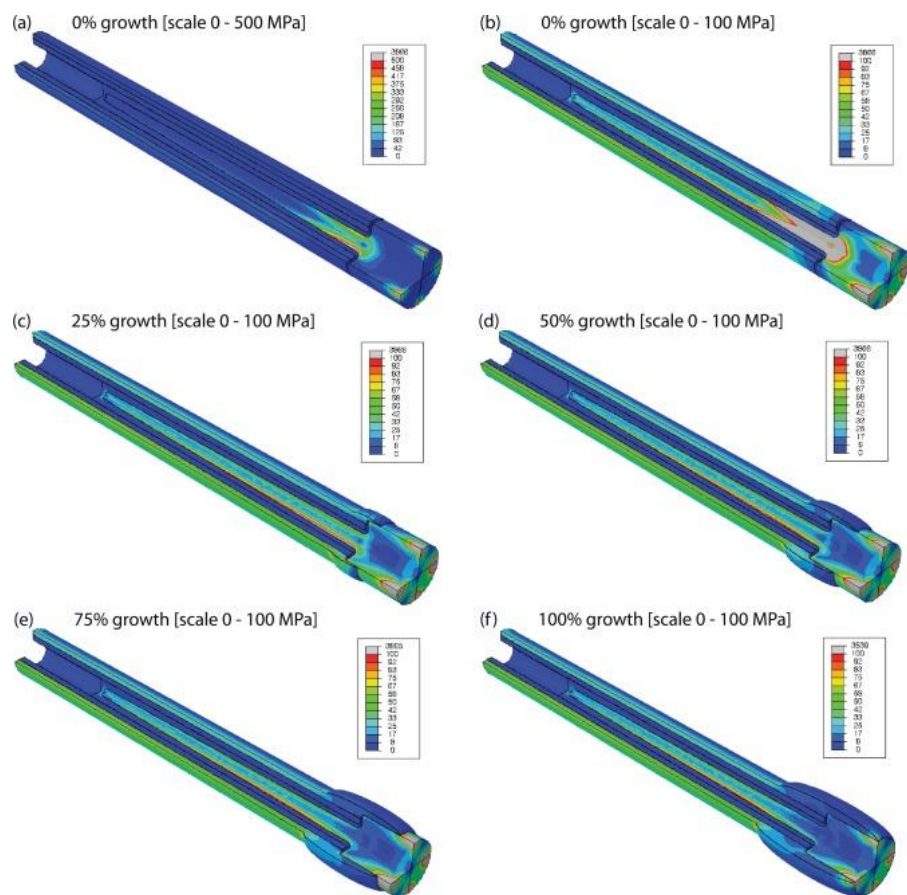


**Figure 1-9 Contour plot of stress distribution (von Mises) in FE model (bone and implant): (a) no growth, scale 0-500MPa, (b) no growth, (c) 25% growth, (d) 50% growth, (e) 75% growth, (f) 100% growth (Fromme et al., 2017).**

Finite element analysis (FEA) confirms that the stem-collar junction is the region subjected to the highest stress (Fromme et al., 2017) and clinical studies indicate that this region to be the most common site of mechanical failure (Agarwal et al., 2010). Endoprosthesis design has moved on to incorporate a HA coated grooved collar in this region, which has led to a markedly improved survivorship.

Fromme et al (Fromme et al., 2017) found that bone growth over the HA collar reduces the stress in the stem of the implant (Figure 1-9). This effect is greatest at the stem collar junction, which is the site of most mechanical failures from fatigue fracture. It is a reasonable to suggest from this work that ECBB over the HA collar reduces the risk of implant failure. Myers et al (Myers et al., 2007) observed a decrease in revision rate by 24% at 10 years for distal femoral replacements with the introduction of the HA collar. Coathup et al (Coathup et al., 2015) found reduced progression of loosening seen radiographically of

those distal femoral replacements with an HA coated collar compared to those without.

Another issue with lack of osseointegration at the shoulder of the implant is stress shielding. More of the stress is transferred from the shoulder of the implant into the tip of the stem. This leads to resorption of bone at the implant shoulder leading to weakness and fracture. ECBB where it integrates with the surface of the implant allows for a more physiological load transfer reducing the stress shielding (Fromme et al., 2017).

One of the current commercially available designs is a plasma sprayed solid  $Ti_6Al_4V$  collar with 1mm spaced vertical and horizontal grooves across its surface. Plasma spray HA is known to conduct bone growth across gaps of up to 1mm even in the presence of  $500\mu m$  of micromotion (Soballe, 1993). HA coated collars have been used at the shoulder of endoprostheses abutting against the transection site to enhance osseointegration (Figure 1-6, Figure 1-10).

It is clear that the need to maximise the ECBB occurring at the shoulder of the implant has many advantages. Reducing AL and improving longevity of the implant is paramount when considering that implant failure is catastrophic and leads to increased morbidity for the patient. It is therefore prudent to explore other technologies that will offer options in order to evolve the current design.



**Figure 1-10 AdHAesio HA Collar from Stanmore Implants**

Increasing innovation in additive manufacturing (AM), also known as three-dimensional (3D) printing and rapid prototyping, is bringing about a paradigm shift in translational medico-surgical research. This novel technology allows for the manufacturing of objects with complex geometries. A completely porous

collar can be produced using AM techniques. An open porous structure enables bone ingrowth into the collar forming a stronger bond when compared with just surface ongrowth. In theory bone can grow directly from the cortical bone at the transection site into the porous structure. AM allows the complete control over the specifications of the porous metal. The pore size and shape as well the strut size can be controlled highly accurately. As a result the biomechanical properties of the implant can be controlled to more closely mimic that of bone.

Direct bone contact is necessary to allow for effective stress transfer (Fromme et al., 2017). In order to achieve this, the AM collar requires a bioactive coating. Plasma spraying is a line of sight technique that will only coat the outer surface of a 3D printed scaffold. Electrochemically deposition of coatings is an alternative technique that allows coverage of the entirety of a complex structure. The remainder of this section introduces the concepts of porous metals and additive layer manufacturing together with coating techniques. The concept of substituted HA coatings will also be discussed as these have been shown to have greater bioactivity when compared with standard HA. One of the aims of this thesis is to develop a porous HA coated collar.

#### **1.6.4 Porous metals and pore size**

A surge in the use of trabecular metals such as porous tantalum has been seen recently, as a result in advances in the manufacturing processes involved and reduction in cost of production.

Reconstruction of bone defects in arthroplasty and bone tumour surgery using porous metals are becoming popular practice and provide an alternative to allografts and autografts. Their open cell structure allows bone to permeate through allowing osseointegration. Biomechanical characteristics of porous metals are closer to that of trabecular bone and therefore reduce stress shielding and subsequent osseous resorption around a prosthesis when compared to implants where stiffer designs are utilised and biomechanical properties are mismatched (Palumbo et al., 2011).

In order to induce bone growth the metal must have a minimum porosity of 60% (Bram et al., 2006). This favours cell ingrowth into the porous space, vascularisation and transport of metabolic products. Biocompatibility is also governed in part by porosity, a study by Tuchinsky et al (Tuchinskiy and Loufy, 2003) showed that a less porous metal, when inserted into mice, caused a greater foreign body reaction when compared to a more porous structure, both of which had identical chemical compositions. Pore shape and topography can also dictate cell ingrowth with square shaped pores performing better than round (Goodman et al., 1993) and rough pore surfaces providing increased surface area for bone attachment (Li et al., 2004). Given that the collar will be used in an area of high stress concentration and subject to loading, it is attractive to have a porous structure where the pores are not too large as it would weaken the construct that may eventually fail.

Theoretically the pore size to enhance bone ingrowth should be at least similar to that of bone trabeculae and osteons which are several tens of micrometers thick (Jasty et al., 2007). Klawitter et al (Klawitter et al., 1976) suggested a minimum pore size of 50 $\mu$ m to allow for the development of a vascular system through the porous structure, with a minimum of 200 $\mu$ m to allow for bone growth. Since this work, investigation into the optimum scaffold pore size has moved on. Studies utilising scaffolds of mean pore sizes between 20 $\mu$ m to 1500 $\mu$ m have been conducted for bone tissue engineering applications successfully (Elema et al., 1990, Pilliar, 1987, Engh, 1983, Hungerford and Kenna, 1983, Bucholz, 2002, Laptev et al., 2004, Murphy et al., 2010).

Many of the studies conducted on the effectiveness of pore size on bone ingrowth have investigated porous calcium phosphates, which are used for bone graft substitute materials. High porosity and pore sizes were recommended with scaffolds with low void volumes showing enhanced osteogenic outcomes. This would lead to significantly reduced mechanical properties of the scaffold and therefore it was recommended to have pore sizes greater than 300 $\mu$ m (Karageorgiou and Kaplan, 2005). Smaller pore sizes favoured hypoxic conditions and therefore bone formation would be preceded by chondrogenesis whereas larger pores would allow direct bone formation (Taniguchi et al., 2016). Unfortunately calcium phosphates are subject to

resorption over the study time and therefore pore size throughout the experiment is not always constant. Theoretically porosity and pore size also dictates the rate of resorption of these calcium phosphate materials (Bohner and Baumgart, 2004) and therefore is a possible confounding factor. Liu et al (Liu, 1997) however reported that there was no evidence that bone growth into a porous structure is inhibited by porosities between 12% to 80% and pore sizes less than 1µm up to 1500µm.

Ti implants with a pore size of 1000µm have been shown to cause a significant increase in cell metabolic activity and cell density when compared to a pore size of 500µm *in vitro* (Van Bael et al., 2012). Van Der Stok et al (Van der Stok et al., 2013) investigated the effect of porosity (68% and 88%) of Ti<sub>6</sub>Al<sub>4</sub>V implants with a constant pore size (490µm) and found no difference with regards to bone formation *in vivo*. *In vivo* work by Yang et al (Yang et al., 2014) (1100µm) and Wu et al (Wu et al., 2013) (710µm) involved implanting additively manufactured implants into cervical defect in sheep. Both studies suggested that porous metals allowed for enhanced bone ingrowth. Biomechanical testing proved that mechanical bone-implant stability was higher with the porous implant when compared with a polyetheretherketone (PEEK) cage (Wu et al., 2013).

Various methods have been developed to produce porous constructs (Ryan et al., 2006). A method used for some porous tantalum implants is chemical vapor deposition of tantalum chloride onto a carbon backbone. This method is precise with the morphology of the pores relying on the initial porous structure of the carbon back bone. Other less well controlled methods of producing porous structures for orthopaedic use include sintering of powders, solid state foaming, compression and sintering of Ti fibers and polymeric sponge replication (Taniguchi et al., 2016). These methods however do not allow for the accurate control of the porous metal specifications. Additive layer manufacturing provides an avenue with which pore size and shape together with strut size can all be modified to maximise osseointegration via ECBB.

### 1.6.5 Implant materials

The mechanical properties decide the type of material that will be selected for a specific application. The materials used to replace bone must have a modulus which matches that of its surrounding bone. A high degree of mismatch between the material and bone will lead to biomechanical incompatibility and hence lead to implant failure. Those implants manufactured from materials that have greater stiffness when compared to surrounding bone prevent the bone from being subjected to stress and loading as forces are transferred through the implant instead. This results in bone resorption and implant loosening known as 'stress shielding'. Ideally a material should be used which combines high strength and a modulus that mimics that of bone to avoid the stress shielding phenomenon (Geetha et al., 2009).

Materials used for implant production must not illicit any form of inflammatory, allergic or toxic reaction in the host. Biocompatibility is measured by the reaction of the human body to the implant (Williams, 2008). Biocompatibility is dictated by the host response induced by the material and the degradation of the material within the host. Thrombosis and adhesion of blood products to the material together with non-adhesive fibrous encapsulation of the implant occur from incompatibility causing significantly poorer outcomes for the implant.

Implants must be manufactured using materials with high corrosion and wear resistance. Allergic and toxic reactions are a result of metal ion release from low corrosion and wear resistant materials (Hallab et al., 2005). Wear debris can also cause implant loosening and tissue reactions when deposited (Sargeant and Goswami, 2006). Therefore corrosion and wear characteristics are very important in determining implant longevity.

Commonly used materials in implant production include cobalt chromium, Ti and its alloys. Cobalt chromium possesses a higher modulus than bone that leads to poor transfer of loads onto bone causing stress shielding. Corrosion of cobalt chrome releases cobalt and chromium ions into the body causing toxicity (Okazaki and Gotoh, 2005, Wapner, 1991). Ti based materials are popular due to high strength, low density, corrosion resistance, biocompatibility, low modulus

(Geetha et al., 2009). Specific strength of Ti alloys is higher than that of any other commercially used implant material (Geetha et al., 2009). It is this reason why Ti<sub>6</sub>Al<sub>4</sub>V is being used to produce an ingrowth collar by AM. There are however issues with the use of Ti alloys as these implants are notch sensitive and subject to wear when in contact with itself or other metals (Miller and Holladay, 1958).

## 1.7 Additive layer manufacturing

### 1.7.1 What is it?

AM has been defined as a ‘process of joining materials to make objects from 3D model data, usually layer upon layer, as supposed to subtractive fabrication manufacturing technologies’ (Schmid et al., 2014). Adopters of AM have contributed to the \$3.07 billion worldwide revenue by the end of 2013 (Wohlers, 2014). This extraordinary growth is due to the advantages of AM over traditional techniques.

The 3D model is constructed by either scanning a real 3D object, manipulating data from imaging data (x-ray, computed tomography or magnetic resonance imaging) or direct production from a computer-aided design (Collins, 2014). The material to be ‘printed’ can be in various forms (Figure 1-11). Table 1-4 describes the common AM processes and principles.

<b>Binder Jetting</b>	Layers of powder are joined by deposited liquid bonding agents.
<b>Direct energy deposition</b>	Laser is used to fuse materials by melting as they are being laid down.
<b>Material extrusion</b>	Material is dispensed through a nozzle to form an object.
<b>Material jetting</b>	Droplets of build material are laid down.
<b>Powder bed fusion</b>	Thermal energy (e.g. laser) selectively fuses regions of powder bed.
<b>Sheet lamination</b>	Sheets of material are cut and bonded to form an object.
<b>Vat photo-polymerisation</b>	Liquid photopolymer is selectively cured by light activated polymerisation.

**Table 1-4 ASTM standard terminology for AM technologies.**

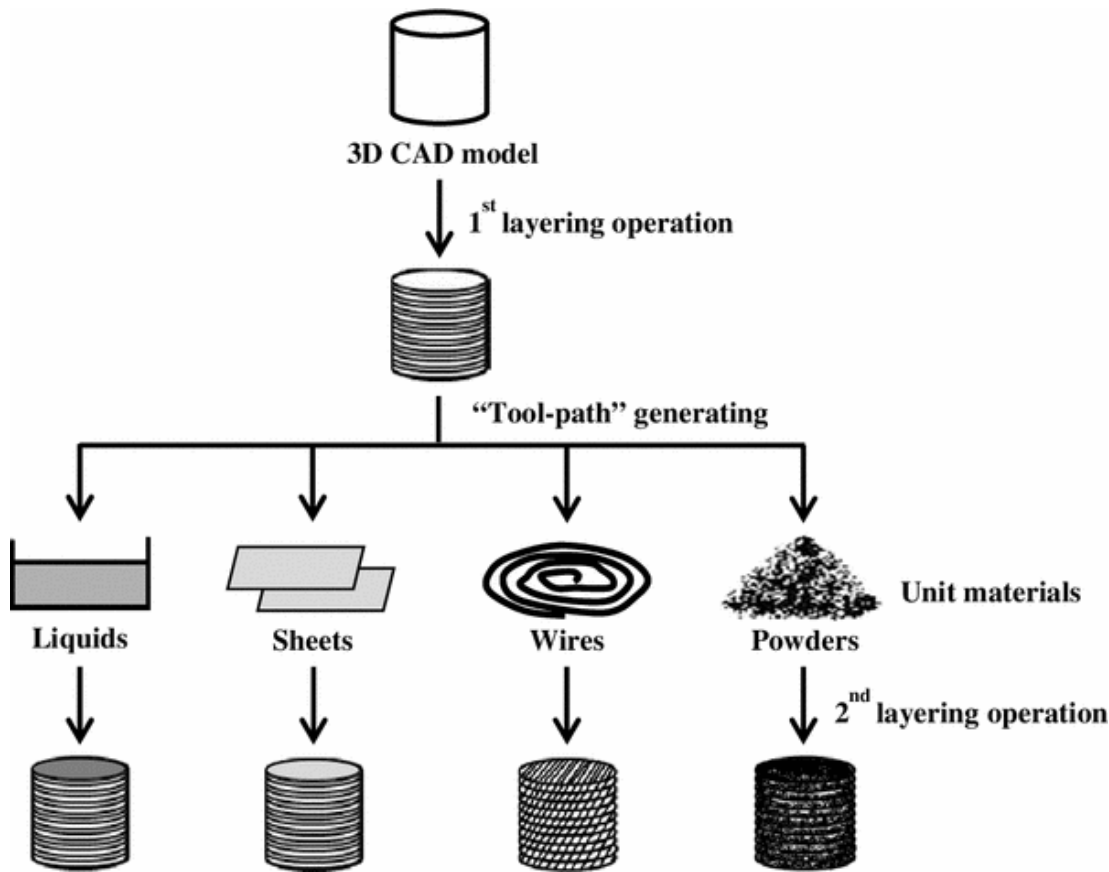


**Figure 1-11 Schematic representation of AM principles using different materials (Zhai et al., 2014), computer-aided design (CAD)**

The most commonly used AM technique is selective laser sintering (SLS), a type of powder bed fusion (Figure 1-12). The powder is fed up from the feed container and spread by the rollers into layers which are fused together by the deflected laser to form a solid layer that is also fused to the layer below. The build cylinder or platform is then lowered and the next powder layer is laid down by the roller. At the end of the process a solid object is formed and can be retrieved after the un-fused powder is removed. This process can be used to print metal and metal alloys (Leuders et al., 2013) as well as polymers (Schmid et al., 2014) and ceramics. AM technologies differ according to the composition of the material being used and how the layers are packed together (Ventola, 2014) and the majority of fabrication techniques can produce details of 50-200 $\mu\text{m}$ , alternative methods of AM such as stereolithography can build objects with sub-micron resolution (Maruo and Ikuta, 2002). Stereolithography is a vat photo-polymerisation technique that cures layers of photo-sensitive resin using an energy source (e.g. laser) on a moveable platform (Figure 1-12) (Melchels et al., 2010). The resin should be a liquid that rapidly solidifies upon illumination

with light and it is this which remains the main limiting factor with STEREO LITHOGRAPHY as only a few are commercially available. It is hoped that as our understanding of physiology and the AM technology advances, fully functional 3D-printed tissue can be formed (Collins, 2014).

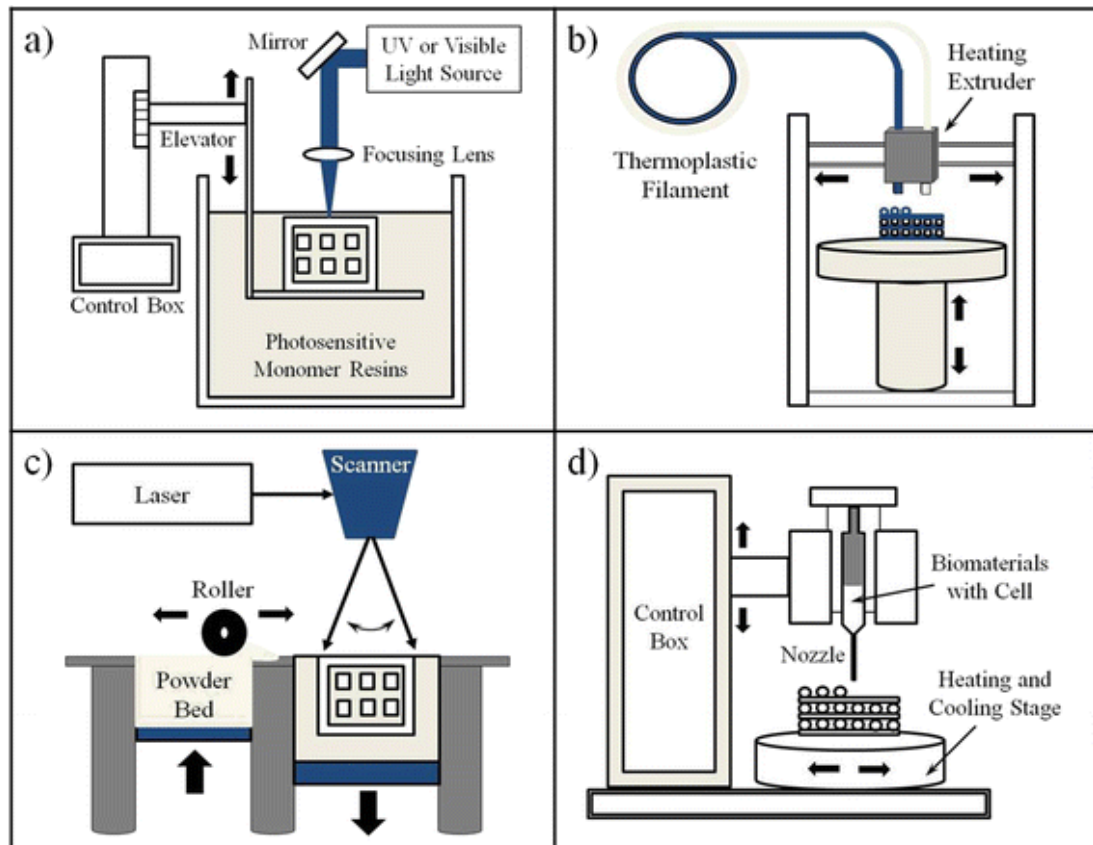


**Figure 1-12 Schematics of (a) vat polymerization, (b) fused filament fabrication, (c) selective laser sintering and (d) inkjet printing (Gu et al., 2016).**

Bioprinting will use living cells combined with scaffolds that can be 3D printed to form tissues. This area of manufacturing is new and is still in the early experimental stage but the possibility of creating functional replacement tissues and regenerative tissue is a concept that is attractive and may one day be an important treatment option for a number of tissues. The vascularisation of grafts is still a limiting factor in bioprinting. The synthesis of any tissue past a threshold thickness of 200µm requires adequate perfusion and hence a viable vascular network but to date this has not been produced successfully in vivo (Gibbs et al., 2014). Preliminary studies have produced human-scale bioprinted tissues including skin, cartilage and a vascular graft construct of fused cellular vascular rods (Murphy and Atala, 2014). The sourcing of cells as well as their viability on 3D-printed scaffolds are still issues. Long-term viability of cells on scaffolds

manufactured by 3D printers has yet to be determined. Additionally, growth factors required in bioprinting are expensive and show attenuation of effects in situ (Gibbs et al., 2014). These challenges are still yet to be surmounted, not only within the scientific sphere, but also within the remit of mass commercialization of additively manufactured implants.

AM in medical research is becoming well-established in a number of surgical fields, encompassing head and neck (Gong and Yu, 2012, Deshmukh et al., 2012, Da Cruz and Francis, 2015), cardiothoracic (Diaz Lantada et al., 2010, Sodian et al., 2011), urological (Stone et al., 2015), plastic and reconstructive (Chae et al., 2014, Ciocca et al., 2010, Xu et al., 2015), hepatobiliary (Watson, 2014) as well as orthopaedic surgery (Banerjee et al., 2014, Barnes, 2015, Chen et al., 2012).

## **1.7.2 Additive manufacturing in orthopaedics**

### **1.7.2.1 Materials and material properties**

Commonly used materials for custom AM items in orthopaedics include Ti alloy, PEEK, HA, polymethylmethacrylate, polypropylene-polyester, and acrylic based resins (Tack et al., 2016). The ability to use a range of materials to produce objects using AM is extremely appealing.

Ti and its alloys are popular in the manufacture of implants due to their high specific strength, low stiffness, good corrosion and fatigue resistance in biological media even in contrast to stainless steel and cobalt-chrome alloys (Murr et al., 2010). A mismatch between the elastic modulus of wrought Ti<sub>6</sub>Al<sub>4</sub>V and bone remains. As load bearing hip or knee implants are not manufactured patient specific in terms of material properties compared with the patients' bone, this biomechanical mismatch can vary from patient to patient. AM can be used to produce items with open porous structures that have significantly reduced stiffness or elastic moduli, better matching that of bone (Murr et al., 2010). This has many advantages including reducing stress shielding around load bearing implants. Vaezi et al (Vaezi et al., 2016) have recently published results on AM PEEK/HA composites that have yield and compressive strength within the range of human cortical bone suitable for load bearing applications. These

principles can be applied to the many aforementioned materials to form implants and scaffolds according to both patients' bone density and anatomical location of implantation.

### **1.7.2.2 Pre-operative planning in orthopaedics**

Similar to the other surgical subspecialties, AM is emerging as an important component in planning (Minns et al., 2003) orthopaedic procedures that may involve unique anatomical arrangements (Faur et al., 2013, Schwartz et al., 2015). Recent studies have successfully investigated approaching complex anatomy in the hip (Hughes et al., 2014), knee (Van Haver et al., 2014), shoulder (Stoffelen et al., 2015) and pelvis (Wu et al., 2015). 3D replicas of areas of interest have allowed physical notions of volume, scale and deformity to be appreciated better by the production of an accurate physical model. These advantages would otherwise not be obtained when simply viewing radiographs, CT or MRI (Debarre et al., 2012). One study in particular showed pre-operative plans could be applied to osteotomies for epiphyseal malunion, shoulder arthroplasty as well as trochleoplasty of the femur (Debarre et al., 2012). Van Haver et al concluded that rapid prototyping was a viable method to compare knee abnormalities to that of a control replica with normal anatomy (Van Haver et al., 2014). A 12 month multicentre study found that the commissioning surgeons whom requested models to be manufactured for pre-operative planning found it to be invaluable (Sanghera et al., 2001). Preoperative evaluation of intra-articular fractures using AM models have been reported to be helpful in the planning of procedures and patient education for upper and lower limb cases (Bizzotto et al., 2016).

A systematic review by Tack et al (Tack et al., 2016) of AM technology used for surgery found that it substantially reduced operative times (Table 1-5) in spinal surgery when involved in pre-operative planning. Using AM surgical guides also reduced times in foot and ankle surgery but had little effect on other subspecialties.

<b>Subspecialty, role of AM</b>	<b>No. of studies</b>	<b>Average time (mins)</b>
Hip, model for pre-operative planning	2	0.75
Spine, model, for pre-operative planning	2	-45.5
Foot & ankle, surgical guides	1	-12
Hip, surgical guides	4	-0.025
Knee, surgical guides	20	-6.73

**Table 1-5 Reported impact of operative time with AM application, negative average time values correspond to shorter operative times, modified from (Tack et al., 2016)**

### **1.7.2.3 Custom intra-operative guides**

At the time of writing this thesis the use of AM intra-operative guides is by far the most frequent application of this technology in orthopaedics with its uptake in total knee arthroplasty (TKA) being the most popular. 3D-printed patient specific (PS) blocks provide an alternative to computer navigation and standard instrumentation in TKA. Decreased instrument turnover, operating times and accurate alignment (Renson et al., 2014) as well as costs savings (Lombardi and Frye, 2012) have been seen. A reduction in length of hospital stay, incision length (Noble et al., 2012), blood loss (Boonen et al., 2012) and transfusion rates (Kassab and Pietrzak, 2014) have also been noted. The use of guides in total hip arthroplasty (THA) is less well published however they have been used to facilitate placement of acetabular components and found to have greater accuracy compared with conventional methods (Zhang et al., 2011b).

The emerging use of PS cutting blocks for high tibial osteotomies have shown promise with a reduction of surgical time (Perez-Mananes et al., 2016) together with reduced radiation and high accuracy of correction in single and multi-planar osteotomies (Victor and Premanathan, 2013). AM surgical guides are also being used for malunion/deformity correction in both upper (humerus, elbow, forearm, wrist) and lower limbs (femur, feet) with improved accuracy and ‘good’ outcomes (Popescu and Laptoiu, 2016).

Spinal surgeons are using AM guides for pedicle screw placement. They have shown to be highly accurate with case series involving cervical (Lu et al., 2011b), thoracic (Lu et al., 2011a) and lumbar procedures (Merc et al., 2013). Bellanova et al (Bellanova et al., 2013) performed tibial tumour resections from 4 patients using AM cutting guides and commented that it had improved

accuracy of the resection and suggested it may allow for improved reconstruction using a well matched allograft. Similarly, tumour-free margins with highly accurate resections were performed in 11 patients for pelvic tumours using PS guides (Gouin et al., 2014).

Custom instrumentation does not have to be disposable and patient specific but can be manufactured surgeon-specific. AM allows improved access to surgeons wishing to develop their own instruments for individual surgical techniques.

#### **1.7.2.4 Implants**

An AM Ti alloy calcaneum implant has been successfully inserted after a total calcanectomy for a chondrosarcoma. The implant had polished regions for the talocalcaneal and calcaneocuboidal joints together with porous regions and areas for tendon and ligament re-attachment (Imanishi and Choong, 2015).

AM lends itself to customized endoprosthetic design as large defects can be reconstructed using easily accessible imaging such as CT and MRI. Recently, Liang et al reported good short term results with the use of iliac, and varieties of hemi-pelvic AM endoprostheses in a series of 35 patients (Liang et al., 2017) to reconstruct the pelvis after tumour resection. AM implants are not restricted to orthopaedic oncology with implant companies using this technology for their catalogue of primary and revision arthroplasty products. Trabecular Titanium™ (Lima Corporate SPA, Udine, Italy) is used to augment defects in complex primary and revision hips. This trabecular metal is also been applied to the surface of acetabular shells such as the Delta-TT™ (Lima Corporate SPA, Udine, Italy) to allow for improved bone ingrowth. Surface modification then moved to fully porous components such as the REDAPT™ revision acetabular cup (Smith & Nephew, UK), which is a completely porous component allowing deeper bone penetration and theoretically improved fixation. Arcam (Arcam AB, Stockholm, Sweden) is an AM technology company who recently celebrated 10 years of work with Lima (Lima Corporate SPA, Udine, Italy) (2017), one of the early adopters of AM in implant manufacturing and it is therefore clear that AM in orthopaedics is not a new phenomenon although recent growth is significant.

The Mayo Clinic has reported the successful use of a 3D printer to create customised hips for patients, paving the way for furthered use of 3D customised joint bioprints (Zukas and Zukas, 2015, 2013). CT scans of patients with complicated anatomy and unusual deformities were used to create 3D hip models. These models were transferred to the manufacturer and a specific total hip arthroplasty implant created (Theobald).

In the upper limb, Stoffelen et al (Stoffelen et al., 2015) reported a custom-made glenoid implant for a patient's severe shoulder defect that achieved excellent results at 2.5 years of follow-up. In trauma, patient-specific external fixators for long bone fractures demonstrated minimally invasive accurate reduction. This is difficult to achieve without increasing the operating time, encroaching on the zone of injury or having to resort to expensive robotic or navigational techniques (Qiao et al., 2015). For fragility fractures expandable screws manufactured using SLS have been tested in ovine models. A 41% increase in failure force was observed when compared to traditional screws with these screws thought to also be less sensitive to variations in bone quality (Oldakowski et al., 2016).

3D-printed Ti alloy vertebrae, the first of its kind, were used to replace those affected by tumours. AM allowed for a more anatomical shape and accurate fixation (Feng, 2016). Phan et al reports the first use of an AM implant designed for C1/2 arthrodesis where at 2 month follow-up there was a significant reduction in occipital neuralgia and sub-occipital pain (Phan et al., 2016).

#### **1.7.2.5 Tissue Engineering**

Tissue engineering aims to regenerate, restore and replace defective or injured tissue. In order for scaffolds to achieve this they must provide a structure that allows for cell attachment, migration, transfer of growth factors and waste products all whilst keeping its structural integrity (Gu et al., 2016). AM is one of the most appropriate methods to produce scaffolds fulfilling these criteria.

Using stereolithography derived techniques, Bian et al (Bian et al., 2012) was able to produce a scaffold for osteochondral defects composing of bony and cartilaginous elements. It resulted in a 2-phase structure of an AM  $\beta$ -tricalcium

phosphate porous plug with a Type I collagen cap. Biomechanical studies confirmed its ability to withstand physiological loads and preliminary *in vitro* studies suggests favourable cellular attachment.

AM porous Ti augments were evaluated using histology and pull-out tests in an *in vivo* model. The results of bone infiltration into the cylindrical constructs as well as pull-out tests showed that these 3D-printed metal implants had good fixation and thus represent a promising avenue to improving bone defect reconstruction (Demol et al., 2012).

Du et al (Du et al., 2015) fabricated SLS bone scaffolds using a composite powder of polycaprolactone and HA as a basic building material, *in vitro* work using mesenchymal stem cells shows that these scaffolds allows for cellular adhesion, proliferation and growth.

One study utilised rapid manufacturing technology in order to investigate geometric parameters such as shape and pore size on the biological performance of synthetic bone graft substitutes. The unique designs were 3D-printed and when implanted intramuscularly, were shown to be both osseointegrative and osseointegrative (Habibovic et al., 2008).

Additional research points to these scaffolds having good mechanical properties (Ronca et al., 2012). AM allows for the production of scaffolds with fine-tuned mechanical properties by changing the pore geometry within a single construct. This allows the manufacture of 3D printed scaffolds being used to reproduce the complex muscle tendon junction. Other manufacturing processes cannot provide the ability to produce a single scaffold with changing biomechanical properties. These may be the future of soft tissue reconstructions (Merceron et al., 2014).

The surface profile or topography is known to be one of the many factors that dictate cellular proliferation and differentiation. McMurray et al (McMurray et al., 2011) showed that AM nanostructured surfaces can be used to maintain cellular differentiation over an 8 week *in vitro* study. This may suggest that surfaces on

implants modified by AM can potentially improve osseointegration without the need for coatings or growth factors.

### **1.7.3 Other production considerations with additive manufacturing**

As AM is an increasingly adopted, costs will reduce due to adjustments in economies of scale. According to the U.S. Department of Commerce the costs in AM systems have already decreased by more than half from 2001 to 2011 (Thomas, 2014).

Post printing processes also need to be performed to produce the final 3D printed product. How the product is cleaned depends on the techniques and materials used for its manufacture. Porous metal alloy constructs will entail a more difficult removal of residual particles post-manufacture compared to other products with less complex topography and internal geometry (Morrison et al., 2015).

Post production processes may be used to improve the mechanical characteristics of objects produced using AM. The presence of porosity in an AM manufactured metal alloy (Wei, 2008, Iijima et al., 2013) or ceramic (Zhao et al., 2006) object can prove detrimental to its ability to withstand stresses. However this has now been addressed due to further developments in SLS techniques. Post processing techniques such as heat treatments and hot isostatic processing is used which further consolidates the implants to improve mechanical properties. Hot isostatic pressing (HIP) or hipping is where the object is placed in a sealed chamber and a pressure at a certain temperature is produced to exert a specific load. HIP has been shown to improve the hardness, tensile strength, tensile yield stress, and ultimate yield stress of metal alloys (Murr et al., 2012) and ceramics (Zhao et al., 2006).

### **1.7.4 Future perspectives**

In terms of future outlook, there is great interest among AM researchers in investigating the production of implants of varying textures, porosities and strengths. It is hoped that further understanding of these structural parameters

in AM will eventually enable the manufacturing of patient-specific total joint replacements (Banerjee et al., 2014).

The exponential growth in AM is due to its ability to produce complex shapes by applying material to only where it is required with the initial 'printed' item being very close to the final design. This limits the need for further post-production processes and has been shown to reduce waste of up to 75% (Zhai et al., 2014). AM does not require any form of fixtures or moulds, neither does it require the manufacture of tools to make a product which drastically reduces cost and production times of up to 25% (Duchamp, 2013). The global orthopaedic market was valued at 4.3 billion USD in 2015 with AM products forecast for substantial growth, pushing the boundaries of manufacture, biomedical engineering and orthopaedic surgery.

### **1.8 Surface modification to enhance bioactivity**

In order to enable direct bone contact with the porous 3D printed collar its surface must be coated as  $Ti_6Al_4V$  itself is inert. Although Ti alloy supports osseointegration and is biocompatible, it is not very osseoconductive. For 3D printed porous structures coatings have the potential to increase their osseoconductivity. For massive prostheses direct ECBB is important as it reduces stresses at the stem and allows a more physiological transfer of load through the implant into the bone.

As the bioactivity of HA and its success in improving osseointegration (Cook et al., 1992) is well known, the electrochemical deposition of HA described by Redeppening et al (Redepenning et al., 1996) will be used to coat a  $Ti_6Al_4V$  porous collar so that it can be coated in full allowing for enhanced bioactivity of the complete porous structure.

### **1.9 Hydroxyapatite**

Biological fixation is the process by which implants become firmly bonded to the host skeleton by the ongrowth or ingrowth of bone onto its surface without the use of bone cements (Jaffe and Scott, 1996, Thomas, 1994, Ducheyne and

Cuckler, 1992). This concept was first introduced in the 1960s in Japan with the use of HA on load bearing implants as an alternative to cement.

Currently, there is a general agreement that the chemical purity of HA should be as high as possible ( $\geq 90\%$ ) with a calcium phosphate ratio (Ca:P) of 1.67 for implant coating. This is followed by most manufacturers to ensure consistent implant performance. There is no agreement on the crystallinity, which can vary from 50% to 90% (usually around 70%). The crystalline HA phase may include both the non-molten core of a particle and the new, re-crystallized HA phase which was melted in the process.

The key requirements of HA coatings can be seen in Table 1-6.

<b>Requirement</b>	<b>Definition/function</b>
Biocompatibility	Inducing an appropriate host response in a specific application
Bioactivity	Ability to interact with surrounding tissues
Osseointegrativity	Ability to provide a scaffold for new bone formation
Osseoinductivity	Ability to stimulate the differentiation of mesenchymal stem cells down an osteogenic lineage
Dominant crystalline phase	Prevent fast resorption of coating in body fluids
Amorphous phase	Promote early osseointegration without a loss in the coating stability
Dissolution of HA	Programmed dissolution rate in body fluids to match in vivo healing process
Defined elemental composition	Match the elemental composition of the mineral phase of bone
Surface morphology of bone-coating interface	Enable osteoblast attachment and differentiation and bone material ingrowth (osseointegration)
Strong adhesion to implant	Prevent mechanical failures under load-bearing conditions
Therapeutic capabilities	Can aid in the delivery of drugs and growth factors

**Table 1-6 The ideal characteristics of a calcium phosphate coating, modified from Surmenev et al (Surmenev et al., 2014).**

Ti and its alloys are commonly used to manufacture orthopaedic implants due to their superior biomechanical properties, corrosion resistance and biocompatibility (Abdel-Hady Gepreel and Niinomi, 2013, Grubl et al., 2002, Liu et al., 2004). However, as mentioned previously Ti is a bio-inert material that has poor osseointegrative and osseoinductive properties (Garcia-Gareta et al., 2013). Therefore, it is desirable to coat the implant surfaces with a bioactive layer such as HA. HA ( $\text{Ca}_{10}(\text{PO}_4)_6(\text{OH})_2$ ) is the biomaterial of choice for orthopaedic applications due to its bioactive properties. HA also has a similar chemical composition and crystalline structure to apatite, the most abundant inorganic component in the human skeleton (Tadic et al., 2002). Its use has

been shown to improve longevity of orthopaedic implants in clinical use. Despite the strong bond between HA and bone it has been recognised that the interface between HA and the implant is often weaker (Zheng et al., 2000).

Stoichiometric HA consists of 39.9% calcium, 18.5% phosphorous, 41.4% oxygen and 3.4% hydroxide (weight percentage) with a calcium phosphate molar ratio of 1.67. The molar ratio of the HA in human bone is not stoichiometric (lower than 1.67) and additionally contains other ionic substitutions within its crystal structure (Gadow et al., 2010). Different substitutions cause various affects upon the osseointegrativity, bioactivity and resorbability *in vivo* (Shepherd et al., 2012).

HA is also the most abundant calcium phosphate phase in bone mineral (Khan et al., 2014). A HA coating on metal prostheses facilitates early bone ingrowth and osseointegration post implantation, and improves implant fixation strength (Cook et al., 1992, Cook et al., 1988, de Groot et al., 1987, Goodman et al., 2013). HA has also been shown to promote osteogenic differentiation in *in vitro* models (Oreffo et al., 1998). Studies involving MSCs reveal increased differentiation down the osteogenic lineage when cultured on HA surfaces (Garcia-Gareta et al., 2013, Nishio et al., 2000, Ohgushi et al., 1993). Coating metal implant surfaces with a layer of HA creates a bioactive, osseointegrative and potentially an osseointegrative surface (Goodman et al., 2013, Tisdell et al., 1994). In an *in vitro* study, Garbuz et al has demonstrated an 800% increase in bone ingrowth when augmenting porous tantalum with calcium phosphate and alendronate (Garbuz et al., 2008). Augmenting the surface of HA collars with MSCs have also shown success in improving osseointegration of endoprostheses (Coathup et al., 2013a, Kalia et al., 2006). Clinical research is still limited regarding the efficacy of coated porous metals and bone ingrowth.

### **1.9.1 Substituted Hydroxyapatites**

In order to reflect the mineral component of bone, various substitutions, both cationic and anionic have been produced with *in vivo* and *in vitro* studies showing changes in biological response and physical properties of different substitutions. Despite the advantages of synthetic HA, it differs to biological

apatite with regards to its stoichiometry, composition and crystallinity (Khan et al., 2014). One way of improving the bioactivity of synthetic HA is to add ionic substitutions so that it more closely resembles the chemical composition of bone mineral (Li et al., 2011).

### 1.9.2 Silicon

Among the various trace elements (Na, Mg, Zn, Sr, Si) present in natural bone, silicon (Si) is essential for bone mineralisation and connective tissue development (Schwarz and Milne, 1972, Carlisle, 1970). *In vitro* studies demonstrated that silicate-substituted HA (SiHA) increased metabolic activity of human osteosarcoma cells (Gibson et al., 2009), and enhanced adhesion of human osteoblasts and osteoblast cell activity (Botelho et al., 2006). Additionally, SiHA increases *in vivo* bioactivity, leading to earlier and increased bone ingrowth compared to pure HA (Hing et al., 2006, Patel et al., 2002, Patel et al., 2005). Si substituted porous granules have also been shown to be osseointegrative (Coathup et al., 2011).

### 1.9.3 Strontium

Strontium (Sr) is known for its dual ability to inhibit osteoclast-mediated bone resorption and promote osteoblast-mediated bone formation (Brennan et al., 2009). The use of Sr in improving bone density is well established and is being used clinically for the management of osteoporosis in the form of Sr ranelate (Reginster et al., 2005). *In vitro* studies confirm that Sr ranelate increases mRNA and protein levels of OPG and suppressed those of receptor activator of NF $\kappa$ B ligand (RANKL) (Brennan et al., 2009) thereby affecting both osteoblast and osteoclast activity. Sr ranelate given orally has been shown to improve osseointegration of Ti (Maïmoun et al., 2010) and HA coated (Li et al., 2010) Ti implants in rat models. Traces of Sr (0.008-0.01%) are found in bone as well as areas of high metabolic turnover. There is now growing evidence that Sr when incorporated into an HA coating can further enhance osseointegration of metal implants both *in vitro* (Capuccini et al., 2008, Maïmoun et al., 2010, Yang et al., 2015) and *in vivo* (Offermanns et al., 2015, Yang et al., 2012b, Li et al., 2010).

Biomaterials research has seen a surge in the development of both dry and wet chemical techniques of coating materials with HA coatings. Pioneering work in the 1980s led to the development of plasma spraying of HA coatings (Surmenev et al., 2014). Plasma spraying is a line of sight technique and will only coat the outer surface of porous metals leaving the inner pore surface bare. Therefore the coating of porous metals remains challenging. A variety of other techniques have also been developed that may enable improve surface coverage including sol-gel (Zhang et al., 2011a), micro-arc oxidation (Legostaeva et al., 2013), electrospray deposition (Bosco et al., 2013), alternate soaking deposition (Yoshioka et al., 2009), drop-on-demand microdispensing (Thian et al., 2013), electrophoretic (Boccaccini et al., 2010) and electrochemical deposition (Qiu et al., 2011).

## **1.10 Coating techniques**

### **1.10.1 Plasma spray**

This process involves the use of heat from ionized inert gas (plasma) to partially melt ceramic or metal powders. These partially molten powders are then sprayed onto the substrate to be coated where they cool and fuse with neighbour particles and with the substrate. Plasma spraying is economically viable due to ease of operation, low substrate temperature and low cost (de Groot et al., 1987, Herman, 1988, Ong and Chan, 2000) however the process may cause microstructural changes on the surface of the coated object (Ellies et al., 1992). The heated process can cause HA coatings to show secondary phases such as tricalcium phosphate, calcium oxide, tetracalcium phosphate as well as amorphous CaP. In order for coatings to remain stable long term the dissolution characteristics of the coating is critical. The presence of amorphous CaP increases the dissolution of the coating. Furthermore, the bone remodelling process associated with osteoclasts, that occurs at the surface of the coating lowers pH to as low as 4 in some places and therefore it is imperative to understand the stability of the HA coating below physiological pH (7.4) (Mohseni et al., 2014).

Plasma sprayed HA coatings on Ti have shown positive results, reporting new direct bone growth onto the coatings with very good adhesion between bone and HA coating. Due to the brittle nature of the HA coatings it is prone to fracture, non-uniformity in coating density, wear of the coating layer, weak bond with the coated substrate and alteration in its structure (Mohseni et al., 2014). The first generation of HA coatings were relatively thick and delamination of the coating was seen in hip replacements. This is due to the mismatch in the material stiffness under bending leading to failure at the implant coating interface. The initial reticence to use HA was associated with these thick coatings and the effect that fragments of HA which found their way into the bearing increased polyethylene wear.

Further work modifying these techniques to allow the incorporation of other elements have been conducted to boost further the bioactive characteristics of the HA coating. These include the production of SiHA, carbonated HA, Zn, Mg and Al substituted HA, Ag-HA and fluoridated HA to name a few. Due to the physical processes used during the coating process the incorporation of biological substrates such as growth factors involved in bone growth or healing is not possible (Mohseni et al., 2014). This is the main reason why there has been a trend to develop wet-chemical techniques to allow for a hybrid organic and inorganic coatings to be made.

Clinical evidence is now available on the use of plasma sprayed HA coated orthopaedic implants due to its wide use commercially. Uncemented total hip replacements with non-bioactive porous coatings have been used in the past but due to issues of osteolysis and stress shielding the long-term stability of these implants have been in question (Manley et al., 2002, Kim et al., 2013). HA coated femoral components have been shown to reduce component migration with improved survivorship (Soballe et al., 1993). These implants could also ensure improved postoperative range of motion and function, reduction in thigh pain, and reduce incidence of femoral osteolysis (Chen et al., 2015). Human retrieval studies have confirmed that HA coated implants have significantly greater bone ingrowth and attachment (Coathup et al., 2001) although concerns regarding the technique used to coat implants have been raised as it has been

thought that delamination of the HA coating with particle migration may cause third body wear as well as stimulate bone loss (Bloebaum et al., 1994).

### **1.10.2 Hot isostatic pressing (HIP)**

This is an alternative method to increase the density of an HA coating on a Ti substrate and involves the use of pressurised gas at a certain temperature to exert a specific load. The HA coated implant is placed in an air-tight sealed container where it is exposed simultaneously to both pressure and heat (Herø et al., 1994). Typical pressures involved in HIP ranges from 100-320MPa with temperatures in some cases exceeding 2000°C. HIP technique allows for better temperature control and therefore a more homogenous coating is produced (Larker and Larker, 1991).

Studies have found HIP coatings to be susceptible to cracking much like the plasma spray technique. The very nature of HIP HA coatings are very dense and minimally porous however clinical uses of HA require the coating to be porous to allow for bone ingrowth and integration. HIP is generally used as a post treatment to improve adhesion of the HA coating to the substrate.

Wie et al found that HIP processed HA endosseous Ti implants had no greater osseointegration when compared to plasma sprayed HA implants in vivo, although these HA coated implants showed significantly greater osseointegration than uncoated roughened Ti counterparts. They had concluded that increased coating density formed by the HIP processing did not reduce the bioactive properties of the HA (Wie et al., 1998).

### **1.10.3 Thermal spray coating**

This method includes flame spray, electrical arc spray and plasma arc spray techniques which refers to each of the heating sources. These sources are used to melt the coating material and the molten particles are accelerated towards the substrate to be coated using jets.

Thermal spraying of HA onto substrates is very similar to plasma spraying with low cost and high deposition rate being main advantages (Yang et al., 2005). It

is able to produce coating thicknesses from 30 to 200µm. Thermal sprayed HA coatings suffer from poor adherence to the coated surface and non-uniform crystallinity that may reduce lifespan of the implant (Hanyaloglu et al., 2001, Hamdi et al., 2000). Furthermore due to the high sintering temperatures, crack propagation on the surface of the coating is seen (Zyman et al., 1994).

Shimazaki et al utilised the thermal spraying technique to coat Ti implants with a silver containing coating. They concluded that this was a viable technique that allows for the reduction in early infection post-operatively (Shimazaki et al., 2010).

#### **1.10.4 Pulsed laser deposition**

This can be used to produce ceramic thin films where a high-powered laser is used to vaporise a stock of coating material. This vaporised material is then ejected and condensed onto the substrate forming a thin film. Subsequent laser pulses form layer upon layer of the coating (Bao et al., 2005). A clear advantage of pulsed laser deposition (PLD) is the ability of the technique to retain the stoichiometry of the coating as the laser ablation vaporises the compound as a whole at the same time. An issue with PLD is the splashing of larger particulates onto the coating substrate (Bao et al., 2005). Several methods have been used to prevent this from occurring in particular the use of a mechanical particle filter (Cheung, 1994). The film produced from PLD only has a small area of uniform coating thickness and structure due to angular distribution of the vaporised material. Scaling up PLD for commercial large scale use is challenging and a number of different methods have been proposed (Bao et al., 2005).

CaP coatings produced using PLD that have been shown to be osseoconductive in *in vitro* studies (Bigi et al., 2005).

#### **1.10.5 Wet-chemical coating techniques**

Biomimetic techniques were developed during the 1990s where the substrates to be coated were modified by CaP seeds or functional groups that allow for CaP nucleation on the substrate surface. The modified material is then

immersed in a CaP supersaturated simulated body fluid. The ion concentration, pH and temperature closely match that of human plasma and as a result a uniform CaP layer forms on its surface. This process allows for the inclusion of biofunctional substances such as therapeutic agents, trace elements, proteins, bisphosphonates, bone morphogenic protein, vitamins and antibacterial agents. The nature of the coating technique does not denature these active components and potentially therefore a coating resembling native bone can be developed (Surmenev et al., 2014).

#### **1.10.6 Dip coating**

This technique involves deposition of a wet liquid film onto a substrate after being submerged in a liquid medium. Once the substrate has been immersed in the medium it is removed and a thin layer of coating is deposited once volatile components of the medium have evaporated. This technique can be used to coat both simple and complex shapes with a relatively short turnover. Coatings of 0.05-0.5mm thicknesses can be obtained using dip coating. Again, due to the high sintering temperatures required as a post-coating treatment, the coating is prone to cracking (Li et al., 1996). Although not commercially available, Mavis et al (Mavis and Taş, 2000) have developed several HA liquid coating mediums and have produced highly porous HA coatings.

#### **1.10.7 Ion beam assisted deposition (IBAD)**

IBAD involves bombarding the substrate surface with a specific ion energy beam in combination with physical vapour deposition of the coating in a vacuum environment. The major advantage of IBAD over other techniques is its ability to form coatings that are highly adhesive to the substrate (Ohtsuka et al., 1994).

#### **1.10.8 Sputter coating**

Material is expelled from a target (source) onto a substrate utilising gas plasma to remove material from the negatively charged target which is then deposited. HA coatings using this technique have been successful with coatings from 0.5 to 3µm thick. These coatings were however found to have low crystallinity,

which in turn will increase the dissolution of the coating in an in vivo environment.

### **1.10.9 Electrochemical deposition**

Electrochemical (EC) deposition involves the migration of charged ions that are suspended dissolved in solution onto an electrode which is coated under the influence of an electric field (Sarkar and Nicholson, 1996). This method is advantageous as it involves low cost equipment, easy to set up and has the ability to coat complex shapes (Ducheyne et al., 1990). EC deposition allows for a high degree of control over the coating characteristics through the regulation of various coating parameters. There is a large range of coating thicknesses that can be produced using EC deposition ranging from the nanometre to the millimetre scale.

There is increasing development of HA coatings using EC techniques due to its ability to form uniform, highly pure coatings, ability to impregnate porous substrates and to produce HA substituted coatings (Li et al., 2011) to name a few. EC deposition can be performed at relatively low temperatures and therefore avoids the formation of amorphous phases. Adhesion of EC coatings onto the substrates are formed by metallurgical bonds rather than mechanical, which are expected to be stronger. EC coatings are porous and this is advantageous when considering the need for bone ingrowth and implant osseointegration. However porosity can also cause the coating to degrade due to penetration of bodily fluids into its structure. Sintering can be used as a post coating treatment to reduce porosity by increasing density. This can cause the cracking of the coating due to the difference in thermal expansion coefficients between the coating (e.g. HA) and the substrate (e.g. Ti) (Zhang et al., 2001).

Zhang et al (Zhang et al., 2001) have shown EC nanostructured HA coatings to have adhesive strengths greater than thermal sprayed HA coatings. The corrosion resistance of this HA is far higher than that of thermal sprayed HA in simulated body fluid at room temperature. High quality HA can be produced using EC techniques, strength of adhesion of these coatings surpass the levels required as set out by the Food and Drug Administration (FDA) (Nahler and

Nahler, 2009). In-vitro studies have also confirmed that after 2 months of testing, the amount of EC HA coating remaining was far greater than that of plasma sprayed HA. Ma et al (Ma et al., 2003) found EC HA had shown good adhesion onto the Ti substrate as well as exhibiting a uniform thickness. It is thought this was due to the uniform dispersion of HA in suspension (Wei et al., 1999).

Mobility of the particles in suspension is partially dictated by particle size in suspension as well as the charges present (Yamashita et al., 1997, Ferrari et al., 1998). Some studies have sintered the coating post deposition to improve its density. This has led to decomposition of the HA coating, degradation of the metal substrate and cracking of the HA coating (Albayrak et al., 2008).

While plasma spraying is the most commercially used technique, EC deposition has several advantages (Table 1-7). This “non-line-of-sight” technique enables a high degree of control over crystalline deposition, coating thickness and chemical composition. It is cost effective and takes place at low temperature. Perhaps most advantageous with respect to musculoskeletal tissue engineering is the potential for coating complex 3D shapes and incorporating bioactive molecules (Li et al., 2011, Redepenning et al., 1996, Redepenning et al., 2003).

<b>Technique</b>	<b>Thickness</b>	<b>Advantages</b>	<b>Disadvantages</b>
Thermal spraying	30–200 $\mu\text{m}$	High deposition rates, low cost	Line of sight technique; high temperatures induce decomposition; rapid cooling produces amorphous coatings
Sputter coating	0.5–3 $\mu\text{m}$	Uniform coating thickness on flat substrates; dense coating	Line of sight technique; expensive time consuming; produces amorphous coatings
Pulsed laser deposition	0.05–5 $\mu\text{m}$	Coating with crystalline and amorphous; coating with dense and porous	Line of sight technique
Dip coating	0.05–0.5 mm	Inexpensive; coatings applied quickly; can coat complex substrates	Requires high sintering temperatures; thermal expansion mismatch
Sol–gel	< 1 $\mu\text{m}$	Can coat complex shapes; Low processing temperatures; relatively cheap	Some processes require controlled atmosphere processing; expensive raw materials
Electrochemical deposition	0.1–2.0 mm	Uniform coating thickness; large range of thicknesses, rapid deposition rates; can coat complex substrates; low cost	Difficult to produce crack-free coatings; requires high sintering temperatures if needed
Biomimetic coating	< 30 $\mu\text{m}$	Low processing temperatures; can form bonelike apatite; can coat complex shapes; can incorporate bone growth stimulating factors	Time consuming; Requires replenishment and a constant of pH of simulated bodyfluid
Hot isostatic pressing	0.2–2.0 mm	Produces dense coatings	Cannot coat complex substrates; high temperature required; thermal expansion mismatch; elastic propertydifferences; expensive; removal/interaction of encapsulation material

**Table 1-7 adapted from Yang et al (Yang et al., 2005) for alternative methods of coating with HA.**

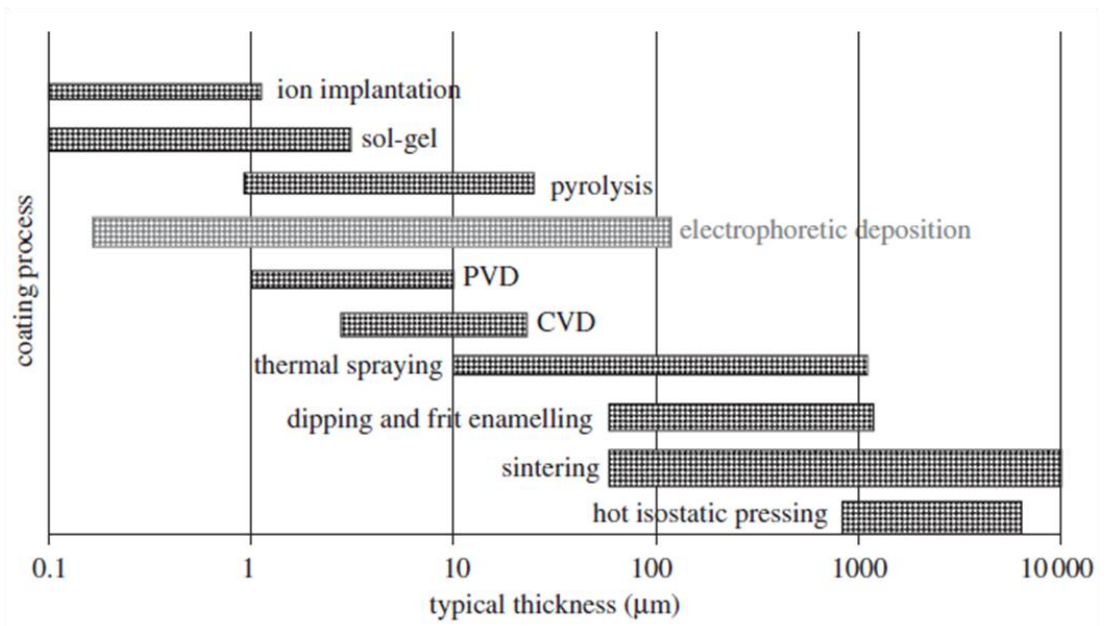


**Figure 1-13 Typical thickness of coatings obtained by different process methods, showing the versatility of EPD in that it can produce a wide range of thicknesses of relevance for orthopaedic applications (Sridhar et al., 2002).**

## **Aims and Hypotheses of thesis**

The work in this thesis combines the concept of an additively manufactured porous collar augmented with an electrochemical coating to produce a highly osseoconductive scaffold that maximises ECBB when used as part of an endoprosthesis.

The aims of this thesis are:

- 1. Identify if bone tumour patients would benefit from an improved design of the HA ingrowth collar used as part of distal femoral replacements.**
- 2. Establish if a selective laser sintered HA coated porous implant can be used as an alternative ingrowth region for endoprostheses.**
- 3. Develop the electrochemical technique for coating porous Ti alloy implants with HA (EHA), silicate-substituted (ESiHA) HA and strontium-substituted HA (ESrHA).**
- 4. To evaluate *in vitro* the bioactivity of the various electrochemical deposited coatings in comparison with the current gold standard plasma sprayed coating.**
- 5. To evaluate *in vivo* the osseointegration of selective laser sintered Ti alloy implants in combination with the various HA coatings.**

The hypotheses of my thesis are:

- 1. Bone tumour patients undergoing chemotherapy will show less ECBB and osseointegration when compared with those that do not receive chemotherapy.**
- 2. Selective laser sintered HA collars provide an alternative ingrowth region that allows for greater osseointegration *in vivo*.**
- 3. Electrochemically deposited HA, SiHA and SrHA can be produced with coating thickness and morphology able to be controlled using different current densities and deposition times.**
- 4. ESiHA and ESrHA coatings show greater bioactivity *in vitro* when compared with EHA and controls (plasma spray and uncoated).**

5. EHA, ESiHA, ESrHA coatings when combined with laser sintered porous scaffolds allow for improved osseointegration *in vivo*.

## **Chapter 2. Early Radiographic Loosening of Distal Femoral Replacements in Patients Undergoing Chemotherapy**

## 2.1 Introduction

Osteosarcomas are the most common bone sarcoma in children and adolescents and represent fewer than 1% of all cancers overall with an incidence of 5 per 1,000,000 in children aged 19 and younger in the USA (Anderson, 2016). Although osteosarcomas affect all ages there is a clear bimodal distribution with peaks in the pubertal/adolescent patient age group as well as those in their 7<sup>th</sup> decade. Not only does the tumour location indicate the likelihood of the development of metastases but complete surgical removal is important in order to minimise the risk of further neoplasia (Meyers et al., 1993). Sarcomas are an aggressive group of tumours and it was noted that those who underwent appropriate treatment still did not survive due to metastases. 20% of patients present with signs of metastases however the majority of patients with sarcoma have micro-metastases, which can cause disease relapse. Now there is an overall 68% survivorship at 5 years for all bone and soft tissue sarcomas (Howlader et al., 1975-2013).

Several studies in the 1980s have shown that the introduction of an aggressive adjuvant chemotherapy regime improves survival of patients with osteosarcomas (Eilber et al., 1987, Link et al., 1986). Before this time the standard treatment of osteosarcomas was amputation of the extremity. However improving patient mortality rates shifted the focus to limb salvage involving segmental resection of the tumour with reconstruction using endoprostheses.

Custom endoprostheses require time for manufacture that may delay chemotherapy and worsen prognosis. Rosen et al (Rosen et al., 1979) demonstrated that the use of neoadjuvant chemotherapy where patients were treated pre-operatively during the time where the custom endoprosthesis was being fabricated was beneficial. The success of neoadjuvant chemotherapy was reflected in a number of other subsequent studies, which confirmed that this practice was safe, prepared the limb for surgery and further improved mortality rates. As a result neoadjuvant chemotherapy with limb salvage has become the standard treatment of osteosarcomas and approximately 80% of patients with these tumours are now being treated in this fashion (Allison et al., 2012).

Although chemotherapy has significantly lowered the risk of metastatic disease, complications from reconstructive techniques continue to result in late morbidity. According to Jeys et al (Jeys et al., 2008) AL is the most common reason for failure of endoprostheses and accounts for 28.6% of all failures. Implant fixation requires the bone to be healthy and viable. A number of *in vivo* studies have shown substantial effects of doxorubicin, cisplatin and ifosfamide on osteotomy healing and incorporation of segmental cortical autografts (Virolainen et al., 2005). For bone tumour implants ECBB where bone forms over the implant shaft and stabilises the fixation has been shown to reduce loosening (Fromme et al., 2017). Coathup et al (Coathup et al., 2013b) showed that 98% of distal femoral replacements survive to 10 years if their HA collar had osseointegrated compared to only 75% if they had not. Radiologically, AL initially manifests itself with the development of a 'gap' of localised cortical bone loss at the bone-shoulder implant junction where the bone is in direct contact with the shoulder of the implant. Over time, as osteolysis increases, there is a development and progression of periprosthetic bone-cement radiolucent lines that advance along the interface eventually leading to AL of the component (Coathup et al., 2015).

Given that the mainstay of the treatment of bone and soft tissue sarcomas is limb reconstruction in conjunction with chemotherapy it is important to show the effect of chemotherapy on the osseointegration of endoprostheses. This allows us to identify whether or not the current design of the HA collar can achieve adequate osseointegration when a neoadjuvant chemotherapy regime is used. This is the first time the effect of chemotherapy is being evaluated on the radiological signs of loosening.

**The aim of this study was to investigate the effect of multi-drug chemotherapy on the osseointegration of the HA collar and early AL of massive distal femoral bone tumour prostheses.**

**The hypotheses were:**

- 1. Patients undergoing chemotherapy will show less ECBB than those patients not receiving chemotherapy.**

2. Patients undergoing chemotherapy would show less osseointegration of their endoprosthesis than those not receiving chemotherapy.
3. Patients undergoing chemotherapy would exhibit earlier radiographic signs of AL compared with patients who did not receive chemotherapy.

## 2.2 Patients and methods

A retrospective case-control study was conducted where adult patients who had undergone limb reconstruction using distal femoral replacements (DFRs) with HA ingrowth collars were selected. Annual follow-up radiographs were analysed for 3 years proceeding their initial operation. Electronic patient records were searched to form this database. 1, 2 and 3 year postoperative radiographs were sourced for each patient using the local Picture Archiving and Communication System (PACS, Centricity, GE Healthcare, Buckinghamshire, UK). A total of 34 patients with a 3 year follow-up were included in our study with 16 and 18 in the chemotherapy and non-chemotherapy groups respectively (Figure 2-1). Demographic data is summarised in Table 2-1.

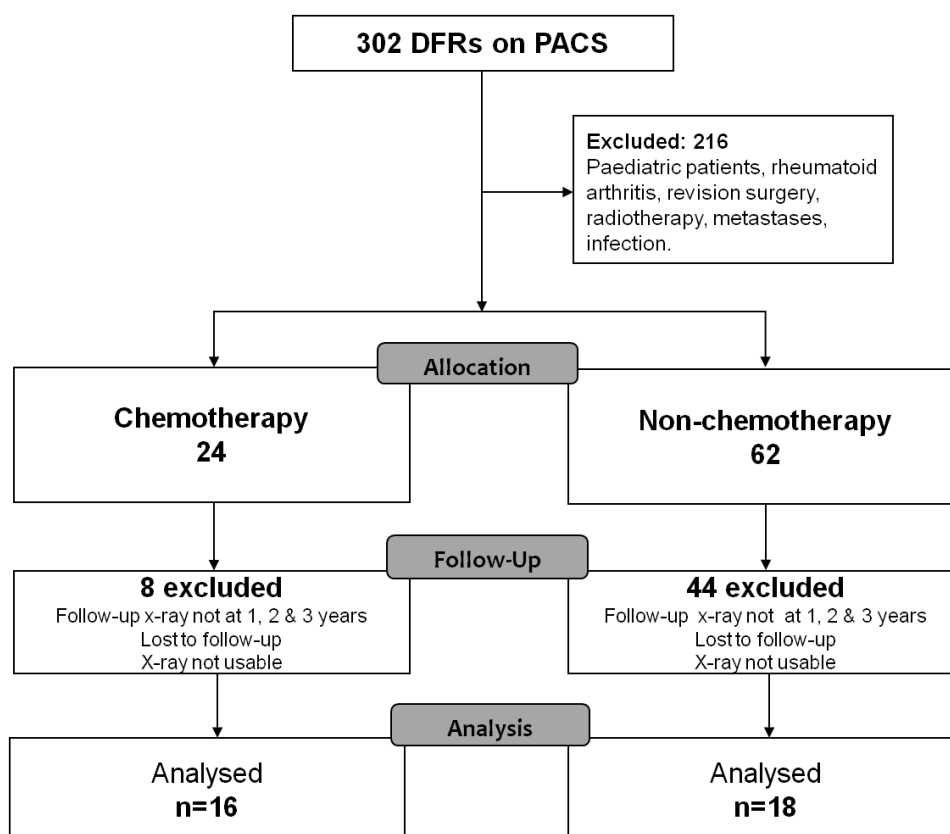


Figure 2-1 CONSORT flow diagram.

Variable	Chemotherapy	Non-chemotherapy	p-value
Age (years, IQR)	31 (19-50)	35 (29-44)	0.395 <sup>a</sup>
Gender (M:F)	9:6	9:9	0.566 <sup>b</sup>
Resection level (%)	39.5 (33-48.5)	26.2 (24.8-29.7)	<0.001 <sup>a</sup>

Table 2-1 comparisons of demographic data across chemotherapy and non-chemotherapy groups. <sup>a</sup>Mann-Whitney U test, <sup>b</sup>χ<sup>2</sup> test.

The selection criteria were chosen in particular to exclude cases where the potential for bone growth and osseointegration were not biased between the groups. Paediatric (those not exhibiting radiographic skeletal maturity) patients were excluded based on differing rate of bone turnover and healing potential compared to adults. If numbers of paediatric patients in each group were equal, this would not be an issue but numbers of paediatric patients compared to adult patients for benign conditions not requiring chemotherapy were rare and therefore would introduce error. Primary DFRs where chosen as greater periosteal stripping present in revision cases would hinder the potential for ECBB (Dwek, 2010). Rheumatoid patients were excluded based on their long-term steroid and disease modifying drug use. Radiotherapy directly to or near the transection site was again a criterion for exclusion as this would inhibit any potential bone regeneration (Boden and Sumner, 1995). Those DFRs used for metastatic cases from primaries other than bone and soft tissue sarcomas were excluded due to the various other medications used in their management, which may affect ECBB.

A number of patients were excluded from the study as the appropriate radiographs were not present. A radiograph performed 1 month on either side of the 1, 2 and 3 year follow-up dates were acceptable. Those patients lost to follow-up were also excluded. Patients with radiographs of insufficient quality were also excluded from the study.

Demographic data (age and gender) as well as diagnosis, resection level, extracortical bone growth, osseointegration, gap at transection site and radiolucent line score (RLL) were all measured for each radiograph. The two main arms of the study included patients who received chemotherapy and patients who did not receive chemotherapy as part of their treatment with the latter group being defined as the control group. The control group included patients that were all diagnosed with giant cell tumours. Patients who underwent DFRs and received chemotherapy were a more heterogeneous group (Table 2-2). All DFRs included in this study were manufactured by Stanmore Implants Ltd (Elstree, Hertfordshire, UK) and manufactured on a customised case-by-case basis. All procedures were performed in one institution and no patients were recalled for the purposes of this study.

Case No.	Diagnosis	Chemotherapy	Agents
1	Osteosarcoma	Neoadjuvant and adjuvant	Cisplatin, doxorubicin, methotrexate
2	Osteosarcoma	Neoadjuvant and adjuvant	Cisplatin, doxorubicin, methotrexate
3	Osteosarcoma	Neoadjuvant and adjuvant	Cisplatin, doxorubicin, methotrexate with maintenance pegylated interferon <sup>a</sup>
4	Osteosarcoma	Neoadjuvant and adjuvant	Cisplatin, doxorubicin, methotrexate
5	High grade pleomorphic sarcoma	Neoadjuvant and adjuvant	Cisplatin, doxorubicin
6	Osteosarcoma	Neoadjuvant and adjuvant	Cisplatin, doxorubicin, methotrexate
7	High grade spindle cell sarcoma	Neoadjuvant and adjuvant	Cisplatin, doxorubicin
8	Osteosarcoma	Neoadjuvant and adjuvant	Cisplatin, doxorubicin, methotrexate
9	Ewing's sarcoma	Neoadjuvant and adjuvant	VIDE (neoadjuvant), VAI (adjuvant) <sup>b</sup>
10	High grade pleomorphic sarcoma	Neoadjuvant and adjuvant	Cisplatin, doxorubicin
11	High grade spindle cell sarcoma	Neoadjuvant and adjuvant	Cisplatin, doxorubicin
12	Ewing's sarcoma	Neoadjuvant and adjuvant	VIDE (neoadjuvant), VAC (adjuvant) <sup>c</sup>
13	High grade spindle cell sarcoma	Neoadjuvant and adjuvant	Cisplatin, doxorubicin
14	Osteosarcoma	Neoadjuvant and adjuvant	Cisplatin, doxorubicin, methotrexate
15	High grade spindle cell sarcoma	Neoadjuvant and adjuvant	Cisplatin, doxorubicin, methotrexate <sup>d</sup>
16	Osteosarcoma	Adjuvant	Cisplatin, doxorubicin

**Table 2-2 Patients included in chemotherapy group with chemotherapy regimen.** <sup>a</sup>5 of 12 cycles of methotrexate omitted due to complications. <sup>b</sup>Randomised to VAI as part of Euro-Ewing 99 study. <sup>c</sup>Randomised to VAC as part of Euro-Ewing 99 study. <sup>d</sup>Methotrexate and cisplatin stopped at later cycles due to complications.

### 2.2.1 Radiographic analysis

Radiographic analysis was performed by a separate objective observer who had been trained to complete the scoring system. They were unaware of whether the patient whose radiograph they were scoring had received chemotherapy or not and hence blinded. Antero-posterior and lateral radiographs were used to quantify all measurements (Figure 2-2). Resection level was defined by the proportion of the femur that had been resected, taken from the joint line to the transection site, expressed as a percentage of the total length of the femur. The amount of extracortical bone growth was quantified by measuring the maximal length (mm) and thickness (mm) of the extracortical bone pedicle growing from the level of the shoulder of the HA collar in

orthogonal regions (anterior (A), posterior (P), medial (M) and lateral (L)) surrounding the HA collar and implant shaft on the radiographs. Osseointegration was quantified by expressing the length (mm) of the extracortical bony pedicle in direct contact with the HA collar for each region (A, P, M, L) as a percentage of the full length (mm) of the collar as measured on the radiograph. The overall osseointegration of the collar was calculated by averaging the integration occurring in each plane. The presence of a gap between the shoulder of the HA collar and the transection site was observed and quantified in each region (A, P, M, L) with no gap being denoted as 0mm.

To evaluate early loosening of the cemented intramedullary stem the RLL score was calculated for each radiograph (Coathup et al., 2013b). The cement mantle surrounding the intramedullary stem is split into 12 equal zones, with 6 on either side of the stem midline (Figure 2-2). A score of one is given if a zone contains a radiolucent line at the cement-bone interface suggesting loosening. This was done for both AP and lateral radiographs, therefore the maximum RLL score that can be given for any DFR is 24. Measurements were taken blindly and the assessor did not know whether they were scoring the radiograph of a patient who had received or not received chemotherapy.

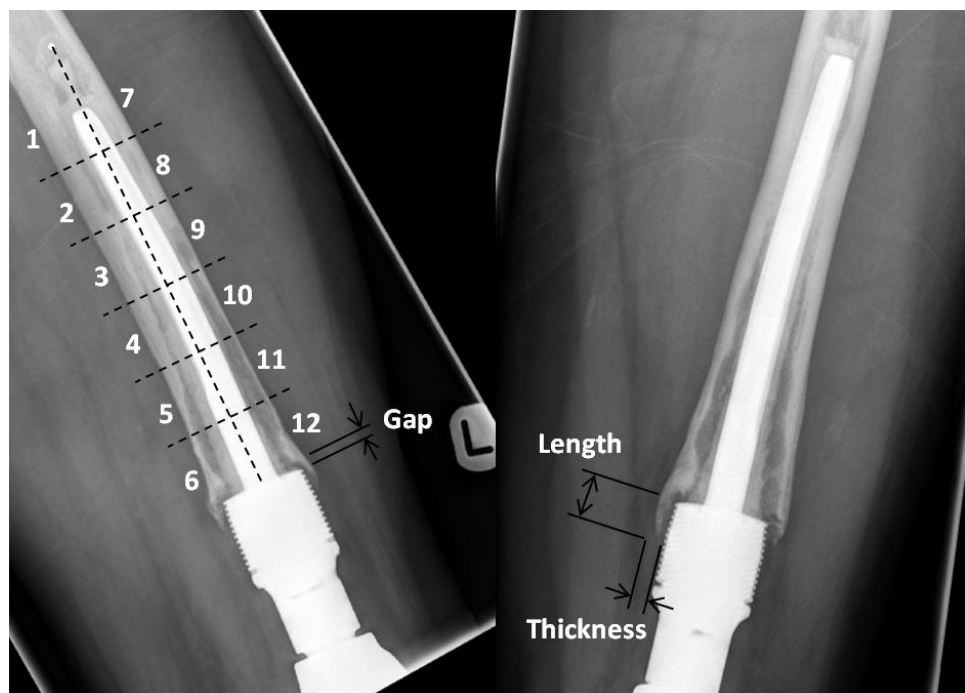


Figure 2-2 AP (right) and lateral (left) radiographs of DFR intramedullary stem showing the zones used for the RLL score together with length, thickness and gap distances measured around HA collar. Radiolucent lines are evident in all zones in the lateral radiograph giving a maximum score of 12.

### **2.2.2 Statistics**

Statistical analysis was performed using SPSS Statistics (v22, IBM, New York, USA). Data was tested for normality using the Shapiro-Wilk test and non-parametric data was compared using a Mann-Whitney U test. Multiple data comparisons for non-parametric data were compared using a Kruskal-Wallis test. Categorical data was compared using  $\chi^2$  test.  $p < 0.05$  was considered to be significant. Correlation analysis was conducted using Pearson's correlation coefficient with  $p < 0.05$  being seen as significant.

## 2.3 Results

Analysis revealed differences in osseointegration, gap formation and early loosening of the HA collar and intramedullary stems in patients receiving chemotherapy as part of their management compared to patients that do not.

A summary of extracortical bone growth, osseointegration, gap size and RLL score can be found in Table 2-3.

Group	Variable	Year 1	Year 2	Year 3
Non-chemo	Pedicle length (mm)	1.9 (0-10.7)	7 (0.9-14.5)	6.5 (1.1-15.8)
	Pedicle thickness (mm)	1 (0-2.9)	2 (0.2-3.8)	1.9 (1-3.8)
	Osseointegration (%)	2.6 (0-15.2)	11.4 (0-33)	12.8 (0.4-30.1)
	Gap (mm)	0.7 (0.4-1.7) <sup>a</sup>	0.6 (0-2) <sup>b</sup>	1.8 (0.1-2.7) <sup>c</sup>
	RLL	5 (2.8-7.3)	2.5 (0.8-5.5)	6.5 (4-11.3) <sup>d</sup>
Chemo	Pedicle length (mm)	1.9 (0-12.5)	6.7 (0-12.6)	8.3 (0-18)
	Pedicle thickness (mm)	0.5 (0-4.4)	1.4 (0-3.6)	0.8 (0-4.5)
	Osseointegration (%)	3.8 (0-18.8)	7.2 (0-24)	0 (0-30)
	Gap (mm)	0 (0-7) <sup>a</sup>	0.2 (0-1) <sup>b</sup>	3.2 (2.6-4.1) <sup>c</sup>
	RLL	5(0-8)	6 (3-9)	14 (4-18) <sup>d</sup>

**Table 2-3 Summary of data (median, IQR) for variables throughout the 1<sup>st</sup>, 2<sup>nd</sup> and 3<sup>rd</sup> post-operative year radiographs between the non-chemotherapy and chemotherapy groups. <sup>abcd</sup>p<0.05.**

### 2.3.1 Extracortical bone growth

Growth in the length of the extracortical bone pedicle is observed in both groups over the first three years. The pedicles became thicker until the 3<sup>rd</sup> postoperative year at which point they atrophied slightly. These observations do not translate into a statistical difference in the amount (length, thickness) of the extracortical bone growth seen on radiographs during the 3 years following endoprosthetic reconstruction. There is no statistical difference in the amount of bone growth between the non-chemotherapy and chemotherapy groups.

### 2.3.2 Osseointegration

The overall osseointegration of the HA collar with extracortical bone growth increases with time in the non-chemotherapy group but this is not reflected statistically (p=0.232) (Table 2-3). For patients undergoing chemotherapy, osseointegration of the collar peaks at 2 years but there was a large reduction in the 3<sup>rd</sup> year. Analysis of osseointegration occurring in each region (A, P, M, L) reveals significantly greater (p=0.021) osseointegration occurring posteriorly in

the non-chemotherapy group when compared to the chemotherapy group in year 3.

### 2.3.3 Gap

A significant difference in the size of the gap developing between the HA collar and transected cortex in the two groups was seen on the lateral aspect in the first ( $p < 0.01$ ) and second year ( $p = 0.039$ ) and medially in the third year ( $p = 0.024$ ). When comparing gap size over time, the size of the gap did not change in the non-chemotherapy group ( $p = 0.504$ ) but became larger in the chemotherapy group ( $p < 0.01$ ). A mild increase in gap size is observed between the first and second year followed by a significant increase in the third year ( $p < 0.01$ ) in this group.

### 2.3.4 Radiolucent Line (RLL) Score

The RLL score of the chemotherapy group increased over time ( $p < 0.01$ ) representing an increase in early radiographic loosening of the intramedullary cemented stem over the first three years. In contrast no change in RLL score was observed in the non-chemotherapy group ( $p = 0.061$ ). The disparity in RLL between the two groups becomes greater over time reaching a statistical significance at year 3 ( $p = 0.044$ ) (Figure 2-3).

### 2.3.5 Correlation analysis

Resection length was found to not correlate with any of the other variables. Greater osseointegration of the HA collar was found to significantly correlate negatively to the RLL score. In contrast, gap formation and RLL score were found to be significantly positively correlated (Table 5).

		<b>Gap</b>	<b>RLL</b>	<b>Osseointegration</b>
<b>Resection length</b>	Coefficient	-0.078	0.193	0.086
	p-value	0.493	0.086	0.450
<b>Osseointegration</b>	Coefficient	-0.177	-0.265	-
	p-value	0.097	0.012*	-
<b>RLL</b>	Coefficient	0.304	-	-
	p-value	0.004*	-	-

**Table 2-4 Correlation analysis between variables with Pearson correlation coefficients and p-values. \* $p < 0.05$ .**

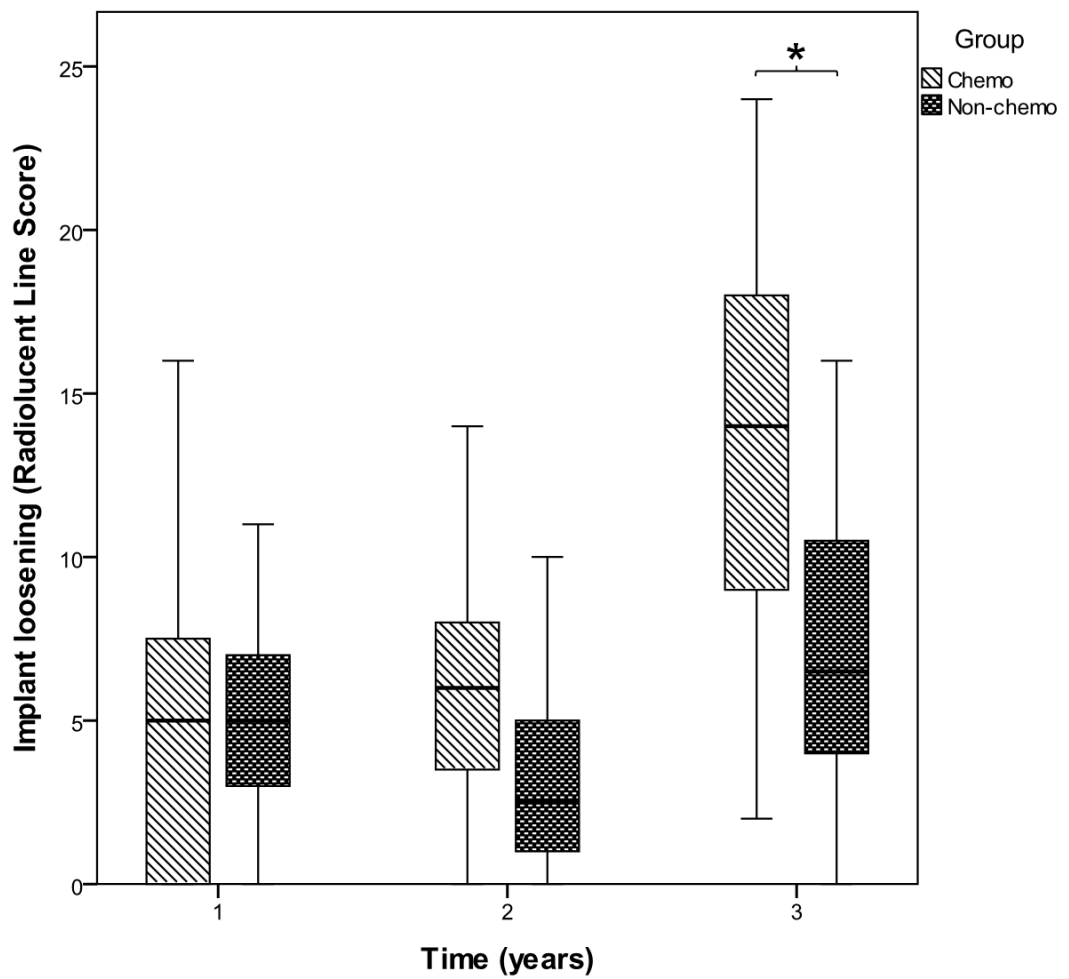


Figure 2-3 Boxplot of radiolucent line scores (RLL) for non-chemotherapy and chemotherapy groups over time. \* $p < 0.05$ .

## 2.4 Discussion

This is the first study to show that multidrug chemotherapy accelerates radiographic signs of AL of distal femoral replacements and reduces osseointegration in the early years, which is in keeping with my initial hypothesis.

A number of *in vivo* studies utilising dog, rabbit and rat models have shown substantial affects of doxorubicin, cisplatin and ifosfamide on osteotomy healing and incorporation of segmental cortical autografts, with histologic evidence of poor new bone formation and decreased stiffness and strength of healed osteotomies (Virolainen et al., 2005). Our search has not revealed there to be any clinical studies related to the effect of chemotherapy on osseointegration. A study evaluating the cortical hypertrophy around the Compress® distal femoral endoprosthesis (Biomet, Inc, Warsaw, IN, USA) showed greater hypertrophy around the implant in patients not receiving chemotherapy in the first postoperative year (Avedian et al., 2007). In contrast Muscolo et al (Muscolo et al., 2005) found that the use of chemotherapy did not have a significant effect on the overall allograft survival rates in patients undergoing reconstruction using osteoarticular allografts for musculoskeletal sarcomas.

The work in this chapter shows that there was no difference in the amount of ECBB over the HA collar. A number of other studies have shown the contrary with bone turnover (Virolainen et al., 2005) being clearly affected by the use of chemotherapy. Avedian et al (Avedian et al., 2007) found chemotherapy to temporarily adversely affect bone growth at the bone-implant interface however, after 1 year they observed no differences between the two groups. Either chemotherapy has no true effect on extracortical bone growth or the 3 year follow-up period in our study is not long enough to detect the difference in ECBB between the two groups. There may be several possibilities associated with the effect of chemotherapy: 1) The effects of chemotherapy on bone remodelling are temporary and over a longer period of time bone remodelling reverts back; 2) That the effects of the chemotherapy are permanent and will therefore lead to long term changes in bone remodelling; 3) That the effects of chemotherapy on bone remodelling are temporary but the changes in bone

remodelling during the temporary period effect the long term bone formation around the implant

Osseointegration of extra cortical bone in DFRs has been shown to be effective in reducing loosening (Cannon, 2015). This work has shown a significant difference in the amount of osseointegration that occurred posteriorly within 3 years. It can be concluded that multi-drug chemotherapy did not affect bone growth, but did show an effect upon osseointegration of the HA collar.

Osseointegration can be described on a cellular level by the attachment of osteoblasts onto the implant surface and subsequent extracellular mineralisation. Osteoblasts attach to substrates using a complex of collagen and molecules known as integrins (Barrere et al., 2006). One of the most important attachment proteins that integrins attach to is fibronectin, of which human blood plasma levels reduce significantly when the patient is exposed to chemotherapy. These reduced levels can be seen as early as the next day following chemotherapy (Choate and Mosher, 1983) with up to a 50% reduction in levels seen over 3 weeks from the initiation of chemotherapy (Brodin et al., 1983). Treatment with cisplatin has been shown to directly reduced gene expression of fibronectin by almost 2.5 times (Carminati et al., 2010). Reduced osseointegration of HA collars in patients undergoing chemotherapy could therefore be due to the negative effect of chemotherapy on cell attachment.

A large gap as a result of osteolysis and the inhibition of bone formation at the shoulder of the implant will cause increased strain on the stem leading to loosening (Perren, 2002). The amount of strain and therefore loosening is dictated by the extent of osseointegration of the extra cortical bone and the quality of the intramedullary stem fixation. It is important to consider both the gap size and RLL score when assessing implant loosening. DFRs in chemotherapy patients show a greater gap formation and higher RLL score than the control group. These two indicators of early loosening furthermore are positively correlated. Finite element analysis has shown osseointegration of extra-cortical bone reduces stresses passing through the implant (Fromme et al., 2017, Chao and Sim, 1990), this supports this statement as early loosening of the intramedullary stem is negatively correlated with osseointegration of the

extra-cortical bone. In conclusion, loosening is related to lack of osseointegration with greater loosening occurring in the chemotherapy group.

There are no clinical studies that have analysed the effect of multi-drug chemotherapy on bone growth in the absence of disease. Although it cannot be guaranteed that the results in this chapter are due to the chemotherapy alone and not the underlying sarcoma, it is highly probable that the former is true given the *in vivo* evidence available using validated animal models (Burchardt et al., 1983, Friedlaender et al., 1984, Pelker et al., 1985).

## 2.5 Conclusion

An understanding of the involvement of multi-drug chemotherapy on the osseointegration and loosening of endoprostheses is imperative to allow for continued development of limb salvage procedures and implants. This work has shown that radiographic evidence of loosening of distal femoral replacements can be seen as early as 3 years and that differences in osseointegration of the HA collar is observed in the 1<sup>st</sup> postoperative year. Clinically this is important as bone tumour units should consider these findings when following up their patients and provide more stringent follow-up to those patients receiving chemotherapy, particularly in the initial years post-operatively given the increased risk of loosening. This work has shown that the current collar design does not lead to the same level of osseointegration in patients receiving chemotherapy as it does in patients not receiving chemotherapy. A large percentage of patients with distal femoral implants also receive chemotherapy and therefore implants that promote osseointegration of ECBB would be advantageous. Early signs of radiographic loosening can also be exhibited in the non-chemotherapy group therefore it can also be justified that the demand for a novel ingrowth region is not only restricted to chemotherapy receiving tumour patients but also to patients undergoing reconstruction using massive segmental prostheses. In the next chapter of this thesis the osseointegration of a novel porous ingrowth collar manufactured using SLS will be compared to the current solid grooved collar design in an *in vivo* model of segmental replacements.

## **Chapter 3. Augmenting Osseointegration of Endoprostheses using Laser Sintered Porous Collars**

### 3.1 Introduction

The work presented in my previous chapter showed that there is a need for an ingrowth device that allows for improved osseointegration in patients undergoing limb reconstruction using endoprostheses. A number of studies have used an ingrowth region adjacent to the bone at the transection site to promote ECBB (Chao et al., 2004, Chao and Sim, 1990, Chao and Sim, 1992, Blunn and Wait, 1991, Sim and Chao, 1979, Taylor et al., 1997). Bony bridging is where bone from the cortex adjacent to the transection site, grows out and over the shaft of the prosthesis. Potentially, osseointegration at the shoulder of the implant may reduce the risk of AL by improving stress transfer within the cement mantle, reduce mechanical loosening and prevent inappropriate loading of the Ti alloy stem which may lead to fatigue failure. Bony bridging can also prevent migration of fluid and wear particles along the bone implant interface by forming a seal and load the bone in a physiological manner reducing bone resorption associated with stress shielding (Chao and Sim, 1990, Taylor et al., 1997, Unwin et al., 1996, Ward et al., 1993).

Direct bone-implant contact is required for advantageous stress transfer during loading and Tanzer et al (Tanzer et al., 2003) reported that although patient radiographs indicated extra-cortical bone osseointegration and direct bone-implant contact within the coated ingrowth collar, histological analysis revealed no true extra-cortical bone-implant osseointegration. Results showed that a fibrous tissue layer was present between bone and the coating. This contrasts with the study by Coathup et al (Coathup et al., 2013b) where histological analysis showed mature lamellar bone within the grooves of HA-coated ingrowth collars with bone observed in direct contact with the HA coated implant surface. In this study it was also demonstrated that implants that had osseointegrated demonstrated increased survivorship compared to implants without radiographic evidence of osseointegration in the collar region.

ECBB and osseointegration in the collar region therefore appears to be important in reducing implant loosening in patients with massive segmental implants. However in some cases even though bony bridging may occur, osseointegration may not be reliably obtained. Ingrowth areas on massive

segmental implants are generally similar to the ones that are used for hip and knee replacements and are often surfaces composed of fiber metal or porous metal sintered coatings. A porous SLS collar located at the shoulder of the implant, may allow greater bone ingrowth directly from the transected cortical surface and through and within the implant structure. This porous design may further improve the amount and reliability of osseointegration in this region (Bram et al., 2006).

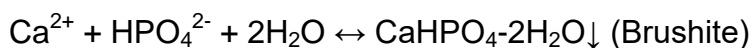
A HA coating deposited using an EC technique could be used to introduce a uniform HA layer within a complex porous structure. In this chapter, an EC deposited HA coating was used to coat selective laser sintered porous collars. The EC coating method used was adapted from Redepenning et al. (Redepenning et al., 1996) and the process involves submerging the substrate to be coated into a CaP solution and passing a controlled current through it. A series of chemical reactions occur which subsequently leads to the formation of a layer of HA on the implant surface (Equation 1, Equation 2, Equation 3, Equation 4).



**Equation 1 EC reaction where the current passing through the solution can control the pH.**



**Equation 2 Acid base reaction, determined by pH**



**Equation 3 Precipitation reaction, influenced by the concentration of  $\text{HPO}_4^{2-}$ .**



**Equation 4 Conversion of brushite into HA by immersion in NaOH for 72hrs.**

In order to allow for the ingrowth collar to withstand stresses and compressive loads it must have structural integrity. The different experimental collar designs must maintain their mechanical properties and therefore variables such as the strut size have to be adjusted. As a result the smaller pore design comprises of a 700 $\mu\text{m}$  pitch length with a strut size of 300 $\mu\text{m}$ , the larger pore design has a 1500 $\mu\text{m}$  pitch length with a strut size of 750 $\mu\text{m}$ . The resultant approximate pore diameter is 550 $\mu\text{m}$  and 1125 $\mu\text{m}$  for the small and large pore scaffolds respectively. As well as those studies discussed in 1.6.4, Fukuda et al (Fukuda et al., 2011) showed that laser sintered pores of 500 $\mu\text{m}$  and 600 $\mu\text{m}$  showed

significantly higher osseointegration compared with other groups with the upper limit of pores investigated in this study being 900µm. This study showed bone ingrowth to a depth of 5mm. In this chapter a larger pore size was also chosen to investigate optimisation of the pore size with regard to osseointegration in an ovine tibial mid shaft segmental model.

In this chapter, bone growth within two EHA coated porous ingrowth collar designs were investigated. Bone growth within a small pore and large pore porous collar was compared with conventional plasma sprayed grooved collar following a 6 month post-operative period.

**The aim of this part of my thesis was to investigate the use of selective laser sintered porous collars as an alternative design to the solid grooved collar implants in a large segmental defect model.**

**The hypotheses were that:**

- 1. An EC technique can be used to apply a HA coating within a porous structure.**
- 2. Porous collars allow bone to permeate through its structure with direct bone-implant contact.**
- 3. Small pore porous design allows for the greatest amount of bone implant contact.**

## 3.2 Materials and Methods

### 3.2.1 Manufacture of collars

Fifteen skeletally mature mule sheep were used for the purposes of this investigation reported in this chapter. Custom-made midshaft diaphyseal implants were manufactured where each implant contained a proximal and distal collar (Figure 3-1). Three different collars were manufactured and investigated in this chapter. The control group comprised of 5 implants with grooved collars (G) on either end. To investigate the use of porous ingrowth collars, 5 implants consisted of a proximal and distal small pore (SP) collar and 5 implants consisted of a proximal and distal large pore (LP) collar.



Figure 3-1 Custom diaphyseal implant with a proximal and distal grooved collar.



Figure 3-2 Exploded view of custom diaphyseal implant without collars showing halving joint and screw location.

In all groups the collar was integral with the implant shaft and stem and the implant joined together by a halving joint. Screws were inserted in the transverse plane (Figure 3-2). In all groups the implant was made from Ti alloy (containing 6% aluminium and 4% vanadium) and the screws from

commercially pure Ti. The reason that the screws were made from commercially pure Ti was that at surgery the ends of the screws were swaged over to prevent rotation and loosening. Commercially pure Ti is softer than Ti alloy allowing the ends of the screws to be deformed more easily. Both proximal and distal intramedullary stems were cemented within the tibia. The stem of the implant was manufactured such that where it made contact with the collar it was recessed, allowing the ingress of excess cement as the intramedullary stem is inserted during surgery. This would therefore allow contact between the cortical bone and collar interface without an interposing cement layer.

In the control collar group, the grooves were arranged longitudinally and circumferentially and were spaced 1 mm apart and measured 1 mm in width and 1 mm in depth. These grooves are of the same size and shape that is used on HA collars to treat human patients. The Ti alloy porous collars were made by SLS (Eurocoating, Italy) and were manufactured with a central hole where the collar was press fit onto the stem of the proximal diaphyseal half replacement. The SP collars were HA coated using an EC coating technique whereas G and LP collars were plasma sprayed with a highly crystalline (>85%) HA coating that measured 70µm in thickness (Plasma Biotal, Tideswel, Derbyshire, UK) (Figure 3-3).

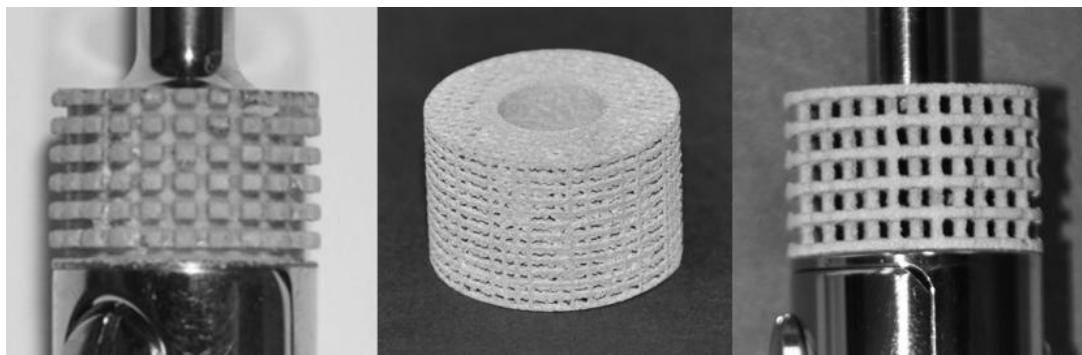


Figure 3-3 Pictures of grooved (left), small pore (middle) and large pore (right) collar designs.

### 3.2.2 EC deposition of HA onto SP porous collars

SP and LP collars were ultrasonically cleaned in 10% Decon 90, distilled water, 99% Industrial Methylated Spirit (IMS) for 15 minutes at each stage and then left to air-dry.

A supersaturated 0.13M CaP solution was prepared by adding 30g of  $\text{Ca}(\text{H}_2\text{PO}_4)_2$  (C8017; Sigma-Aldrich, UK) to 1L distilled water. The solution was vigorously stirred for 1 hour and filtered using Whatman 540 filter paper (GE Healthcare, UK) to obtain a clear solution by removing the suspended CaP crystals. Porous collars were submerged in CaP solution and attached to the negative terminal of a DC Dual Power Supply pack (Peak Tech, Telonic Instruments Ltd, UK) to act as the cathode with a platinum ring (20mm diameter x 1.5mm thickness) as the anode. A current of 175mA measured by a FLUKE 867B Graphical Multimeter (Fluke Corporation, USA), was passed through the actively stirred solution for 40mins. The initial CaP precipitate ( $\text{Ca}_2\text{HPO}_4 \cdot 2\text{H}_2\text{O}$  (Brushite)) was converted into HA,  $\text{Ca}_5(\text{PO}_4)_3\text{OH}$ , by soaking the collars in 0.1M NaOH solution for 72h. The NaOH solution was produced by adding 2g of NaOH (480878, Sigma-Aldrich, UK) to 500ml distilled water which was then vigorously stirred for 30mins. Finally, the porous collars were gently rinsed with distilled water and left to air dry before being autoclaved prior to implantation. CaP deposition on the collar and coating characterisation was completed using scanning electron microscopy (JSM-35C; Jeol, Welwyn Garden City, UK), energy dispersive x-ray spectroscopy (EDS UK, Leicester, UK) and x-ray diffraction techniques (XRD, Bruker, Massachusetts, USA).

### **3.2.3 Surgery**

All procedures were carried out in accordance with the UK Animal Scientific Procedures Act 1986 at the Royal Veterinary College, North Mymms. Home Office Licences were held by all those taking part in any surgical procedure. One implant was inserted into the right tibia of each sheep and implants were kept in situ for 6 months.

### **3.2.4 Analgesia**

Intramuscular xylazine at 0.1mg/kg 10 minutes before induction of anaesthesia was used to pre-medicate the sheep. Ketamine (2mg/kg) and midazolam (2.5mg) was administered intravenously to induce anaesthesia. To protect the airway and to allow ventilation, the animal was intubated and anaesthesia was maintained with 2% halothane and oxygen for the duration of the procedure.

Intra-operative pulse oximetry, ECG and end-tidal carbon dioxide were monitored.

### **3.2.5 Insertion of diaphyseal implants**

Animals were placed in supine position and the right hind leg was shaved. Betadine® (Purdue Products L.P., Stamford, Connecticut, USA) surgical scrub was applied to the area followed by Betadine® antiseptic solution. The animal was then transferred into the operating theatre at which point the surgical site was further prepared with Hydrex Surgical Scrub (MidMeds Ltd. Loughton, UK) which is a chlorhexidine based aqueous antimicrobial.

Sterile drapes were placed leaving the anteromedial right tibia exposed. A longitudinal 60mm incision over the midshaft of the right tibia was made starting 50mm distal to the tibial tuberosity. A 50mm section of tibia was removed 60mm from the tibial tuberosity using a pneumatic saw. The periosteum from this section was removed intact.

Both the proximal and distal intramedullary canals were prepared for implantation by removing the bone marrow followed by repeated washing with saline (sterile 0.9% NaCl solution) (Figure 3-4). If canals were felt to be too narrow, further reaming was undertaken to accommodate a cement mantle of approximately 1.5-2mm surrounding the intramedullary stems of the diaphyseal implants. Implants were cemented in place with the use of Palacos R cement with Gentamicin (Biomet Europe, South Wales, UK). The two halves of the implant were joined centrally as described in 3.2.1 and the surrounding fascia, muscle and skin were closed. A spray dressing (Opsite®, Smith & Nephew, Gallows Hill, Warwick, UK) was applied to the wound prior to recovering the animal.

Post-operatively the animals were allowed to weightbear immediately as tolerated. Antibiotics (Exenel™, ceftiofur hydrochloride, 1ml/50kg, Pfizer Animal Health, Tadworth Surrey, UK) and analgesia (Vetergesic™, buprenorphine, 0.6mg/animal, Reckitt and Colman Products Ltd. Hull, UK) were administered

for 3 days following the procedure. Animals were recovered in individual pens and once able were group housed.

Animals were euthanized 6 months post-operatively by intravenous overdose of 0.7mg/kg pentobarbitone (20, K. M. Loveridge Ltd. Southampton, UK). None of the animals were sacrificed prematurely due to implant failure.

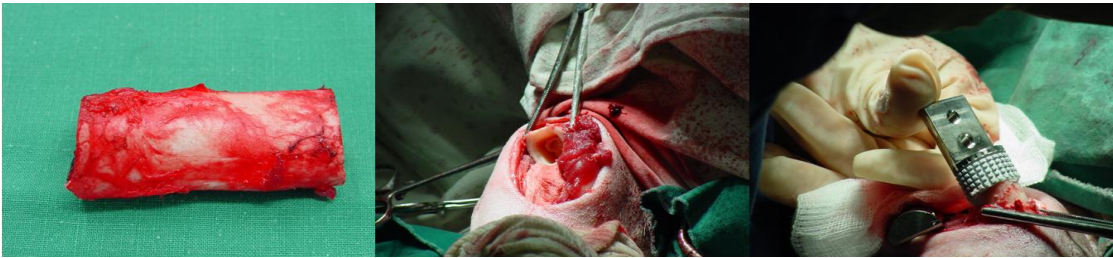


**Figure 3-4 (Left) 5cm resected mid-diaphyseal segment, (middle) prepared proximal femoral intramedullary canal, (right) proximal half of diaphyseal implant with grooved collar cemented in place.**

### **3.2.6 Radiological analysis**

Antero-posterior and medio-lateral radiographs were taken of the implant upon retrieval of whole tibiae at 6 months using an MX4 X-ray machine (PLH Medical Ltd, Watford, UK). The ECBB around each collar was quantified in both the AP and the ML planes. ECBB resulted in a pedicle of bone that was measured from the shoulder of the collar using different parameters and as used in the previous chapter; maximum thickness of extracortical growth (mm), maximum length of extracortical growth (mm) and surface area of extracortical growth ( $\text{mm}^2$ ) (Figure 3-5) were measured and compared between groups. Measurements were calibrated using AxioVision LE64 software (v4.9.1.0, Carl Zeiss Microscopy GmbH, Oberkochen, Germany) using known diameters of the implant intramedullary stem prior to tissue analysis.

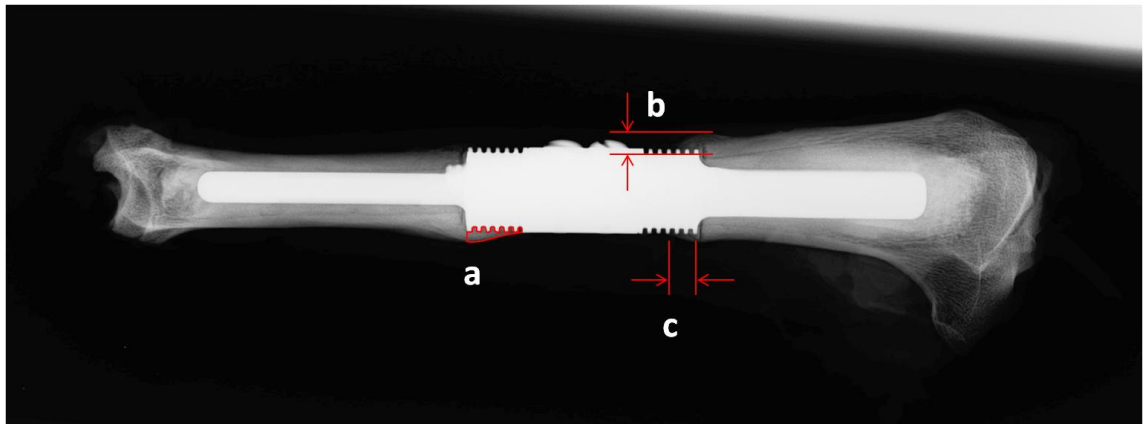


**Figure 3-5** ML radiograph of ovine tibia with midshaft implant in situ showing measurements taken for radiographic analysis; (a) surface area of bone pedicle from shoulder of implant, (b) maximal thickness of bone pedicle from shoulder of implant, (c) maximal length of pedicle from shoulder of implant.

### **3.2.7 Histomorphometry**

Following retrieval, samples with the implant in situ were stripped of excess soft tissue and fixed in 10% neutral buffered formalin for a minimum period of 2 weeks. Specimens underwent dehydration in successive increasing concentrations of industrial methylated spirit (IMS), de-fatted in a 50:50 mixture of alcohol/ether, immersed in 50% IMS and 50% resin mixture (LR White Resin, London Resin Company Ltd, Reading, Berkshire, UK), and followed by immersion in 100% resin. Each collar was embedded in hard grade acrylic resin (LR White, London Resin Company, Reading, UK). Each of the embedded samples were halved through the centre in the longitudinal plane using a 2mm diamond blade (EXAKT 311, EXAKT Technologies, Norderstedt, Germany). A section was prepared from one half for electron microscopy and a second section was prepared for staining and histological analysis (approximately 80 $\mu$ m in thickness) (Table 3-1). Thin sections were stained with Toluidine Blue and Paragon to identify soft tissue and bone. Stained slides were viewed under an Olympus light microscope (Axioskop, Carl Zeiss, Welwyn Garden City, UK) and images analysed using ImageJ software (v1.49, National Institutes of Health, USA) using a combination of freehand and thresholding techniques.

The total surface available for bone attachment for each collar was quantified by measuring the length (mm) of the collar surface in each thin section. Osseointegration was quantified by measuring the length (mm) of the collar surface with direct bone attachment. For porous collars this included the outer

and inner pore surfaces. The proportion of the surface with direct bone contact (%) was calculated for each collar using these measurements.

Subgroup analysis of the porous collars was also undertaken with the total inner porous surface area (mm<sup>2</sup>), area of soft tissue (mm<sup>2</sup>) and area of bone (mm<sup>2</sup>) within pores being measured for the SP and LP collars.

<b>Stage</b>	<b>Length of time</b>
10% neutral buffered formalin	2 weeks
30% IMS	1 week
50% IMS	1 week
70% IMS	1 week
90% IMS	1 week
100% IMS	1 week
100% IMS	1 week
100% IMS	1 week
50:50 IMS:Ether	1 day
50:50 IMS:Ether	1 day
50:50 IMS:Ether	1 day
100% IMS	1 day
100% IMS	1 day
100% IMS	1 day
50:50 IMS:Resin	1 week
100% Resin	1 week
100% Resin	1 week
100% Resin	1 week
Embed in resin	-

**Table 3-1 Preparation protocol for the production of thin sections. IMS, industrial methylated spirit**

### **3.2.8 Statistics**

Statistical analysis was performed using SPSS Statistics (v22, IBM, New York, USA). Data was tested for normality using the Shapiro-Wilk test and the Mann-Whitney U and Kruskal-Wallis tests were used to compare groups where p<0.05 were considered significant.

### 3.3 Results

#### 3.3.1 Evaluation of coating

Energy dispersive x-ray spectroscopy (EDS) of the electrochemical CaP coating reveals a Ca:P of 1.53 with XRD confirming both crystal and amorphous phases present in the coating (Figure 3-6). High amplitude narrow peaks and low amplitude wide peaks related to crystal and amorphous phases respectively. SEM confirmed deposition of the coating throughout the surface of the small pore collar (Figure 3-7).

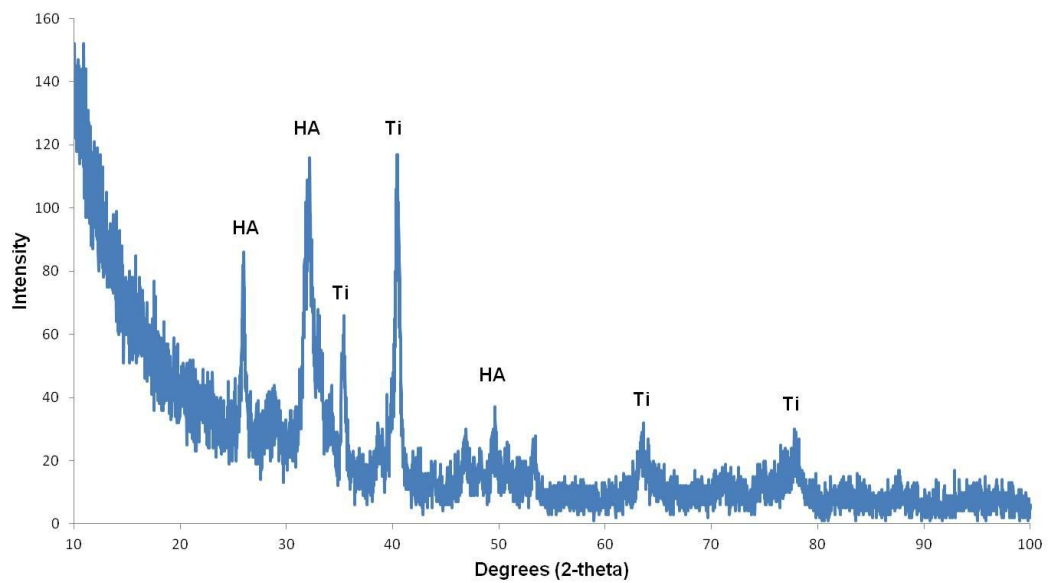


**Figure 3-6 X-ray diffraction spectra of EC coating identifying peaks for hydroxyapatite (HA) and titanium (Ti).**

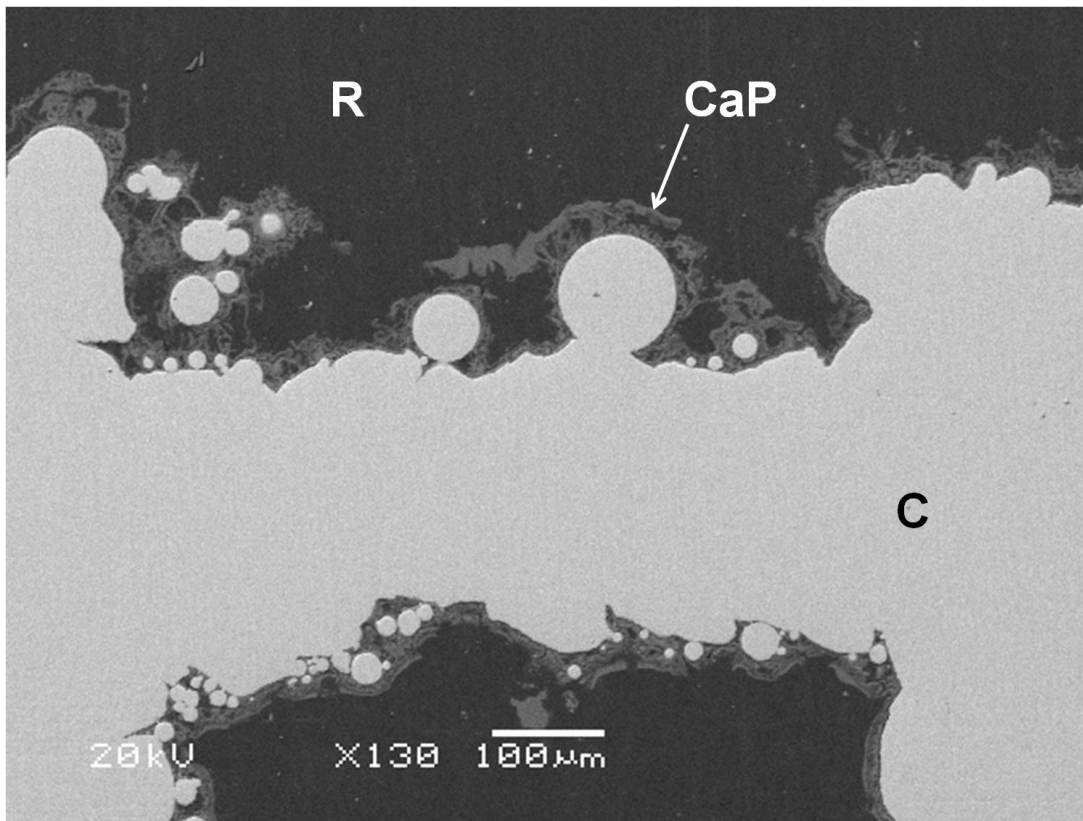


**Figure 3-7** Backscattered scanning electron microscope image of SP collar cross-section showing electrochemical deposited CaP coating on strut surface. Scale bar shown, x130 magnification. R; resin, CaP; EC deposited CaP coating, C; Titanium alloy collar.

### 3.3.2 Radiological analysis of extracortical bone growth

During surgery, all attempts were made to stop cement extruding out of the canal and over the collar during stem insertion that would have prevented the collar from abutting directly against the cortex and creating a gap. Occasionally in both SP and LP groups this cement issue was noted but in all cases bone was able to grow across the gap from the transected cortex and into the porous collar where cement was not present (Figure 3-13).

From the radiographs significantly greater amounts of extra-cortical bone formation was measured adjacent to the grooved design when compared to both porous collar groups ( $p < 0.01$ , Figure 3-8, Figure 3-9). Similarly, the surface area of the EC pedicle at the shoulder of the implant was also significantly greater around the grooved collar compared to both porous collar designs ( $p < 0.01$ , Figure 3-10). These findings are summarised in Table 3-2.

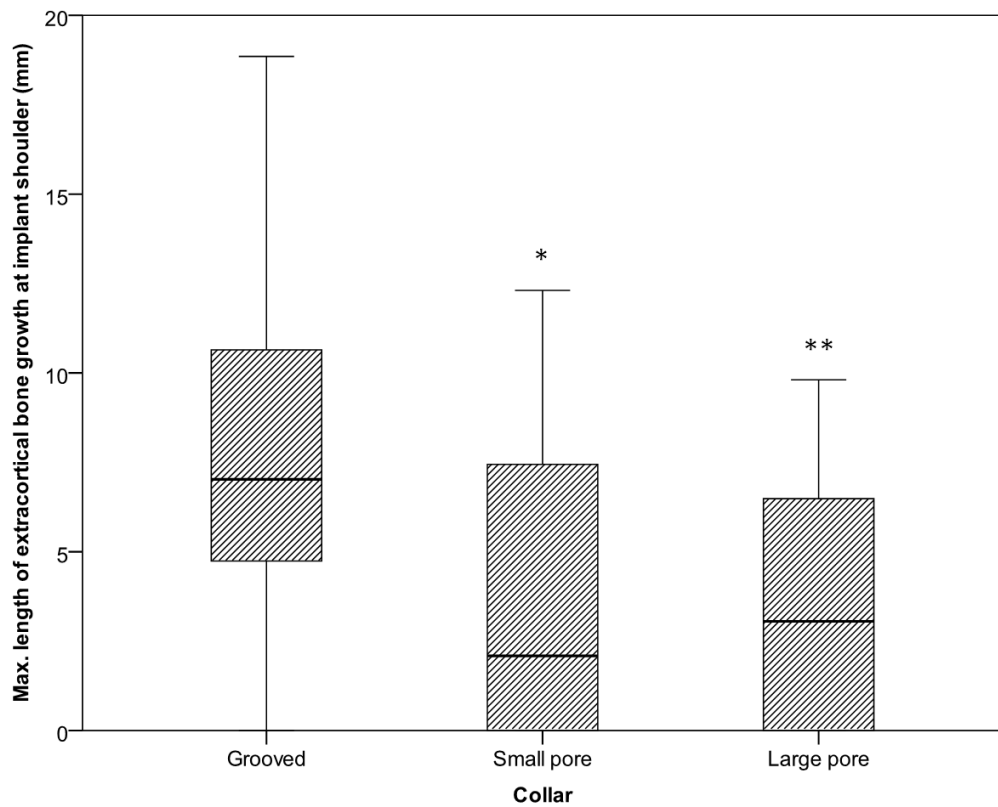


**Figure 3-8** Boxplot showing length of pedicle growth observed radiographically from shoulder of each collar design. \*small pore Vs grooved  $p=0.004$ , \*\*large pore Vs grooved  $p=0.001$ .

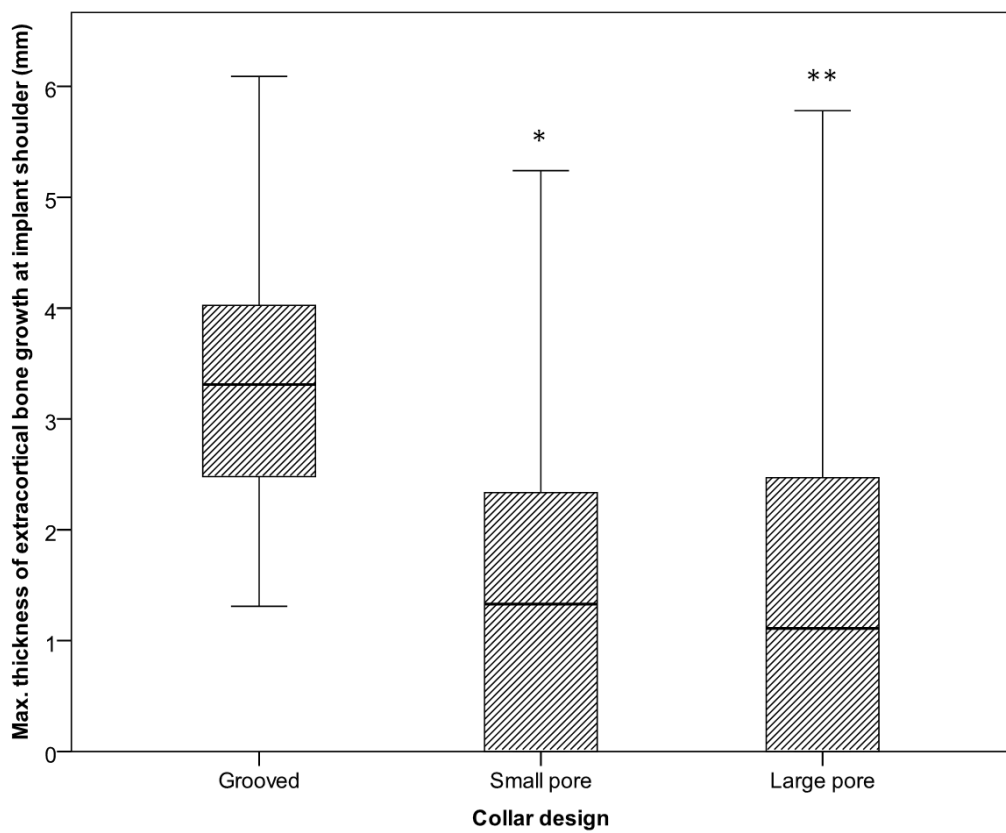


**Figure 3-9** Boxplot showing thickness of pedicle growth observed radiographically over each collar design. \*small pore Vs grooved  $p<0.001$ , \*\*large pore Vs grooved  $p<0.001$ .

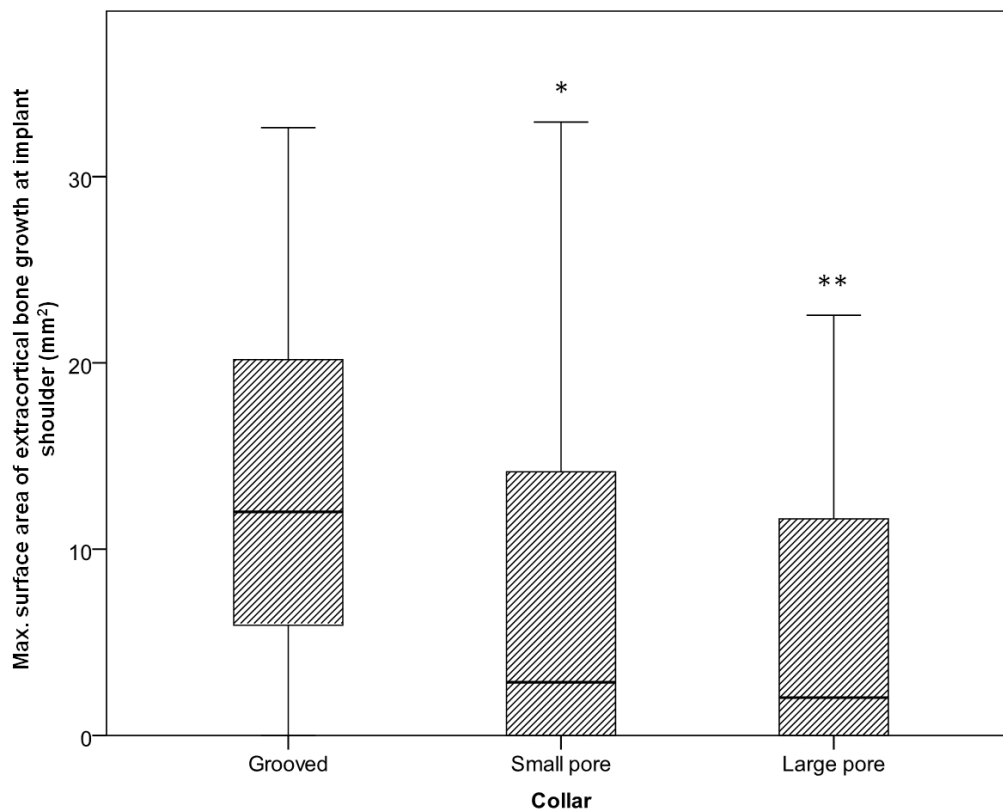


**Figure 3-10** Boxplot showing surface area of pedicle growth observed radiographically over each collar design. \*small pore Vs grooved  $p=0.005$ , \*\*large pore Vs grooved  $p=0.002$ .

	Grooved collar	Small pore collar	Large pore collar	p-value <sup>a</sup>
Max. length of pedicle (mm)	7.02 (4.73-10.72)	2.09 (0-7.84)	3.05 (0-6.64)	0.002
Max. thickness of pedicle (mm)	3.31 (2.46-4.07)	1.33 (0-2.43)	1.11 (0-2.51)	<0.001
Surface area of pedicle (mm <sup>2</sup> )	12 (5.89-20.31)	2.86 (0-15.28)	2.03 (0-11.85)	0.002

**Table 3-2** Results of measurements of ECBB around each collar type with medians (IQR) shown. <sup>a</sup>Kruskal-Wallis test.

### 3.3.3 Histomorphometric analysis of collar surface size and pore content

The surface available for bone contact (mm, IQR) for SP collars (224.88, 203.51-235.95) and LP collars (105.72, 82.89-133.45) was significantly greater when compared to the G collar group (33.32, 28.5-41.56). SP collars showed a significantly larger surface even when compared to LP ( $p=0.016$ , Figure 3-11).

Greatest bone contact (mm, IQR) with the implant surface was seen in the porous groups, with SP (72.39, 34.72-114.32) and LP (42.87, 4.5-84.53) collars showing significantly greater bone attachment than the G (13.11, 4.99-17.75) group (Figure 3-11).

When comparing the proportion (% , IQR) of the entire collar surface with bone attachment for each of the designs there was no statistical difference across the SP (37.4, 15.88-73.08), LP (61.5, 13.6-95.2) and G (42.3, 16.6-93.2) collars.

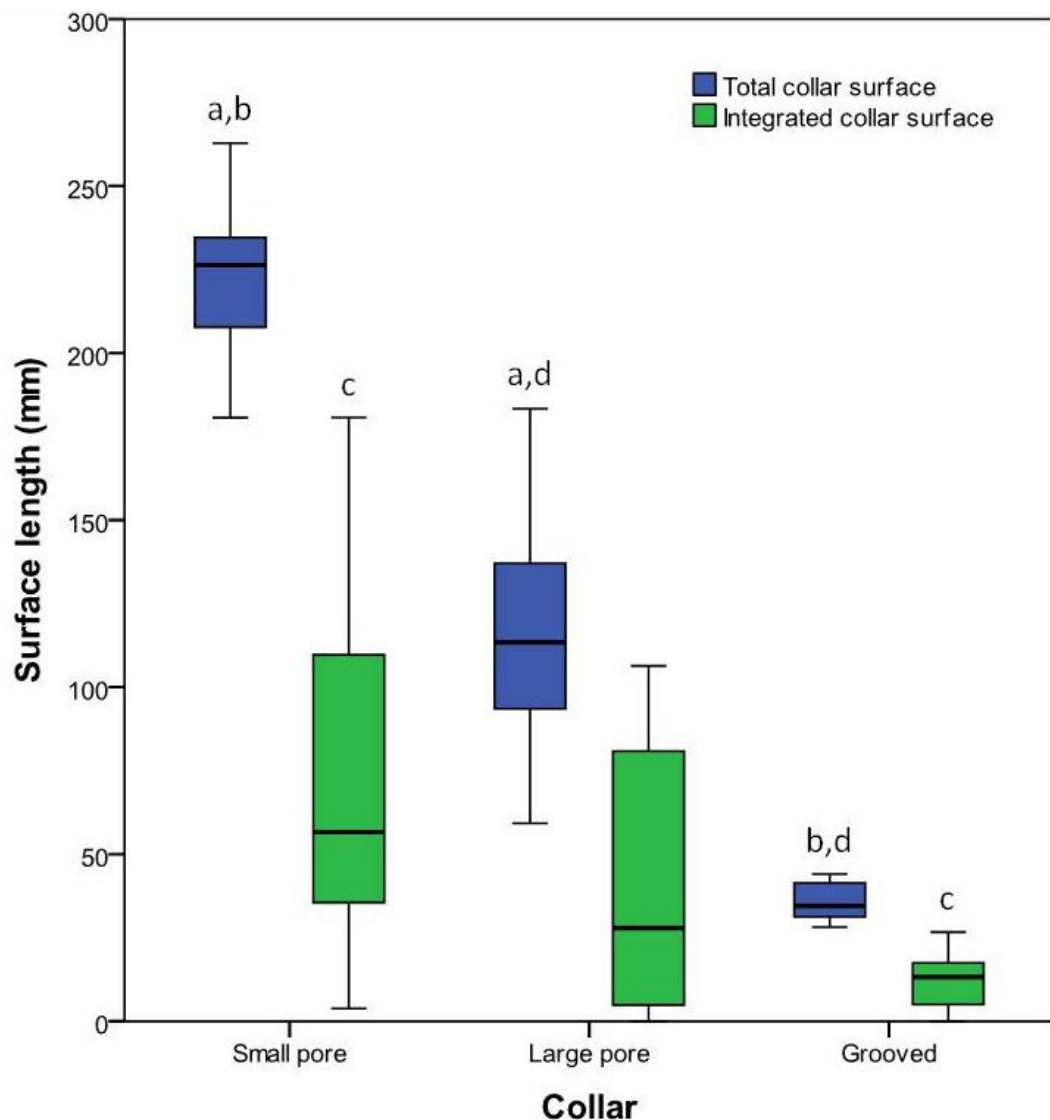


**Figure 3-11** Boxplot showing histomorphometric results for total surface of collar available for integration together with actual osseointegration for each of the collar types. Significant p-values of pair-wise comparisons are <sup>a</sup>0.016, <sup>b</sup><0.001, <sup>c</sup><0.001, <sup>d</sup><0.001.

A significantly ( $p=0.006$ ) greater area of cement ( $\text{mm}^2$ , IQR) was found within LP (1.37, 0.45-2.55) Vs SP (0.26, 0-1.03). A statistically ( $p=0.002$ ) greater amount of soft tissue was found compared to bone in the pores of the SP collar (Figure 3-12). Significantly greater amounts of bone and soft tissue were found compared to cement in both porous collar designs. Results are summarised in Table 3-3.

	Small pore collar	Large pore collar	p-value <sup>a</sup>
Bone area(mm <sup>2</sup> )	8.72 (3.63-12.3)	7.85 (0.71-19.49)	0.970
Soft tissue area (mm <sup>2</sup> )	19.35 (15.91-22.84)	17.58 (4.83-28.54)	0.543
Cement area (mm <sup>2</sup> )	0.26 (0-1.03)	1.37 (0.45-2.55)	0.015
p-value <sup>b</sup>	<0.001	<0.001	

Table 3-3 Median (IQR) histomorphometric measurements quantifying areas of bone, soft tissue and cement found within collar thin sections together with p-values. <sup>a</sup>Mann-Whitney U test: comparing the amount of bone/soft tissue/cement between the collars. <sup>b</sup>Kruskal-Wallis test: comparing the amount of bone/soft tissue/cement content within each collar.

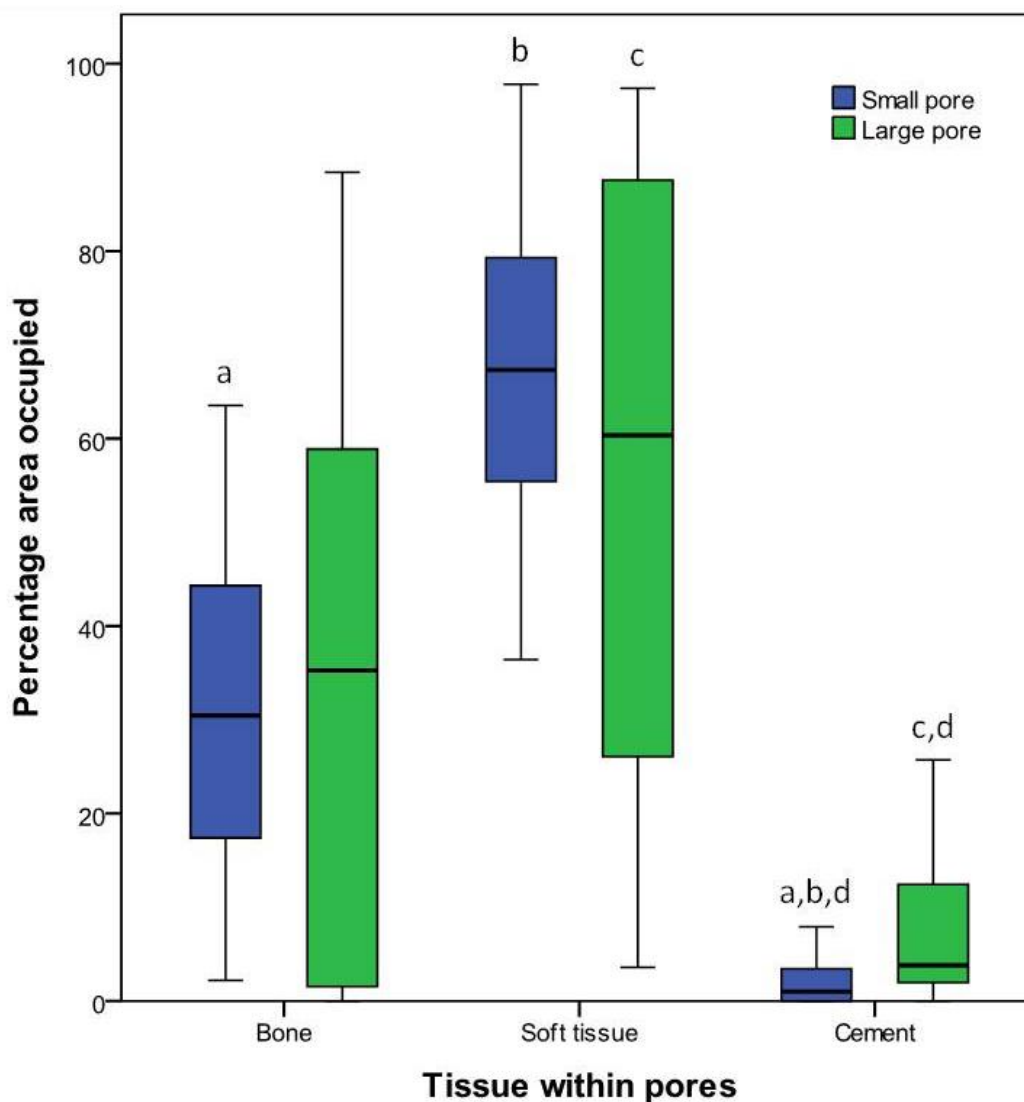
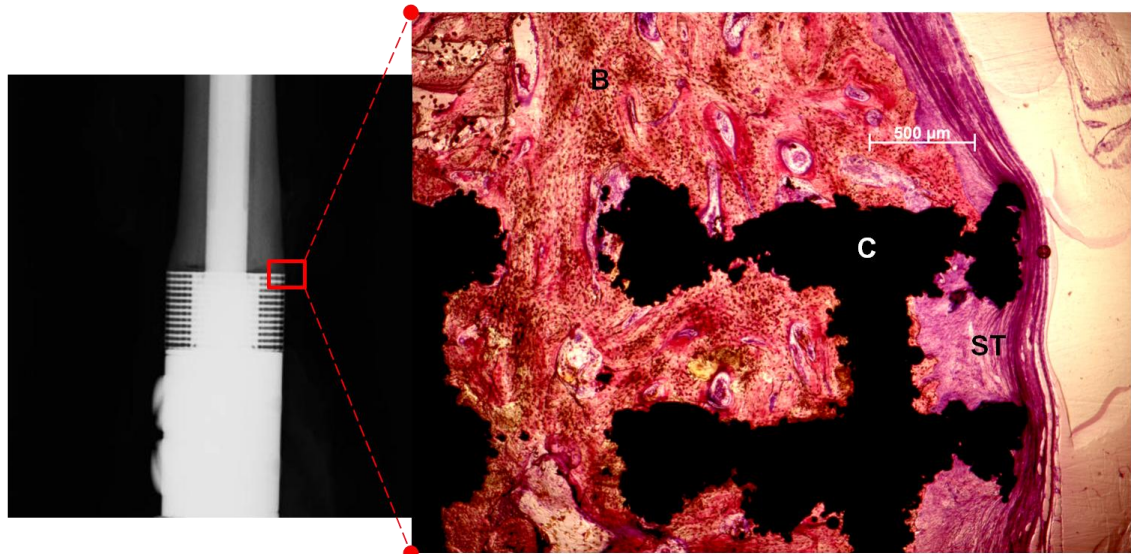


Figure 3-12 Boxplot showing histomorphometric results for inner pore contents of SLS collars. Significant p-values of pair-wise comparisons are <sup>a</sup>0.003, <sup>b</sup><0.001, <sup>c</sup><0.001, <sup>d</sup>0.015.

### 3.3.4 Histological appearance of bone ingrowth into the collars

Osseointegration was seen in both the distal and proximal collars of all implants.

Bone ingrowth into the grooved HA collar was associated with extra cortical bony formation and formed directly onto the surface of the implant. Only part of the available area for bone ingrowth had osseointegrated and this occurred predominantly adjacent to the bone at the transection site. The bone that formed on the collar adjacent to the transection site was mature lamellar bone however, at the pedicle tip, which was furthest away from the transection site, woven bone was seen.



**Figure 3-13 (Left) radiograph of SP collar in situ, (Right) Light microscope image showing interface between porous collar and transection site. x2.5 magnification. Toluidine blue and Paragon stain used. B; Bone (pink), ST; Soft tissue (purple), C; Collar (black). Scale bar shown.**

In the porous collar groups bone formation was associated with bone growth from the transected cortical surface up and into the collar with limited extra-cortical bone bridging (Figure 3-13). Bone osseointegrated within the porous Ti alloy strut surface. Within the pores bone was observed to grow peripherally on the pore surface and integrate rather than developing centrally within the pore space and growing outwards onto the surface (Figure 3-14). Adjacent to the transection site, in both porous groups, cement penetrated the pores. The depth of penetration of this cement varied between 0 and 5 mm and was greatest with LP collars however, in all cases the cement never entirely covered the transected surface of the cortex and bone formation in the porous collars was continuous with cortical bone. Bone formed by intramembranous ossification with no evidence of endochondral bone formation. For the LP collars, the HA coating was evident only on the outer surface of the porous metal struts and its

position was consistent with the plasma sprayed line of site coating. In the SP collars the EC deposited HA coating had resorbed.

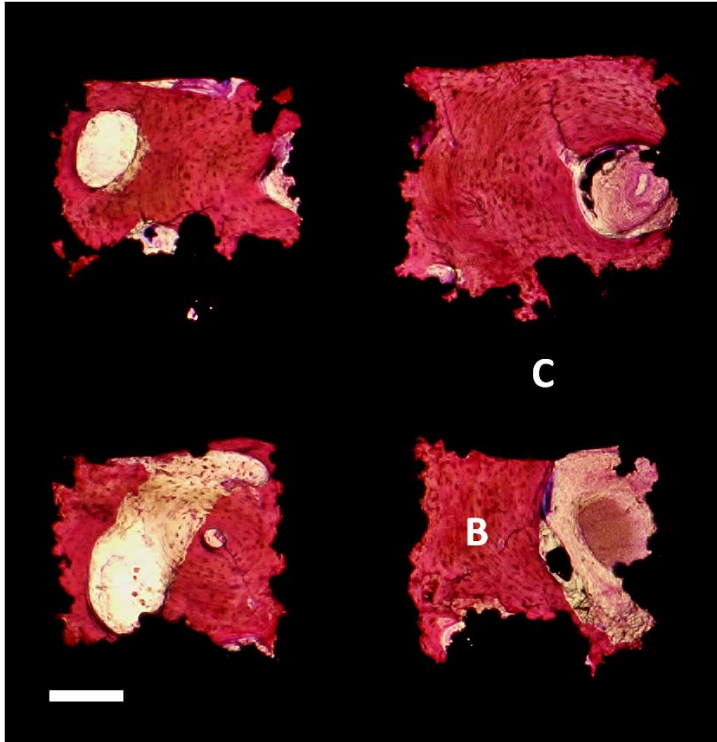


Figure 3-14 Light microscope image of inner pores of SP collar. Scale bar 200 $\mu$ m, x2.5 magnification, stained with Toluidine blue and Paragon. Bone (B, pink) and collar (C, black).

### 3.4 Discussion

The concept of obtaining bone ingrowth at the junction of the body of the implant came from the observation that heterotopic bone formation, albeit in variable amounts, often occurs at this site after large bony resections (Chao and Sim, 1992). This concept has been used in prostheses that replace large segmental diaphyseal defects, however osseointegration of the surface with direct bone-implant contact has only ever been demonstrated where a HA plasma coated structure has been used (Myers et al., 2007). It has been shown that, ECBB where the bone is osseointegrated onto the shaft of the implant can increase implant survival at 10 years by over 20% (Coathup et al., 2013b).

In this chapter porous collars made using a SLS technique were developed to enhance the fixation of massive segmental implants. Results showed that a porous structure significantly increased osseointegration where bone permeated through the porous structure from cortical bone at the transection site. Compared to other massive segmental implants that have surface ingrowth areas or grooved surfaces, bone ingrowth in porous collars occurs mainly by a process of bone growth directly from the transection site into the scaffold (ingrowth) and is not associated with extra-cortical bone formation and surface ongrowth.

It has been proposed that extra-cortical bridging and bone ingrowth prevents AL by sealing the bone implant interface. It is theorised that this prevents wear debris and joint fluid from accessing the bone implant interface, thereby, decreasing the risk of osteolysis at the bone-cement-implant interfaces (Ward et al., 1993). Alternatively it has been shown that osteoclast activation from pressurised joint fluid causes bone resorption (Van der Vis et al., 1998b, van der Vis et al., 1998a) and in a large segmental implant where osseointegration at the shoulder does not occur, the bone implant interface is in contact with joint fluid, which may be pressurised leading to early loosening. It is expected that the greater osseointegration seen with a porous collar in this study would result in a more robust seal. Another possibility is that ECBB and osseointegration diverts the load from the stem resulting in reduced stresses and reduced mechanical failure. Osseointegrated ECBB would also transmit load more

physiologically by loading the cortex directly adjacent to the collar surface at the transection site. This would prevent stress shielding and consequently enhance fixation. This may be particularly important for adolescent patients where a small diameter stem is used to fit into the small intramedullary cavity of these young and still growing patients. As the patient grows the endosteum remodels and although a shell of bone often remains around the cement, so called metaphysealisation of the cortex (Blunn and Wait, 1991) occurs leading to strength of the fixation being reduced. Osseointegrated ECBB would reduce stresses passing along the stem and thus reduce loosening in these young patients. The stem when inserted in young patients becomes undersized as the patient grows and body mass increases. This could lead to mechanical failure later in adult life but osseointegrated ECBB would possibly alleviate this.

Completely porous metals can be created by several different manufacturing methods; examples include Hedrocel (trabecular metal), which is porous tantalum made by chemical vapour deposition from tantalum chloride gas onto a carbon scaffold (Zardiackas et al., 2001). Ti foams have recently been made by foaming and sintering producing controlled interconnected porosity and complex surface topography and these materials have been proposed as a new type of biomaterial (Wazen et al., 2010). Both Hedrocel and porous Ti foams are available commercially as bone ingrowth structures however; with these materials it is difficult to change the pore size and to alter the geometry of the implant. Ti alloy implants can be made by either e-beam or SLS, which is a form of 3D printing where implants can be manufactured from a data file generated using computer aided design. Different mesh sizes can be used in a single implant and where appropriate and in order to provide the appropriate strength, these may be joined to solid metal made by SLS or electron beam. In this chapter, a collar that had a cross-sectional shape similar to the resected bone was investigated and it is conceivable that customised implants matching the shape of the transected bone in humans could be easily and cost effectively made using this technology.

One of the critical factors for bone ingrowth is the size of interconnecting pores. Several investigators have studied bone ingrowth into porous systems with different pore sizes (Bobyne et al., 1980, Bloebaum et al., 1998). The diameter of

interconnecting pores seems to dictate the quality of tissue growing into the porosity. The consensus seems to be that the optimal pore size for mineralized bone ingrowth is 100–400  $\mu\text{m}$  (Bucholz, 2002, Elema et al., 1990, Engh, 1983, Hungerford and Kenna, 1983, Laptev et al., 2004, Pilliar, 1987). In our study where we used pore sizes of between 550 and 1125  $\mu\text{m}$  there appeared to be little difference in the amount of new bone formation. Porous ingrowth collars situated in the femoral diaphyseal region are subject to different forces compared to porous backings on acetabular shells for example and therefore the collar design must reflect this in terms of porosity, strut thickness and length. The design of the porous collar structure must be stiff enough to withstand compression under weightbearing yet compliant enough to prevent stress shielding. These porous implants rely on cortical bone growth to penetrate deep within its structure and its design must encourage this to occur by avoiding stress shielding and allowing the development of a vascular system (Kanczler and Oreffo, 2008). Porous layers on the backs of acetabular shells are reliant on superficial penetration of bone tissue or in some instances surface attachment with no penetration of the cancellous bone. This is the basis for the current data on 'optimal pore size', a very different situation from an ingrowth region on an endoprosthesis implant.

In this study one of the porous implant surfaces was plasma sprayed with HA coating whilst the other had a biomimetic CaP coating that was electrodeposited according to Redepenning et al (Redepenning et al., 1996). After 6 months the plasma sprayed coated implant retained its coating, which was restricted to the outer strut surfaces but the electrodeposited coating had been resorbed. This can be explained by the low crystallinity of the EC coating compared to commercial plasma sprayed HA. Even with complete resorption of our EC coating there was no apparent difference in bone formation between the porous collars at 6 months.

HA coatings have been used experimentally to deliver growth factors to encourage bone formation and osseointegration. Using a canine model rather than an ovine one, the plasma sprayed HA coating of a sintered bead surface was used as a carrier for BMP7 and was shown to encourage bone ingrowth (Saran et al., 2011). Plasma sprayed HA coatings onto a fibre metal ingrowth

region was used as a carrier for TGF-B3 and was shown to enhance bone formation across gaps and enhanced osseointegration of the implant in a caprine model (Sumner et al., 1995). Using electro-deposited HA to coat the inner struts of the porous surface and to deliver growth factors may further increase osseointegration.

A cement layer at the shoulder of the implant may have been more important for the porous collars than for the grooved collar, which relied on extra-cortical bone formation. This is because bone ingrowth for the porous collars originated from the transected cortical bone surface whereas bone growth into a HA grooved collar is from the periphery of the cortical bone. A layer of cement between the implant and the collar in this position impedes bone ingrowth. Although when we inserted the implant, care was taken not to get cement between the bone and the shoulder, practically this is difficult to prevent as pressurization of the cement tended to create this layer. A solution to this may be to use uncemented implant stems.

There are other ways that implant fixation can be improved for massive segmental prostheses. The Compress® Compliant Pre-Stress Implant (Biomet, Warsaw, IN) imposes a compressive force between the implant shoulder and the cortical bone. Compliant pre-stress osseointegration is a relatively new implant technology and may have improved survival compared with traditional implants (Pedtke et al., 2012). This device achieves immediate compliant fixation onto host bone using a spindle that attaches directly onto the cut end of the bone. The spindle is secured by tightening a nut across a series of Belleville washers that act as springs and generate a compliant compression force across the bone-prosthesis interface. Loading forces are transmitted directly onto the host bone in an axial direction resulting in bone growth at the bone prosthesis interface and osseointegration (Kramer et al., 2008).

In this study a cylinder of porous metal was used where the cylinder was press fitted onto a continuation of the cemented stem. This was secure and prevented the implant being completely made by the SLS methods although this could have been possible. In this way the overall strength of the implant is maintained

as appropriate but a greater bone ingrowth area was made available using this technology.

### 3.5 Conclusion

The work in this chapter has shown that the concept of porous ingrowth collars manufactured from Ti alloy using a SLS technique, allowed for significantly greater osseointegration when compared to the commercially available solid grooved collar design. Although both the SP and LP designs allowed for significantly greater surface area for potential osseointegration, it only translated into a statistically significantly greater amount of osseointegration for the SP design. Histologically, greater osseointegration was observed with the SP collar as the full surface of this design was coated compared to only the outer surface of the LP collar, which was plasma sprayed.

The focus for the following chapters will be to refine the biomimetic CaP coating as well as develop Si and Sr substituted HA coatings using *in vitro* techniques. These bioactive coatings will then be used in conjunction with SLS Ti alloy structures in an *in vivo* model to evaluate which combination of coating and pore size allows for optimum osseointegration to form my final chapter.

**Chapter 4. Development, Characterization and Evaluation of the  
Bioactivity of Silicate and Strontium Substituted  
Hydroxyapatite Coatings**

## 4.1 Introduction

This chapter describes the development and *in vitro* testing of three HA coatings deposited using an EC technique. The groups investigated were (i) an electrochemical HA (EHA) coating, (ii) an electrochemical silicate-substituted HA coating (ESiHA) and (iii) an electrochemical strontium-substituted HA coating (ESrHA). The overall aim was to develop a HA coating for application onto the porous SLS collars described in the previous chapter.

Natural bone is composed of HA with multiple ionic substitutions. Bone mineral therefore exhibits calcium, phosphate and hydroxyl deficiencies when compared to stoichiometric HA (Ca:P 1.67). Ca:P ratios of bone mineral range from 1.37 to 1.87 (Hing et al., 2006) due to these various anionic and cationic substitutions. Carlisle et al (Carlisle, 1970) performed a series of investigations on the importance of Si in bone formation. These initial studies observed Si levels of 0.5 weight percentage (wt%) in areas of new bone formation. The weight percentage is a way of expressing the composition of a mixture of compound relative to its total weight. Schwarz then went onto confirm the importance of Si as a cross-linking agent in connective tissue and its importance in vascular health (Schwarz and Milne, 1972, Schwarz et al., 1977). This initiated the drive for the formation of biomaterials containing Si. As a result, there is now increased evidence that the presence of Si in bioactive glasses and glass ceramics increase bioactivity and osseointegration with bone. The ionic dissolution products of bioactive glasses up-regulate osteoblast proliferation and gene expression (including BMP-2).

Silicate ions ( $\text{SiO}_4^{4-}$ ) substitute phosphate ( $\text{PO}_4^{3-}$ ) ions in the HA lattice (Equation 5). In order to compensate for the substituted silicate groups and loss of phosphate groups, a hydroxyl group must also be released to balance the molecular charge. This also allows for the Ca:(P+Si) ratio to remain at 1.67, the same as stoichiometric HA.



**Equation 5 Silicate substitution within HA lattice.**

This substitution increases bioactivity either through a change in the surface chemistry of the HA (surface Si availability and/or charge) or the dissolution of Si into the surrounding area (Pietak et al., 2007). *In vivo* models with increasing Si levels within bone graft substitutes showed improved osseointegration with bone (Patel et al., 2002, Patel et al., 2005). Further *in vivo* work by Hing et al (Hing et al., 2006) observed that a 0.8wt% of Si was optimal in achieving the greatest bone ingrowth. The increased bioactivity of the 0.8wt% SiHA is thought to be as a result of protein adsorption, osteoblast-like cell attachment and cell responses such as increased ALP activity. The same study revealed that the higher Si content (1.5wt%) was detrimental with a slower mineral apposition rate and reduced new bone formation in an *in vivo* model over 12 weeks. Multiple methods can be used to form a SiHA coating, including a sol-gel technique (Ruys, 1993), hydrothermal methods (Tanizawa and Suzuki, 1994), aqueous precipitation (Jarcho et al., 1976), magnetron co-sputtering (Thian et al., 2005) and EC deposition techniques (Li et al., 2011, Huang et al., 2013).

Sr is a trace element found in areas of high bone turnover. As described in section 1.9.3 of my thesis, Sr has been found to inhibit osteoclast activity via the RANKL pathway and expression of OPG. Sr has also been shown to stimulate osteogenic differentiation of mesenchymal stem cells (Capuccini et al., 2008) via the Wnt pathways reporting an optimal Sr content of 3-7 atomic percentage (at%). The atomic percentage is different from the previously reported wt%, as it gives the percentage of one kind of atom relative to the total number of atoms. The osseoinductive nature of Sr potentially allows for greater osseointegration of implants that have been coated with a Sr containing material such as HA. Interestingly, Sr has antibacterial properties and although this is advantageous in the context of orthopaedic surgery, it is not the focus of this work. Sr ions substitute Ca ions within the HA lattice to form  $\text{Ca}_{10-x}\text{Sr}_x(\text{PO}_4)_6(\text{OH})_2$  with x being dependant on the molar ratio of Sr within HA. Sr has a large atomic radius and as a result causes lattice distortion and expansion upon substitution. This in turn allows SrHA to dissolve more rapidly than pure HA (Geng et al., 2015). SrHA coatings can be produced by a multitude of similar techniques to those used to produce SiHA. These techniques include plasma spraying (Fielding et al., 2012), sol-gel (Balamurugan et al., 2009), pulsed laser deposition (Boanini

et al., 2012), physical vapour deposition (Ozeki et al., 2013) as well as EC deposition (Yang et al., 2015).

Section 3.1 of this thesis outlines the reactions that occur during the formation of EHA using a technique derived from Redepenning et al (Redepenning et al., 1996). The current passing through the circuit and the surface area of the anode and cathode dictate the current density. The current density controls the pH at the surface of the substrate to be coated and hence will dictate the rate at which brushite is deposited. Brushite crystal morphology and coating thickness is controlled by the deposition time (Redepenning et al., 1996). Current density and deposition times are therefore key parameters in the production of coatings using an EC technique. Many investigations have analyzed the effect of an electric field on HA deposition and higher voltages have the advantage of faster deposition rates, shorter deposition times and higher deposition thicknesses (Zhitomirsky and Gal-or 1997, Mondragon-Cortez and Vargas-Gutierrez, 2004, Mondragón-Cortez and Vargas-Gutiérrez, 2003).

The thickness of a coating on the implant surface affects its resorption and mechanical properties as well as its susceptibility to failure. De Groot et al (de Groot et al., 1987) concluded that a 50 $\mu$ m thick plasma sprayed HA coating was optimal. This thickness reduced fatigue failure, which was significantly greater in coatings thicker than 100 $\mu$ m. A 50 $\mu$ m thick HA coating provided significantly increased shear strength when compared to a 200 $\mu$ m thick coating as shown in an *in vivo* study (Wang et al., 1993). Coating failure can occur in different locations depending upon thickness. Fracture at the coating-bone interface was observed with a 50 $\mu$ m thick coating. In comparison, failure of a 200 $\mu$ m thick coating was observed at the implant-coating interface, within the coating layer and at the coating-bone interface when investigated over a 12 week *in vivo* period. Failure was reported to be a cumulative effect between residual coating stresses and exposure to body fluids (Wang et al., 1993).

ESiHA and ESrHA coatings have been shown to increase significantly the osteogenic differentiation of mesenchymal stem cells when investigated *in vitro* (Yang et al., 2015, Thian et al., 2005). Stem cells are undifferentiated precursor cells that have the capability to self-renew and to differentiate into at least one

or more mature cell types (Krause, 2002). If provided with certain environmental stimuli, they are capable of generating cell types belonging to other tissues, and this process is known as stem cell plasticity or multipotency. Many adult tissues contain populations of stem cells that have the capability to self-renew after injury, disease or aging and these cells can be found within the tissues or in other tissues that serve as stem cell reservoirs. The bone marrow is a source of adult hematopoietic stem cells and MSCs (Pittenger et al., 1999). MSCs give rise to cells that form mesenchymal tissue, including bone, cartilage, tendon, muscle, ligament and marrow stroma (Burder et al., 1994). They express a fibroblastic morphology and in tissue culture conditions a heterogeneous population from bone marrow is obtained after the removal of the non-adherent contaminating haematopoietic cells (Fox et al., 2007).

The International Society for Cellular Therapy defined MSCs as; cells that are tissue plastic adherent under standard culture conditions; those that positively express the cell surface markers CD105, CD73 and CD90 and lack expression of CD45, CD34, CD14, CD11b, CD79 $\alpha$ , CD19 and HLA class II (Dominici et al., 2006, Boxall, 2012); those cells that differentiate into osteocytes, adipocytes and chondrocytes in vitro under standard differentiation conditions (Miron and Zhang, 2012).

Cell activity is influenced by surface topography and this will be discussed in the later chapters. The discs used in the following experiments underwent commercial sandblasting and therefore the surface roughness needs to be defined. It is quantified commonly by calculating the arithmetical mean roughness value or Ra (Figure 4-1). This is the mean of the absolute values of the profile deviations from the mean line over a defined sampling length. The mean line is the reference line about which profile deviations are measured. These parameters can be measured using both contact and non-contact profilometry techniques.

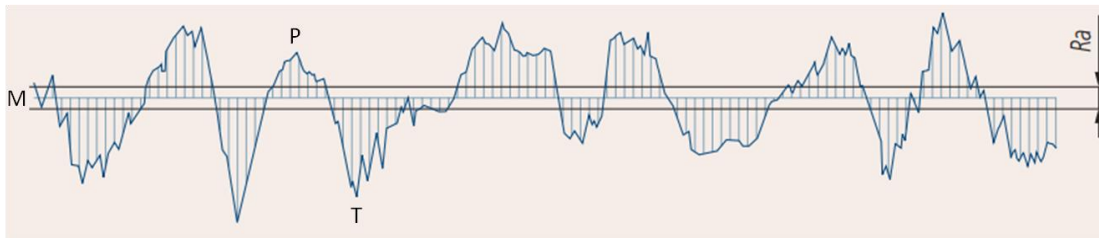


Figure 4-1 Surface profile shown with the mean line (M), the peaks (P) and troughs (T) of the asperities together with the Ra.

The aims of this study were to:

- 1) Optimise a method of EC depositing HA, SiHA and SrHA coatings onto roughened Ti alloy surfaces.
- 2) Assess the bioactivity of each coating by quantifying proliferation and osteogenic differentiation of human mesenchymal stem cells (hMSCs) when seeded these coatings.

The hypotheses were that:

- 1) Current density and deposition time determine HA coating morphology and thickness with and without ionic substitution of Si and Sr.
- 2) Surfaces coated with ESiHA and ESrHA will significantly increase hMSC proliferation and osteogenic differentiation when compared with an EHA surface.

## 4.2 Methods

### 4.2.1 Sample preparation

Medical grade Ti alloy ( $\text{Ti}_6\text{Al}_4\text{V}$ ) discs of 10mm diameter and 3mm thickness were used in this study. In order to achieve a commercial grade roughened surface for coating that is identical to orthopaedic implants, one flat surface of each disc was sandblasted using alumina particles ( $\text{Al}_2\text{O}_3$ ) (Kenco Techniques Ltd. UK) to produce an Ra of  $6711\pm 1.41\text{nm}$  (Tesa Rugosurf 90G, Tesa Technologies, Hexagon, Stockholm, Sweden) by measuring each disc in the centre and in 4 quadrants, the average of which was calculated. The discs were then ultrasonically cleaned in 10% Decon 90, distilled water and 99% IMS for 15 minutes at each stage and then left to air-dry.

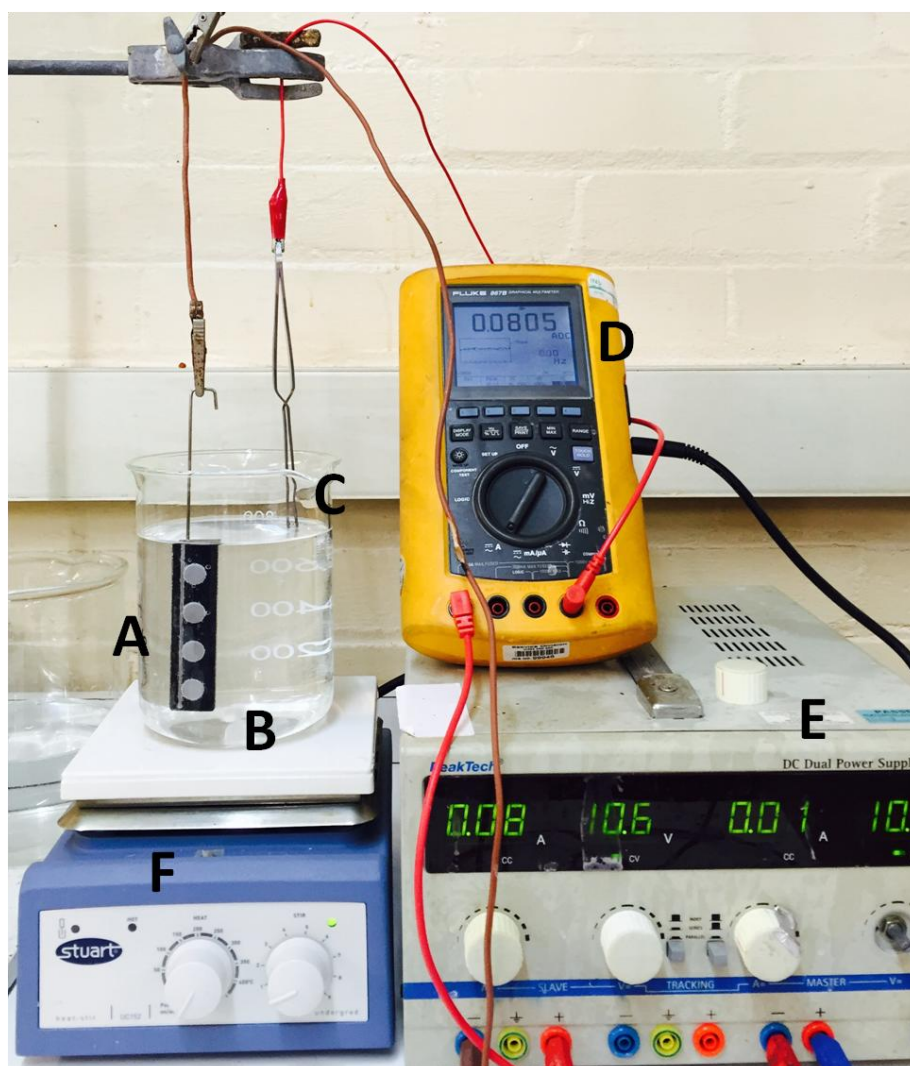


Figure 4-2 Apparatus setup for EC coating of EHA, ESiHA and ESrHA. (A): cathode 4 disc holder with 4 Ti alloy discs in situ; (B): beaker with electrolyte solution; (C): anode with platinum ring for EHA and platinum wire for ESiHA and ESrHA; (D): multimeter; (E): power supply; and (F): heat-stirrer.

Sections 4.2.3, 4.2.4 and 4.2.5 of this thesis describe the coating method for EHA, ESiHA and ESrHA respectively. The coating method was developed by investigating the coating produced using a variety of parameters outlined in Table 4-1 based on the methods of Redepenning et al (Redepenning et al., 1996), Li et al (Li et al., 2011) and Liang et al (Liang et al., 2014).

#### **4.2.2 Disc holder, surface area and current density**

The custom polyethylene disc holder was manufactured in house. An 8x11x100mm block was used with cut outs for 4 discs allowing them to be held via a press fit mechanism. A groove was made alongside the cut outs as a guide for a Ti wire that connected to the negative terminal of the power supply. This wire was in contact with the discs and formed part of the press fit mechanism. The role of the wire was to enable all discs to conduct a current allowing them to be coated.

The total cathodic surface area comprised of the exposed area of four Ti<sub>6</sub>Al<sub>4</sub>V discs (3.768cm<sup>2</sup>) and the surface area of Ti wire. 85mm of the wire was submerged in the electrolyte solution. The diameter of the wire was 1.6mm, giving an exposed wire area of 4.298cm<sup>2</sup> and giving a total 8.066cm<sup>2</sup>. Only 0.5mm of the disc sat proud of the holder and exposed to the electrolyte solution hence the full surface area of the disc was not used as part of this calculation. Current density was calculated using Equation 6, therefore the current needed to achieve the current density required for the experiment can be also derived via Equation 6.

$$\text{Current density (mA/cm}^2\text{)} = \text{Current (mA)} / \text{Surface area (cm}^2\text{)}$$

**Equation 6 Calculating current density using current and surface area.**

#### **4.2.3 Electrochemical deposition of HA coating (EHA)**

A similar setup was used as outlined in section 3.2.2 of this thesis. The volume of the electrolyte was kept constant with 1 disc to every 200mls of supersaturated CaP solution. As numerous discs were required to be coated using this method a custom made jig which holds up to four discs was manufactured from polyethylene. The holder and Ti alloy wire (to allow for

conduction of current) were then submerged in 800mls of solution (Figure 4-2). The Ti discs acted as the cathode with a platinum ring (described in 3.2.2) as the anode. The solution was kept at room temperature and gently stirred to remove poorly adhered crystals from the metal surface, with the use of a magnetic stirrer-hotplate (Heat-Stir UC 152, Stuart, Staffordshire, UK). Once coated, the discs were immersed in 0.1M NaOH for 72 hours after which they were gently rinsed with distilled water and allowed to air-dry.

Table 4-1 outlines current and deposition times used to coat the discs to produce the varying HA coatings.

#### **4.2.4 Electrochemical deposition of SiHA coating (ESiHA)**

Preparation of the SiHA electrolyte solution was based on the methods described by Li et al (Li et al., 2011). 0.133g of  $\text{CaCl}_2$  (26224; BDH Ltd., UK), 0.164g of  $\text{NH}_4\text{H}_2\text{PO}_4$  (216003; Sigma-Aldrich) and 0.041g of  $\text{Na}_2\text{SiO}_3 \cdot 9\text{H}_2\text{O}$  (S4392; Sigma-Aldrich) were dissolved in 1L distilled water.  $\text{Na}_2\text{SiO}_3 \cdot 9\text{H}_2\text{O}$  acted as the Si source with NaCl as the conducting agent. The solution was brought to a pH of 6 by the addition of 10% HCl and 10% NaOH at room temperature (AR15 pH meter; Accumet®, Fisher Scientific, UK).  $\text{Ti}_6\text{Al}_4\text{V}$  discs (acting as the cathode) were mounted in the disc holder and submerged in the prepared solution with a disc:solution ratio of 1:200ml. The solution was gently stirred, heated to 85°C and maintained at that temperature for the duration of the coating process using a magnetic stirrer-hotplate and an aluminum foil heat jacket. Current densities were monitored using a FLUKE 867B Graphical Multimeter (Fluke Corporation, USA) and controlled using a DC Dual Power Supply pack (Peak Tech, Telonic Instruments Ltd, UK). Once coated the discs were placed in 0.1M NaOH solution for 72 hours at room temperature after which they were gently rinsed with distilled water and allowed to air dry.

#### **4.2.5 Electrochemical deposition of SrHA coating (ESrHA)**

Deposition of the SrHA coating was based on the methods described by Liang et al (Liang et al., 2014). 6.66g of  $\text{CaCl}_2$ , 4.14g of  $\text{NH}_4\text{H}_2\text{PO}_4$ , 1.057g of  $\text{SrCl}_2$  (439665; Sigma-Aldrich) and 11.69g of NaCl were dissolved in 1L of distilled water. The  $\text{SrCl}_2$  acted as the Sr source with the NaCl as the conducting agent.

The solution was brought to a pH of 4.5 by the addition of 10% HCl and 10% NaOH at room temperature. Ti<sub>6</sub>Al<sub>4</sub>V discs were mounted in the disc holder and submerged in the prepared solution with a disc:solution ratio of 1:200ml, with the discs acting as the cathode. The solution was gently stirred, heated to 60°C and maintained at that temperature using a magnetic stirrer-hotplate and an aluminum foil heat jacket. The anode was a platinum wire as described previously, which was connected to the electrode and immersed in the solution. Current densities were monitored using a FLUKE 867B Graphical Multimeter and controlled using a DC Dual Power Supply pack. Once coated the discs were placed in 0.1M NaOH solution for 72 hours at room temperature after which they were gently rinsed with distilled water and allowed to air dry.

Coating type	Combination	Current density (mA/cm <sup>2</sup> )	Deposition time (mins)
Electrochemical HA (EHA)	A	10	5
	B	10	10
	C	10	15
	D	20	5
	E	20	10
	F	20	15
	G	30	5
	H	30	10
	I	30	15
Electrochemical SiHA (ESiHA)	J	5	5
	K	5	10
	L	5	15
	M	10	5
	N	10	10
	O	10	15
Electrochemical SrHA (ESrHA)	P	15	20
	Q	15	40
	R	20	20
	S	20	40
	T	25	20
	U	25	40

**Table 4-1 Current densities and deposition times used to produce EHA, ESiHA and ESrHA coatings on Ti alloy discs. n=6 for each combination.**

#### **4.2.6 Analysis of surface morphology and thickness of EC coatings**

Imaging of the EHA, ESiHA and ESrHA coated discs was performed using light microscopy (Keyence, Japan). Surface morphology was also observed using scanning electron microscopy (SEM, JEOL JSM 5500 LV, Tokyo, Japan and Philips XL30 FEGSEM, Philips Ltd, Guildford, Surrey). Thickness and uniformity of the coatings were analysed by embedding the coated discs in hard grade acrylic resin (LR White Resin, Agar Scientific) and cutting them centrally and

transversely using a diamond band saw (EXACT, Germany). Samples were then polished by hand using increasingly fine Si carbide grinding papers (Buehler, Germany). Polished samples were sputter coated with gold palladium (K550, EmiTech Ltd, UK) and analysed using backscatter SEM. Coating thickness was quantified and compared in each of the experimental groups. Four equidistant images taken at the same magnification along the length of the surface were analysed. Four coating thickness measurements were taken per image giving 16 thickness measurements per coating.

#### **4.2.7 Characterisation of coating**

After the analysis outlined in section 4.2.6 of my thesis was completed, a single combination of current density and deposition time was chosen for each of the EHA, ESiHA and ESrHA coatings based on coating uniformity and thickness. Three discs were coated using these specifications. Elemental analysis of the coatings was performed using EDS (EDAX, EDAX Inc., USA). An EDS spectra was obtained from the centre of the four quadrants of each disc as well as the centre of the disc itself. The crystallinity of each coating was analysed using X-ray diffraction (XRD, Bruker D8-Advanced, Bruker Ltd, Coventry, UK).

#### **4.2.8 Cell culture and maintenance**

Human mesenchymal stem cells (hMSCs) isolated from a bone marrow aspirate obtained from a healthy donor patient at the Royal National Orthopaedic Hospital, was used in this study under the appropriate research and ethics approval.

hMSCs were cultured in DMEM+ which consisted of Dubelcco's modified eagles medium (DMEM, D6429, Sigma-Aldrich, UK) supplemented with 10% fetal calf serum (FCS, First Link, UK) and 100 units/ml of penicillin and streptomycin (P/S, Gibco, UK).

Cryovials containing hMSCs were removed from liquid nitrogen storage and placed in a 37°C water bath. 1ml of DMEM+ was added to the cells and transferred to a universal tube. An additional amount of DMEM+ was added to the universal tube leaving the cells to equilibrate over a 5 minute period. Once a

total volume of 16mls was reached the suspension was centrifuged at 2,000 rpm over a period of 5 minutes. The supernatant was discarded and the pellet was re-suspended in 1ml of DMEM+. The cells (passage 2) were transferred into a T75 culture flask (Corning, USA) with 10ml of DMEM+ and cultured under standard conditions within an incubator (37°C with 5% CO<sub>2</sub>). Growth medium was changed every 3-5 days and cells were regularly observed using phase-contrast light microscopy. Once cells had reached 80-90% confluence (% total surface area of the flask covered in cells), they were passaged. DMEM+ within the flask was carefully discarded and the cells were washed with sterile cold phosphate buffered saline (PBS). Once washed, the PBS was also discarded. The cells grew as adherent monolayers within the culture flask and in order to remove the cells, a mechanism which is mediated by Ca<sup>2+</sup> dependant proteins, enzymatic disaggregation was utilised. The cells were trypsinised by adding 1ml of trypsin-5.3mM EDTA.4Na solution (Gibco, UK) and incubated for 5 minutes under standard conditions at which point the cells lifted off the flask surface. Trypsinisation was stopped by adding a 1:1 volume of DMEM+ as the FCS in the DMEM+ contained trypsin inhibitors halting the reaction.

#### **4.2.8.1 Cell Viability**

Cell viability was measured by adding 0.4% trypan blue solution (T8154, Sigma-Aldrich) in a 1/10 dilution with the cell suspension. Using a phase-contrast light microscopy and a haemocytometer, the number of viable cells was measured. Those cells that were clear and unstained were noted as living and those that were stained blue were considered dead. Trypan blue is a dye with two azo chromophores. The chromophore is negatively charged and therefore only reacts with the cell if there is membrane damage. The remainder of the cell suspension was centrifuged (2,000 rpm for 5 minutes) to produce a pellet. The pellet was re-suspended in 1ml of DMEM+ after the supernatant was discarded using a 21-gauge needle and syringe. Approximately 3,000-4,000 cells were seeded per cm<sup>2</sup> of surface area with 0.1333ml of DMEM+ per cm<sup>2</sup> of surface area. DMEM+ was changed every 3-5 days until the cells reached 80-90% confluency and until passage 5 at which point they were used in the following *in vitro* experiments.

## **4.2.9 Characterisation of human mesenchymal stem cells (hMSCs) using tri-lineage differentiation**

MSCs were characterised by demonstrating their multipotency. This was carried out by differentiating them along the adipogenic, chondrogenic and osteogenic lineages.

### **4.2.9.1 Osteogenic differentiation**

MSCs were isolated, expanded and trypsinised as described in 4.2.8.  $3 \times 10^4$  cells were plated onto Thermanox® (Nalge Nunc International, NY, USA) coverslips that were placed at the bottom of the wells of a 6 well-plate. 1ml of osteogenic media was added to each of the wells. Plates were transferred into an incubator and the cells cultured under standard conditions (37°C and 5% CO<sub>2</sub>). Osteogenic media consisted of DMEM+ containing 5mM  $\beta$ -glycerophosphate, 50 $\mu$ g/ml L-ascorbic acid and 10nM dexamethasone. The supplemented growth medium was changed every 2-3 days. Using an Alizarin red stain, calcium deposition was observed at day 22.

### **4.2.9.2 Adipogenic differentiation**

During adipogenic differentiation, cells were exposed to 100ml of complete medium with 100 $\mu$ l of 0.1mM dexamethasone, 1ml of 45mM isobutylmethylxanthine, 10 $\mu$ l of 10mg/ml insulin and 250 $\mu$ l of 50mM indomethacin. Media was refreshed every 2-3 days. Cells were cultured for 21 days after which the presence of intra-cellular lipid droplets was determined using Oil Red O staining.

### **4.2.9.3 Chondrogenic differentiation**

During chondrogenic differentiation,  $5 \times 10^5$  cells were pelleted in a centrifuge tube to form an aggregate. Serum-free chondrogenic media (10ml) consisting of DMEM, 1% penicillin/streptomycin,  $10^{-7}$  M dexamethasone, 50 $\mu$ g/ml Ascorbate-2-Phosphate, 10% ITS (mixture of recombinant human insulin, human transferrin, and sodium selenite), 1nM sodium pyruvate and 10 ng/ $\mu$ l human recombinant TGF- $\beta$ 1 was added to the pellet culture. Control pellets were cultured in normal media (DMEM, 10% FCS, 1% penicillin/streptomycin). Pellets

were cultured for 21 days, with media changes every 3-5 days using supplemented chondrogenic media. Chondrogenic differentiation within the pellets was confirmed using Alcian blue which stained glycosaminoglycans deposited within the extracellular matrix.

#### **4.2.10 Culture of hMSCs on EHA, ESiHA and ESrHA coatings**

##### **4.2.10.1 Groups and timepoints**

Two control groups and 3 experimental groups were included in this study. Commercial grade plasma sprayed HA coated discs (Plasma Biotol, Hertfordshire, UK) and uncoated roughened discs were used as controls. After the methods described in 4.2.5 and 4.2.6 was completed, an optimal EHA, ESiHA and ESrHA coating was chosen and these 3 experimental groups were used to quantify and compare hMSC cell morphology, metabolic activity and osteogenic differentiation.

Once all the discs were sterilised by autoclaving, a disc from each group was placed into the wells of a well plate and seeded with 50,000 MSCs. These were incubated for 60 minutes under standard conditions (37°C and 5% CO<sub>2</sub>) after which a further 2ml of DMEM+ was added to each well. The plates were kept in the incubator under the same conditions and the DMEM+ was changed every 3-5 days.

The following parameters were quantified:

- 1) Cell metabolic activity as quantified using an AlamarBlue® and deoxyribonucleic acid (DNA) assays (3 repeats),
- 2) Osteogenic differentiation using an ALP assay (3 repeats) and
- 3) Cell morphology was observed using SEM (3 repeats)

In each of the 5 groups investigated, results were quantified at 3, 7 and 14 days of culture with additional SEM analysis (3 repeats) at 28 days.

#### **4.2.10.2 AlamarBlue® activity assay**

AlamarBlue® (AbD Serotec, UK) is an indicator of metabolic activity, which due to a redox reaction in the cytochrome oxidase chain changes colour from blue to pink. The colour change therefore is an indicator of cell proliferation and cytotoxicity.

AlamarBlue® was diluted in DMEM to form a 10% working solution. DMEM+ was removed from each of the wells to be used as part of the ALP and DNA assays. 5mls of the working solution was placed in each well submerging the discs. The plates were incubated at 37°C and 5% CO<sub>2</sub>. After 4 hours of incubation, 50µl from each well was pipette in triplicate into a 96 well-plate (FluoroNunc™). Absorbance at 590nm was measured using a plate reader (Flouroskan Ascent, Labsystems, USA). Results were compared with a negative control of 50µl working solution placed in an empty well.

#### **4.2.10.3 ALP assay**

For ALP analysis triplicates of 50µl of growth medium were removed from each of the wells containing the discs and transferred onto a 96 well-plate (FluoroNunc™). An equal volume of p-Nitrophenyl phosphate (N7653 Sigma-Aldrich) was added to each of the triplicates and the absorbance was measured at 405nm using a plate reader (Tecan, Infinite M200 PRO, Switzerland). Readings were given in U/L and ALP levels were normalised to the number of cells by measuring the amount of DNA in each sample, therefore ALP/DNA was expressed as U/µg (Oreffo et al., 1998). A plot was created with known concentrations of standards against their absorbance at 460nm. Equations with a correlation coefficient of 0.95 or above were considered acceptable for calculating DNA concentration. Normalised ALP activity per µg of DNA was then calculated (U/µg).

#### **4.2.10.4 DNA assay**

For DNA analysis samples were washed with PBS and lysed by adding 500µl of sterile distilled water at 37°C. Three freeze(-80°C)-thaw cycles were performed. Samples were transferred to Eppendorf tubes and spun at 10,000rpm for

10min. 100µl of supernatant for each sample was pipette in triplicate into a 96 well-plate (FluoroNunc™) and 100µl of 0.2µg/ml Hoescht 33258 dye (14530, Sigma-Aldrich) added to each of the triplicates. The adenine-thymidine-Hoescht 33258 specific fluorescence was read at 460nm using a plate reader (Flouroskan Ascent, Labsystems, USA).

100µl of standards ranging from 20 to 0.3125µg/ml of DNA (Sigma-Aldrich, UK) were also loaded in triplicate and Hoescht 33258 was added to these. The amount of DNA in the samples was calculated as µg of DNA using a standard curve (Moe et al., 1994).

#### **4.2.11 SEM**

The samples designated for SEM analysis were washed with PBS and fixed using 2.5% glutaraldehyde (Agar Scientific, UK) in a 0.1M sodium cacodylate buffer (pH 7.4, Agar, Scientific UK) for 1 hour. After washing with 0.1M sodium cacodylate buffer twice for 5 minutes, the samples underwent dehydration using serially increasing concentrations of IMS (20-60%) followed by ethanol (70-100%). Each step was completed twice (5 minutes each) before moving onto the next concentration. The samples were finally treated three times for 5 minutes with hexamethyldisalazine (Agar Scientific, UK) and left to dry overnight. The discs were mounted onto stubs, gold/palladium sputter coated (Emitech, K550, Emitech, UK) and observed under SEM (JEOL JSM 5500LV).

#### **4.2.12 Statistical analysis**

All data was tested for normality using a Shapiro-Wilk test. Parametric and non-parametric data were compared using a student t-test and Mann-Whitney U test respectively. Multiple comparisons were made using a Kruskal-Wallis test for non-parametric data and ANOVA (with a bonferroni correction) for parametric data.  $P < 0.05$  was seen to be significant. All analysis was completed using SPSS (SPSS Inc., IBM, v22, Chicago, IL).

## 4.3 Results

### 4.3.1 EC coatings

The methods described in 4.2.2, 4.2.3 and 4.2.4 produced EHA, ESiHA and ESrHA coatings respectively. Each method resulted in the formation of white adherent coatings on the roughened disc surface. Current density and deposition time combinations of F, H and I could not be performed as the DC dual power supply used could not sustain the current density required throughout the full time period.

#### 4.3.1.1 Light Microscopy

An uncoated roughened  $Ti_6Al_4V$  disc observed using light microscopy is shown in Figure 4-3.

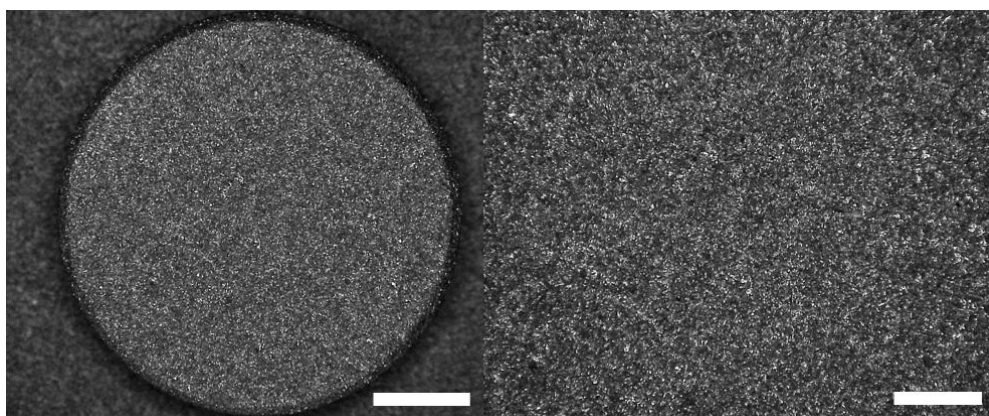


**Figure 4-3 (Left) Roughened  $Ti_6Al_4V$  disc from above, scale bar shown equivalent to 2.5mm. (Right) Roughened surface of disc, scale bar shown equivalent to 1mm.**

Using light microscopy, the EHA coating was observed to be roughened much like the underlying metal surface topography. Increased current densities and deposition times formed coatings with an increasingly greater number of crystal clusters. The lowest current density over the longest deposition time formed the most even surface with the fewest clusters of crystals (Figure 4-4).

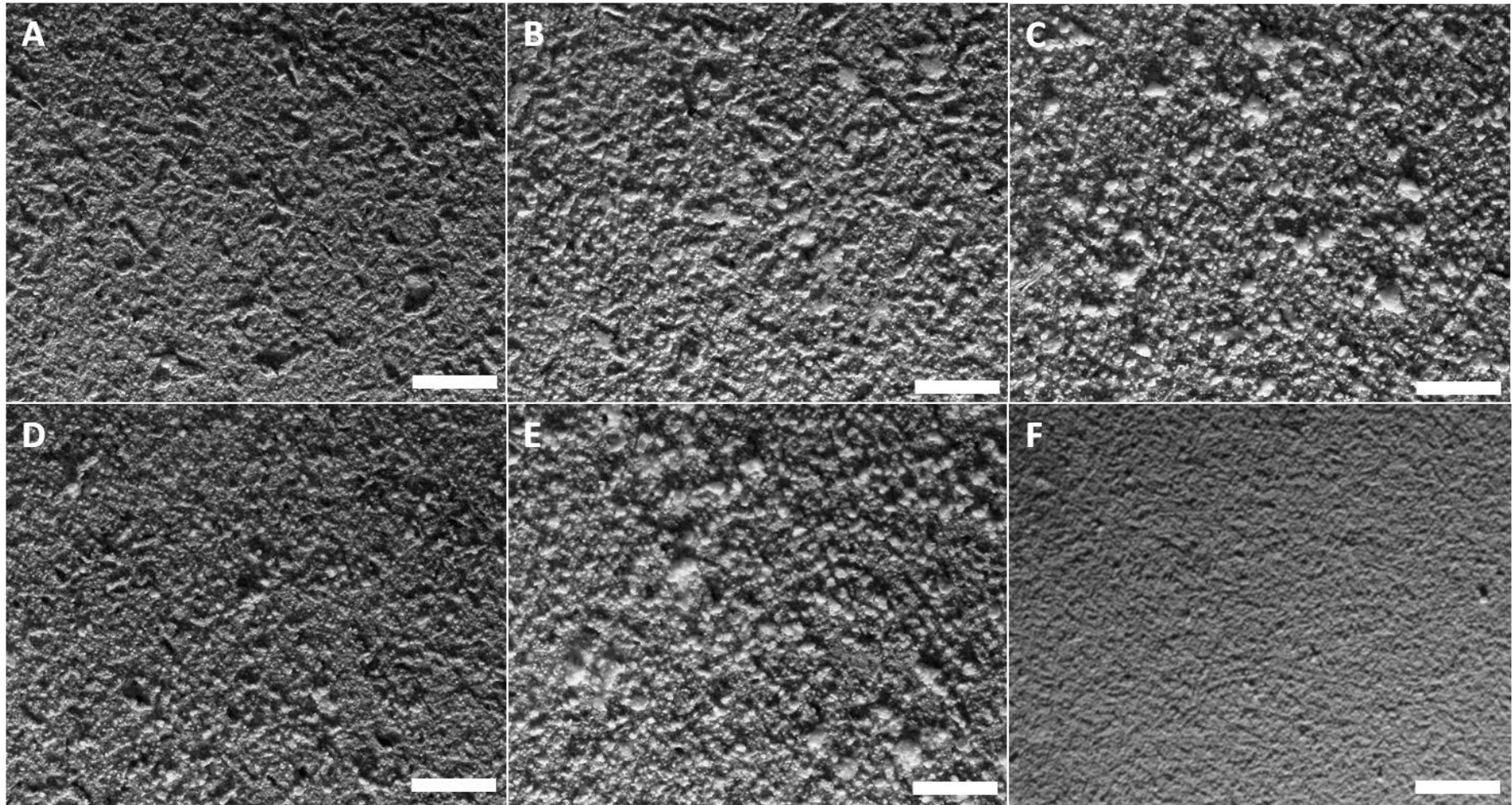
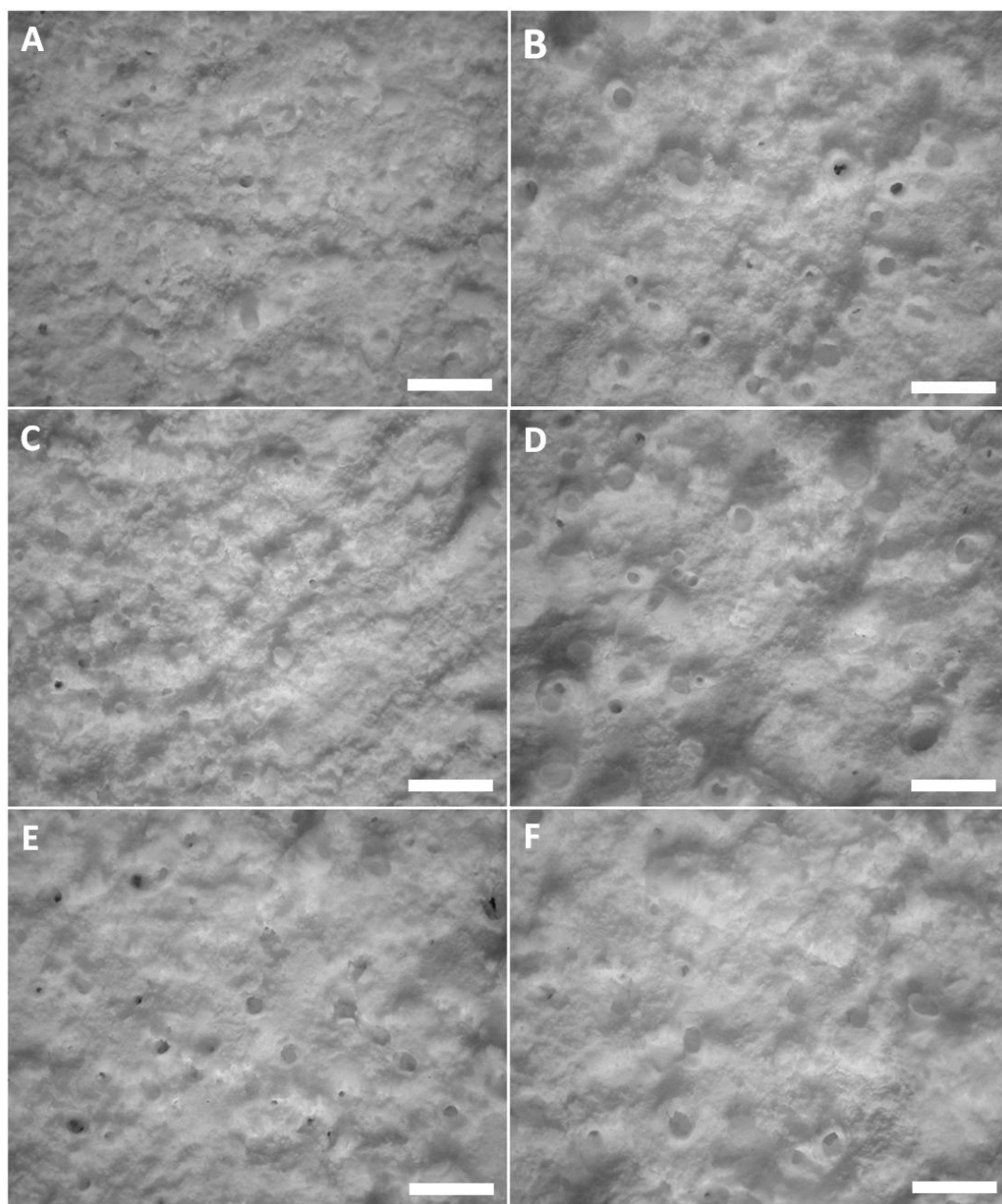


Figure 4-4 Light microscopy images of EHA coatings with oblique light source. Scale bar shown is equivalent to 1mm. A)  $10\text{mA}/\text{cm}^2$  over 5 minutes, B)  $20\text{mA}/\text{cm}^2$  over 5 minutes, C)  $30\text{mA}/\text{cm}^2$  over 5 minutes, D)  $10\text{mA}/\text{cm}^2$  over 10 minutes, E)  $20\text{mA}/\text{cm}^2$  over 10 minutes and F)  $10\text{mA}/\text{cm}^2$  over 15 minutes.



**Figure 4-5** Light microscopy images of ESrHA coatings with oblique light source. Scale bar shown is equivalent to 1mm. A) 15mA/cm<sup>2</sup> over 20 minutes, B) 15mA/cm<sup>2</sup> over 40 minutes, C) 20mA/cm<sup>2</sup> over 20 minutes, D) 20mA/cm<sup>2</sup> over 40 minutes, E) 25mA/cm<sup>2</sup> over 20 minutes and F) 25mA/cm<sup>2</sup> over 40 minutes.

Negligible differences were found macroscopically when the ESrHA coatings made by varying current densities and time were compared. Figure 4-6, shows the lowest current density with the shortest deposition time (A) compared with the highest current density with the longest deposition time (B).

A thicker ESrHA coating was produced as deposition time increased. The surface topography remained roughened following the application of all coatings however there were also tubules, which formed as the coating deposited around

escaping hydrogen bubbles from the surface of the disc. This was not the case with any other coating (Figure 4-5). The roughened topography does however seem to be relatively more even as the coating thickness increased.

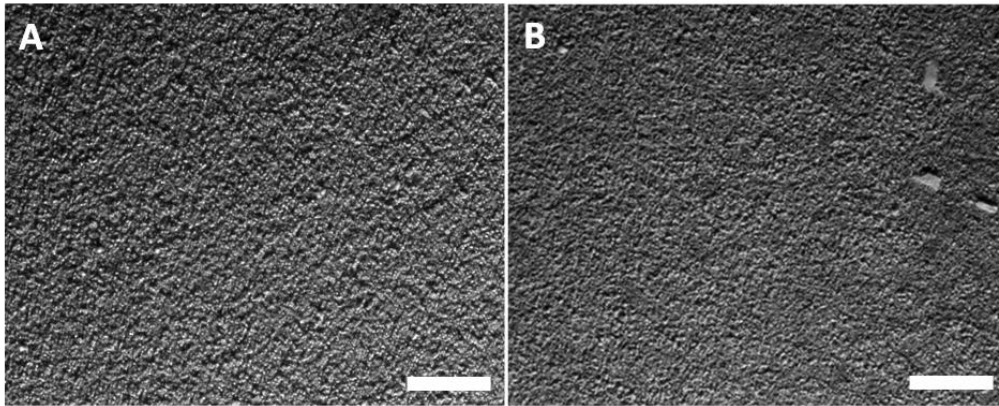


Figure 4-6 Light microscopy images of ESiHA coating with oblique light source. Scale bar shown equivalent to 1mm. A)  $5\text{mA}/\text{cm}^2$  over 30 minutes and B)  $10\text{mA}/\text{cm}^2$  over 60 minutes.

#### 4.3.1.2 Surface morphology - Scanning Electron Microscopy (SEM)

The roughened surface structure of the uncoated Ti alloy disc is shown in Figure 4-7.

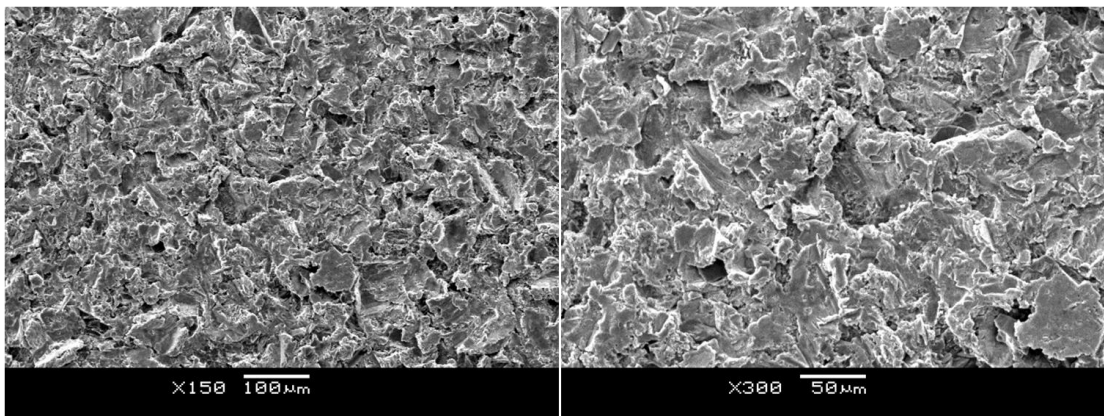
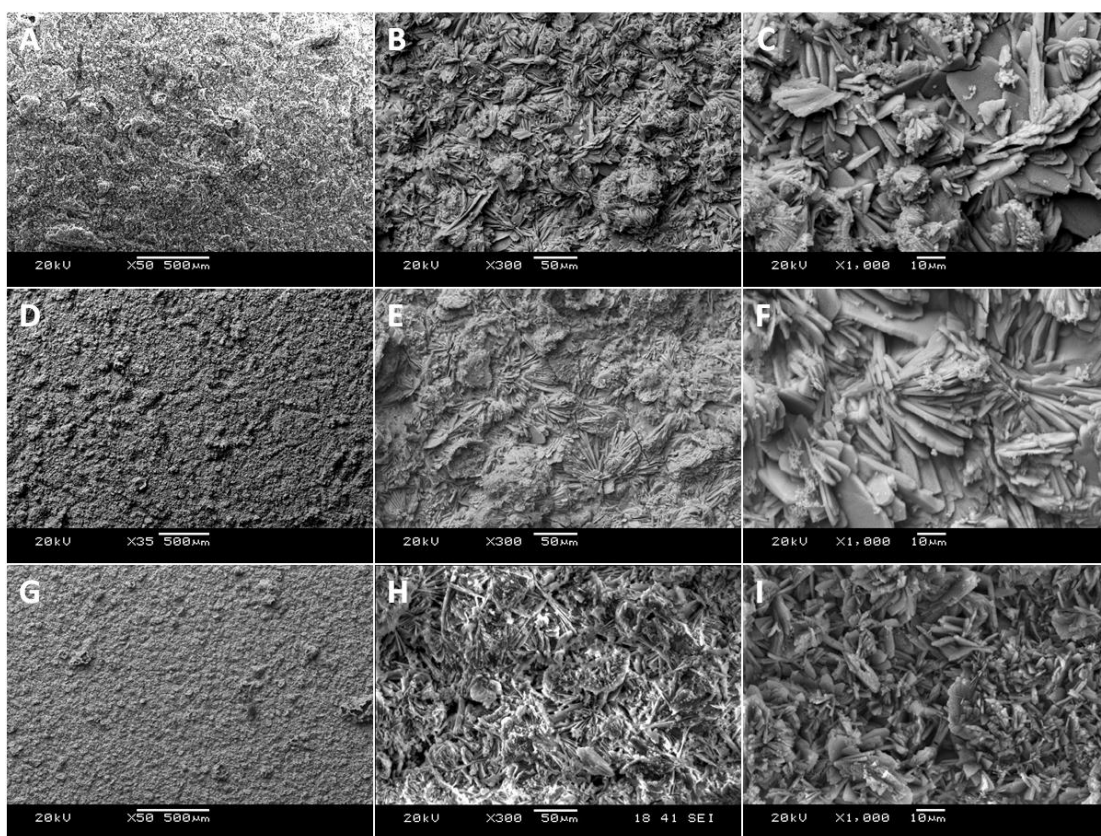


Figure 4-7 SEM images of an uncoated roughened  $\text{Ti}_6\text{Al}_4\text{V}$  disc surface. Scale bar and magnification as shown.

The EHA coating produced similar crystal morphology to that reported by Redepenning et al (Redepenning et al., 1996). Cracks were present in the coating as a result of the conversion of brushite to HA, also reported by Redepenning et al. Large-plate like crystals of HA had coated the disc surface and the coating was seen to follow along the undulating roughened disc topography. No difference in crystal morphology was observed when coatings were applied using different current densities.



**Figure 4-8 SEM images showing surfaces and crystal morphologies of EHA coatings produced from (A-C) 10mA/cm<sup>2</sup>, (D-F) 20mA/cm<sup>2</sup> and (G-I) 30mA/cm<sup>2</sup> current densities. Magnification and scale bars as shown.**

ESiHA coatings formed 2 different types of structures on the coating surface. When compared to the EHA coating, larger plate-like crystals were observed embedded within an even coating of smaller needle shaped crystals typical of those found in a SiHA electrodeposited coating (Figure 4-9). The ESiHA coating deposited onto the entire disc surface and followed the contours of the underlying roughened topography. No change in the structure of the coating or crystal morphology was observed with differing current density and deposition times.

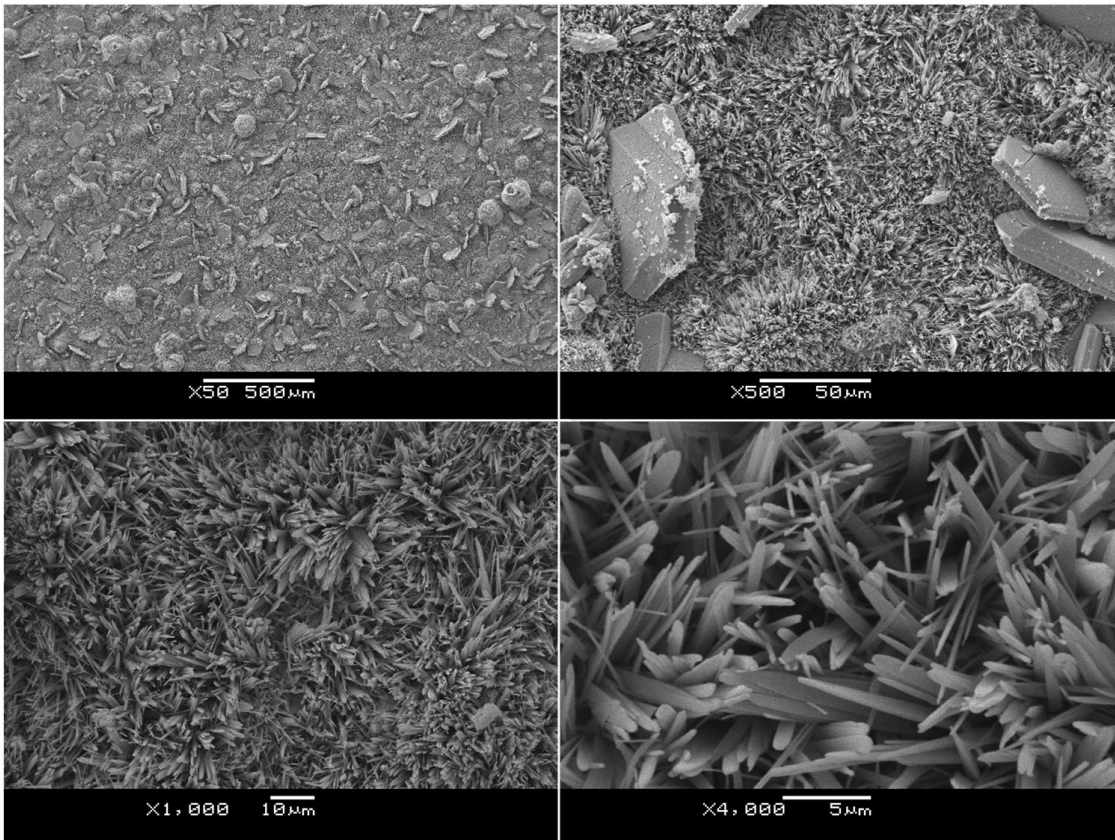


Figure 4-9 SEM images of the surface of the ESiHA coating. Magnification and scale bars are as shown.

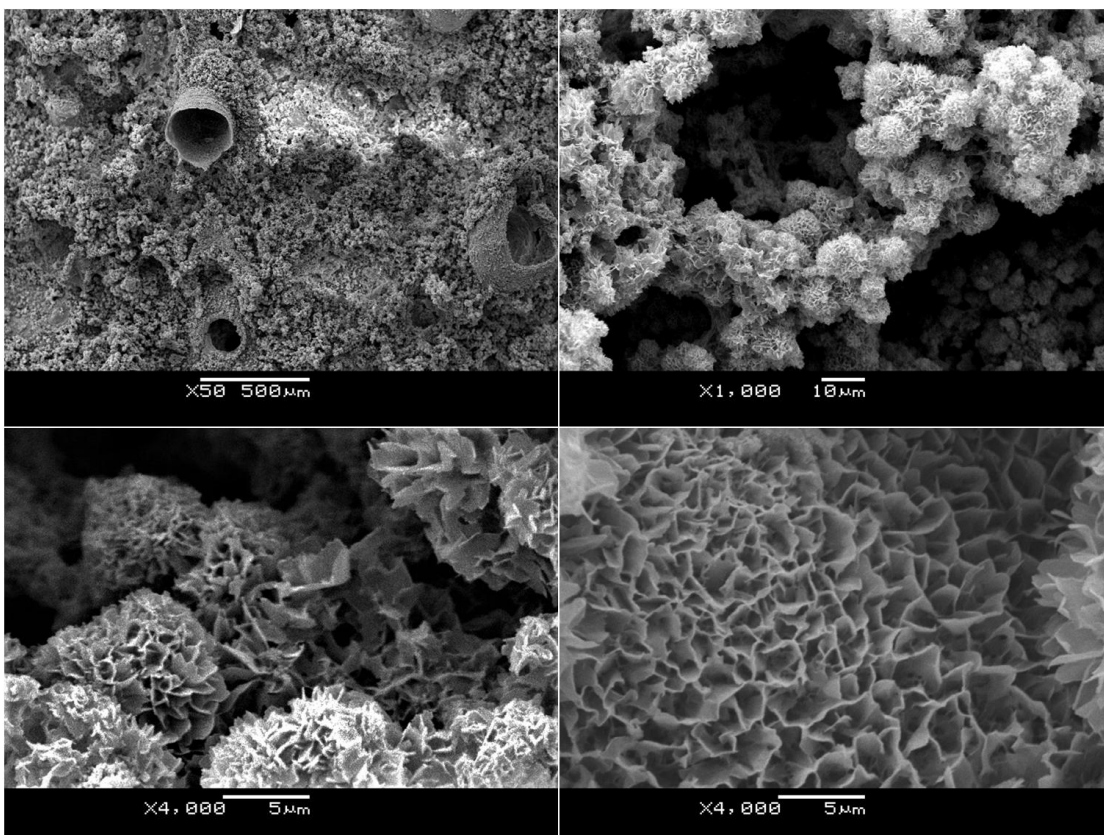


Figure 4-10 SEM images of ESrHA surface. Magnification and scale bars as shown.

ESrHA coatings exhibited an even coating that again followed the underlying rough surface. In all cases, the coating had completely covered the disc surface with no disc surface remaining uncoated. Crystals were of a leaf-like morphology. Neither the current density nor deposition time changed the crystal morphology with identical crystals found throughout all of the parameters investigated. On occasion, these leaf-like crystals formed clusters. Tubular crystal structures were often found deposited on the edges of bubbles produced as part of the cathodic reaction during the coating process.

#### 4.3.1.3 Coating Thickness

All coatings investigated showed differing thicknesses as summarised in Table 4-2.

Coating	Current density (mA/cm <sup>2</sup> )	Deposition time (minutes)	Coating thickness (µm±SD)
EHA	10	5	14.2±1.8
		10	17.1±3
		15	22.4±2.8
	20	5	15.1±5.4
		10	22.5±2.4
		30	16.1±3.2
ESiHA	5	5	10.2±0.1
		10	15.7±4.3
		15	16±3.1
	10	5	21.2±1.9
		10	29.6±2.6
		15	33.7±8.1
ESrHA	15	20	202±82.8
		40	511.1±121.4
	20	20	345.8±65.5
		40	676.1±117.7
	25	20	411.4±78.5
		40	676.9±182.4

**Table 4-2 Summary of the thickness of all coatings produced using varying current densities and deposition times.**

Cross-sections taken through EHA coated discs showed the presence of large crystals within the coating (Figure 4-12). Higher current densities were accompanied by clusters of crystals deposited within a less even coating. These relatively large clusters presented themselves as ‘flares’ (Figure 4-11) that were usually a crystal thick and therefore most likely to be structurally vulnerable when handled. These flares were observed to be up to 100µm in height.

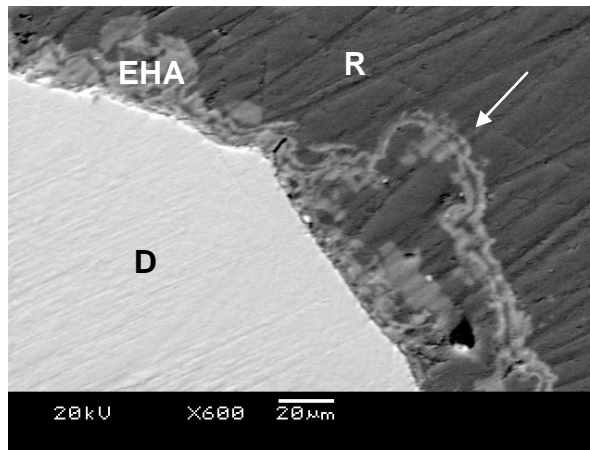


**Figure 4-11** Cross section of 30mA/cm<sup>2</sup>, 5 minute EHA coating showing typical appearance of crystal 'flare' (arrow). Magnification and scale bar as shown. D, disc; EHA; electrochemical HA coating; R, resin.

In the EHA group, a significant difference in coating thickness was found with differing deposition times ( $p=0.003$ ). No significant difference was found in coating thickness when current density was varied ( $p=0.639$ ). The p-values obtained when coating thickness was compared between coatings are summarised in Table 4-3. EHA coatings appeared to be denser when compared to the other coatings investigated (Figure 4-12). Figure 4-15 shows the trend towards thicker EHA coatings with different coating parameters where 20 mA/cm<sup>2</sup> for 10 minutes and 10mA/cm<sup>2</sup> at 15 minutes resulted in the thickest coating.

The ESiHA coating was more difficult to identify on the cross-sectioned resin samples as their crystal size was much smaller compared with the EHA and ESrHA groups. A significantly thicker coating was produced when a current density of 10mA/cm<sup>2</sup> was applied when compared with coatings formed at a current density of 5mA/cm<sup>2</sup> ( $p<0.001$ ). Overall there was no significant difference when the thickness of the coatings produced at different deposition times were compared ( $p=0.112$ ). Table 4-4 shows the p-values obtained in the ESiHA coated group. Both current density and deposition time had a synergistic effect on ESiHA coating thickness, a trend similar to that seen in the EHA coated group (Figure 4-16).

ESrHA coatings were thicker than the EHA and ESiHA coatings (Table 4-2). Cross-sections revealed a less dense laminar structure when compared to the

other coatings (Figure 4-12, Figure 4-13 and Figure 4-14). The tubular structures can be seen by the large circular cross-sections.

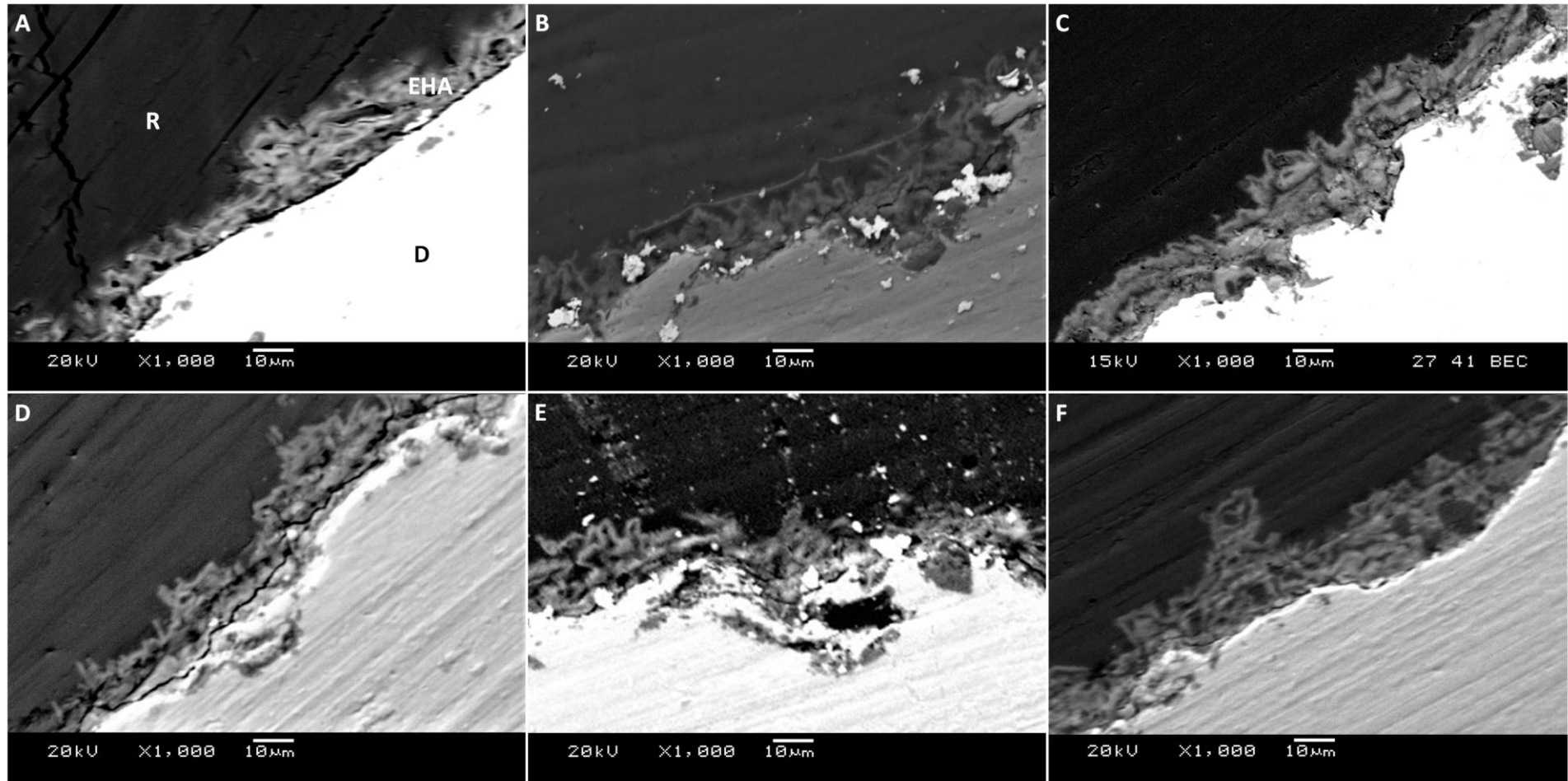


Figure 4-12 SEM images of cross sections of discs (D) embedded in resin (R) showing the thickness of the coating (EHA). (A)  $10\text{mA}/\text{cm}^2$  over 5 minutes, (B)  $10\text{mA}/\text{cm}^2$  over 10 minutes, (C)  $10\text{mA}/\text{cm}^2$  over 15 minutes, (D)  $20\text{mA}/\text{cm}^2$  over 5 minutes, (E)  $20\text{mA}/\text{cm}^2$  over 10 minutes and (F)  $30\text{mA}/\text{cm}^2$  over 5 minutes.

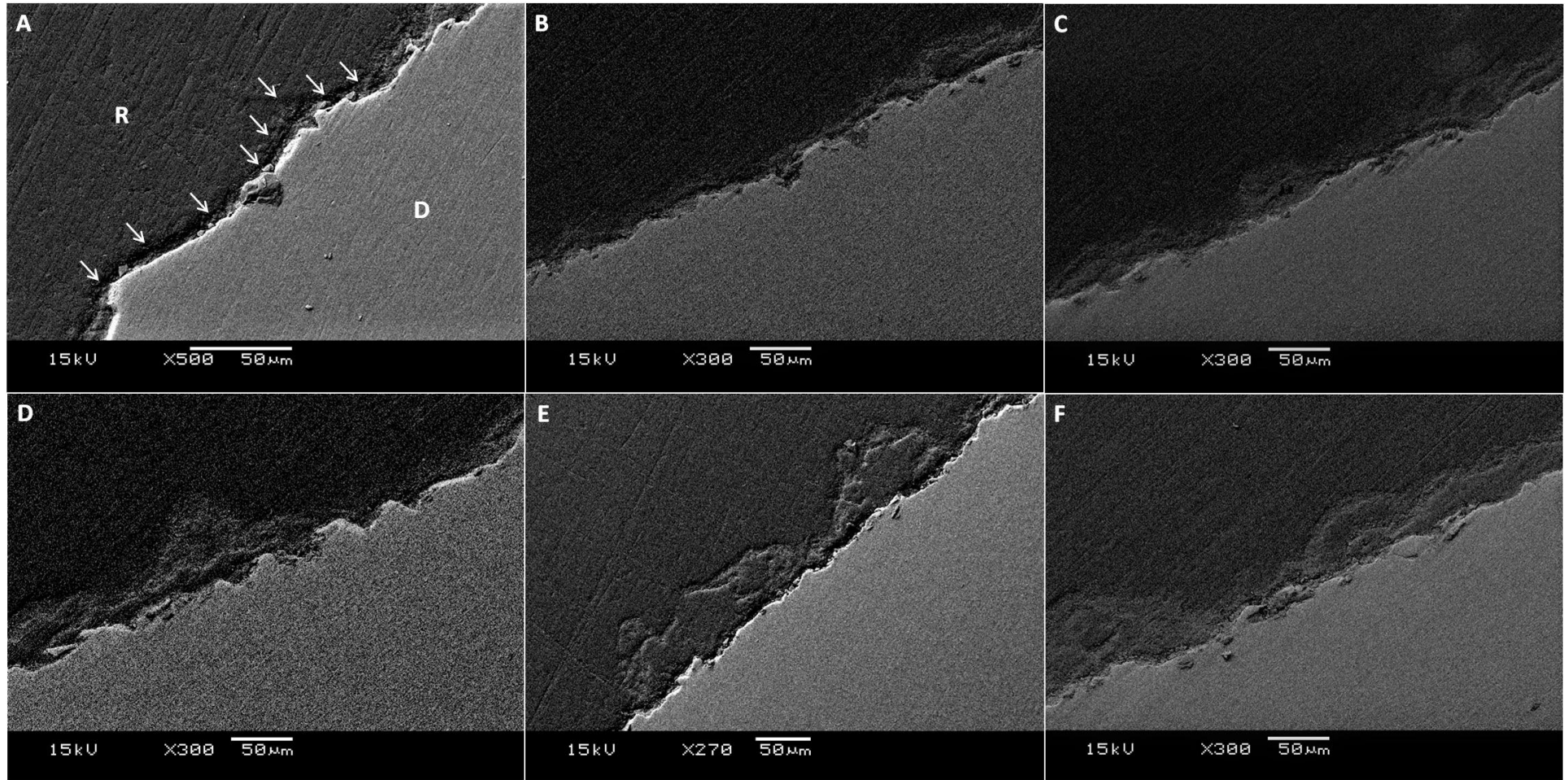


Figure 4-13 SEM images of ESiHA (white arrow) coated disc (D) cross sections embedded in resin (R). (A)  $5\text{mA}/\text{cm}^2$  over 5 minutes, (B)  $5\text{mA}/\text{cm}^2$  over 10 minutes, (C)  $5\text{mA}/\text{cm}^2$  over 15 minutes, (D)  $10\text{mA}/\text{cm}^2$  over 5 minutes, (E)  $10\text{mA}/\text{cm}^2$  over 10 minutes and (F)  $10\text{mA}/\text{cm}^2$  over 15 minutes.

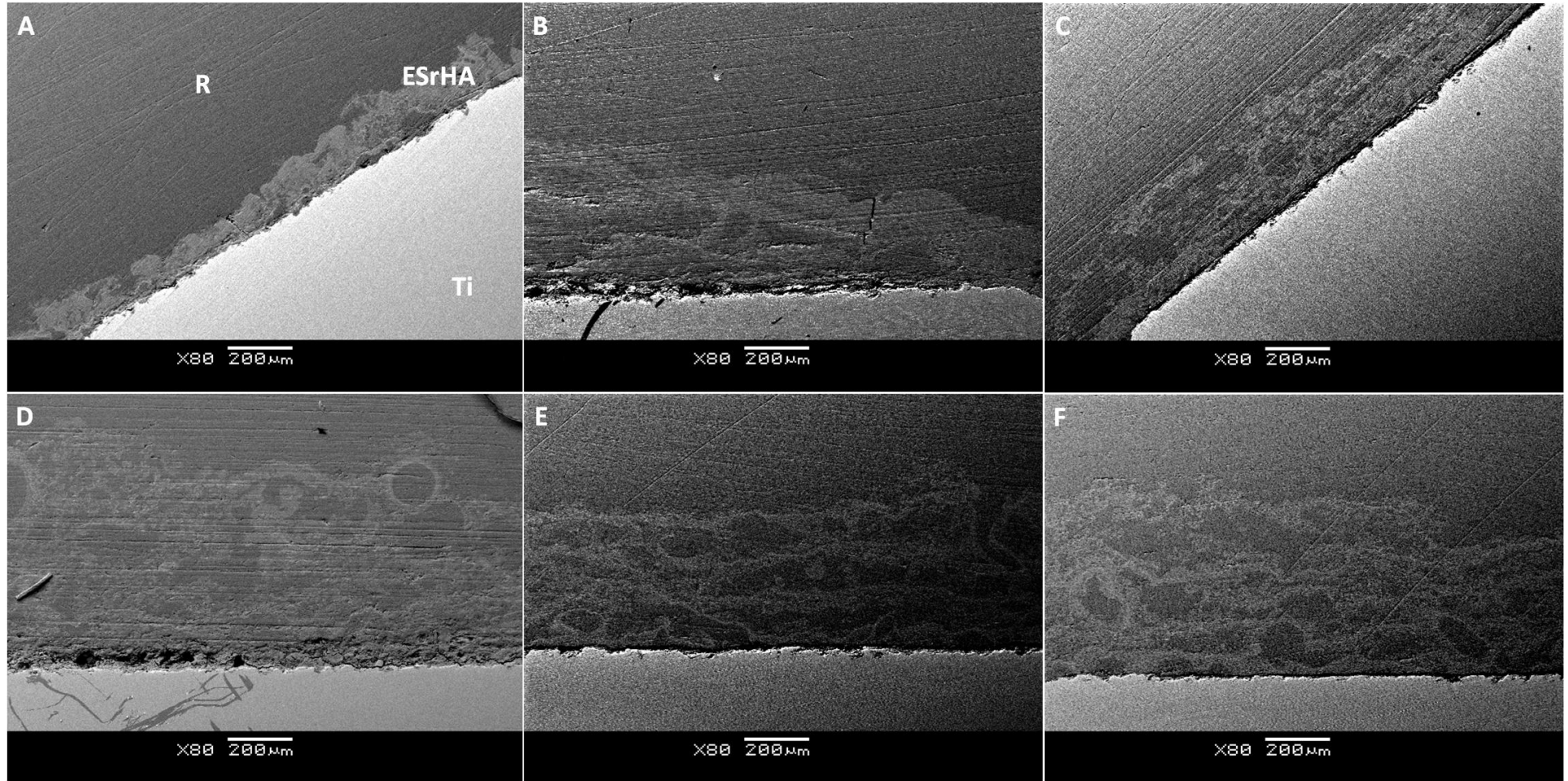
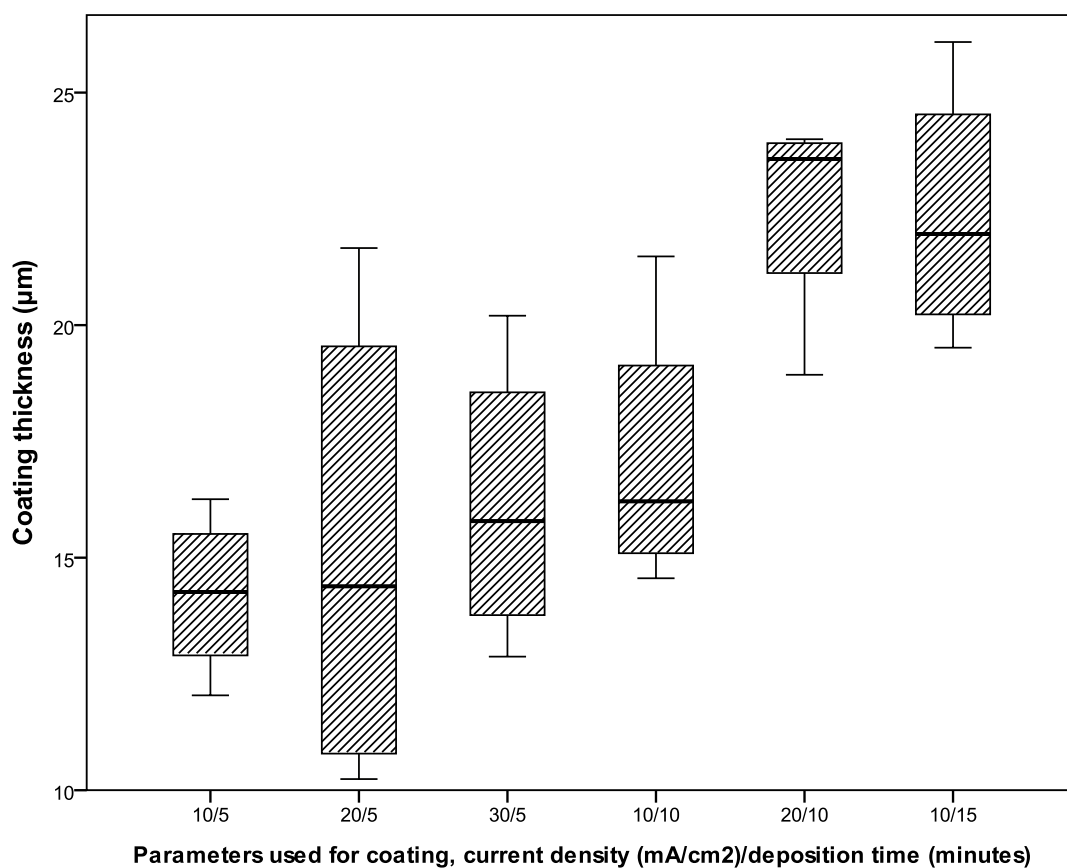


Figure 4-14 SEM images of ESrHA coated disc (Ti) cross sections embedded in resin (R). (A)  $15\text{mA}/\text{cm}^2$  over 20 minutes, (B)  $15\text{mA}/\text{cm}^2$  over 40 minutes, (C)  $20\text{mA}/\text{cm}^2$  over 20 minutes, (D)  $20\text{mA}/\text{cm}^2$  over 40 minutes, (E)  $25\text{mA}/\text{cm}^2$  over 20 minutes and (F)  $25\text{mA}/\text{cm}^2$  over 40 minutes.



**Figure 4-15** Boxplot of thickness of EHA coating ( $\mu\text{m}$ ) produced by different current densities ( $\text{mA}/\text{cm}^2$ ) over varying deposition times (minutes).

	10/5	10/10	10/15	20/5	20/10	30/5
10/5	-	1	<i>0.037</i>	1	<i>0.033</i>	1
10/10	-	-	0.544	1	0.484	1
10/15	-	-	-	0.093	1	0.233
20/5	-	-	-	-	0.082	1
20/10	-	-	-	-	-	0.206

**Table 4-3** p-values for pair-wise comparisons of thickness of coating with different current density/deposition time combinations.  $p < 0.05$  is considered to be significant and are identified in italics.

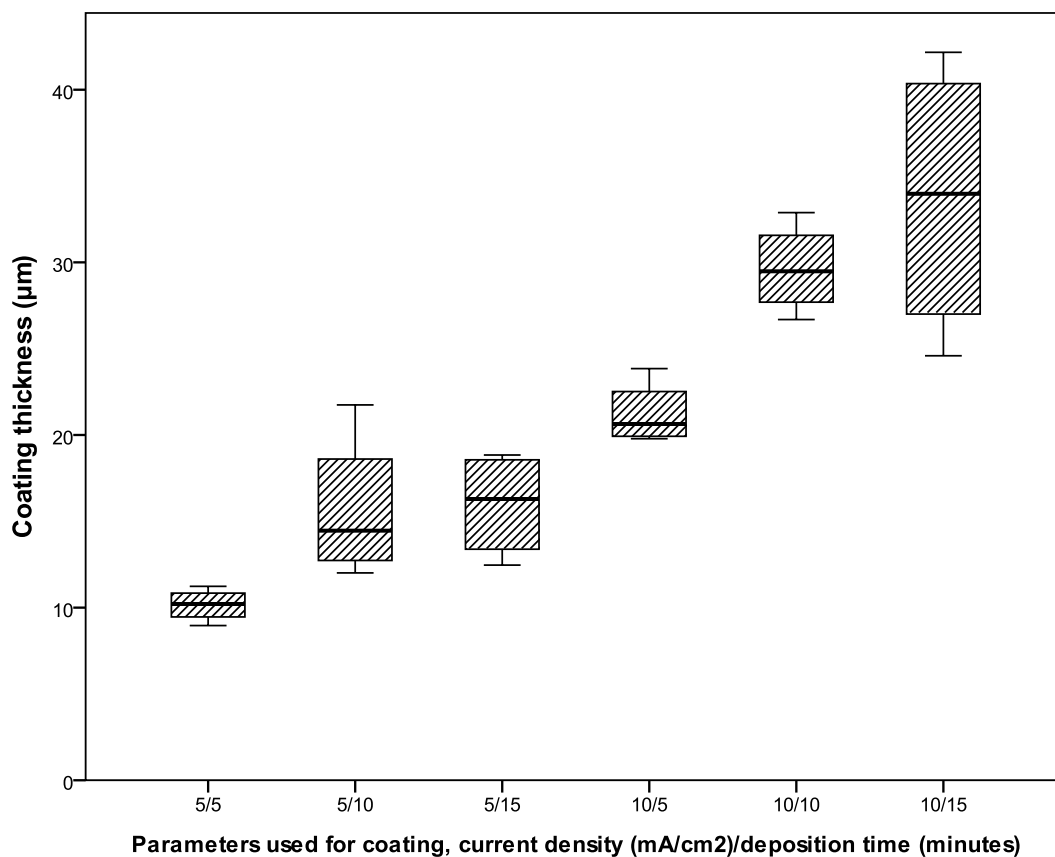
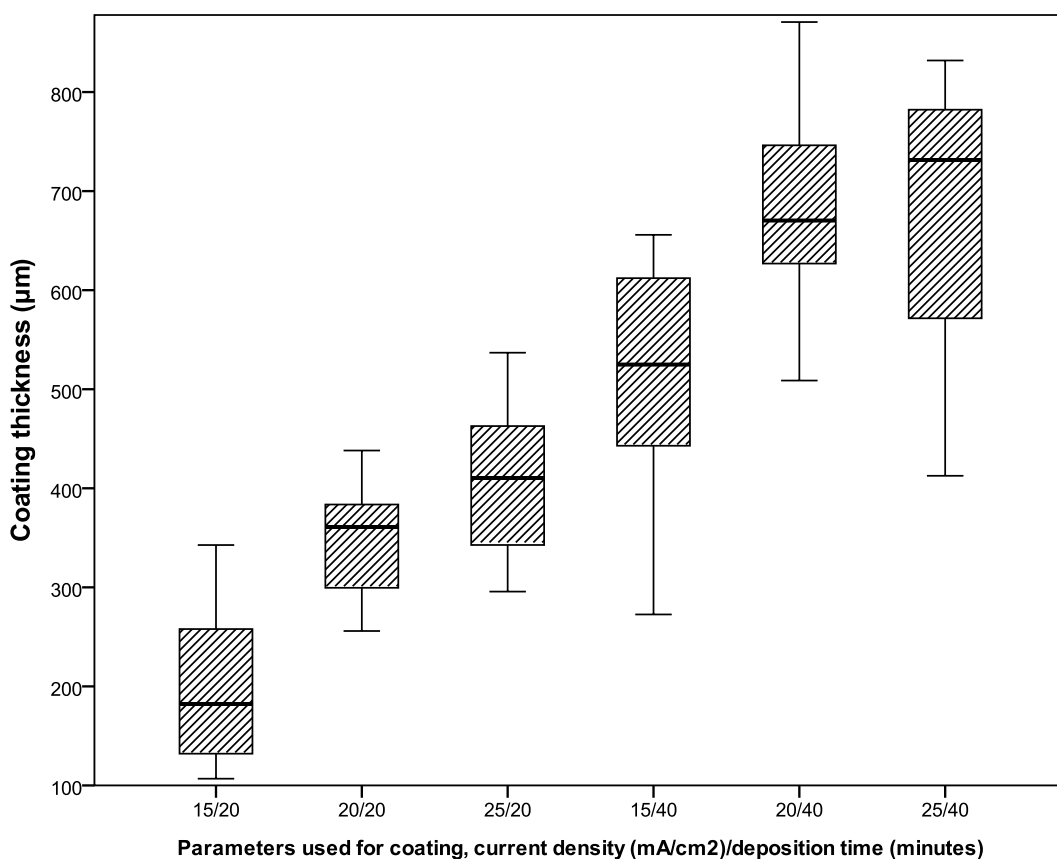


Figure 4-16 Boxplot of thickness of ESiHA coating ( $\mu\text{m}$ ) produced by different current densities ( $\text{mA}/\text{cm}^2$ ) over varying deposition times (minutes).

	5/5	5/10	5/15	10/5	10/10	10/15
5/5	-	1	0.963	<i>0.022</i>	<i>&lt;0.001</i>	<i>&lt;0.001</i>
5/10	-	-	1	1	<i>0.003</i>	<i>&lt;0.001</i>
5/15	-	-	-	1	<i>0.003</i>	<i>&lt;0.001</i>
10/5	-	-	-	-	0.160	<i>0.008</i>
10/10	-	-	-	-	-	1

Table 4-4 p-values for pair-wise comparisons of thickness of coating with different current density/deposition time combinations.  $p < 0.05$  is considered to be significant and are identified in italics.



**Figure 4-17** Boxplot of thickness of ESRHA coating ( $\mu\text{m}$ ) produced by different current densities ( $\text{mA}/\text{cm}^2$ ) over varying deposition times (minutes).

	<b>15/20</b>	<b>15/40</b>	<b>20/20</b>	<b>20/40</b>	<b>25/20</b>	<b>25/40</b>
<b>15/20</b>	-	<i>&lt;0.001</i>	0.083	<i>&lt;0.001</i>	<i>&lt;0.001</i>	<i>&lt;0.001</i>
<b>15/40</b>	-	-	<i>0.024</i>	<i>0.008</i>	0.348	0.123
<b>20/20</b>	-	-	-	<i>&lt;0.001</i>	1	<i>&lt;0.001</i>
<b>20/40</b>	-	-	-	-	<i>&lt;0.001</i>	1
<b>25/20</b>	-	-	-	-	-	<i>0.001</i>

**Table 4-5** p-values for pair-wise comparisons of thickness of coating with different current density/deposition time combinations.  $p < 0.05$  is considered to be significant and are identified in italics.

The **10mA/cm<sup>2</sup>-15mins** for EHA, **10mA/cm<sup>2</sup>-10mins** for ESiHA and **15mA/cm<sup>2</sup>-20mins** for ESRHA with thicknesses of  $22.4 \pm 2.8 \mu\text{m}$ ,  $29.6 \pm 2.6 \mu\text{m}$  and  $202 \pm 82.8 \mu\text{m}$  respectively were chosen due to their structural characteristics. These coatings underwent elemental analysis and their bioactivity was evaluated with a cell culture experiment.

#### **4.3.1.4 Elemental analysis (EDS)**

The Ca:P ratio for EHA, Ca:(P+Si) for ESiHA and (Ca+Sr):P for ESRHA was 1.53, 1.36 and 1.65 respectively. Each coating had a lower Ca:P ratio when compared to stoichiometric HA (1.67). The ESiHA and ESRHA coatings

contained 0.29wt% (0.23at%) Si and 6.4wt% (1.68at%) Sr respectively (Table 4-6). Examples of spectra are shown in Figure 4-18.

<b>Coating</b>	<b>EHA</b>	<b>ESiHA</b>	<b>ESrHA</b>
<b>Ratio</b>	1.53±0.04	1.36±0.07	1.65±0.15
<b>wt% (±SD)</b>	-	0.29±0.13	6.41±0.70
<b>at% (±SD)</b>	-	0.23±0.10	1.68±0.22

**Table 4-6 Summary of coating Ca:P ratios and levels of elemental substitution.**

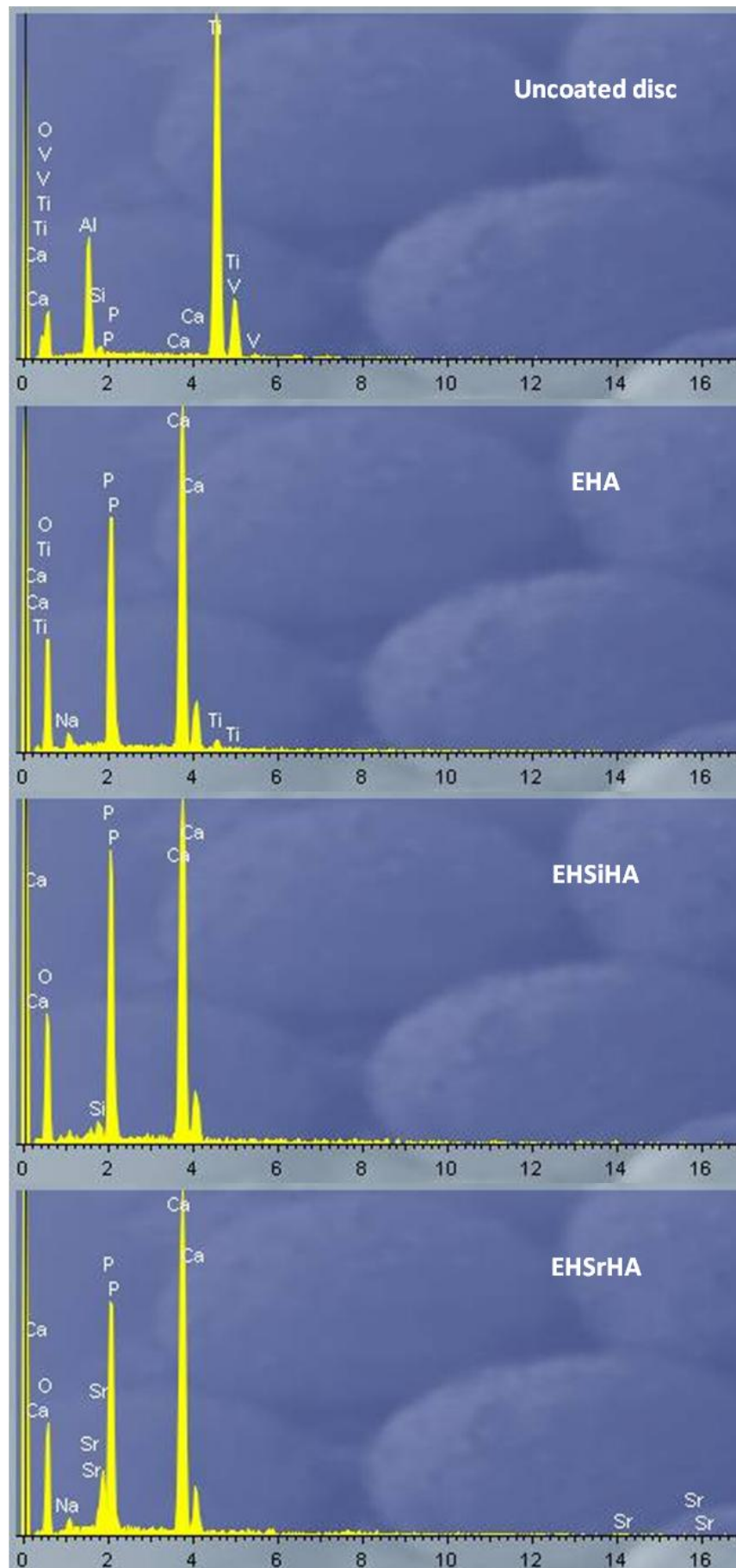
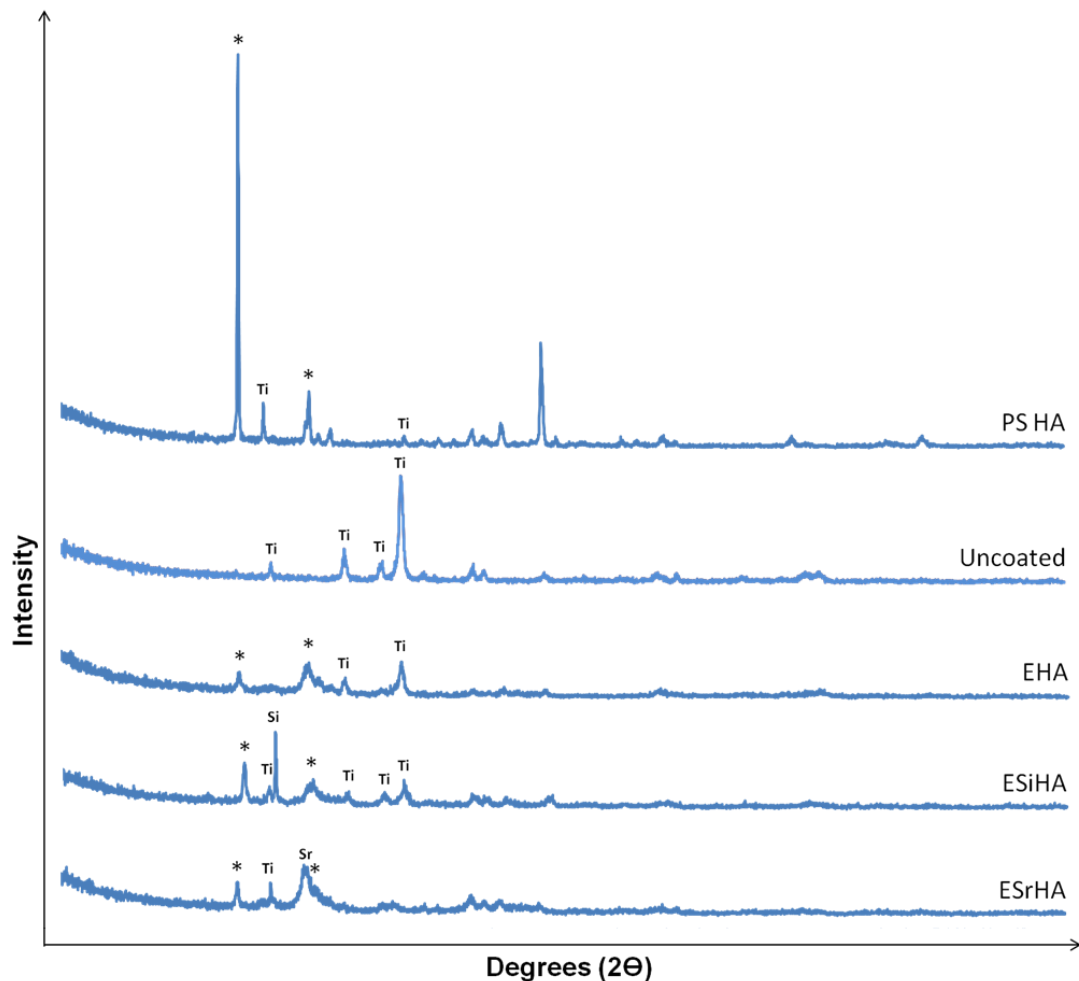


Figure 4-18 EDS spectra of coatings. Ca, calcium; O, Oxygen; Ti, titanium; V, vanadium; Al, aluminium; Si, silicon; Sr, strontium; Na, sodium. x-axis = Energy (keV)

### 4.3.1.5 Crystallinity

XRD analysis was performed by Prof. J. Knowles (Eastmann Dental Institute). Spectra demonstrated that all coatings investigated contained both crystalline and amorphous phases. None of the EC coatings developed contained the same level of crystallinity as a commercially available plasma sprayed HA coating (>85%) (Figure 4-19).



**Figure 4-19** XRD spectra of all coatings as labelled. \* denotes HA peaks with Si and Sr referring to the silicon or strontium present within the coating. Ti peaks are identified due to the underlying disc.

In order to identify peaks associated with the HA coating, uncoated control discs were also analysed using XRD (Figure 4-19). A similar spectra was identified for EHA, ESiHA and ESrHA coatings, all of which exhibited lower amplitude peaks which were less narrow compared to the plasma sprayed HA spectra. All coatings showed a crystalline structure with some amorphous phases. The Si and Sr were found on the spectra and therefore further confirmation that the coating contained a crystalline form of the substituted elements.

### 4.3.2 Characterisation of hMSCs

Following osteogenic differentiation of isolated hMSCs, results showed that calcium deposits stained with Alizarin Red confirmed the presence of osteoblasts. Oil Red O stained the intracellular lipid content of differentiated adipocytes. These cells were observed to be shorter in length and less spindle shaped when compared with hMSCs. Isolated pellets of differentiated chondrocytes stained blue with Alcian Blue confirming that stem cells had successfully undergone chondrogenic differentiation.

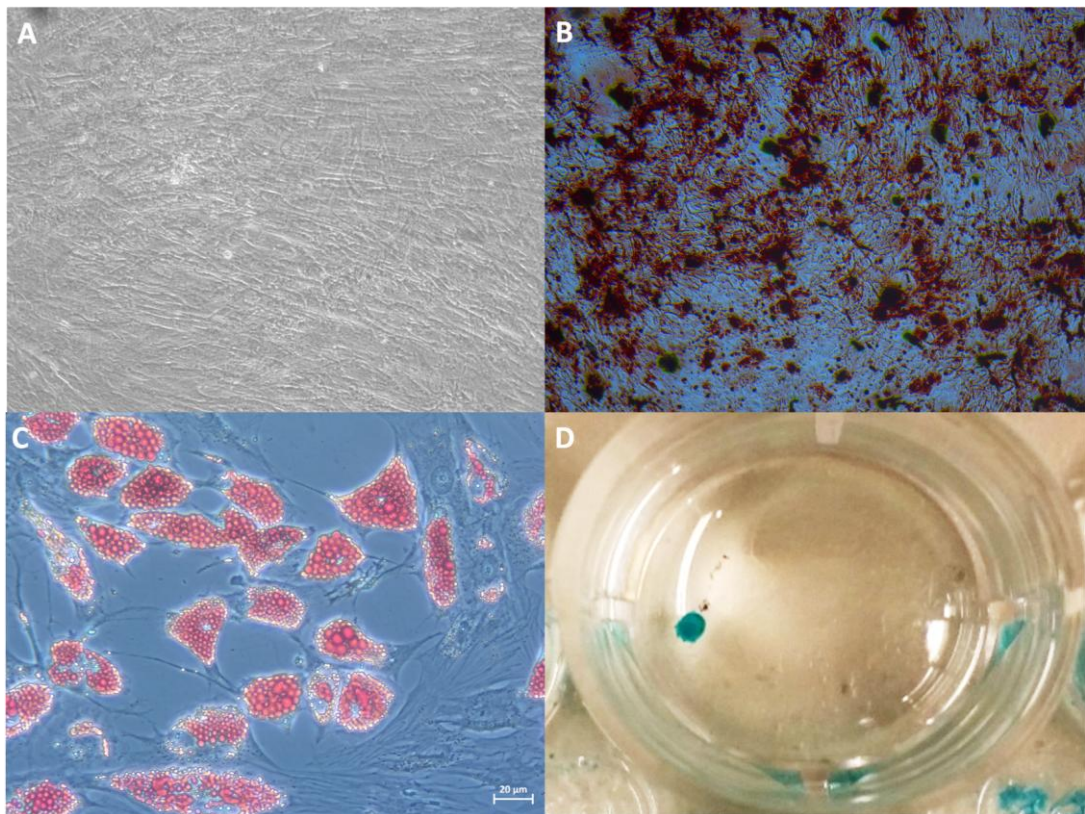


**Figure 4-20 (A) control culture of hMSCs in DMEM+. (B) Red stained calcium deposits from osteoblasts with Alizarin Red stain. (C) Red stained lipid within adipocytes with Oil Red O stain. (D) Blue pellet confirming presence of chondrocytes with Alcian Blue stain.**

### 4.3.3 Cell proliferation and differentiation on EHA, ESiHA and ESrHA coatings

#### 4.3.3.1 Cell proliferation: AlamarBlue® assay

All data was found to be parametric and therefore an ANOVA with bonferroni post-hoc correction was used to analyse the results. A significant difference was found in the metabolic activity of cells on EHA ( $p < 0.001$ ) and ESrHA ( $p = 0.23$ ) coatings over time. Cell proliferation on EHA at day 14 was significantly higher than that on day 3 ( $p < 0.001$ ) and day 7 ( $p < 0.001$ ). Proliferation on ESrHA decreased between day 3 and day 7 ( $p = 0.025$ ). Significantly different levels of metabolic activity was observed between the coatings on days 3 ( $p < 0.001$ ) and 7 ( $p = 0.001$ ) with no difference between the coatings found at day 14 ( $p = 0.062$ ). Summary of results can be found in Table 4-7 with pair-wise comparisons across timepoints, at day 3 and at day 7 are in Table 4-8, Table 4-9 and Table 4-10 respectively.

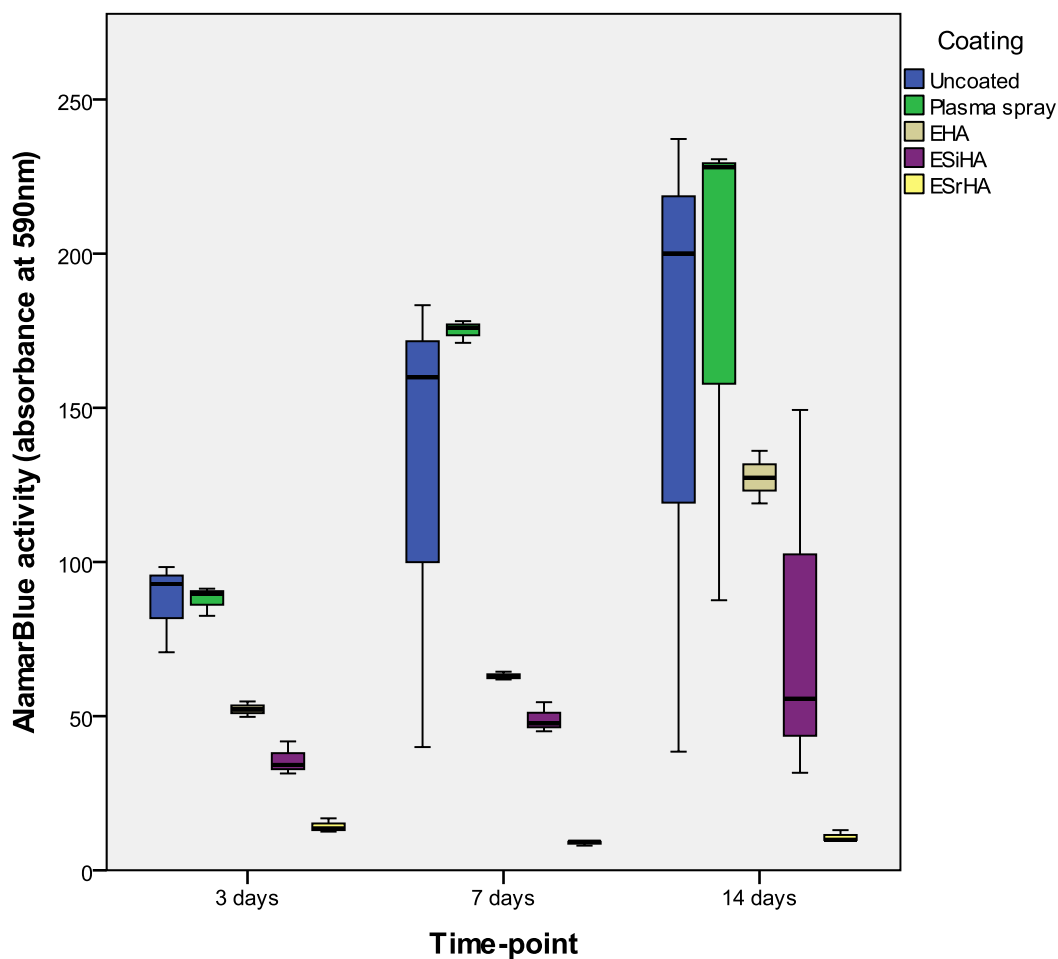


Figure 4-21 Boxplot showing the AlamarBlue® activity for each of the coatings at each time-point.

Timepoint (days)	Coating	AlamarBlue® assay
3	Uncoated	92.9±14.6
	Plasma sprayed	89.7±4.7
	EHA	52.1±2.5
	ESiHA	34.1±5.4
	ESrHA	13.5±2.3
7	Uncoated	159.9±76.8
	Plasma sprayed	176.0±3.6
	EHA	62.7±1.3
	ESiHA	47.6±4.9
	ESrHA	9.3±0.7
14	Uncoated	200.0±105.6
	Plasma sprayed	228.0±81.8
	EHA	127.3±8.5
	ESiHA	43.6±62.1
	ESrHA	9.9±1.8

**Table 4-7 AlamarBlue® assay result (mean±SD) for coatings per timepoint (day)**

Comparison (Coating, Timepoint)	p-value
EHA, 3 Vs EHA, 14	<0.001
EHA, 7 Vs EHA, 14	<0.001
ESrHA, 3 Vs ESrHA, 14	0.034

**Table 4-8 Significant pair-wise comparisons over timepoints, p-values as shown.**

Day 3	Uncoated	PS	EHA	ESiHA	ESrHA
Uncoated	-	1	<i>0.002</i>	<i>&lt;0.001</i>	<i>&lt;0.001</i>
PS	-	-	<i>0.002</i>	<i>&lt;0.001</i>	<i>&lt;0.001</i>
EHA	-	-	-	0.220	<i>&lt;0.001</i>
ESiHA	-	-	-	-	0.054

**Table 4-9 p-values for pair-wise comparisons of normalised AlamarBlue® assay results of various coatings at day 3. p<0.05 is considered to be significant and are identified in italics.**

Day 7	Uncoated	PS	EHA	ESiHA	ESrHA
Uncoated	-	1	0.445	0.191	<i>0.018</i>
PS	-	-	<i>0.026</i>	<i>0.012</i>	<i>0.002</i>
EHA	-	-	-	1	0.834
ESiHA	-	-	-	-	1

**Table 4-10 p-values for pair-wise comparisons of normalised AlamarBlue® assay results of various coatings at day 7. p<0.05 is considered to be significant and are identified in italics.**

Plasma sprayed HA and uncoated Ti<sub>6</sub>Al<sub>4</sub>V surfaces showed greater proliferation overall compared to the EC deposited coatings. Of the electrodeposited surfaces EHA showed the significantly greater proliferation at day 3. ESrHA showed the least cell proliferation occurring on its surface.

#### 4.3.3.2 Osteogenic Differentiation: ALP assay

All of the coatings and at all time-points investigated, induced osteogenic differentiation at 3, 7 and 14 days. Both the uncoated and plasma sprayed HA coated control surfaces induced greater osteogenic differentiation compared with the experimental groups.

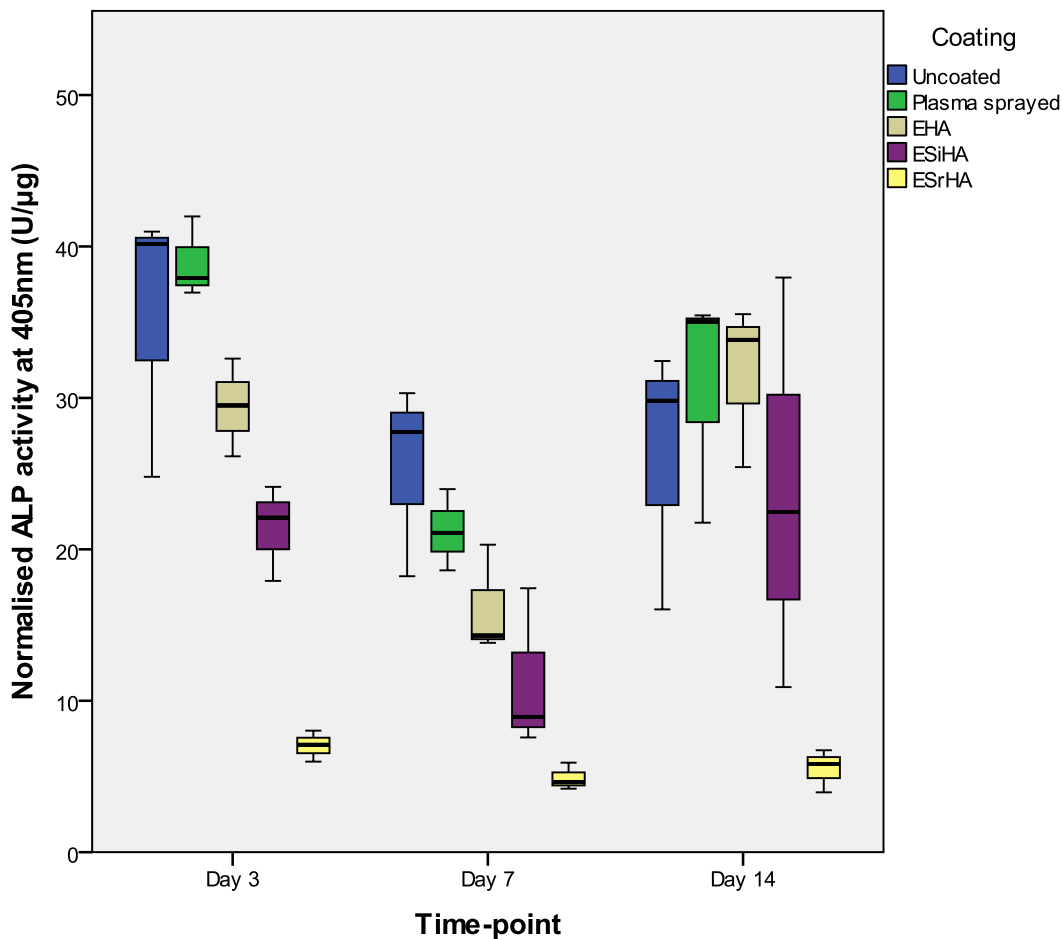


**Figure 4-22** Boxplot showing the normalised ALP assay result for each of the coatings at each timepoint.

A significant difference in ALP levels was observed when the experimental coatings were compared on days 3 ( $p < 0.001$ ), day 7 ( $p = 0.001$ ) and day 14 ( $p = 0.21$ ). Figure 4-22 and Table 4-11 summarises the results obtained and individual pair-wise comparisons obtained for days 3, 7 and 14 are presented in Table 4-12, Table 4-13 and Table 4-14 respectively.

In the plasma spray control group, a significant decrease in ALP was observed between days 3 and 7 ( $p = 0.015$ ). A significant decrease in ALP levels following culture on the EHA coating was also found when days 3 and 7 were compared ( $p = 0.025$ ). This was followed by a significant increase from day 7 to 14 ( $p = 0.012$ ). No significant difference was measured when day 3 and day 14 time-points were compared in the EHA group. No differences in ALP assay was observed for the ESiHA and ESrHA groups over the timepoints.

The EHA group showed the highest mean ALP assay at day 14, although not significant, it suggests this coating may induce the greatest amount of osteogenic differentiation.

Time-point (days)	Coating	Normalised ALP assay (U/µg)
3	Uncoated	35.3±9.1
	Plasma spray	40.0±2.7
	EHA	29.4±3.2
	ESiHA	21.3±3.2
	ESrHA	7.0±1.0
7	Uncoated	25.4±6.7
	Plasma spray	21.2±2.6
	EHA	16.1±3.6
	ESiHA	11.3±5.3
	ESrHA	4.9±0.8
14	Uncoated	26.1±8.8
	Plasma spray	30.7±7.8
	EHA	31.6±5.4
	ESiHA	23.8±13.6
	ESrHA	5.5±1.4

Table 4-11 Normalised ALP assay result (mean±SD) for coatings per timepoint (day)

Day 3	Uncoated	PS	EHA	ESiHA	ESrHA
Uncoated	-	1	1	<i>0.048</i>	<i>&lt;0.001</i>
PS	-	-	0.331	<i>0.011</i>	<i>&lt;0.001</i>
EHA	-	-	-	0.641	<i>0.002</i>
ESiHA	-	-	-	-	<i>0.040</i>

Table 4-12 p-values for pair-wise comparisons of normalised ALP assay results of various coatings at day 3. p<0.05 is considered to be significant and are identified in italics.

Day 7	Uncoated	PS	EHA	ESiHA	ESrHA
Uncoated	-	1	0.232	<i>0.022</i>	<i>0.001</i>
PS	-	-	1	0.170	<i>0.008</i>
EHA	-	-	-	1	0.089
ESiHA	-	-	-	-	0.945

Table 4-13 p-values for pair-wise comparisons of normalised ALP assay results of various coatings at day 7. p<0.05 is considered to be significant and are identified in italics.

Day 14	Uncoated	PS	EHA	ESiHA	ESrHA
Uncoated	-	1	1	1	0.134
PS	-	-	1	1	<i>0.043</i>
EHA	-	-	-	1	<i>0.035</i>
ESiHA	-	-	-	-	0.239

Table 4-14 p-values for pair-wise comparisons of normalised ALP assay results of various coatings at day 14. p<0.05 is considered to be significant and are identified in italics.

#### 4.3.3.3 SEM analysis of cells on disc surfaces

Cells were observed on the surface of all coatings and at all time points investigated (Figure 4-23, Figure 4-24). Cells were fibroblastic in nature with

minimal difference in cell morphology observed over the coatings and through the time-points.

In the uncoated control group, cell number was seen to increase at each time-point until day 28 where a film of cells were seen fully coating the disc surface. Troughs present within the roughened Ti surface were in some cases, bridged by the cells.

Cells cultured on the plasma sprayed HA coated disc surface were similar in number and morphology to the uncoated surfaces and by day 28, a confluent layer of cell growth was observed over the surface. When compared with samples observed at time 0 and similar to the uncoated disc surface, the plasma sprayed coating appeared structurally unchanged following 28 days of cell culture.

Fewer cells were apparent on the EHA coated disc surface when compared to the control groups. Cells were located both on top and in between the HA crystals, bridging them together. Following 28 days of cell culture, HA crystals within the coating were evident and no change in crystal shape or size was observed when the different time points were compared.

Cells cultured on the ESiHA coatings appeared to lie preferentially on the crystal points and bridging the gaps between them. At each of the time-points investigated, fewer cells were observed on the disc surface compared to all the other groups. No change in crystal structure was observed when the pre- and post 28 day coatings were compared.

Cells were found on the ESrHA coating at all timepoints. They formed a membrane across clusters of SrHA crystals. No changes in crystals were seen. The fewest cells were observed on this coating.

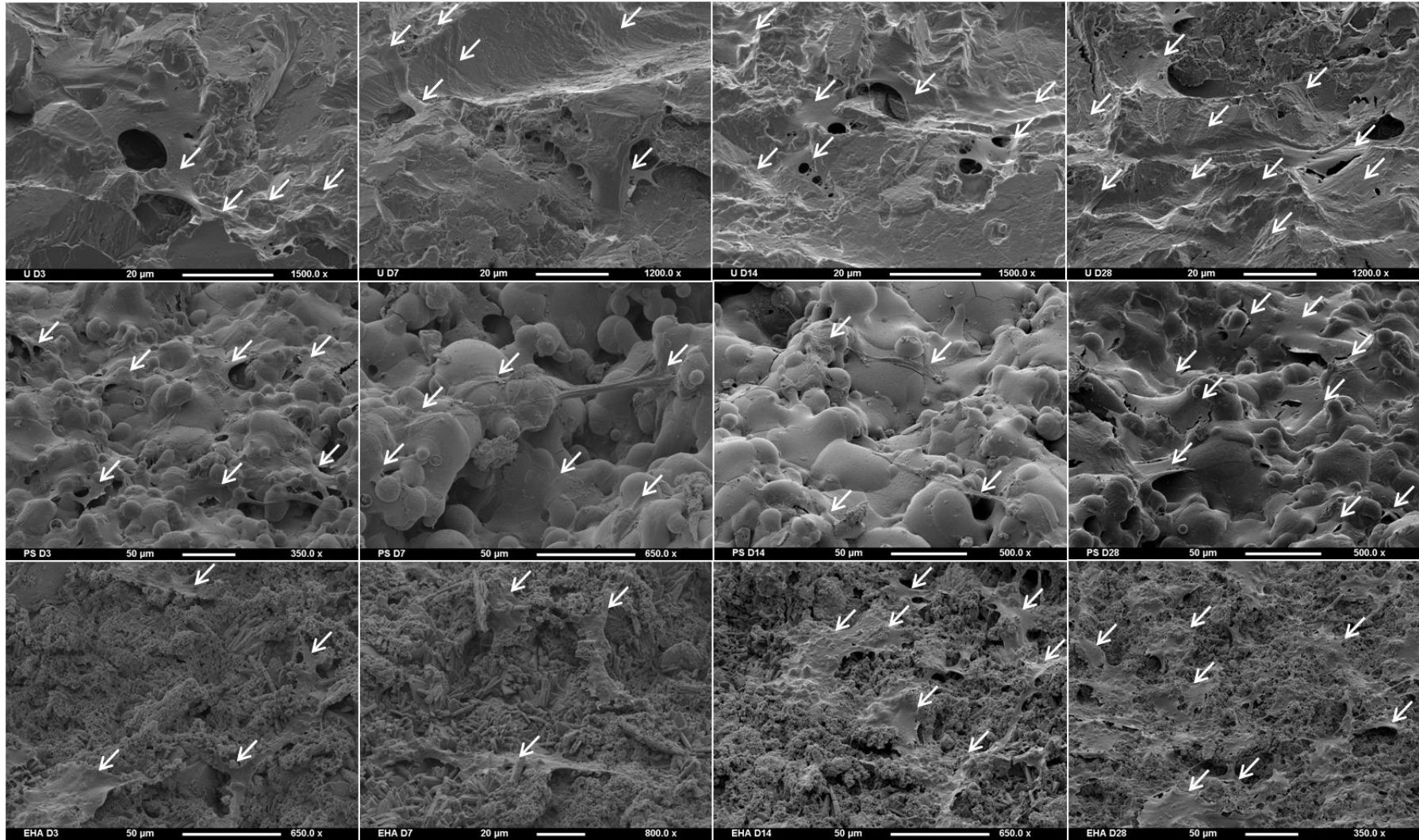
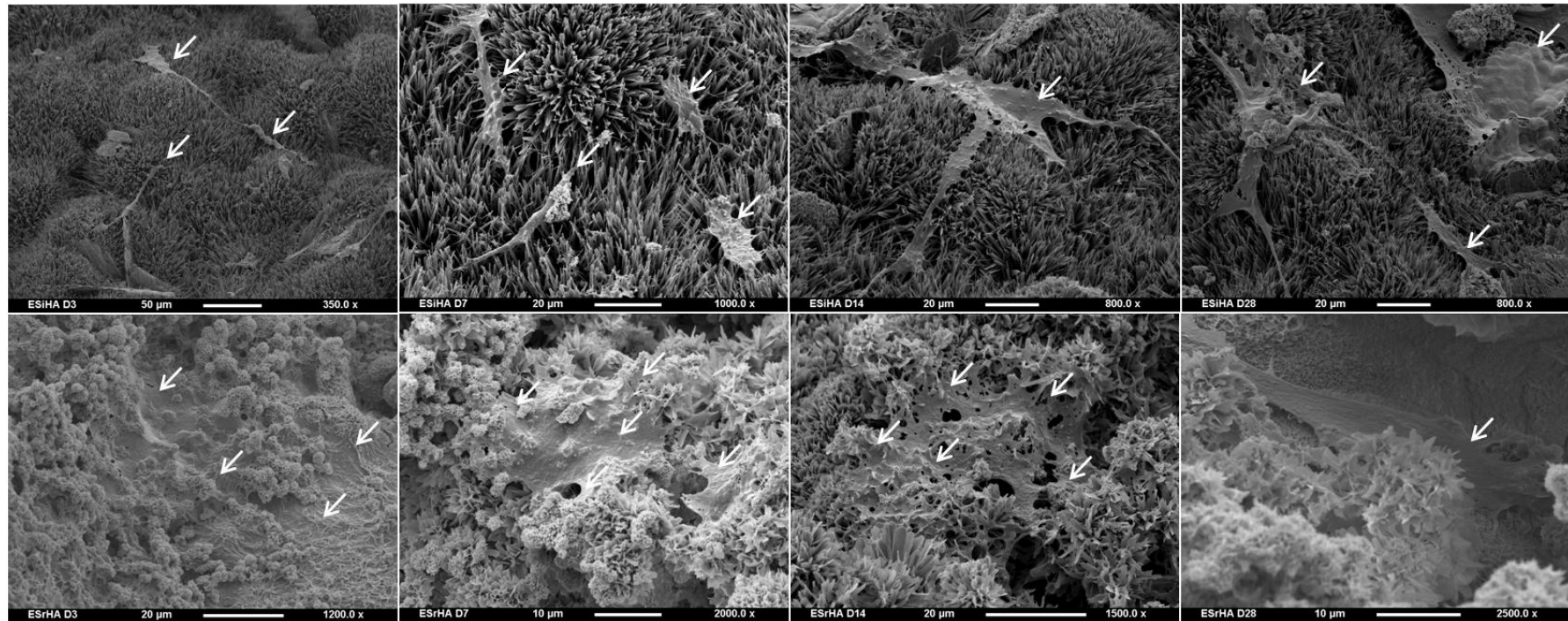


Figure 4-23 Scanning electron micrographs of coating surfaces at different timepoints (days 3 (D3), 7 (D7), 14 (D14) and 28 (D28)). U, Uncoated; PS, Plasma spray; EHA, EC HA. White arrows identify cells. Scale bar and magnification as shown.



**Figure 4-24** Scanning electron micrographs of coating surfaces at different timepoints (days 3 (D3), 7 (D7), 14 (D14) and 28 (D28)). ESIHA, EC silicate-substituted HA; ESrHA, EC strontium-substituted HA. White arrows identify cells. Scale bar and magnification as shown.

#### 4.4 Discussion

In the era of 3D printing and the production of porous structures with complex geometries, EC coatings have had substantial interest of late as they are able to coat these complex shapes. The need for implants with bioactive coatings allowing for greater osseointegration has been outlined in previous chapters. Using the techniques that I developed in this chapter I was able to control coating thickness and bioactivity.

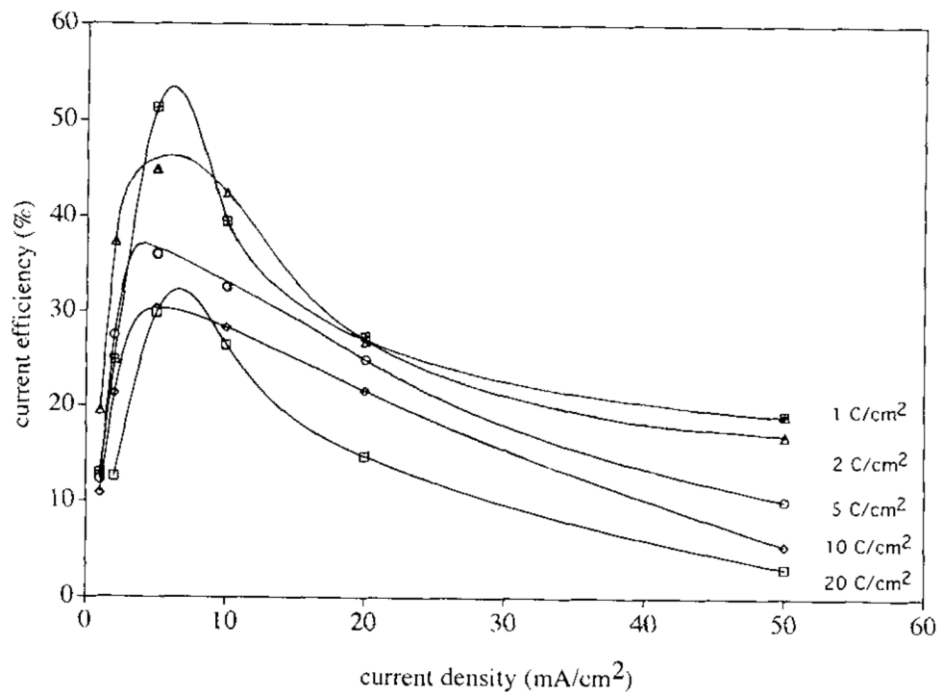


**Figure 4-25 Current efficiency as a function of current density for different total amounts of charge passed, derived from Redepenning et al. (Redepenning et al., 1996)**

All EHA, ESiHA and ESrHA coatings presented in Table 4-1 were produced apart from combinations F, H and I. The higher current densities required for these coatings could not be sustained by the power supply over the deposition times. The current efficiency is defined as the percentage conversion of a set amount of CaP to brushite under a certain current density. If one mole of CaP is converted to 1 mole of brushite under a set current density, there is 100% current efficiency at that current density. As described by Redepenning et al (Redepenning et al., 1996) current efficiency generally decreases as the total amount of charge passing through the circuit increases (Figure 4-25), with charge being a product of current density and deposition time. The cathodic surface (Ti<sub>6</sub>Al<sub>4</sub>V disc) becomes passivated and as a result the current is forced through an increasingly smaller area with time. At the higher current densities

and deposition times, cinder cones develop around pin holes in the coating. The size of the pin holes decrease as the coating is laid down and as a result a greater voltage is required to maintain the same current density (Redepenning et al., 1996) and allow for a constant rate of coating deposition. The DC dual power supply pack used in this experiment could not provide the voltages required to maintain the high current densities over the deposition times as a result of the increasing resistance in the circuit.

Light microscopy and SEM analysis of the EHA, ESiHA and ESrHA coatings investigated in this chapter did not reveal any obvious differences in crystal morphology when each were compared. The coating morphologies observed were similar to those reported by Redepenning et al (Redepenning et al., 1996), Li et al (Li et al., 2011) and Liang et al (Liang et al., 2014) (EHA, ESiHA and ESrHA respectively). All of the coatings developed in this chapter resulted in a fully coated disc surface with no exposure of the underlying Ti alloy surface. In the ESrHA group, the macroscopic tubules seen when observed using both light microscopy and SEM appeared to be more frequent as the current density and deposition times increased. These are most likely the equivalent ESrHA cinder cones which Redepenning et al (Redepenning et al., 1996) described for EHA.

The thickness of the ESrHA coating was much greater than the other coatings produced. All other coatings were below the 50 $\mu$ m threshold described by de Groot et al (de Groot et al., 1987) and Wang et al (Wang et al., 1993). Although some coatings were as low as 14.2 $\mu$ m in thickness, Schmidmaier et al (Schmidmaier et al., 2002) carried out an in vitro biomechanical test and showed significantly increased implant fixation following deposition of a 2 $\mu$ m thick EC deposited HA coating. The optimal thickness of a coating is also dependent on the use of the primary implant. Coatings on exposed implant surfaces are susceptible to physical trauma, for example when being handled by the surgeon during implantation. Thicker coatings are likely to be needed here to prevent complete removal of the bioactive coating. On more protected surfaces, such as the inner pores of a laser sintered collar, there is no exposure to surgeon handling and therefore thinner coatings are more appropriate.

Analysis in this study showed that current density and deposition time influenced the thickness of the coating produced (Figure 4-15, Figure 4-16, Figure 4-17, Table 4-3, Table 4-4, Table 4-5). Across all coatings the higher deposition times and current densities had a synergistic effect in producing thicker coatings. Longer deposition time will naturally produce a thicker coating. The cause for a thicker coating with higher currents can be explained using Equation 7.

$$v=QE/4\pi r\eta$$

**Equation 7** The relationship between electrophoretic velocity ( $v$ ), charge of particle ( $Q$ ), radius of particle ( $r$ ), voltage used to produce electric field ( $E$ ) and  $\eta$  can be considered as a constant as the concentration of HA particles in solution is usually low (Mondragon-Cortez and Vargas-Gutierrez, 2004).

Higher voltages increase the velocity with which particles in solution deposit themselves onto the substrate. Therefore rate of deposition increases and a thicker coating is produced under the same deposition time. In this chapter, significant differences can be seen in the thickness of the coatings produced with the same deposition times ESiHA (Table 4-4) and ESrHA (Table 4-5).

No significant difference was seen in the thickness of the EHA coating deposited when the current parameters were varied. Ions involved in the reaction to produce EHA are less charged compared with ESiHA and ESrHA. The current passing through the solution therefore has less influence over the deposition rate. Furthermore a supersaturated CaP (Redepenning et al., 1996) was used for EHA deposition which greatly increased  $\eta$ , in turn reducing the effect of voltage ( $E$ ) on the electrophoretic velocity and deposition rate.

Meng et al (Meng et al., 2006) showed that particles with differing charge/radius ratios had different EC mobilities with smaller, highly charged particles being highly mobile, these particles were being deposited at lower current densities. Larger particles were found to be incorporated in coatings produced with higher currents which led to the formation of coatings with greater porosity. Although coating porosity was not quantitatively analysed in this chapter, cross-sectional SEM analysis did not reveal any obvious changes in porosity or density when the EHA coating was compared using different current densities. This was most

likely due to the electrokinetic issues mentioned previously regarding the lower charge ions and the greater concentration of CaP solution involved. SEM images for the ESiHA and ESrHA do reveal coatings of greater porosity as the current density and deposition times increase.

An increased level of cell proliferation and ALP expression was observed in response to the uncoated Ti<sub>6</sub>Al<sub>4</sub>V surface when compared to the EHA, ESiHA and ESrHA coated groups. In this experiment, the surface of each of the discs was roughened using a commercial sandblasting technique that utilised Al<sub>2</sub>O<sub>3</sub> particles producing a Ra of 6.711µm. Cells respond to alterations in surface roughness and surface topography as a result of changes in cytoskeletal tension (McBeath et al., 2004). ALP activity has been reported to increase following roughening of a Ti<sub>6</sub>Al<sub>4</sub>V surface (Deligianni et al., 2001). Similarly, higher osteocalcin staining as well as osteopontin and osteocalcin mRNA expression has been observed on rougher surfaces (Yang et al., 2016). The Ra of the uncoated discs lie in the ideal range between 4 and 7µm to allow for high levels of differentiation whilst reducing proliferation as observed by Boyan et al (Boyan et al., 1999). In contrast it has also been shown that increasing roughness of surfaces *in vitro* is detrimental to cellular adhesion, proliferation and differentiation (Anselme et al., 2000). Roughened topographies on a nano-scale closely mimic the *in vivo* cell niche and elicit cell responses. Although surface profilometry was not carried out to measure the surface roughness of these coatings, further work is required to investigate whether the EC coatings produced in this study showed greater roughness compared with the control substrates using non-contact profilometry techniques. Qualitative analysis of surface morphology using SEM suggested that the EC coatings may exhibit a rougher nano-topography than control plasma sprayed HA coatings.

The EHA coating produced in this study had a Ca:P ratio of 1.53 which suggests a reduction in Ca content. This is also known as a bioactive, calcium deficient HA (Bose and Tarafder, 2012). This is similar to the result obtained in a study that also utilised this technique (Garcia-Gareta et al., 2013). This ratio falls within the Ca:P ratios of HA found in natural bone (ranges from 1.37 to 1.87). Differences between calcium deficient HA and bone include the

incorporation of carbonate ( $\text{CO}_3^{2-}$ ) and other trace elements ( $\text{Na}^+$ ,  $\text{K}^+$ ,  $\text{Mg}^{2+}$ ,  $\text{Sr}^{2+}$  and  $\text{Zn}^{2+}$ ) (Bose and Tarafder, 2012).

AlamarBlue® activity suggested that proliferation of the hMSCs grown on EHA increased for each timepoint. A significant increase occurred between day 3 and day 14. No significant difference in cell proliferation or ALP activity was seen when the EHA and uncoated and plasma spray control groups were compared. As previously outlined EC coatings can be used to uniformly coat the surface of complex porous structures as compared to the plasma spray process that applies a coating using a line-of-sight method. The work in this chapter showed that a similar level of bioactivity can be achieved using an EHA coating.

The thickness of the ESiHA coating created was controlled by both the current density and deposition time. Although each parameter appeared to be synergistic, pair-wise comparisons of the different combinations (Table 4-4) suggest that current density has a greater influence. The Ca:(P+Si) ratio for ESiHA (1.36) was fractionally lower than the Ca:P ratios found in natural bone (1.37-1.87). The coating still exhibited bioactivity with AlamarBlue® and ALP assays revealing a degree of hMSC proliferation and osteogenic differentiation. At day 3, osteogenic differentiation on the ESiHA coating was significantly greater ( $p=0.04$ ) than ESrHA, suggesting that the coating has greater osseointegration than the ESrHA. Although there was increased ALP activity associated with the ESiHA compared with the ESrHA coating, there was no statistically significant difference at day 7 and 14. ALP readings for day 14 showed greatest variability compared with the other coatings and timepoints. The reason for this is unclear. One explanation could be that dissolution of the Si content of the coating was less controlled compared to that of the ESrHA and by day 14 the majority of the Si had been released from some of the disc coatings, therefore not producing any further cellular response. The addition of Si to HA is known to increase dissolution of the material in both *in vitro* and *in vivo* environments (Porter et al., 2004). Low bioactivity can also be due to the poor Ca:(P+Si) ratio, which was previously mentioned. SEM analysis of the cells on the ESiHA surface also revealed that the cells lie on the point of the crystals. The ESiHA coating may therefore be perceived by the cells as having a rough topography, which may further inhibit cell proliferation and differentiation

(McMurray et al., 2011). The Si content of the coating was also lower (0.29wt%) than the optimal 0.8wt% suggested by Hing et al (Hing et al., 2006), which could further explain the relatively low proliferation and osteogenic differentiation seen on ESiHA. Zhang et al (Zhang and Zou, 2009) has however shown a significant increase in bioactivity with a 0.39wt% SiHA coating compared with HA under the same conditions. Hing et al (Hing et al., 2006) also showed that a 0.2wt% and 0.4wt% of induced less bone formation than HA without Si in an *in vivo* model at 12 weeks. A higher Si wt% would most likely produce a more bioactive ESiHA, however this is not without limitations as increased Si content can inhibit crystal size and thickness (Li et al., 2011).

The ALP assay is based on the enzymatic activity of ALP, which cleaves the phosphate group of p-nitrophenol phosphate to produce p-nitrophenol. P-nitrophenol production can be monitored at 405nm as it is yellow at alkaline pH (Bowers and McComb, 1966). Extracellular ALP assays were performed as intracellular assays would have involved freeze-thaw cycles in order to lyse the cells. Freeze-thaw cycles destroy the EC coatings from the repeated expansion of PBS that has penetrated into the porous coating upon freezing. The white coating particles within the solution will then cause a spurious result when the sample is undergoing colorimetric analysis.

Elemental analysis revealed a Ca:P ratio of 1.65 for ESrHA was closest to stoichiometric HA (1.67) however Sr content (1.68at%) was lower than the reported 5at% concentration (Drevet and Benhayoune, 2013) needed for optimal induction of cellular changes. Unfortunately the ESrHA coating showed the least bioactivity of all the coatings even with an almost stoichiometric Ca:P ratio and some Sr content. XRD analysis revealed that the ESrHA coating contained amorphous phases with poor crystallinity compared with plasma sprayed HA, this can be explained by the chemistry of SrHA. Sr substitutes Ca in 2 main locations within the lattice structure, M(1) and M(2). When the at% of Sr is greater than 10 in the HA coating, there is a shift in preference to M(2). At this higher at% the M(2) position better accommodates the larger Sr ion as here the metal ions form staggered equilateral triangles centered on an apatite channel. At lower at% such as 1.9, there is a preference for the M(1) position

where the metal ions form strict parallel columns causing low crystalline structures.

Given the amorphous phases and low crystallinity of the ESrHA seen with XRD, it is possible that this coating has a high dissolution rate. It is possible that the Sr released locally into the media from the coating was too high even with a low Sr at% and therefore cause toxicity. Dissolution studies of the coating utilising inductively coupled plasma mass spectroscopy (ICPMS) would confirm this. It would therefore be prudent to ensure in future experiments that the levels of Sr released are reduced. This is achieved by increasing crystallinity of coating and therefore reducing dissolution of Sr or reducing the mass of coating deposited onto the surface, in turn reducing the Sr available for dissolution.

The EHA coating formed with this EC deposition method consisted of calcium deficient HA (crystallized and amorphous). These different phases were formed as the EC deposition process involved several mechanism that include; electrochemical, acid-base and precipitation reactions. The combination of these together with varying current densities and deposition times lead to varying forms of calcium phosphates (Richard et al., 2006) being produced.

## 4.5 Conclusion

The work in this chapter allows the hypothesis to be accepted, as differing the coating parameters, various thicknesses can be produced although morphology is unaffected. Substituted HAs did not significantly improve bioactivity when compared with controls and EHA hence we must reject our second hypothesis.

EC coatings can therefore be applied to  $Ti_6Al_4V$  substrates including SLS structures such as those used in chapter 3 without blocking the open porous structure by fine-tuning the coating parameters.

The cell work in this chapter suggests that these EC coatings are not as osseoinductive when compared with control groups. The focus for the following chapters concentrates on the osseoconductivity of each of the coatings. Given that the eventual porous ingrowth collar will be in close proximity to bone with growth factors in the immediate vicinity, it would be more prudent to focus on the osseoconductive nature of these coatings for the following chapter.

The focus in the proceeding work is to incorporate more Si to increase the bioactivity of ESiHA. A thinner ESrHA coating will be developed to prevent inhibitory high levels of Sr being released into the cellular environment preventing proliferation and differentiation. As suggested, other coating parameters will also be analysed including surface roughness and a dissolution study. MSCs will again be cultured on these coatings to assess bioactivity but using osteogenic media instead to evaluate the osseoconductivity.

**Chapter 5. Development, Refinement, Characterisation and  
Evaluation of the Bioactivity of Silicate and Strontium  
Substituted Hydroxyapatite Coatings**

## 5.1 Introduction

In this chapter I will alter the physical properties and elemental composition of the ESiHA and ESrHA coatings to improve their bioactivity. A number of weaknesses were identified in the coatings developed in Chapter 4 including low Si incorporation within ESiHA and ESrHA being too thick. Furthermore the roughness and dissolution characteristics of those coatings had not been analysed, which are further factors that may affect the coatings bioactivity.

The samples in this chapter have been acid etched to form micro-pits on top of the already roughened topography (Mandracci et al., 2016), this had not been done in the previous chapter. Coating adhesion is thought to be improved with this combination of treatments as it allows for greater interlocking of the coating with the surface (Mohseni et al., 2014) and enhanced nucleation of electrodeposited HA coatings (Lakstein et al., 2009). Analysis of coating adhesion is beyond the scope of this chapter and thesis however by theoretically improving the coating-Ti<sub>6</sub>Al<sub>4</sub>V adhesion, I am reducing the likelihood of the coating being removed when subjected to shear forces in the *in vivo* studies that will follow.

The ESiHA coating was found to have a Ca:P ratio of 1.36 containing 0.29wt% (0.23at%) Si, with a thickness ranging between 10-33µm depending on the coating parameters used. As described in section 4.4 the Si content within the coating was suboptimal compared to the 0.8wt% defined by Hing et al (Hing et al., 2006) and addition of Si also may have increased dissolution of the coating (Porter et al., 2004). In this chapter and in order to overcome possible increased dissolution and low Si wt%, the methodology described in 4.2 was modified. Nano-silicate was used as part of the electrolyte solution as a source of Si using a similar method to Huang et al (Huang et al., 2013) to increase Si wt%.

Post-coating treatments such as annealing, can also improve the crystallinity of the HA coating (Zyman et al., 1994). Studies have shown that annealing can increase crystallinity by up to 50% depending on the method by which the coating was deposited (Koch et al., 2007). Xue et al. (Xue et al., 2004) observed lower dissolution with highly crystalline HA coatings *in vitro*. The

coating was also found to have improved shear strength and reduced coating failure when compared to less crystalline HA coatings *in vivo*. Mechanical coating failure is not a major concern when used in conjunction with a porous SLS scaffold as the inner pores are not exposed to a high degree of physical insult and hence a high adhesive strength although desirable, is not a necessity. Although there is no evidence in literature regarding electrodeposited coating release around implants, theoretically it is possible that loose particles of coating could get released from within the pores causing third body wear on bearing surfaces if used as part of joint replacements. Coating dissolution can be analysed using inductively coupled plasma mass spectroscopy (ICPMS).

Even at the lowest current density and deposition time the mean thickness of the ESrHA coatings developed in the previous chapter was  $202 \pm 82.8 \mu\text{m}$ . SEM analysis of this coating revealed substantial flaring of the coating and a loosely packed structure that seemed comparatively less dense compared to the other coatings. At this thickness there is increased risk of coating-implant failure (Wang et al., 1993). Application of this coating to the porous scaffolds investigated in Chapter 3 would result in a post-coated inner pore diameter of only  $300 \mu\text{m}$ , hence mechanical failure of the coating could easily cause blockage of the inner pores, vastly reducing the porous space available for bone ingrowth. The thickness of coating applied is also an indicator of the volume of coating present. Given the higher risk of mechanical failure, poor crystallinity and theoretical high dissolution rate it is logical to suggest that the thickness of ESrHA should be reduced, thereby lowering the level of Sr being eluted into the local vicinity.

**The aims of this Chapter were to:**

- 1) Optimise the ESiHA and ESrHA coatings produced in Chapter 4 by modifying the methods utilised.**
- 2) Assess the bioactivity of each coating by quantifying the proliferation and osteogenic differentiation of ovine MSCs when seeded onto each surface.**
- 3) Assess the dissolution of Si and Sr from the new ESiHA and ESrHA respectively.**

The hypotheses were that:

- 1) Increasing the Si wt% with the ESiHA coating will improve the proliferation and osteogenic differentiation of MSCs.
- 2) Reducing the thickness and therefore Sr concentration within the ESrHA coating will improve the proliferation and osteogenic differentiation of MSCs.

## **5.2 Methods**

### **5.2.1 Sample preparation**

Each of the discs were prepared using the methods described in 4.2.1. The samples were also acid etched with 2% hydrofluoric acid for 4 minutes. The discs were then ultrasonically cleaned in 10% Decon 90, distilled water and 99% IMS for 15 minutes at each stage and left to air-dry as before.

### **5.2.2 Electrochemical deposition of HA coating**

Control discs were coated with an EC deposited HA coating using the methods described in 4.2.3 with a current density of  $10\text{mA}/\text{cm}^2$  over a 15 minute deposition time.

### **5.2.3 Electrochemical deposition of SiHA coating (ESiHAII)**

Given the low Si content using the previous method (4.2.4), it was decided to use a different electrolyte based on the methods of Huang et al (Huang et al., 2013). The compounds used to produce the electrolyte solution are different as well as the current density, deposition times, pH, temperature and the addition of an annealing process after deposition.

Discs were treated by submerging them in a  $65^\circ\text{C}$  5M NaOH solution for 24 hours whilst being actively stirred. Once washed with distilled water they were allowed to air dry. The electrolyte solution was composed of 1g/l of nano-SiO<sub>2</sub> (637238; Sigma-Aldrich), 0.042M Ca(NO<sub>3</sub>)<sub>2</sub>·4H<sub>2</sub>O (C2786; Sigma-Aldrich), and 0.025M NH<sub>4</sub>H<sub>2</sub>PO<sub>4</sub> (795461; Sigma-Aldrich) in distilled water. The solution was bought to a pH of 4.2 by the addition of 10% HCl solution at room temperature (AR15 pH meter; Accumet®, Fisher Scientific, UK). Discs were placed in a polyethylene holder and submerged in 800mls of the solution and attached to the negative terminal of a DC Dual Power Supply pack (Peak Tech, Telonic Instruments Ltd, UK) to act as the cathode with a 0.063mm diameter platinum wire (Goodfellow Cambridge Ltd., UK) as the anode. The discs were coated using a current density of  $0.8\text{mA}/\text{cm}^2$  at  $65^\circ\text{C}$ . Two different deposition times were investigated; 30 and 45 minutes. The current was maintained with the aid

of a multimeter as described in the previous chapter. The solution was gently stirred throughout and maintained at temperature for the duration of the process using a magnetic stirrer-hotplate and an aluminum foil heat jacket. Once coated the discs were placed in a furnace (RHF 1600, Carbolite Gero, Derbyshire UK) at 300°C for 2 hours for annealing.

#### **5.2.4 Electrochemical deposition of SrHA coating (ESrHAII)**

Discs were coated using the same methods described in 4.2.5 with a current density of 15mA/cm<sup>2</sup> over 2.5 and 5 minute deposition times. The only difference between this method and the methods outlined in 4.2.5 are the shorter deposition times to produce a thinner coating.

#### **5.2.5 Surface morphology and thickness of EC coatings**

Light microscopy (Keyence, Japan) and SEM (Philips XL30 FEGSEM, Philips Ltd, Guildford, Surrey) analysis was performed to image the surface topography. Coating thickness measurements were undertaken as described in 4.2.6.

#### **5.2.6 Coating Characterisation**

EDS and XRD techniques were used as described in 4.2.7. Selected EC coatings and control groups also underwent analysis using non-contact profilometry (Bruker Contour GT, Bruker Ltd, Coventry, UK) to quantify surface roughness.

ICPMS could not be performed to analyse the dissolution profile of ESrHAII as there is background Si artefact from the glassware and therefore it would produce a spurious result. Glassware of accessible apparatus could not be changed and ICPMS was abandoned. I therefore analysed the coating on the discs at each time-point of the cell culture experiment. The wt% of Si and Sr within the coating at day 3, 7, 14 and 28 can be analysed and the dissolution of these elements into the growth medium can therefore be extrapolated.

At each time-point after SEM analysis, the elemental composition of the coatings were evaluated in 5 areas of the disc (centre and within 4 quadrants) using EDS. 5 points on the coating that were not occupied by cells, were selected and the mean Si and Sr wt% calculated and presented as a percentage of the original wt%.

### **5.2.7 Cell culture and maintenance**

Additional hMSCs to those used in Chapter 4, were difficult to source within the time frame of the work in this thesis. Ovine MSCs (oMSCs) were used instead and isolated from bone marrow aspirates obtained from 3 healthy, skeletally mature, commercially cross-bred sheep kindly donated by Dara McCreary (PhD Student).

oMSCs were cultured in DMEM supplemented with 10% FCS and 100 units/ml of penicillin and streptomycin (P/S, Gibco, UK) to form DMEM+.

Cryovials containing oMSCs were removed from liquid nitrogen storage and placed in a 37°C water bath. 1ml of DMEM+ was added to the cells and transferred to a universal tube. An additional amount of DMEM+ was added to the universal tube leaving the cells to equilibrate over a 5 minute period. Once a total volume of 16mls was reached the suspension was centrifuged at 2,000 rpm over a period of 5 minutes. The supernatant was discarded and the pellet was re-suspended in 1ml of DMEM+. The cells (passage 2) were transferred into a T75 culture flask (Corning, USA) with 10ml of DMEM+ and cultured under standard conditions within an incubator (37°C with 5% CO<sub>2</sub>). Growth medium was changed every 3-5 days and cells were regularly observed using phase-contrast light microscopy. Once cells had reached 80-90% confluence (% total surface area of the flask covered in cells), they were passaged. DMEM+ within the flask was carefully discarded and the cells were washed with sterile cold PBS. Once washed, the PBS was also discarded. oMSCs grew as adherent monolayers within the culture flask and in order to remove the cells, they were trypsinised by adding 1ml of trypsin-5.3mM EDTA.4Na solution and incubated for 5 minutes under standard conditions at which point the cells lifted off the

flask surface. Trypsinisation was stopped by adding a 1:1 volume of DMEM+ as the FCS in the DMEM+ contained trypsin inhibitors halting the reaction.

### **5.2.7.1 Cell viability**

Cell viability was determined by adding 0.4% trypan blue solution in a 1/10 dilution with the cell suspension. Using phase-contrast light microscopy and a haemocytometer, cell viability and concentration was determined. Those cells that were clear and unstained were counted as alive and those that were stained blue were considered dead. The remainder of the cell suspension was centrifuged (2,000 rpm for 5 minutes) to produce a pellet. The pellet was re-suspended in 1ml of DMEM+ after the supernatant was discarded using a 21-gauge needle and syringe. Approximately 3,000-4,000 cells were seeded per cm<sup>2</sup> of surface area with 0.1333ml of DMEM+ per cm<sup>2</sup> of surface area. DMEM+ was changed every 3-5 days until the cells reached 80-90% confluency and until passage 3 at which point they were used in the following *in vitro* experiments.

### **5.2.8 Characterisation of ovine MSCs using tri-lineage differentiation**

oMSCs were characterised by demonstrating their multipotency. This was carried out by differentiating them along the adipogenic, chondrogenic and osteogenic lineages as described in 4.2.9.

### **5.2.9 Culture of oMSCs on EHA, ESiHAlI and ESrHAlI coatings**

#### **5.2.9.1 Groups and timepoints**

Two control groups and 3 experimental groups were included in this study. Commercial grade plasma sprayed HA coated discs (Plasma Biotal, Hertfordshire, UK) and uncoated roughened discs were used as controls. The three experimental groups were:

- 1) EHA (10mA/cm<sup>2</sup>, 15 minute deposition time).
- 2) Optimised ESiHAlI coating chosen after 5.2.5 and 5.2.6 were completed.
- 3) Optimised ESrHAlI coating chosen after 5.2.5 and 5.2.6 were completed.

These 3 experimental groups were used to quantify and compare oMSC cell morphology, metabolic activity and osteogenic differentiation.

Discs were sterilised in an autoclave and placed into the wells of a well plate and seeded with 50,000 oMSCs in a volume of DMEM+ with osteogenic supplementation as described in chapter 4.2.9.1. Discs were incubated for 60 minutes under standard conditions (37°C and 5% CO<sub>2</sub>) after which a further 2mls of osteogenic DMEM+ was added to each well. The plates were kept in the incubator under the same conditions and the osteogenic DMEM+ was changed every 3-5 days. These methods are identical to those used in 4.2.10.1 apart from osteogenic growth media being used for this experiment.

The following parameters were quantified:

- 1) Cell metabolic activity as quantified using an AlamarBlue® and deoxyribonucleic acid (DNA) assay (3 repeats).
- 2) Osteogenic differentiation using an ALP assay (3 repeats).
- 3) Cell morphology was observed using SEM (3 repeats).

In each of the 5 groups investigated, results were quantified at 3, 7 and 14 days of culture with additional SEM analysis (3 repeats) at 28 days.

#### **5.2.9.2 AlamarBlue® activity assay**

Identical methods to those described in 4.2.10.2 were used.

#### **5.2.9.3 ALP assay**

Identical methods to those described in 4.2.10.3 were used.

#### **5.2.9.4 DNA assay**

Identical methods to those described in 4.2.10.4 were used.

### **5.2.10 SEM**

The same protocol described in 4.2.11 was used to prepare discs for SEM analysis.

### **5.2.11 Statistical analysis**

Identical statistical methods as described in 4.2.12 were employed to complete the statistical analysis for this chapter.

## 5.3 Results

### 5.3.1 Light microscopy

Macroscopic observation showed no difference in the ESiHAlI coating when the two deposition times (30 and 45 minutes) were compared. The ESiHAlI coating appeared less white in colour when compared to the ESiHA coating (Figure 5-1). Under higher magnification, an increased reflection of light was observed from ESiHAlI (Figure 5-2).

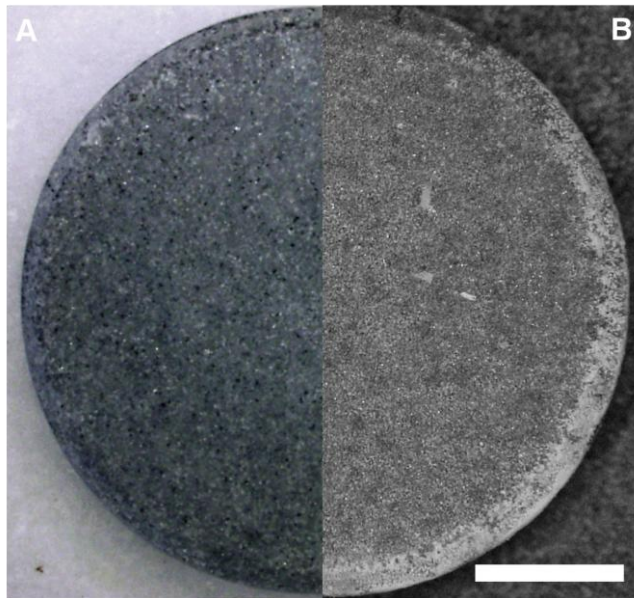


Figure 5-1  $\text{Ti}_6\text{Al}_4\text{V}$  discs with (A) ESiHAlI and (B) ESiHA coatings. Scale bar equivalent to 2.5mm.

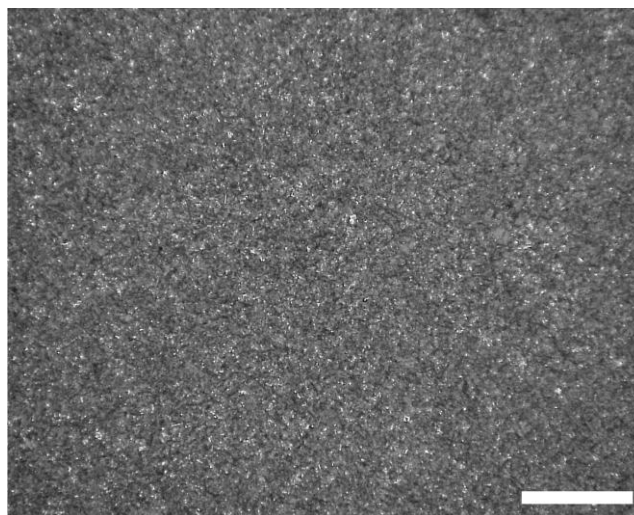
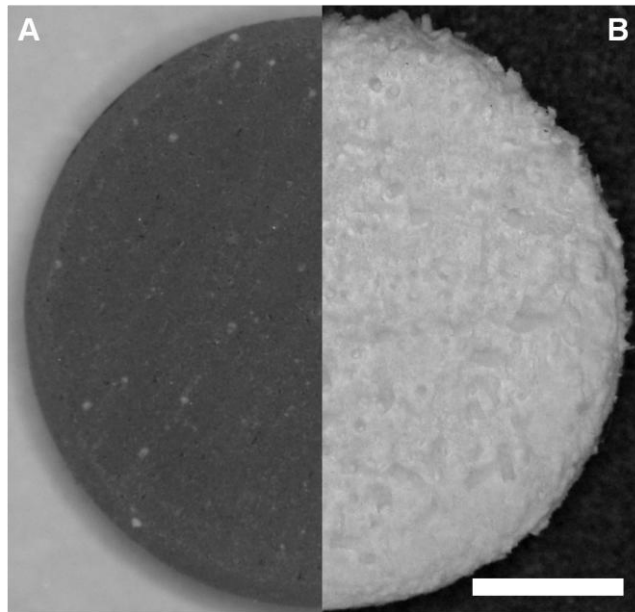


Figure 5-2  $\text{Ti}_6\text{Al}_4\text{V}$  disc surface following deposition of an ESiHAlI coating. Scale bar shown equivalent to 1mm.

Light microscopy revealed no obvious differences in coating topography when the two ESiHAlI coatings produced at 2.5 and 5 minute deposition times were

compared. Overall, reduced coating was observed in the ESrHAlI coated groups when compared to the ESrHA coating (Figure 5-3). The surface of the ESrHAlI coating appeared less undulating with no tubular formations seen under higher magnification (Figure 5-4). The small white specks seen on the surface could possibly be the beginnings of these cinder cones as described in Chapter 4.



**Figure 5-3** Ti<sub>6</sub>Al<sub>4</sub>V with (A) ESrHAlI and (B) ESrHA coatings. Scale bar equivalent to 2.5mm.

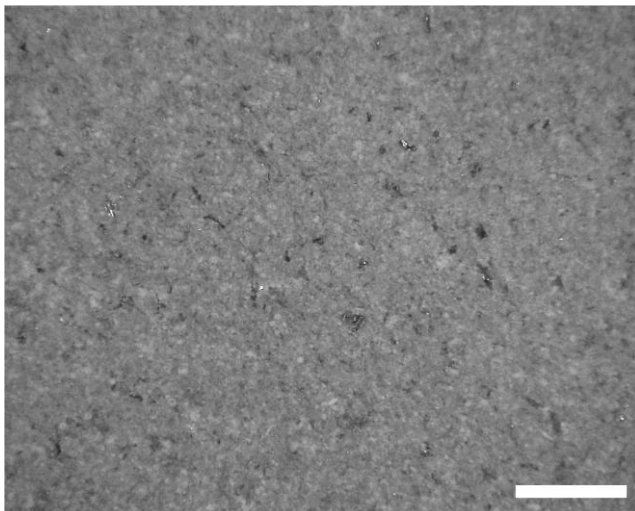


**Figure 5-4** Ti<sub>6</sub>Al<sub>4</sub>V disc surface following deposition of ESrHAlI coating. Scale bar shown equivalent to 1mm.

### 5.3.2 Surface morphology – Scanning Electron Microscopy (SEM)

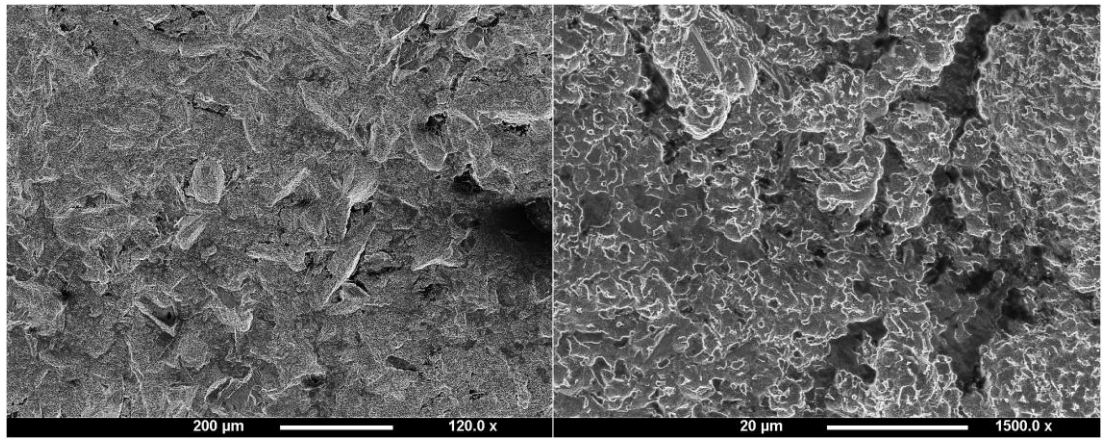


Figure 5-5 Surface morphology of control roughened acid etched Ti<sub>6</sub>Al<sub>4</sub>V disc, micro-pits on the surface can be seen. Magnification and scale bar as shown

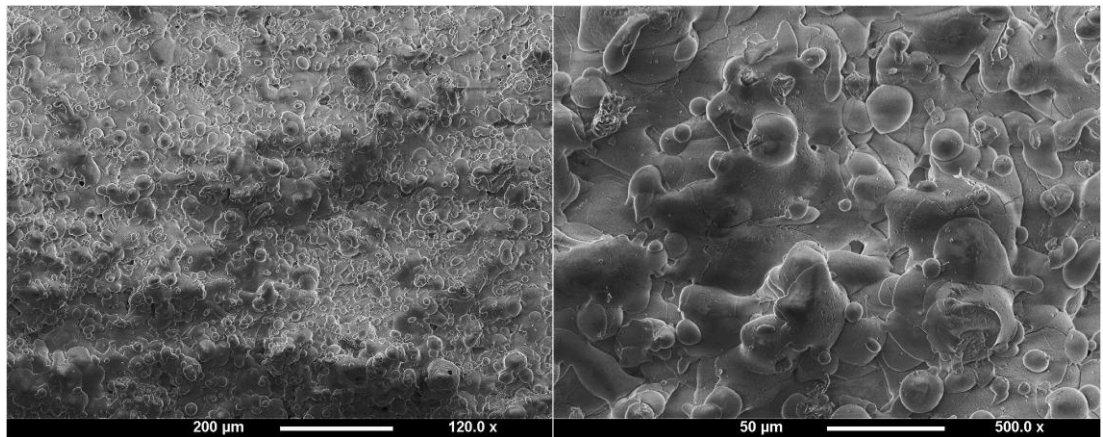


Figure 5-6 Surface morphology of plasma sprayed HA coated Ti<sub>6</sub>Al<sub>4</sub>V discs. Magnification and scale bar as shown.

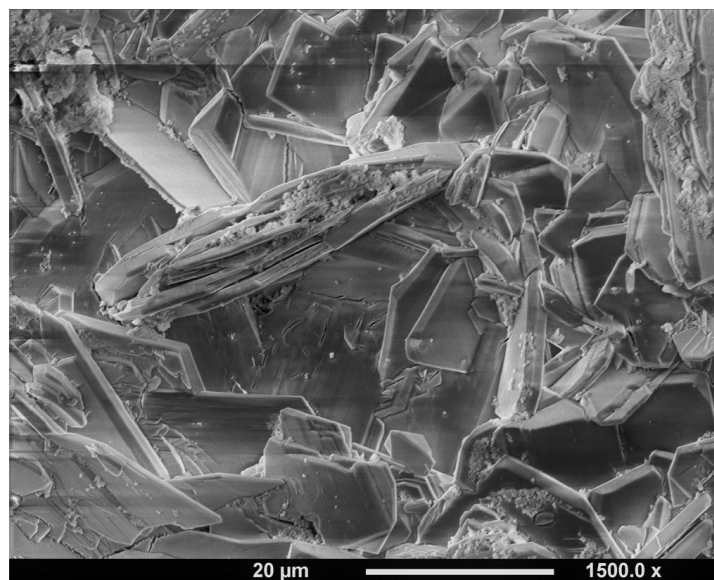


Figure 5-7 Surface morphology of EHA coated Ti<sub>6</sub>Al<sub>4</sub>V disc. Magnification and scale bar as shown.

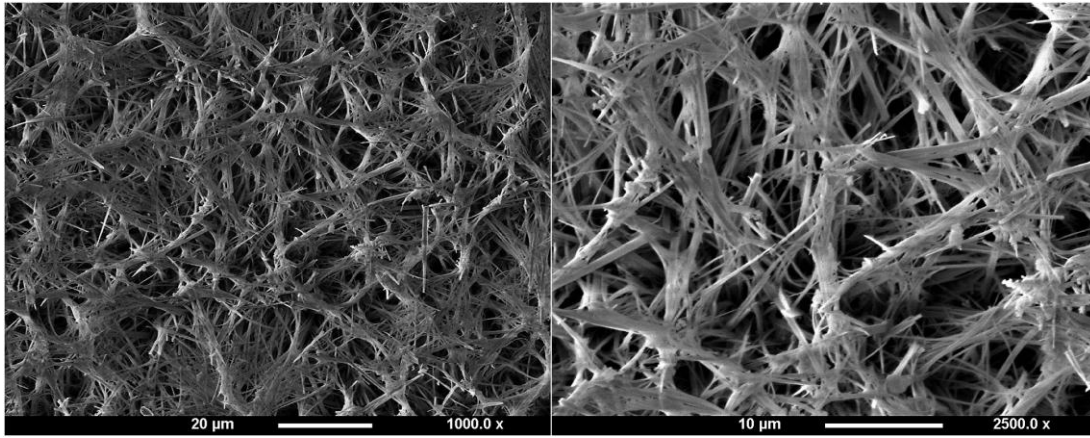


Figure 5-8 Surface morphology of ESiHALL coated  $Ti_6Al_4V$  disc. Magnification and scale bar as shown.

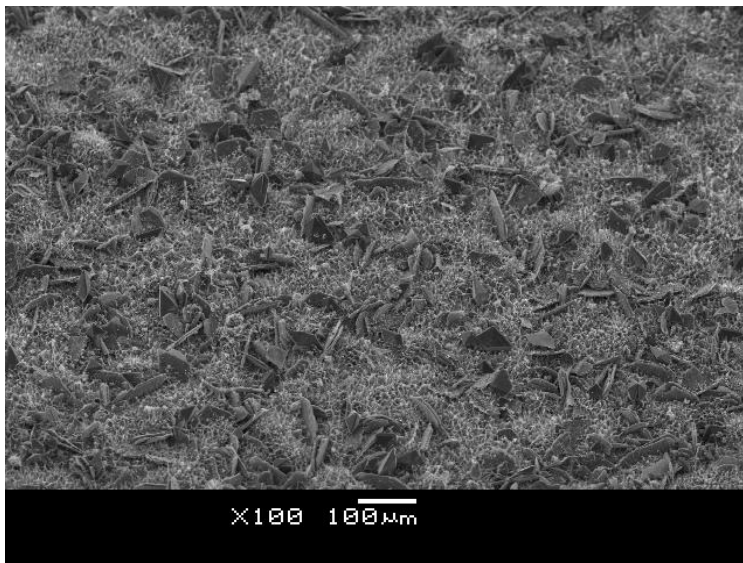


Figure 5-9 Low magnification of ESiHALL coating showing heterogeneous shaped crystals. Magnification and scale bar as shown.

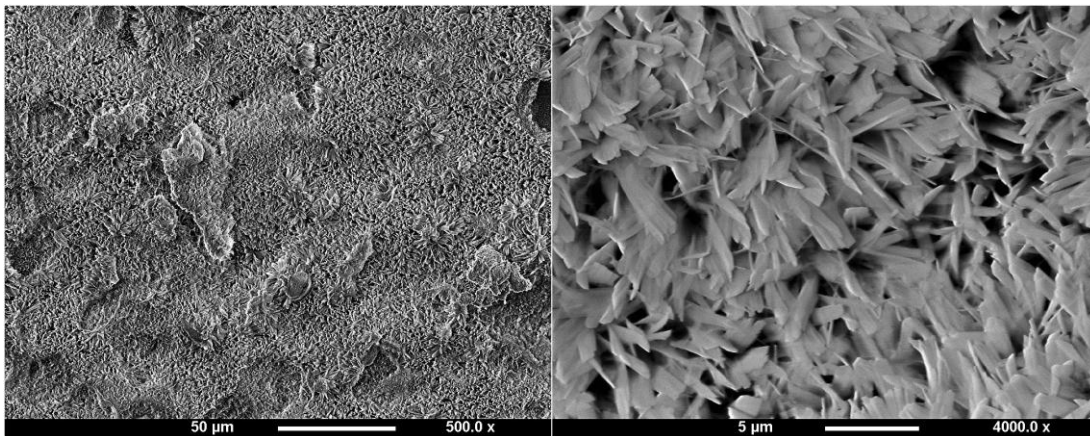


Figure 5-10 Surface morphology of ESrHALL coated  $Ti_6Al_4V$  disc. Magnification and scale bar as shown.

Uncoated acid etched  $Ti_6Al_4V$  (Figure 5-5) exhibited the same undulated rough surface as before (Figure 4-7) with the addition of micro-pits. The plasma spray HA surface showed a globular shaped crystalline structure that followed the

underlying rough surface (Figure 5-6). The repeated EHA coating was observed to be of an identical surface morphology to that produced in the previous chapter (Figure 4-8). The ESiHAlI coating evenly covered the surface with needle shaped crystals similar to that seen in Figure 4-9 however the needles tips group together which was not seen previously. Interspersed within the needle shaped crystals were large plate-like crystals identical to those found in the EHA coating. The morphology of the ESrHAlI coating was much more homogenous than what was seen previously with shorter and broader crystals covering the surface. The surface morphology for the ESiHAlI and ESrHAlI coatings did not change with the differing coating parameters investigated in this chapter.

### 5.3.3 Coating thickness

A significantly ( $p < 0.001$ ) thicker ESiHAlI coating was produced with increasing deposition times (Table Table 5-1, Figure 5-11) and therefore the  $0.8\text{mA/cm}^2$ -45 minute coating was chosen for further characterisation.

Coating	Current density ( $\text{mA/cm}^2$ )	Deposition time (minutes)	Thickness ( $\mu\text{m} \pm \text{SD}$ )
ESiHA II	0.8	30	$9.9 \pm 2.7$
	0.8	45	$19.2 \pm 5.7$
ESrHA II	7.5	2.5	$6.9 \pm 1.4$
	7.5	5	$14.8 \pm 2$
	15	2.5	$14.2 \pm 5.2$
	15	5	$55.6 \pm 21$

**Table 5-1 Summary of thicknesses of ESiHAlI and ESrHAlI coatings produced with varying parameters.**

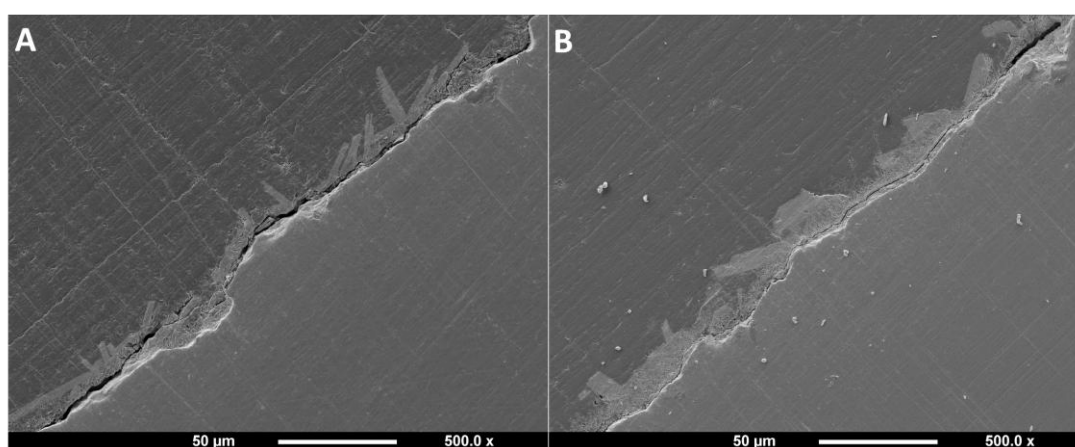


**Figure 5-11 SEM images of ESiHAlI coated disc cross sections in resin. (A)  $0.8\text{mA/cm}^2$  over 30 minutes, (B)  $0.8\text{mA/cm}^2$  over 45 minutes. Magnification and scale bar as shown.**

Current density and deposition time worked synergistically in producing thicker ESrHAlI coatings. At the lower current densities and shorter deposition times, this relationship seemed less linear. Only the 15mA/cm<sup>2</sup> over 5 minute ESrHAlI coating exhibited a significantly greater thickness when compared with the 7.5mA/cm<sup>2</sup> 2.5 minute (p<0.001), 7.5mA/cm<sup>2</sup> 5 minute (p=0.001) and the 15mA/cm<sup>2</sup> 2.5 minute (p=0.001) coatings (Figure 5-12, Figure 5-13). The thick coating was also found to contain loose bodies of coating within its structure.

Cross-sectional analysis of the 15mA/cm<sup>2</sup> 2.5 minute ESrHAlI coating exhibited an even coating with minimal gaps exposing the underlying disc surface (Figure 5-12) when compared to coatings produced using other parameters. This characteristic together with the reduced thickness and lack of loose coating material makes this the preferential ESrHAlI coating.

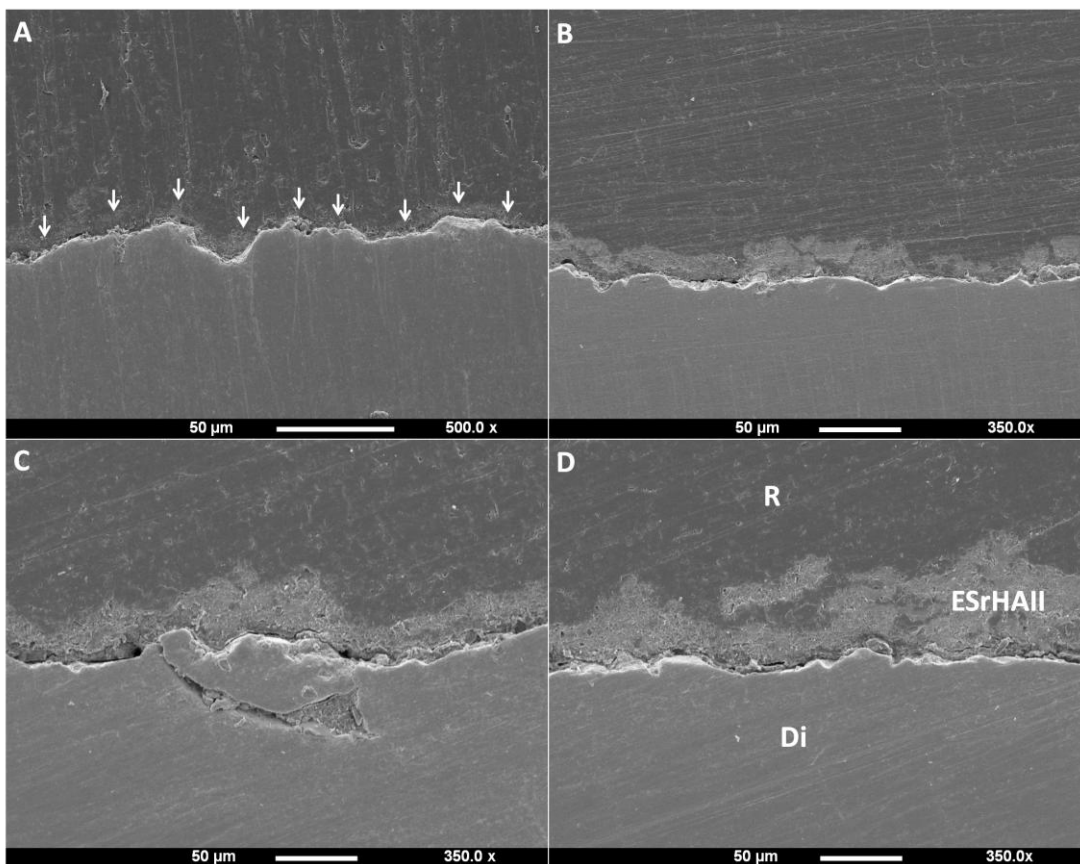
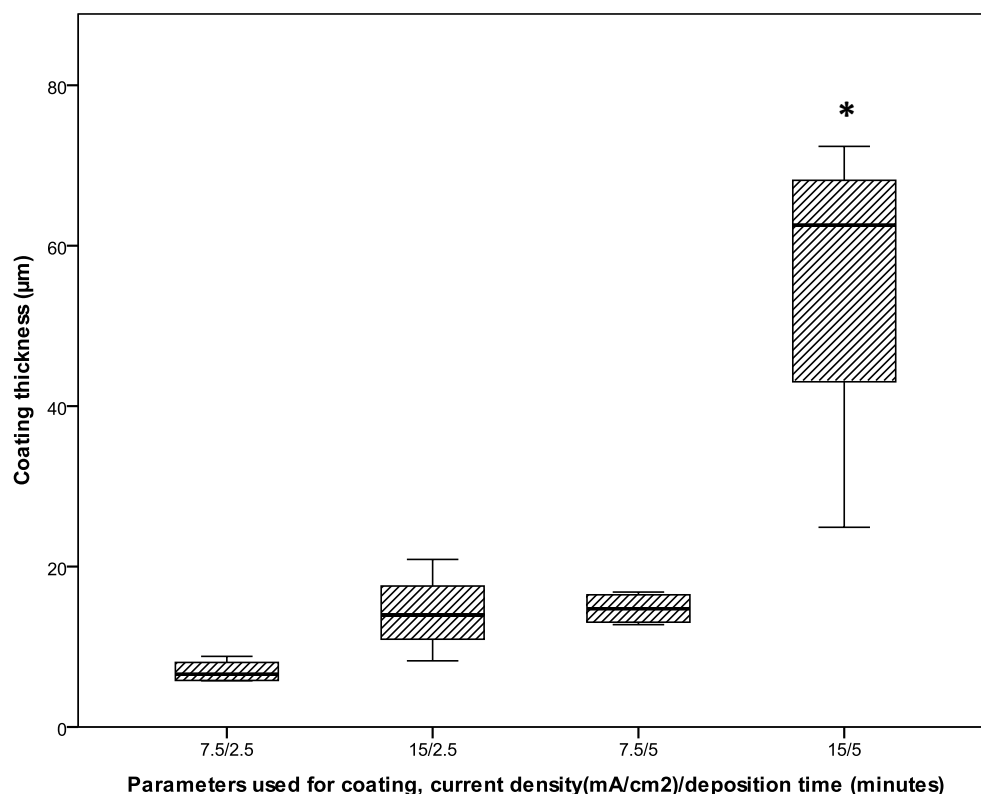


Figure 5-12 SEM images of ESrHAlI coated disc (Di) cross sections in resin (R). (A) 7.5mA/cm<sup>2</sup> over 2.5 minutes, (B) 7.5mA/cm<sup>2</sup> over 5 minutes, (C) 15mA/cm<sup>2</sup> over 2.5 minutes and (D) 15mA/cm<sup>2</sup> over 5 minutes. Magnification and scale bars as shown. White arrows identify coating.



**Figure 5-13** Boxplot of thickness of ESrHAlI coating ( $\mu\text{m}$ ) produced by different current densities ( $\text{mA}/\text{cm}^2$ ) over varying deposition times (minutes). \* $p < 0.001$

### 5.3.4 EDS

Table Table 5-2 summarises EDS results with Figure 5-14 and Figure 5-15 showing relevant spectra. Phase II coatings had lower Ca:P ratios compared with stoichiometric HA (1.67). An increase in Si wt% was achieved with the ESiHAlI coating. A lower Sr wt% was observed with the reduced deposition time used to produce ESrHAlI.

Coating	ESiHA	ESiHAlI	ESrHA	ESrHAlI
Ratio	1.36±0.07	1.13±0.07	1.65±0.15	1.31±0.03
wt% ( $\pm$ SD)	0.29±0.13	1.63±0.81	6.41±0.70	4.08±0.06
at% ( $\pm$ SD)	0.23±0.10	1.26±0.63	1.68±0.22	1.01±0.06

**Table 5-2** EDS results for both phase I and phase II coatings. Ratios are presented as Ca:(P+Si) and (Ca+Sr):P for the appropriate coatings.

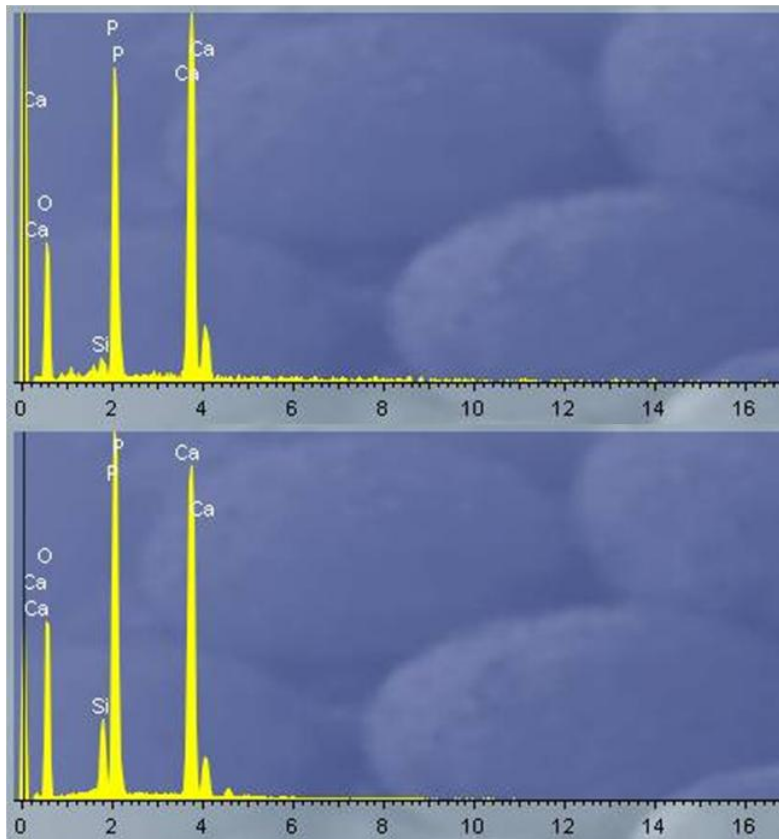


Figure 5-14 EDS spectra of ESiHA (top) and ESiHAII (bottom). Ca, calcium; O, oxygen; P, phosphorous; Si, silicon. x-axis = Energy (keV)

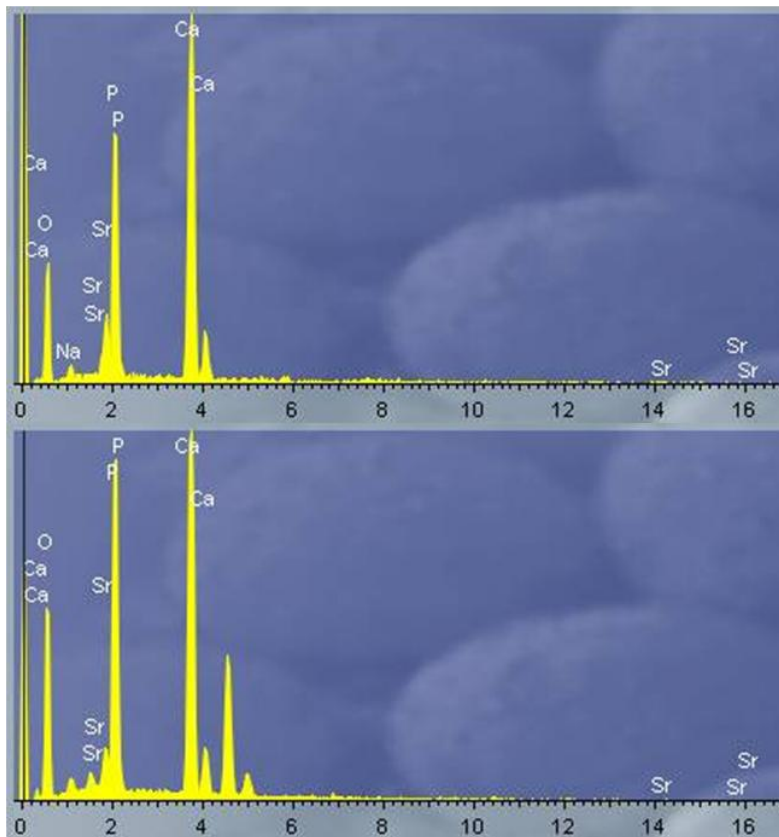
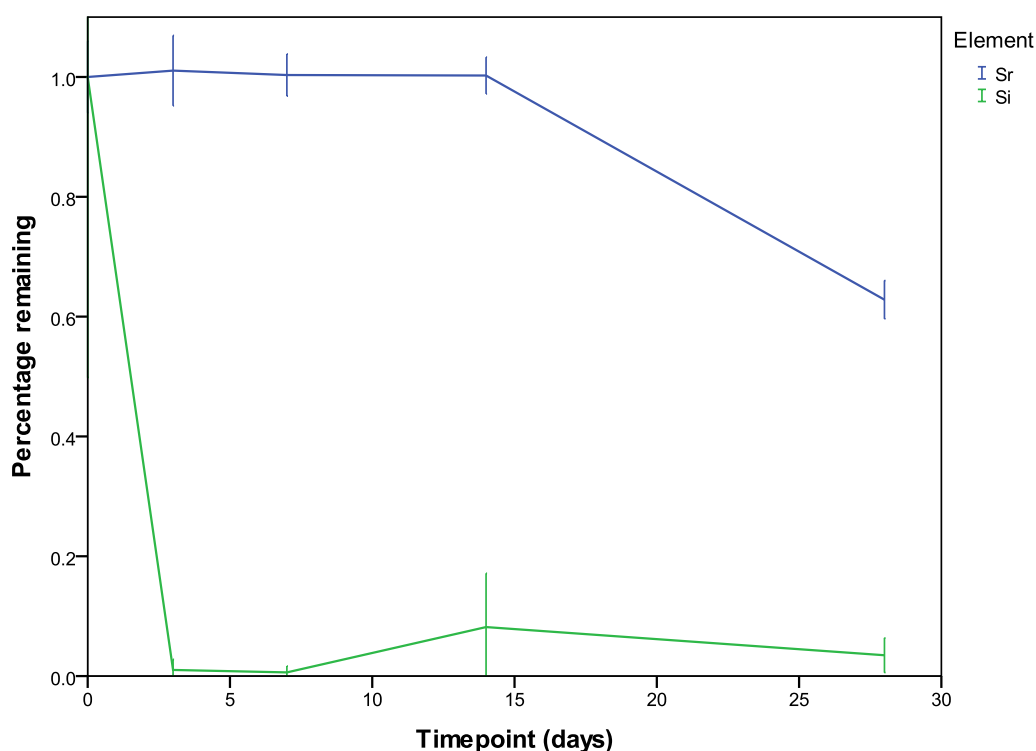


Figure 5-15 EDS spectra of ESrHA (top) and ESrHAII (bottom). Ca, calcium; O, oxygen; P, phosphorous; Sr, strontium. x-axis = Energy (keV)

Elemental analysis of the coating at each time-point revealed a change in Si and Sr content. A significant amount of Si within the ESiHAl coating was lost in the first 3 days of being in media ( $p=0.002$ ). Only  $3.5\pm 3\%$  of the original Si content was present at 28 days post culture. In comparison  $62.8\pm 3.2\%$  of the original Sr content remained in the ESrHAl coating at 28 days with no statistical difference in Sr content observed over the timepoints investigated. This suggests that the dissolution of Si into media is far greater than that of Sr which leaches at a slower rate.



**Figure 5-16** Proportion of element remaining in the coating at each timepoint as determined using EDS analysis. Error bars denote 95% confidence intervals.

### 5.3.5 Crystallinity

None of the new coatings demonstrated the same level of crystallinity as plasma sprayed HA (>85%). ESiHAl and ESrHAl also exhibited a crystalline structure with some amorphous phases. Figure 5-17 shows the XRD spectra for all coatings developed. All exhibited HA peaks apart from the uncoated discs as expected. Si peaks were also found in ESiHA and ESiHAl coatings albeit in different places. Sr peaks were found in both the ESrHA and ESrHAl coatings. The Sr was incorporated into a less crystalline structure in the ESrHAl coatings as exhibited by the reduced peak. This peak was however evident in the

identical position as the ESrHA coating suggesting consistency in the compound incorporating Sr.

Varying peaks of the underlying  $Ti_6Al_4V$  disc was found for all the spectra. The highest peaks found in the uncoated discs with the lowest peaks found in the ESrHA coating.

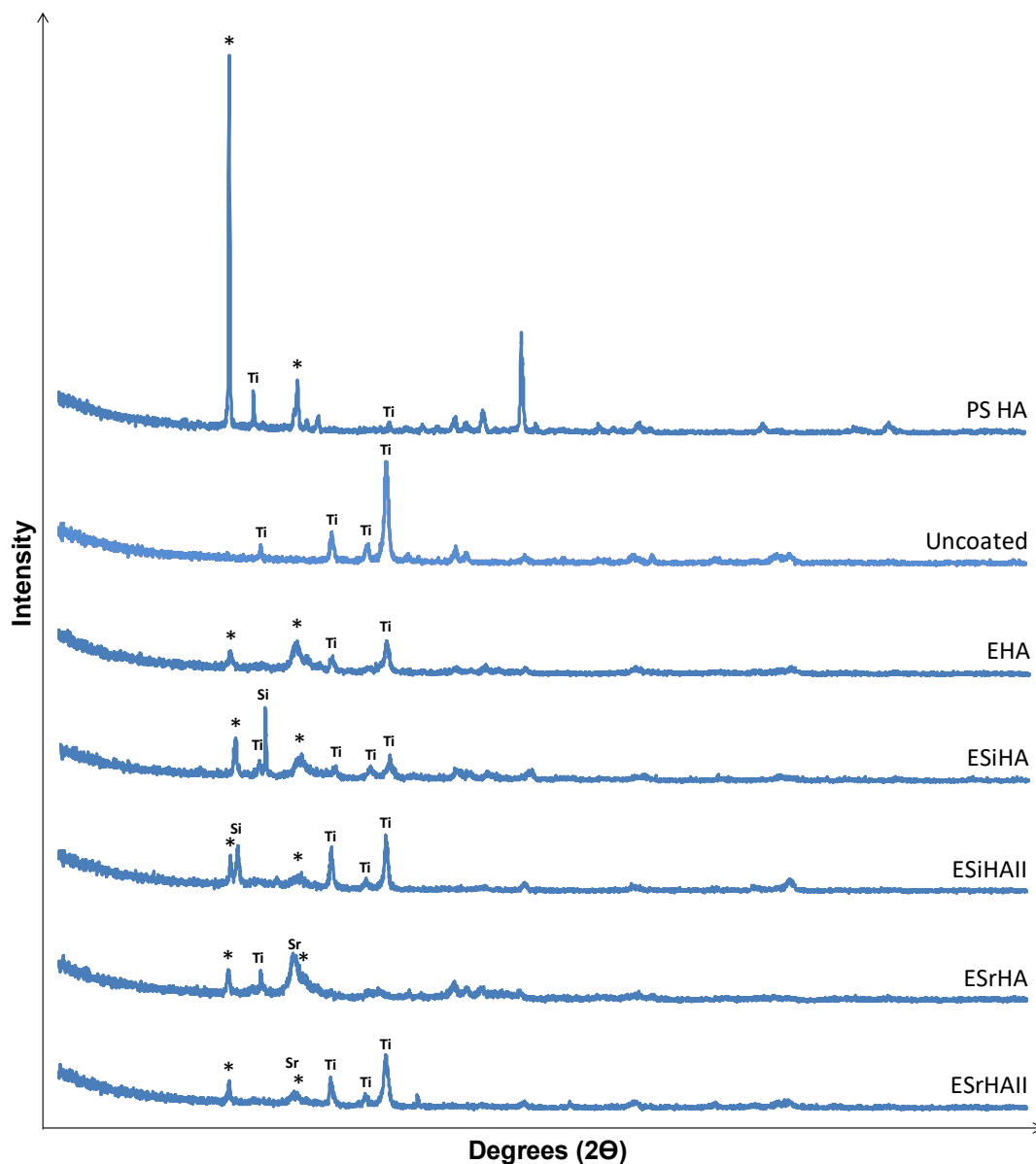


Figure 5-17 XRD spectra of all coatings as labelled. \* denotes HA peaks with Si and Sr referring to the silicon or strontium present within the coating.

### 5.3.6 Profilometry

Table 5-3 summarises the Ra values for each group investigated in this chapter. There was a significant difference ( $p < 0.001$ ) in the Ra between the coatings with Table 5-4 summarising pair wise comparisons. EC coatings exhibited

significantly higher Ra values when compared to controls with the ESiHA coating showing the greatest surface roughness.

Coating	Ra ( $\pm$ SD)
Uncoated	2619.65 $\pm$ 460.54
PS HA	3123.53 $\pm$ 232.23
ESrHAII	3881.97 $\pm$ 76.37
EHA	4192.41 $\pm$ 405.66
ESiHAII	4387.80 $\pm$ 303.98

Table 5-3 Summary of Ra (nm) values for each coating in ascending order

Coating	Uncoated	PS HA	EHA	ESiHAII	ESrHAII
Uncoated	-	0.870	<i>0.001</i>	<i>0.001</i>	<i>0.008</i>
PS HA	-	-	<i>0.024</i>	<i>0.008</i>	0.171
EHA	-	-	-	1	1
ESiHAII	-	-	-	-	0.859

Table 5-4 p-values for pair wise comparisons using ANOVA with bonferroni correction for Ra values of coatings. p<0.05 is considered to be significant and are identified in italics.

Figure 5-18 compares the Ra values of each of the coatings in ascending order of roughness.

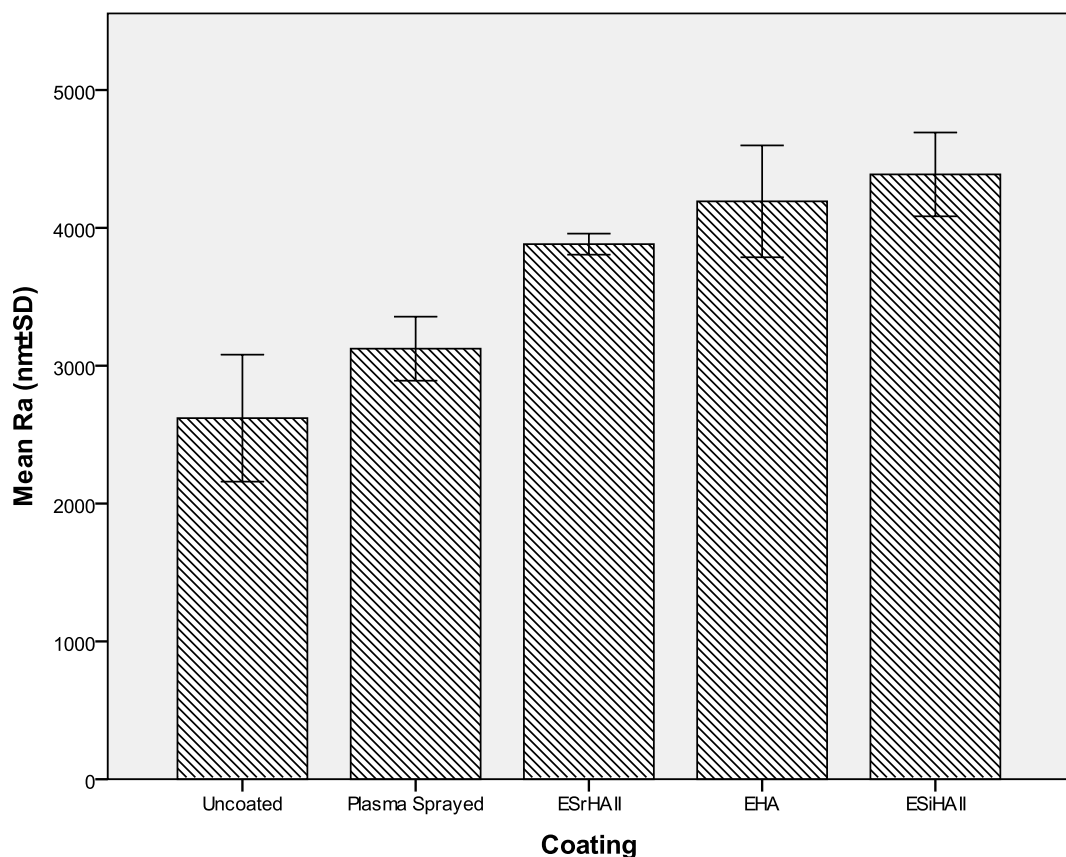


Figure 5-18 Ra for each of the coatings in ascending order.

Figure 5-19, Figure 5-20, Figure 5-21, Figure 5-22 and Figure 5-23 are 3D representations of the surface topography for each of the coatings.

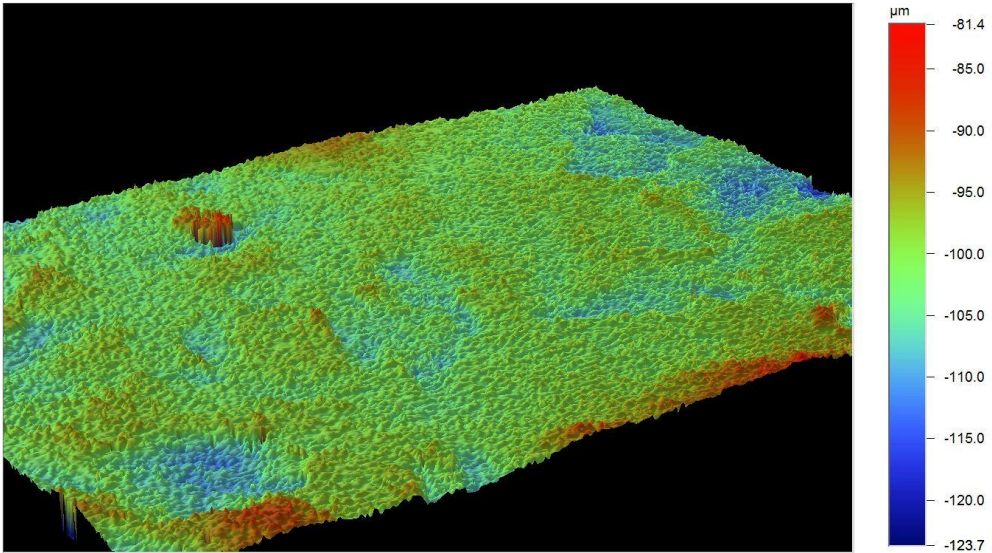


Figure 5-19 3D profile of uncoated disc surface. Scale bar with relative height shown on right.

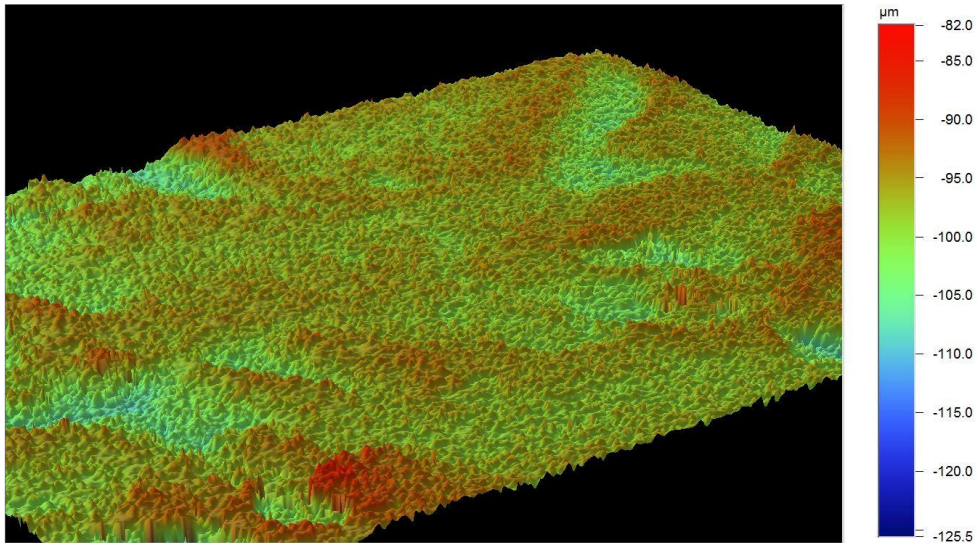


Figure 5-20 3D profile of PS HA disc surface. Scale bar with relative height shown on right.

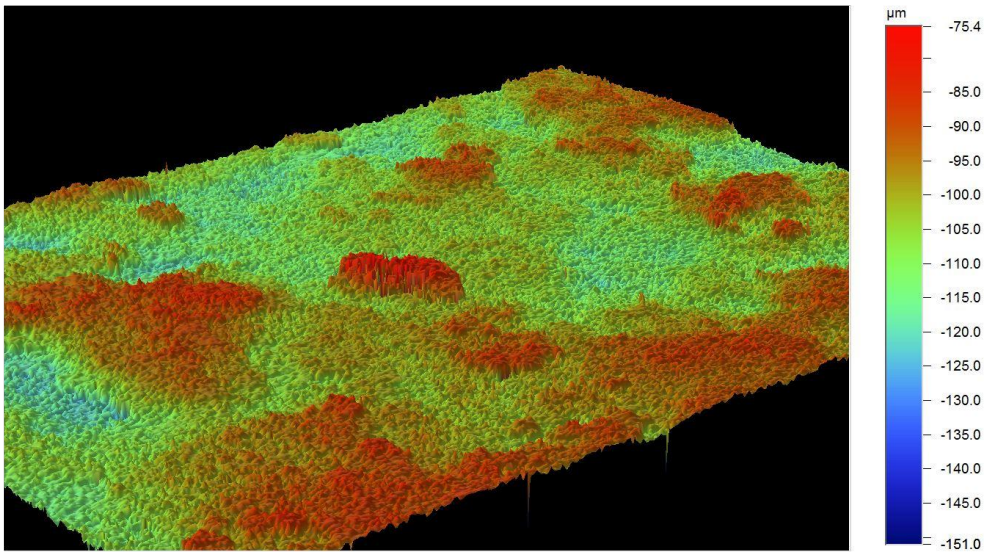


Figure 5-21 3D profile of ESrHA disc surface. Scale bar with relative height shown on right.

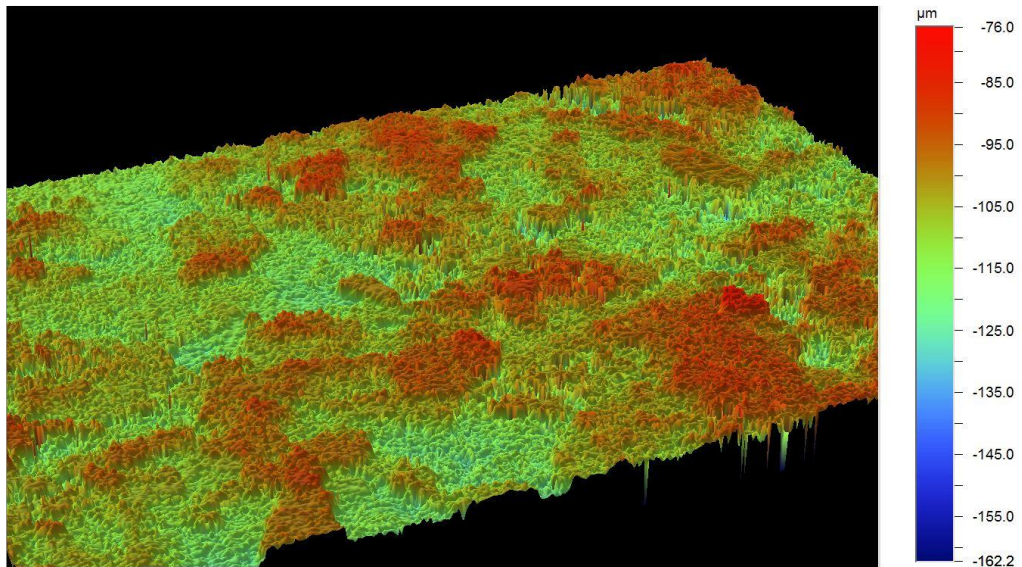


Figure 5-22 3D profile of EHA disc surface. Scale bar with relative height shown on right.

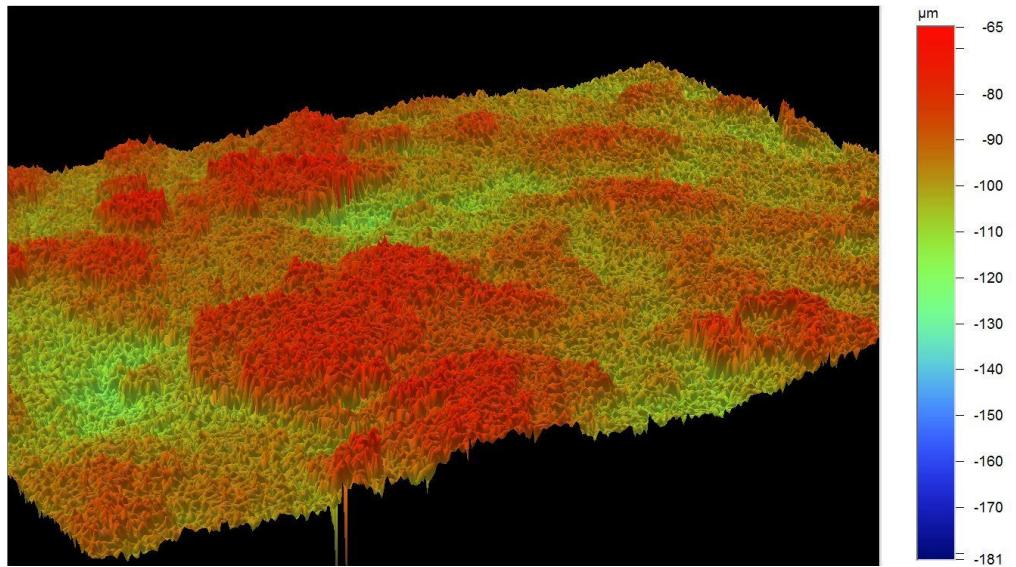
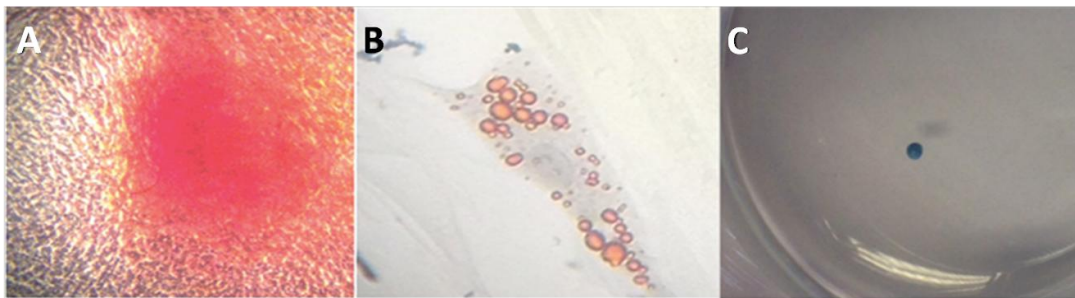


Figure 5-23 3D profile of ESiHAlI disc surface. Scale bar with relative height shown on right.

### 5.3.7 Characterisation of ovine MSCs

Following osteogenic differentiation of isolated ovine MSCs, results showed that calcium deposits stained with Alizarin Red confirmed the presence of osteoblasts. Oil Red O stained the intracellular lipid content of differentiated adipocytes. These cells were observed to be shorter in length and less spindle shaped when compared with sheep MSCs. Isolated pellets of differentiated chondrocytes stained blue with Alcian Blue confirming that stem cells had successfully undergone chondrogenic differentiation.



**Figure 5-24 (A) Red stained calcium deposits from osteoblasts with Alizarin Red stain. (B) Red stained lipid within adipocytes with Oil Red O stain. (C) Blue pellet confirming presence of chondrocytes with Alcian Blue stain.**

### 5.3.8 Culture of ovine MSCs on EHA, ESiHAlI and ESrHAlI coatings

#### 5.3.8.1 Cell proliferation: AlamarBlue® assay

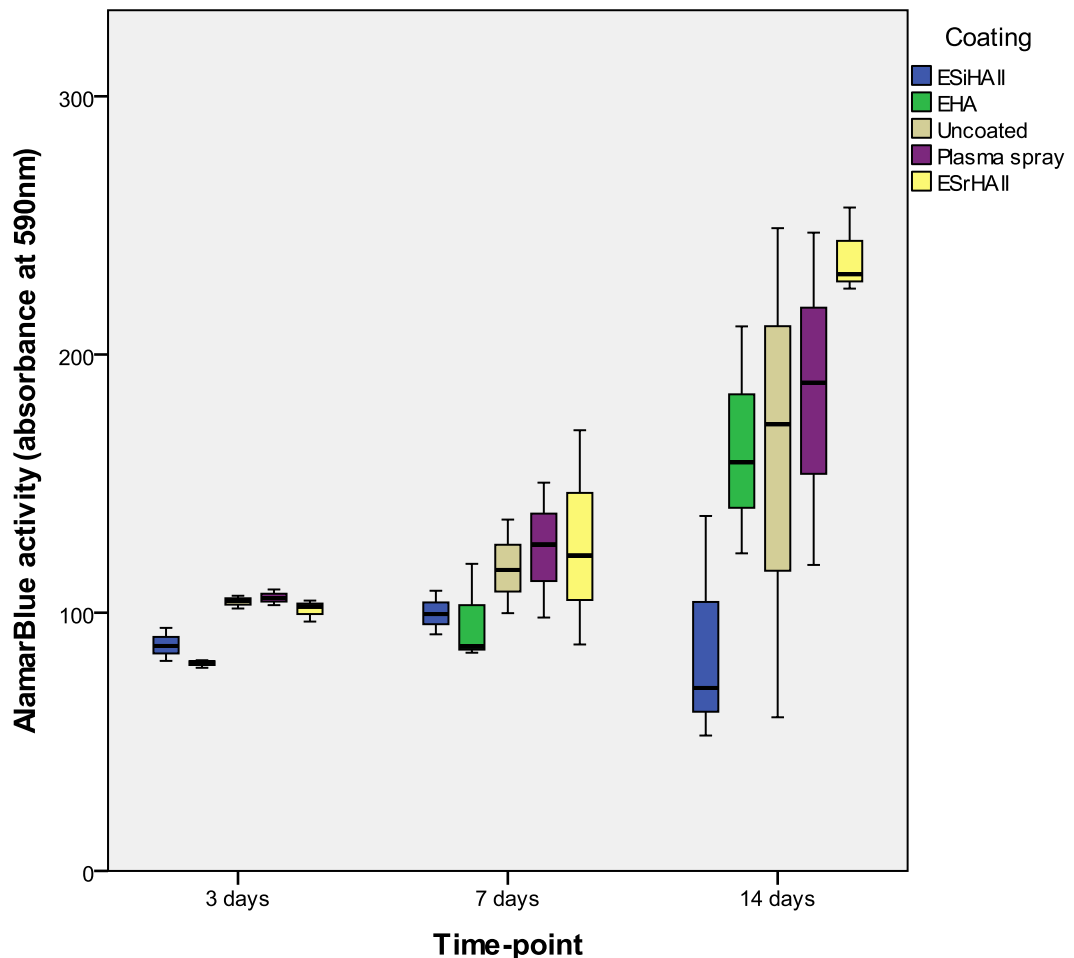


Figure 5-25 AlamarBlue® assay for each coating at 3, 7 and 14 days.

A significant ( $p < 0.001$ ) difference in cell metabolic activity was observed at day 3 between the coatings. No statistical difference in activity was found between the ESrHAlI and controls coatings. Significantly lower activity occurred on the EHA and ESiHAlI coatings compared the uncoated, plasma spray HA and ESrHAlI groups (Table 5-5, Table 5-6).

At day 7, similar patterns of metabolic activity were seen between the coatings with the uncoated, plasma spray HA and ESrHAlI coatings exhibiting higher levels than the EHA and ESiHAlI coatings. This did not translate into a statistical difference.

At day 14, a drop in the metabolic activity was observed for the ESiHAlI coating compared to the activity seen at previous timepoints. The lower metabolic

activity of ESiHAlI was also apparent when compared to the other coatings at the same timepoint. Activity on ESrHAlI increased to beyond the levels seen in the control groups. No statistical difference was found between the coatings at this timepoint.

Multiple comparisons of the coatings across time-points reveal a significant difference in cell proliferation on EHA between days 3 and 14 ( $p=0.031$ ). The metabolic activity seen on the ESrHAlI coating at day 14 was significantly higher than both day 3 ( $p=0.002$ ) and day 7 ( $p=0.006$ ). There is therefore a statistically significant increase in activity occurring on the EHA and ESrHAlI coatings over the length of the experiment.

Time-point (days)	Coating	AlamarBlue® assay ( $\pm$ SD)
3	Uncoated	104.3 $\pm$ 2.5
	Plasma sprayed	105.9 $\pm$ 3.0
	EHA	80.4 $\pm$ 1.5
	ESiHAlI	87.5 $\pm$ 6.4
	ESrHAlI	101.2 $\pm$ 4.2
7	Uncoated	117.5 $\pm$ 18.1
	Plasma sprayed	125 $\pm$ 26.1
	EHA	96.8 $\pm$ 19.2
	ESiHAlI	99.9 $\pm$ 8.4
	ESrHAlI	126.8 $\pm$ 41.7
14	Uncoated	160.5 $\pm$ 95.3
	Plasma sprayed	184.9 $\pm$ 64.5
	EHA	164.1 $\pm$ 44.2
	ESiHAlI	86.9 $\pm$ 44.7
	ESrHAlI	237.9 $\pm$ 16.8

**Table 5-5 Summary of AlamarBlue® assay results for all coatings at all timepoints.**

Day 3	Uncoated	PS	EHA	ESiHAlI	ESrHAlI
Uncoated	-	1	<i>&lt;0.001</i>	<i>0.004</i>	1
PS	-	-	<i>&lt;0.001</i>	<i>0.002</i>	1
EHA	-	-	-	0.486	<i>0.001</i>
ESiHAlI	-	-	-	-	<i>0.016</i>

**Table 5-6 p-values for pair-wise comparisons of normalised AlamarBlue® assay results of varying coatings at day 3.  $p<0.05$  is considered to be significant and are identified in italics.**

### 5.3.8.2 Osteogenic differentiation: ALP assay

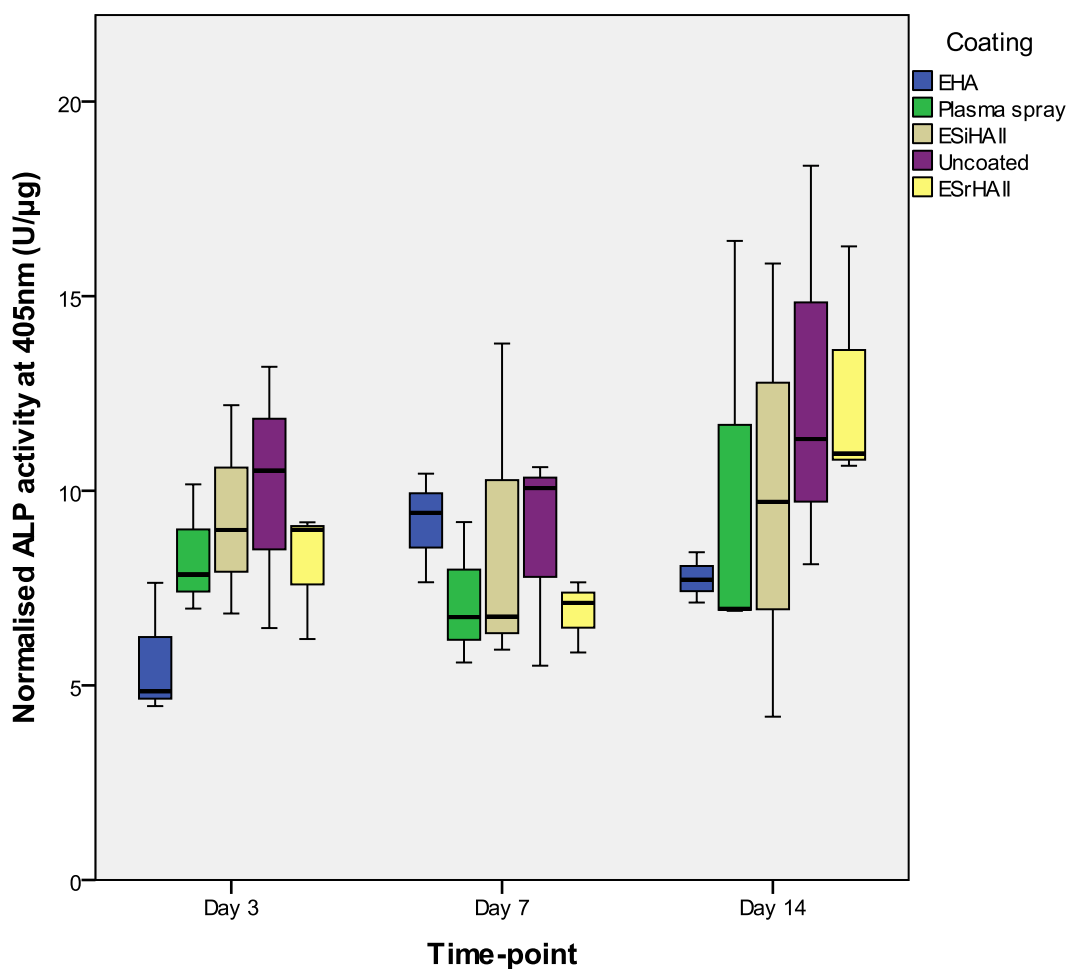


Figure 5-26 ALP assay for each coating at 3, 7 and 14 days.

Timepoint (days)	Coating	Normalised ALP assay (U/µg)
3	Uncoated	10.1±3.4
	Plasma sprayed	8.3±1.6
	EHA	5.7±1.7
	ESiHAII	9.3±2.7
	ESrHAII	8.1±1.7
7	Uncoated	8.7±2.8
	Plasma sprayed	7.2±1.8
	EHA	9.2±1.4
	ESiHAII	8.8±4.3
	ESrHAII	6.9±0.9
14	Uncoated	12.6±5.2
	Plasma sprayed	10.1±5.4
	EHA	7.8±0.6
	ESiHAII	9.9±5.8
	ESrHAII	12.6±3.1

Table 5-7 Summary of ALP assay results (mean±SD) for all coatings at all timepoints.

Sheep MSCs cultured on each of the coatings exhibited osteogenic differentiation at each time point. No significant differences were found between the coatings at each of the time-points investigated.

Significant differences were observed in ALP levels between the time-points for EHA ( $p=0.048$ ) and ESrHA ( $p=0.037$ ). A significant rise was seen between days 3 and 7 for EHA and days 7 and 14 for ESrHA. Figure 5-26 and Table 5-7 summarises the results of the ALP assays for the coatings across the timepoints.

### **5.3.8.3 SEM analysis of cells on disc surfaces**

Cells were observed on the surface of all coatings and at all time points investigated (Figure 5-27, Figure 5-28)

In the uncoated control group, cell number was seen to increase over time. As before the cells occupied the troughs present on the disc surface as well as the peaks. By day 28, granules and larger crystals were observed emerging from the cellular material (Figure 5-29).

A high number of cells were observed on the plasma sprayed HA surface with a confluent monolayer of cells found as early as day 3. With advancing time-points a greater amount of granules were accompanying the cells. By day 28, these granules were not only on the cell surface but also found on the plasma sprayed surface itself.

The lowest numbers of cells were seen on the EHA coating at day 3 compared to the others which continued into day 7 of culture. At day 14 a substantial increase in cells were observed with some discs exhibiting a confluent layer of cells. At day 28 clusters of crystals were observed emerging from the cells instead of the granules and single crystals seen in the uncoated and plasma spray groups. The plate like crystals of HA had not changed structurally under SEM observation during the 28 day culture period.

At day 3 of culture, cells were seen to be more globular in nature on the ESiHAII coating. There seemed to be no preference to where they were located as they lay both on the needle and the plate like crystals. By day 7 cells were found to bridge across and attach to both types of crystals (Figure 5-30). By day 28, cells were still found but the crystal clusters observed on the EHA coatings and the granules seen on the control coatings were not present. As with EHA the

ESiHAlI coating maintained its structure as it was at day 0 throughout the experiment.

Large numbers of cells were present on the ESrHAlI coating throughout all time-points. Crystal clusters were apparent on this coating from day 3 onwards, the earliest of any of the coatings. Cells formed confluent layers at a very early stage which continued into day 28 of culture. The frequency and size of the crystal clusters emerging from the cell layer increased with longer culture times. The ESrHAlI coating also maintained its crystal structure through all timepoints with no apparent change identified.

Filopodial interaction with the coating surface was observed with the EHA, ESiHAlI and ESrHAlI coatings. None was seen with the control groups (Figure 5-30).

EDS analysis of the single and clusters of crystals observed on the coatings showed identical elemental composition with calcium, oxygen and phosphorous identified as being the main elements present.

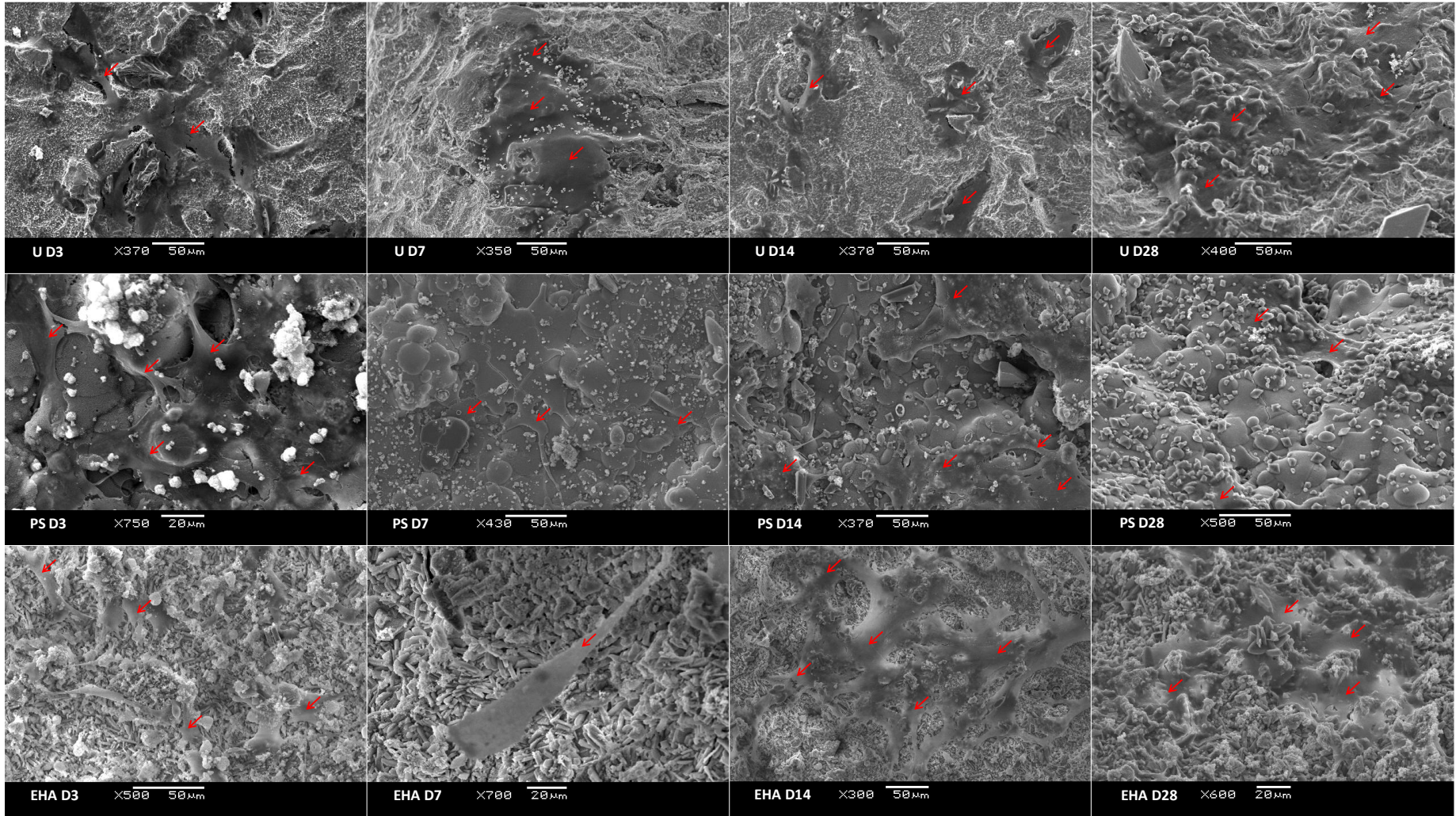


Figure 5-27 Scanning electron micrographs of coating surfaces at different timepoints (days 3 (D3), 7 (D7), 14 (D14) and 28 (D28)). U, Uncoated; PS, Plasma spray; EHA, EC HA. Red arrows identify cells. Scale bar and magnification as shown.

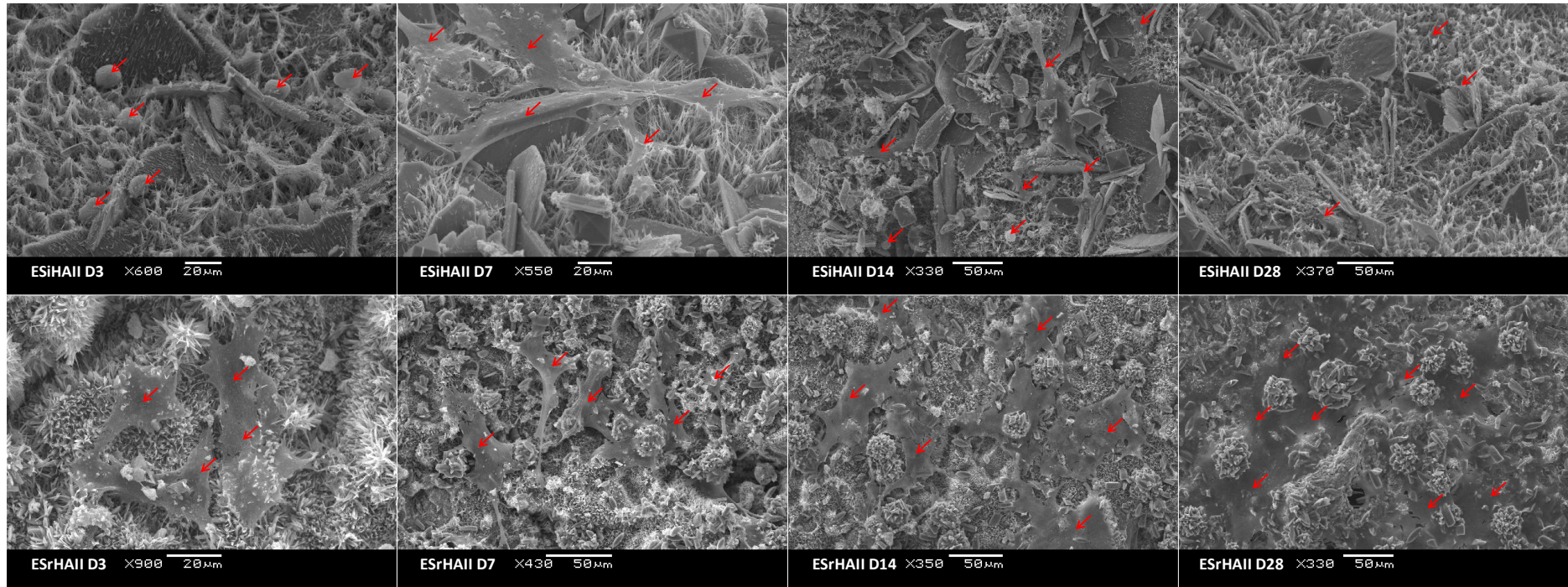


Figure 5-28 Scanning electron micrographs of coating surfaces at different timepoints (days 3 (D3), 7 (D7), 14 (D14) and 28 (D28)). ESiHAlI, EC silicate substituted HA; ESrHAlI, EC strontium substituted HA. Red arrows identify cells. Scale bar and magnification as shown.

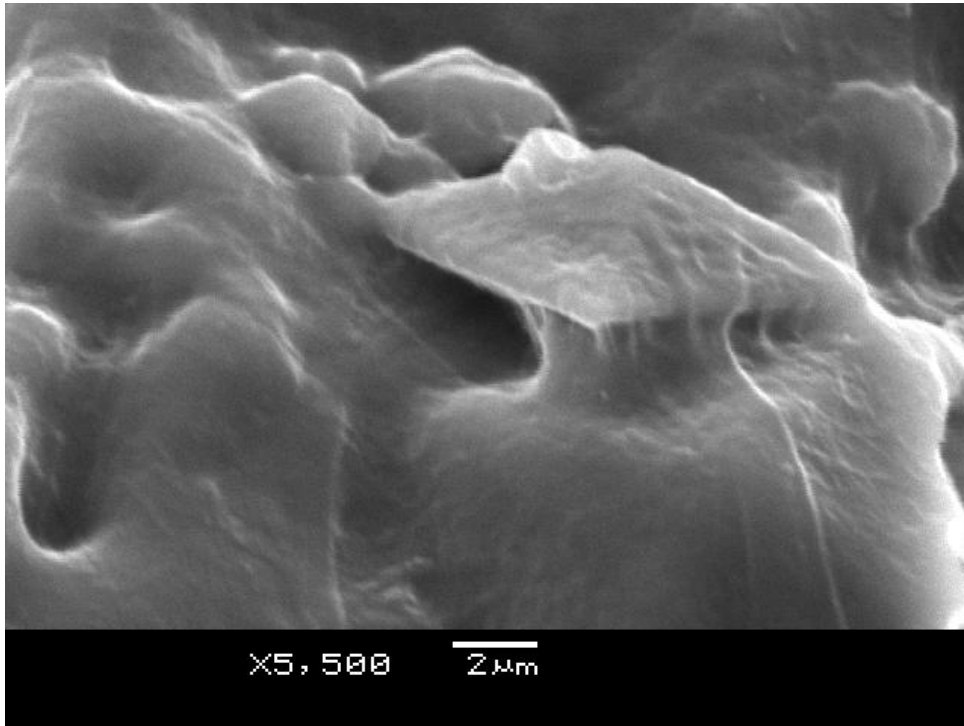


Figure 5-29 Crystal emerging from cell on uncoated disc. Magnification and scale bar as shown.

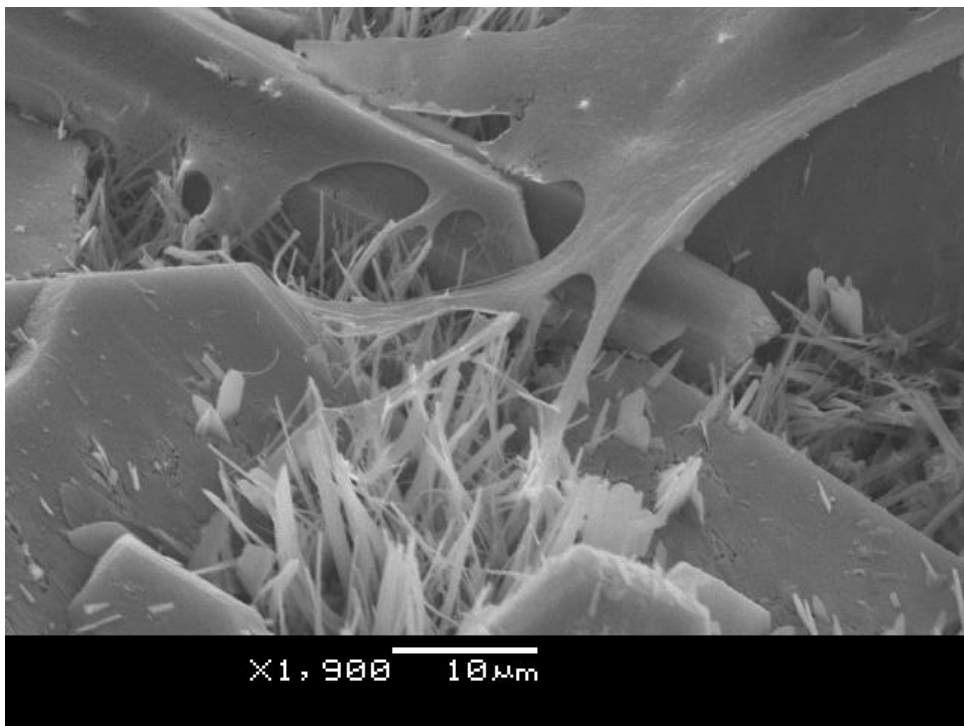


Figure 5-30 Filopodial and nanopodial interaction of cells to both large plate like crystals and needle shaped crystals on ESIHAlI coating. Magnification and scale bar as shown.

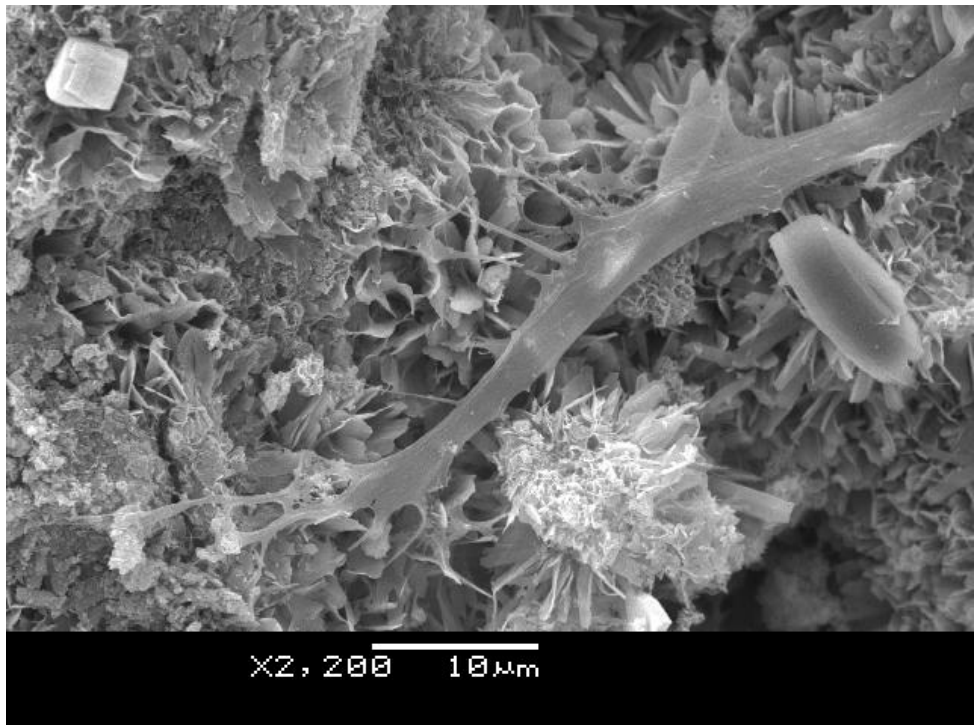


Figure 5-31 Attachment of cell to ESrHAlI crystals. Magnification and scale bar as shown.

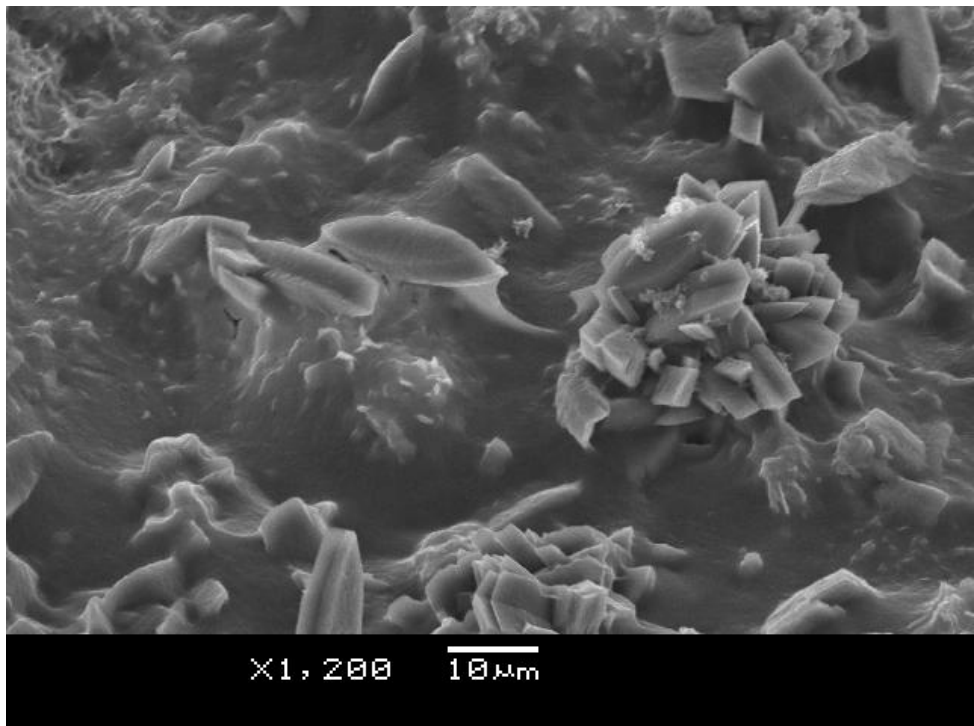


Figure 5-32 Single crystals and crystal clusters emerging from cells on ESrHAlI coating. Magnification and scale bar as shown.

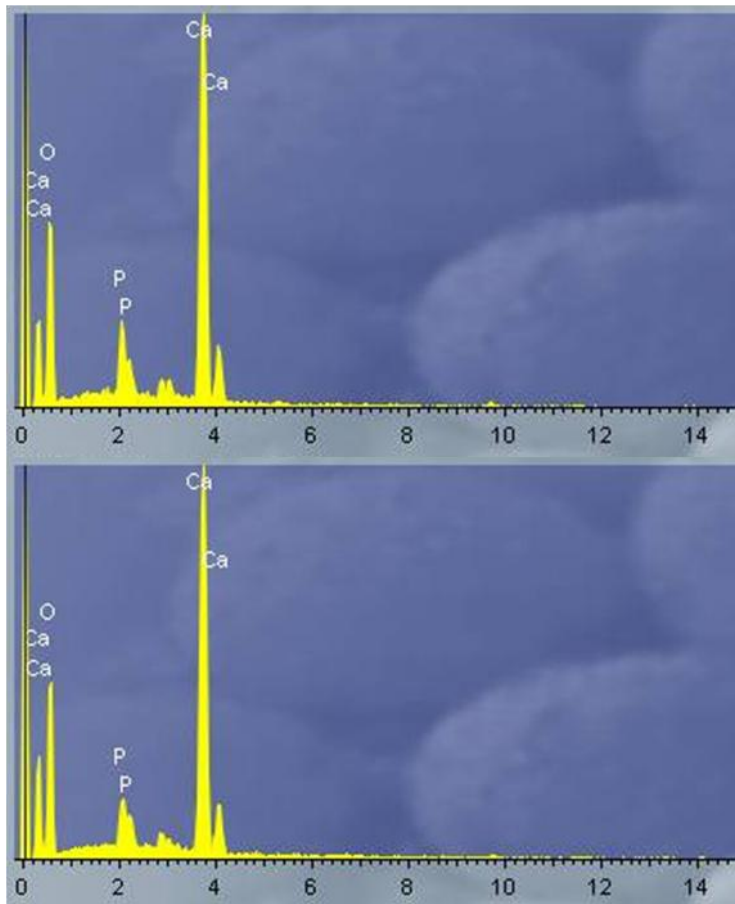


Figure 5-33 Identical EDS spectra of single crystals (top) and crystal clusters (bottom) observed on coatings. Ca, calcium; O, oxygen; P, phosphorous. x-axis = Energy (keV).

## 5.4 Discussion

The physical characteristics, chemical composition and to some extent bioactivity of the new EC coatings developed in this chapter was different to that seen in the previous chapter.

With a Ra of 2620nm, the uncoated surface was the smoothest of all the groups and thus allowed for high levels of proliferation (Washburn et al., 2004) reflected by the significantly higher AlamarBlue® activity when compared with EHA and ESiHAlI at day 3. Greater variability was seen at days 7 and 14. Wide variability at day 14 was possibly due to some samples having a decrease in cell numbers corresponding to cell death due to confluence. SEM analysis did not reveal high numbers of non-viable cells but cell layers did appear confluent at day 28. Non-viable cells were those that exhibited shrinkage, blebbing and the formation of apoptotic bodies (Ziegler and Groscurth, 2004) that can be identified using SEM. Osteogenic differentiation did occur at all time-points and remained fairly constant albeit with a possible upward trend. Proliferation tends to slow down when cells are differentiating, however wide variability amongst the results may reflect that some of the cells are expressing ALP whereas others are not and still undergoing high rates of proliferation in keeping with the variability seen with AlamarBlue®. Interestingly ALP expression is thought to be an early marker of osteogenesis and peaks at 20 days during the matrix maturation phase (Stein et al., 1996) of the osteoblast developmental sequence.

The EHA coating was produced in an identical way as described in Chapter 4. It was included in this chapter to delineate whether it had osseoconductive characteristics and compare its activity to the substituted HA coatings.

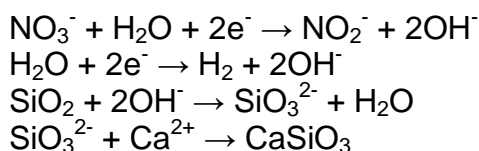
EHA performed poorly with regards to cell proliferation at all time-points by comparison. At day 3 the uncoated, plasma sprayed HA and ESrHAlI coatings exhibited significantly greater proliferation. SEM analysis reveals large numbers of cells on the coating surface with mineral deposits from day 14 onwards. ALP expression in EHA significantly rose from day 3 to 7, this is contrast to other groups where there was no significant difference noted. This suggests an increase in rate of osteogenic differentiation occurring at an earlier stage with

EHA compared with other groups. Earlier differentiation of MC3T3-E1 cells was exhibited on HA discs when compared with plastic surfaces with ALP expression being detectable at day 8 with no activity found on control surfaces (Shu et al., 2003). The same cell line was used by Yang et al (Yang et al., 2012a) comparing its response to HA and Zinc-substituted HA (ZnHA) coatings on Ti. They found a significant increase in ALP activity between 7 and 14 days for both coatings with the ZnHA coating showing greater expression at 7 days with no difference being found at 14 days.

A significant rise in ALP expression of cells on the EHA coating was noted between days 3 and 7 followed by a constant level of ALP expression onto day 14. The relatively lower metabolic activity occurring in cells at later timepoints may reflect the fact that differentiated osteoblasts rarely divide compared with the more immature cells (Malaval et al., 1999).

The aim with ESiHAlI was to produce a coating incorporating a higher wt% of Si with greater crystallinity. This has been achieved with the work in this chapter.

The ESiHAlI coating exhibited similar surface morphology to the ESiHA coating. ESiHAlI crystals were heterogeneous in nature with crystals resembling the ESiHA coating seen previously but also some similar to the EHA crystals. Huang et al (Huang et al., 2013) used a very similar method to produce a SiHA coating and found their method produced a mixed coating of HA and calcium silicate ( $\text{CaSiO}_3$ ). XRD analysis of ESiHAlI reveals peaks with Si at the same  $2\theta$  as the  $\text{CaSiO}_3$  peaks found by Huang et al and different to the Si peaks of ESiHA. The ESiHAlI coating is therefore not a true Si-substituted HA coating but one which is a mixed coating of  $\text{CaSiO}_3$  and HA. The formation of  $\text{CaSiO}_3$  is summarised in Equation 8.



**Equation 8** Serial reactions leading to the formation of  $\text{CaSiO}_3$

This composite EC coated film has advantages. The bond strength of this composite coating is double that of EC deposited HA and close to that of plasma sprayed HA (ISO, 2000, Huang et al., 2013). Treating the Ti<sub>6</sub>Al<sub>4</sub>V discs using NaOH prior to coating has also shown to substantially increase the bond strength between the substrate and the HA layer (Eliaz et al., 2011). This increased bond strength will inevitably be advantageous in preventing the coating from being removed. This composite coating therefore explains the heterogeneity of the crystals seen with SEM. ESiHAlI was annealed in a non-vacuum furnace. This may be disadvantageous as it encourages oxidation due to reaction with atmospheric oxygen and may sub-optimally anneal the composite coating causing a lower Ca:(P+Si) ratio. ESiHAlI is less crystalline than its ESiHA counterpart as suggested by the lower amplitude peaks in their corresponding XRD spectra. Phase composition and crystallinity can be effected by the environment of the annealing process whether it be ambient air or in a vacuum.

The ESiHAlI coating did however exhibit a substantially higher wt% of Si than ESiHA. The 1.63±0.81wt% shows great variability with the amount of Si present in the coating, regardless of this it still is closer to the optimum 0.8wt% defined by Hing et al (Hing et al., 2006). In the same study a 1.5wt% still produced significantly greater bone formation at 6 weeks when compared with 0.4wt%. With regards to coating thickness, a significantly thicker ESiHAlI coating produced with a 45 minute deposition time would reduce the risk of this coating being removed during insertion in subsequent *in vivo* models or the clinical setting. Therefore a 45 minute deposition time produced a more attractive thicker coating.

Although it had been suggested in the previous chapter that ICPMS could be performed to quantify elemental dissolution, it was not possible to complete this as glassware in the equipment available would have given false readings when analysing the dissolution of ESiHA. Subsequently an attempt was made to quantify the Si remaining in the ESiHAlI coating using EDS to give an idea of the rate of Si dissolution. These readings were conducted on those ESiHAlI discs submersed in osteogenic DMEM+ as part of the cell culture work. A significant loss of Si from the coating was evident within the first 3 days.

ESiHAll showed the worst cell metabolic activity out of all the coatings which can most likely be attributed to this. Shie et al (Shie et al., 2011) investigated the effect of various extracellular Si concentrations on the proliferation of MG63 cells. Cells cultured in constant of 4mM concentration of Si within the growth media showed 15-fold greater calcium matrix formation on day 7 than that of control medium. *In vitro* experiments have suggested (Pietak et al., 2007) that release of aqueous Si complexes into the extracellular media has had dose-dependent effects on osteoblast proliferation, differentiation and collagen synthesis. By leaching the majority of the Si content of ESiHAll within the first 3 days, cell activity was not maintained over longer periods as suggested by cell activity assays over a 14 day period. *In vitro* studies have also demonstrated that at high concentrations the positive effects of Si is diminished (Gibson et al., 2009, Hing et al., 2006, Botelho et al., 2006).

ESiHAll exhibited a significantly greater surface roughness when compared with controls. No statistically significant difference in surface roughness was found when the different coatings were compared, yet cell activity significantly differed as described previously. Early studies (Boyan et al., 1999) had defined the Ra of smooth topographies to be less than 0.5 $\mu$ m and rough topographies were defined with a Ra greater than 2 $\mu$ m. By definition all of our groups could be described as having a rough topography however a Ra of 4-7 $\mu$ m has been reported *in vitro* to decrease cell proliferation and increase cell synthetic activity (ALP, osteocalcin, tumour necrosis factor  $\beta$ 1, prostaglandin E<sub>2</sub>) (Boyan et al., 1999). This is possibly why the cellular proliferation seen on ESiHAll was significantly lower at day 3 of culture with it remaining low for the remainder of the timepoints albeit not statistically significant. No significant difference was observed between the ESiHAll and the other coatings with regards to osteogenic differentiation across the timepoints.

SEM analysis of cells seeded onto ESiHAll showed minimal crystal formation. The main constituents of the single crystals and clusters on other coatings as per EDS analysis were calcium, oxygen and phosphorous. Coatings with ALP assays that were greater or lower compared with ESiHAll were still found to have these bone nodules. Si is known to be key in osteogenic differentiation and bone formation, yet the lack of nodules seen with ESiHAll in this

experiment suggests that there was a lack of Si stimulating this process. The early, high rate of Si dissolution is most likely the reason for this.

The aim with ESrHAlI was to produce a thinner coating with the hypothesis that there would be reduced levels of Sr leaching locally causing a detrimental effect upon cellular activity. This hypothesis can therefore be accepted.

ESrHAlI revealed a different morphology when compared with the ESrHA coating from the previous chapter. The lower deposition times used to produce the coating led to the reduced development of cinder cones that were seen with ESrHA. ESrHAlI consisted of a very homogenous layer that followed the underlying surface of the disc. At these lower current densities and deposition times, less of an effect was seen on the coating thickness with a change in coating parameters. A coating with a higher apparent density was produced with  $15\text{mA/cm}^2$  over the 2.5 minutes when compared with a coating produced with  $7.5\text{mA/cm}^2$  over the same deposition time under SEM cross section analysis, although density was not formally quantified. The electrophoretic velocity with which particles are deposited are increased with greater voltage (Mondragon-Cortez and Vargas-Gutierrez, 2004). Increased numbers of particles were deposited forming a seemingly denser coating. Theoretically once particle density on the disc surface is saturated the coating layer will then start to thicken. This is exhibited by the significantly thicker coating seen with the ESrHAlI coating produced over 5 minutes. SEM analysis of this coating also revealed loose bodies of coating material suggesting that a coating of this thickness is fairly fragile and may be a possible mechanism of coating failure. The  $15\text{mA/cm}^2$  2.5 minute coating was selected due to its apparent improved density, thickness and lack of loose coating material.

A lower wt% of Sr was found in ESrHAlI compared with ESrHA. As a shorter deposition time was used to produce the ESrHAlI coating, this is to be expected. The crystallinity of the 2 coatings were similar with Sr peaks found in identical  $2\theta$  positions showing that the Sr has been incorporated within the HA lattice as  $\text{SrPO}_4$ . More Ti peaks were seen to be present in the ESrHAlI XRD spectra as this is a far thinner coating compared with ESrHA, allowing the detection of the underlying  $\text{Ti}_6\text{Al}_4\text{V}$  disc surface.

Profilometry of ESrHAlI revealed a significant difference in Ra when compared with an uncoated disc only. The Ra (3881nm) of ESrHAlI falls short of the 4-7 $\mu$ m which has been stated to reduce cell proliferation but increased differentiation (Boyan et al., 1999). Cell culture experiments revealed significantly higher cell proliferation at day 3 compared with EHA and ESiHAlI coatings, the Ra of which falls within 4-7 $\mu$ m. This suggests that cellular activity is perhaps greater dictated by surface chemistry than surface topography at this roughness. Borsari et al (Borsari et al., 2005) investigated plasma sprayed HA on differing surface topographies of Ti<sub>6</sub>Al<sub>4</sub>V discs with human osteoblast-like cells (MG63). They concluded that a HA coating only had a synergistic positive effect with surface roughness, when the right surface roughness was applied, as no effect of a HA coating was seen on cell activity when applied onto ultra-high roughness surfaces. Experimental groups varied the Ra from 4.1 $\mu$ m to 74 $\mu$ m. Cells seeded onto ESrHAlI was also seen to have significantly increased ALP expression from day 7 to 14 suggesting increasing osteogenic activity. This is parallel with a significant increase in proliferation seen with ESrHAlI at day 14 compared with day 3 and 7. ESrHAlI is far superior to the ESrHA coating produced in the previous chapter with regards to cell activity. This may be due to the reduced Sr wt% or differing surface topography/thickness.

It has been shown that cells on disordered topographies allowed for greater cell adhesion and osteogenic differentiation when compared to topographies that are more ordered. Surfaces consisting of 120nm offset pits 300nm apart has been shown to cause osseointegration in MSC populations (Dalby et al., 2007), this has been supported by complementary studies that suggest feature diameters of 100nm for optimal osteogenesis (Dalby et al., 2014). There is evidence that also demonstrates that cells are sensitive to <50nm alterations in the topographies of surfaces suggesting that nanoscale patterning has potential in dictating the cells phenotype (McMurray et al., 2011). In this experiment, greater filopodial interaction was observed with SEM analysis on the EC coatings when compared with the control groups. ESiHAlI and ESrHAlI crystals were smaller in size than EHA crystals and therefore with further magnification it is possible that 'nanopodia' are also present giving further topographical cues to the cellular cytoskeleton. These nanopodia aid with cell interaction when topographical sensing below 10nm is required such as in the case of crystals in

the ESiHAlI and ESrHAlI coatings (Dalby et al., 2014). This difference in nanotopography could also explain why there was higher ALP expression observed in the ESiHAlI and ESrHAlI coatings than in EHA.

ALP is expressed early in bone development and following osteogenic development with an associated upregulation of other genes (e.g. osteocalcin), ALP expression declines. ALP facilitates the deposition of extracellular matrix before the onset of mineralisation (Koroleva et al., 2015). Osteocalcin is a marker for mineralisation and its production could have been measured to assess the level of osteogenic differentiation occurring with each coating. An osteocalcin assay should therefore be included in future work. Growth media was supplemented with dexamethasone from the start of the experiment. Glucocorticoids are known to inhibit osteocalcin expression (Botelho et al., 2006), it would have therefore possibly affected the assay results as they would have been performed prior to the 14 days.

Von Kossa or Alizarin Red staining of the discs to confirm mineralisation at day 28 was considered however not performed as these stains would not be able to distinguish between physiological and dystrophic mineral (Botelho et al., 2006). For future work a tetracycline label could be added to the medium to visualise mineral nodule formation under microscopy as well as completing the EDS analysis.

## 5.5 Conclusion

The work in this chapter further developed the coatings described in Chapter 4 and has led to improved physical, chemical and biological characteristics of HA coatings containing Si and Sr.

The aims of the chapter have been achieved by modifying methods utilised in chapter 4. ESiHAlI has a greater Si wt% compared with ESiHA which exhibited osseoconductive characteristics with more positive AlamarBlue® and ALP assays than seen in the previous chapter. Cells cultured on a thinner ESrHAlI coating with a lower Sr wt% exhibited higher rates of proliferation and ALP expression. EHA was also shown to be osseoconductive with no difference seen when compared with controls.

Given the complex nature of osteogenic differentiation and numerous factors, feedback mechanisms and cascades involved, it is challenging to simulate this with *in vitro* experimentation. Moreover the timing of cellular events *in vitro* is somewhat different to that seen *in vivo*. For example, with a porous collar, cell proliferation may not proceed immediately after implantation. A blood clot will initially form within the porous structure. This clot will interact with the scaffold material and any CaP coatings. The invading cells required to remodel the clot are likely not to be mesenchymal in origin. It is therefore difficult to predict precisely from *in vitro* data the *in vivo* performance of a material. In the final experimental chapter the EHA coating together with the newly developed ESiHAlI and ESrHAlI coatings will be evaluated in the *in vivo* environment using a validated femoral condyle defect model.

**Chapter 6. Evaluating Osseointegration of Laser Sintered  
Ti<sub>6</sub>Al<sub>4</sub>V Electrochemically Coated Scaffolds Using an Ovine  
Femoral Condyle Defect Model**

## 6.1 Introduction

This final experimental chapter describes the *in vivo* evaluation of the EHA, ESiHAlI and ESrHAlI coatings by investigating their effect on custom made dual-pore (SP and LP) SLS implants. These three coatings were compared with uncoated and commercially plasma sprayed control implants in an ovine femoral condyle defect model.

The aim of this chapter was to evaluate the optimum combination of pore size and coating that allowed for the greatest amount of osseointegration using an *in vivo* model. Chapter 3 showed that implants with smaller pores compared to ones with larger pores displayed greater osseointegration and that the response of MSCs to the EC coatings demonstrated in chapter 5 was positive, it can be hypothesised that:

1. Small pore scaffolds will allow for greater osseointegration.
2. EC coatings will allow for greater osteointegration compared with control groups.
3. ESrHAlI in combination with the small pore design will show the greatest levels of osseointegration.

## 6.2 Materials and Methods

### 6.2.1 Manufacture of implants

Ti alloy porous implants were made by SLS (Eurocoating, Italy) with each implant comprising of two pore sizes. The SP and LP pitch, strut size and relative pore sizes (550 $\mu$ m and 1125 $\mu$ m, respectively) were identical to those used in chapter 3. The pore shape approximated to cuboids. Half of the implant consisted of a SP geometry with the other half being of LP design (Figure 6-1).

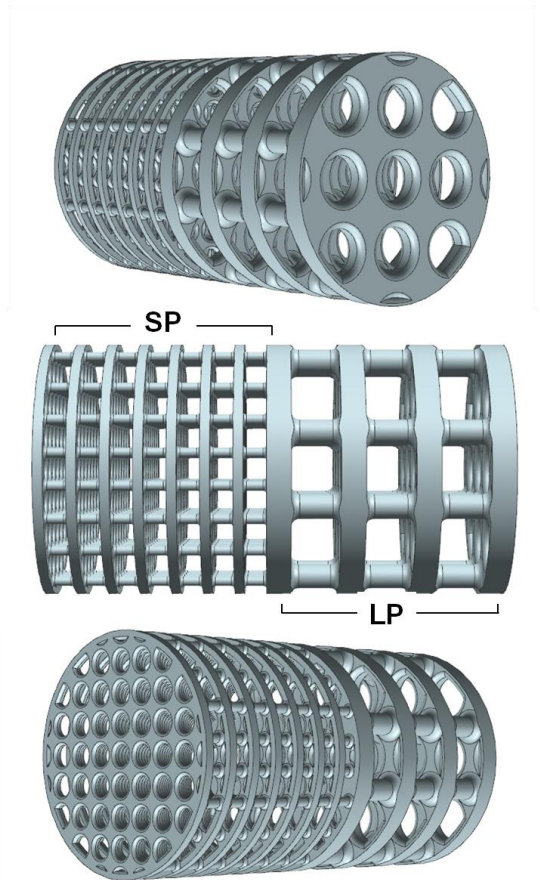


**Figure 6-1** 3D models of selective laser sintered Ti<sub>6</sub>Al<sub>4</sub>V plugs measuring 8x15mm. Small pore (SP) and large pore (LP) regions shown.

All implants underwent acid etching using 2% hydrofluoric acid for 4 minutes. After the acid was neutralised, the plugs were subsequently ultrasonically cleaned in 10% Decon 90, distilled water and 99% IMS for 15 minutes at each stage and left to air-dry prior to being coated.

### 6.2.2 EHA coating of implant

A supersaturated 0.13M CaP solution was prepared by adding 30g of  $\text{Ca}(\text{H}_2\text{PO}_4)_2$  (C8017; Sigma-Aldrich, UK) to 1L  $^d\text{H}_2\text{O}$ . The solution was vigorously stirred for 1h and filtered using Whatman 540 filter paper (GE Healthcare, UK). Implants were submerged in CaP solution and attached to the negative terminal of a DC Dual Power Supply pack (Peak Tech, Telonic Instruments Ltd, UK) to act as the cathode with a platinum ring as the anode. A current density of  $10\text{mA}/\text{cm}^2$  measured using a FLUKE 867B Graphical Multimeter (Fluke Corporation, USA), was passed through the actively stirred solution for 15mins. Using the computer model of the SLS printed design, the surface area of the implant was calculated as  $14\text{cm}^2$ . The current density was calculated using Equation 6 giving a total current of 140mA being used. The initial CaP precipitate ( $\text{Ca}_2\text{HPO}_4 \cdot 2\text{H}_2\text{O}$  (Brushite)) was converted into HA,  $\text{Ca}_5(\text{PO}_4)_3\text{OH}$ , by soaking the implants in 0.1M NaOH solution for 72 hours. Finally, implants were gently rinsed with  $^d\text{H}_2\text{O}$  and left to air-dry before being autoclaved prior to implantation.

### 6.2.3 ESiHAlI coating of implant

Implants were functionalised in a 5M NaOH solution ( $65^\circ\text{C}$ ) for 24 hours whilst being actively stirred. Once washed with  $^d\text{H}_2\text{O}$  they were allowed to air dry. The electrolyte solution composed of 1g/l of nano- $\text{SiO}_2$  (637238; Sigma-Aldrich), 0.042M  $\text{Ca}(\text{NO}_3)_2 \cdot 4\text{H}_2\text{O}$  (C2786; Sigma-Aldrich), and 0.025M  $\text{NH}_4\text{H}_2\text{PO}_4$  (795461; Sigma-Aldrich) in  $^d\text{H}_2\text{O}$ . The solution was brought to a pH of 4.2 with the addition of 10% HCl solution at room temperature (AR15 pH meter; Accumet®, Fisher Scientific, UK). Implants were submerged in the solution and attached to the negative terminal of a DC Dual Power Supply pack (Peak Tech, Telonic Instruments Ltd, UK) to act as the cathode with a 0.063mm diameter platinum wire (Goodfellow Cambridge Ltd., UK) as the anode. The implants were coated using a current density of  $0.8\text{mA}/\text{cm}^2$  at  $65^\circ\text{C}$  for 45 minutes. The current was maintained using a multimeter as with the previous coating. The solution was brought to a pH of 4.2 by the addition of 10% HCl and 10% NaOH at room temperature (AR15 pH meter; Accumet®, Fisher Scientific, UK). The solution was gently stirred throughout and maintained at the temperature for the

duration of the EC deposition using a magnetic stirrer-hotplate and an aluminum foil heat jacket. Once coated, the implants were placed in a furnace (RHF 1600, Carbolite Gero, Derbyshire UK) at 300°C for 2 hours.

#### **6.2.4 ESrHAII coating of implant**

6.66g of CaCl<sub>2</sub>, 4.14g of NH<sub>4</sub>H<sub>2</sub>PO<sub>4</sub>, 1.057g of SrCl<sub>2</sub> (439665; Sigma-Aldrich) and 11.69g of NaCl (S7653; Sigma-Aldrich) were dissolved in 1L of <sup>d</sup>H<sub>2</sub>O. The SrCl<sub>2</sub> acted as the Sr source with the NaCl as the conducting agent. This was filtered using Whatman 540 filter paper. The solution was brought to a pH of 4.5 by the addition of 10% HCl and 10% NaOH at room temperature. The implants, as before, acted as the cathode. The solution was gently stirred and heated to 60°C. The anode was a platinum wire as described previously, which was connected to the electrode and immersed in the solution. EC deposition was performed using a current density of 15mA/cm<sup>2</sup> over 2.5 minutes controlled using a multimeter and a DC Dual Power Supply pack as previously described in 5.2.4. Once coated the discs were placed in 0.1M NaOH solution for 72 hours to convert brushite to HA at room temperature after which they were gently rinsed with distilled water and allowed to air dry.

#### **6.2.5 In vivo study design**

Eight skeletally mature mule sheep were used for the purposes of this study. Femoral condyle defect implants were manufactured as described in 6.2.1. Control groups comprised of uncoated implants (U) and implants plasma sprayed with a highly crystalline (>85%) HA (Plasma Biotal, Tideswel, Derbyshire, UK). Experimental groups were implants coated in EHA, ESiHAII and ESrHAII. Thirty implants in total were used, with 6 implants in each group. Two implants were inserted into the femoral condyles bilaterally; therefore 4 implants were inserted per sheep. These four implant positions were right proximal, right distal, left proximal and left distal. Implants from each group were placed in each of these defects so that there was an almost even distribution of sites for each type of implant. Furthermore the implants were also placed in either a SP inward or SP outward direction to ensure that the orientation of the SP and LP regions of the plug were matched. Figure 6-2 and Table 6-1 outlines

the locations and orientation of the implants for each group. Implants were autoclaved prior to insertion.

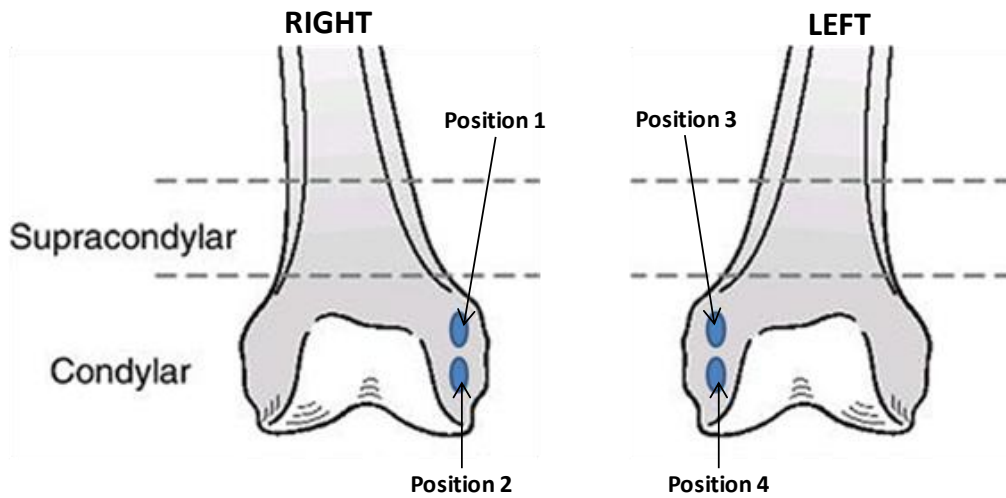


Figure 6-2 Diagrammatic representation of implant and defect positions within femoral condyle.

	POSITION 1	POSITION 2	POSITION 3	POSITION 4
1	U*	PS*	EHA*	ESiHAlI*
2	ESrHAlI*	U	PS	EHA
3	ESiHAlI	ESrHAlI	U*	PS*
4	EHA*	ESiHAlI*	ESrHAlI*	U
5	PS	EHA	ESiHAlI	ESrHAlI
6	U*	PS*	EHA*	ESiHAlI*
7	ESrHAlI*	U	PS	EHA
8	ESiHAlI	ESrHAlI		

Table 6-1 Plug position and orientation within condyle defects. U, uncoated; PS, plasma sprayed; EHA, electrochemical HA; ESiHAlI, electrochemical SiHA 2<sup>nd</sup> phase; ESrHAlI, electrochemical SrHA 2<sup>nd</sup> phase. \*SP orientated inwards.

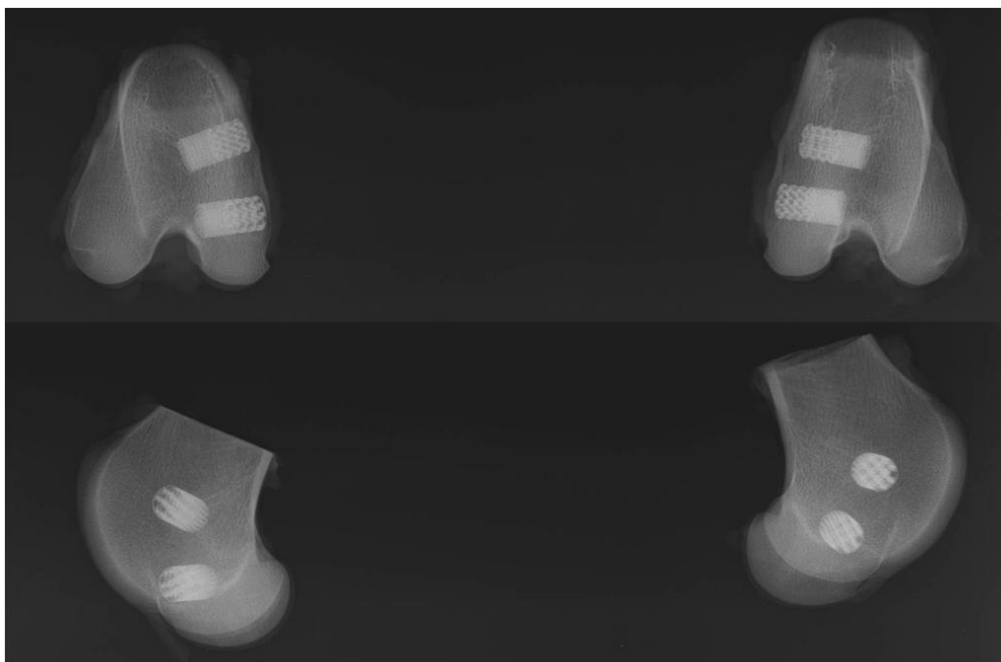


Figure 6-3 Anteroposterior (above) and mediolateral (below) radiographs of retrieved femoral condyles with implants in situ.

All animals recovered well in single pens and were allowed to weight bear immediately post-operatively. When fully weight bearing the animals were group housed in a large indoor pen. Implants were kept in situ for 6 weeks at which point they were retrieved surrounded by bone for histological analysis.

### **6.2.6 Surgery**

All procedures were carried out in accordance with the UK Animal Scientific Procedures Act 1986 at the Royal Veterinary College, North Mymms. Home Office Licences were held by all those taking part in any surgical procedure.

### **6.2.7 Analgesia**

Ketamine (2mg/kg) and midazolam (2.5mg) was administered intravenously to induce anaesthesia. To protect the airway and to allow ventilation, the animal was intubated and anaesthesia was maintained with 2% Fluothane and oxygen for the duration of the procedure. Intra-operative pulse oximetry, ECG and end-tidal carbon dioxide were monitored.

### **6.2.8 Insertion of implants into femoral condyle defects**

Animals were placed in a supine position and the right and left hind leg was shaved. Betadine surgical scrub was applied to the areas followed by Betadine antiseptic solution. The animal was then transferred into the operating theatre at which point the surgical site was further prepared with Hydrex Surgical Scrub (MidMeds Ltd. Loughton, UK) which is a chlorhexidine based aqueous antimicrobial.

Sterile drapes were placed leaving the medial right and left distal femur exposed. A longitudinal 60mm incision over the medial femoral condyle of the left femur was made. Sharp and blunt dissection was performed until the medial femoral condyle was exposed. The periosteum overlying the area was split, elevated and retracted. Two 8x15mm defects were drilled in the femoral condyle in the proximal and distal positions using a custom drill bit. The appropriate implants were inserted by press fitting into the defects and the overlying tissues were closed in layers. This procedure was repeated on the

right side for the remaining two further implants. A spray dressing (Opsite®, Smith & Nephew, Gallows Hill, Warwick, UK) was applied to the wound prior to recovering the animal.

Post-operatively the animals were allowed to weight-bear immediately as tolerated. Antibiotics (Exenel™, ceftiofur hydrochloride, 1ml/50kg, Pfizer Animal Health, Tadworth Surrey, UK) and fentanyl patches (Vetergesic™, buprenorphine, 0.6mg/animal, Reckitt and Colman Products Ltd. Hull, UK) were administered for 3 days following the procedure. Animals were recovered in individual pens and once able were group housed.

Animals were euthanised at 6 weeks post-operatively by intravenous overdose of 0.7mg/kg pentobarbitone (20, K. M. Loveridge Ltd. Southampton, UK).

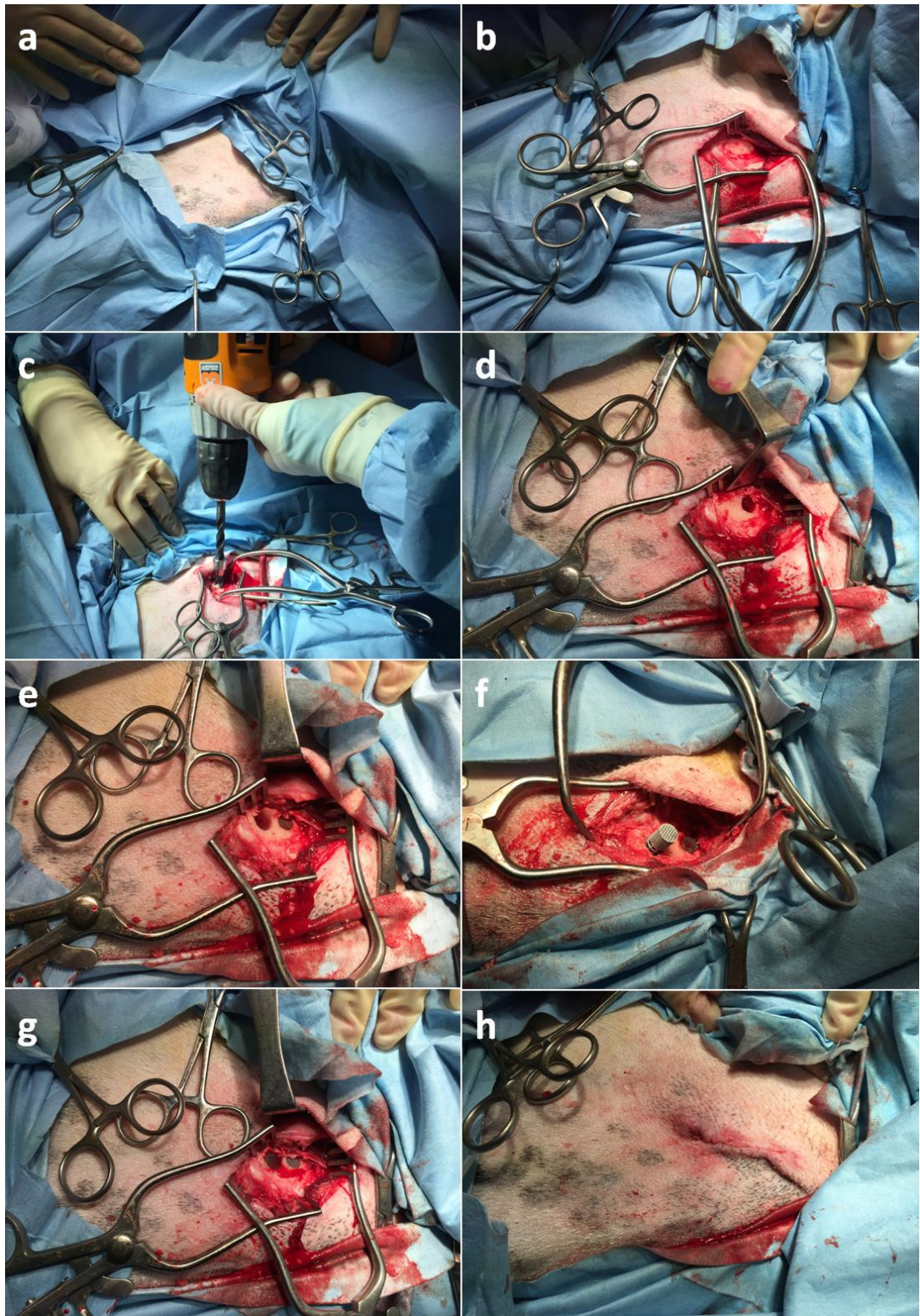


**Figure 6-4** Operative stages of inserting implant into defects. Starting from surgical site preparation (a) followed by incision and exposure of condyle (b). Drilling and sequential insertion of each implant is performed (c-g) followed by closure of the wound (h).

### 6.2.9 Histomorphometry

Following retrieval, samples fixed in 10% neutral buffered formalin (NBF) for a minimum period of one week. Specimens underwent dehydration in successive

increasing concentrations of IMS, de-fatted with 100% chloroform and immersed in 50% IMS and 50% resin mixture (LR White Resin, London Resin Company Ltd, Reading, Berkshire, UK), followed by 100% resin. Each plug was embedded in hard grade acrylic resin (LR White, London Resin Company, Reading, UK), sectioned through the centre in the longitudinal plane and thin sections were prepared (approximately 80µm in thickness). Thin sections were stained with Toluidine Blue and Paragon to identify soft tissue and bone. Stained slides were viewed under an Olympus light microscope (Axioskop, Carl Zeiss, Welwyn Garden City, UK) and images analysed using ImageJ (v1.49, National Institutes of Health, USA). Thicker sections made in the same plane were polished and examined using backscattered scanning electron microscopy (JEOL 3500 C, Tokyo Japan). The coating layer was observed using SEM.

The total length of surface available for integration (mm) and length of surface with direct bone contact (mm) was quantified for each implant. Freehand scaled measurements were taken using ImageJ to quantify these values. The proportion of the surface with direct bone contact (%) was calculated. The total inner porous surface area (mm<sup>2</sup>), area of soft tissue (mm<sup>2</sup>) and area of bone (mm<sup>2</sup>) within pores was measured for each of the implants using freehand and thresholding techniques with ImageJ. The proportion of the inner porous space containing bone and soft tissue was calculated using these values.

#### **6.2.10 Statistics**

Statistical analysis was performed using SPSS Statistics (v22, IBM, New York, USA). Data was tested for normality using the Shapiro-Wilk test and the non-parametric Mann-Whitney U test or Kruskal-Wallis test was used to compare groups. Parametric data was compared using the independent samples T-test or a One Way ANOVA where  $p < 0.05$  were considered significant.

<b>Stage</b>	<b>Length of time</b>
10% neutral buffered formalin	1 week
30% Alcohol	3 days
50% Alcohol	3 days
70% Alcohol	3 days
90% Alcohol	3 days
100% Alcohol	3 days
100% Alcohol	3 days
100% Alcohol	3 days
100% Chloroform	1 day
100% Chloroform	1 day
100% Chloroform	1 day
100% IMS	1 day
100% IMS	1 day
100% IMS	1 day
50:50 IMS:Resin	3 days
100% Resin	3 days
100% Resin	3 days
100% Resin	3 days
Embed in resin	-

**Table 6-2 Preparation protocol for the production of thin sections.**

## 6.3 Results

### 6.3.1 Histological appearance of bone ingrowth into implants

Osseointegration was observed in all implants inserted into condyle defects. Bone was seen growing directly into the porous implant from the surrounding cancellous and cortical bone. At 6 weeks, the majority of pores were not fully filled with bone but there was significant bone growth at the interface with the surrounding bone. Significantly greater bone growth on the implant surface was observed of the EC coated implants compared with the uncoated and plasma sprayed groups. Bone grew in a centripetal manner with greater growth on the porous surface which gradually reduced towards the centre of the porous cylinder. No obvious difference was seen between the osseointegration of small pore and large pore regions of the implants.

At 6 weeks, the plasma spray coating and the EC coatings were still present on the Ti<sub>6</sub>Al<sub>4</sub>V surface. The plasma sprayed HA coating was seen to penetrate the porous scaffold poorly, with minimal HA present within the pores and the majority on the outer surface. The large pore structure allowed for a greater amount of the plasma sprayed HA into the pores compared to the small pore structure, but this did not appear to improve osseointegration significantly. EC coatings were found to coat the outer and inner porous surfaces completely. These were observed to be highly osseoconductive with greater bone growth throughout the whole porous structure rather than bone attachment being limited to the just outer surface as with the uncoated implant. The largest amount of bone was seen in the EHA group with bone forming on the inner pore surface and across the struts of the pores (Figure 6-5, Figure 6-6). The crystalline structure of the EHA coating was easily observed using backscattered SEM. Its thickness is observed to be as expected from the work completed in chapter 4 ( $22.4 \pm 2.8 \mu\text{m}$ ). EHA appeared as wisps over the surface of the implant which was rough due to the projecting outer surface of the small fused Ti alloy powder particles. The ESiHAlI coating is observed as being of a similar thickness expected from the work in chapter 5 ( $19.2 \pm 5.7 \mu\text{m}$ ) however it was less easily visible as the ESiHAlI crystals are of a submicron diameter when compared with those of EHA, which can be approximately  $5 \mu\text{m}$  in

thickness. The ESrHA coating was similar to EHA and easily seen with SEM cross-sections. The coatings for EHA, ESiHAII and ESrHAII followed the topography of the pores closely and no loose fragments were seen. None of the pores of the implant was found to be blocked and none of the pores were filled by the coatings. As a result bone grew in a centripetal fashion and was found on the surface of the pore rather than forming centrally within the porous space. Direct bone attachment was seen with all the experimental EC variants of HA (Figure 6-6). Both lamellar and woven bone was seen within the pores and surrounding the struts of the SLS scaffolds (Figure 6-6). Multiple lacunae within the bone are seen with larger Haversian canals also identified.

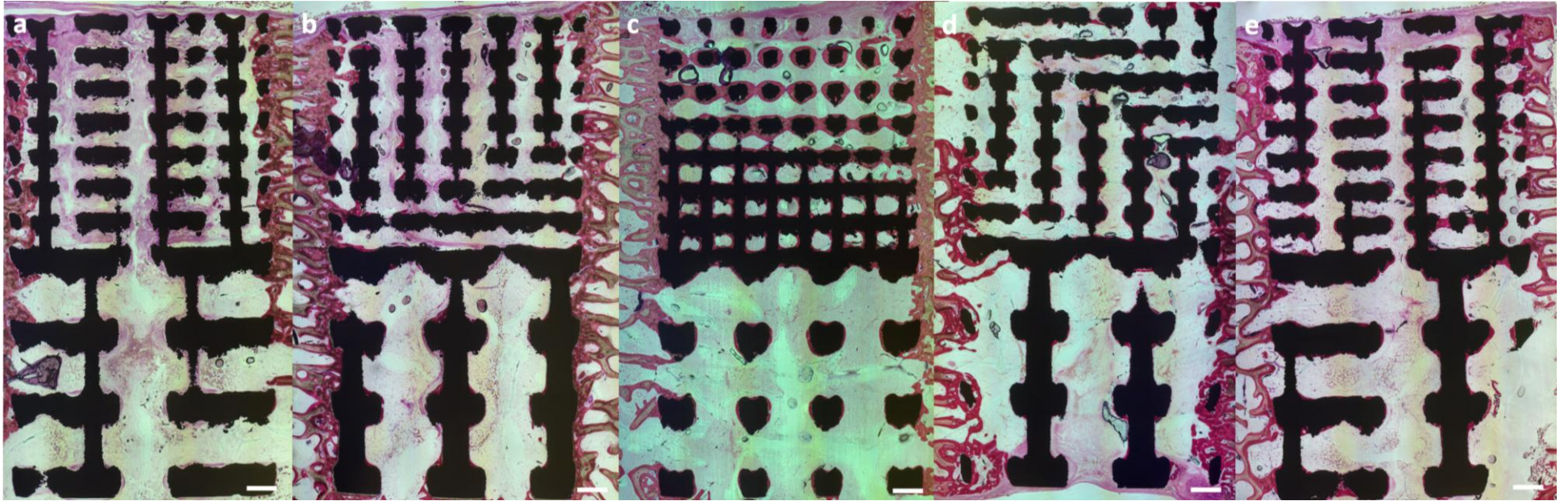


Figure 6-5 Light microscope image of implant within femoral condyle defect. x2.5 magnification. Toluidine blue and Paragon stain used. Bone, pink; Soft tissue, purple; Implant, black. Scale bar shown equivalent to 1mm. (a) uncoated, (b) plasma sprayed, (c) EHA, (d) ESiHAlI and (e) ESrHAlI.

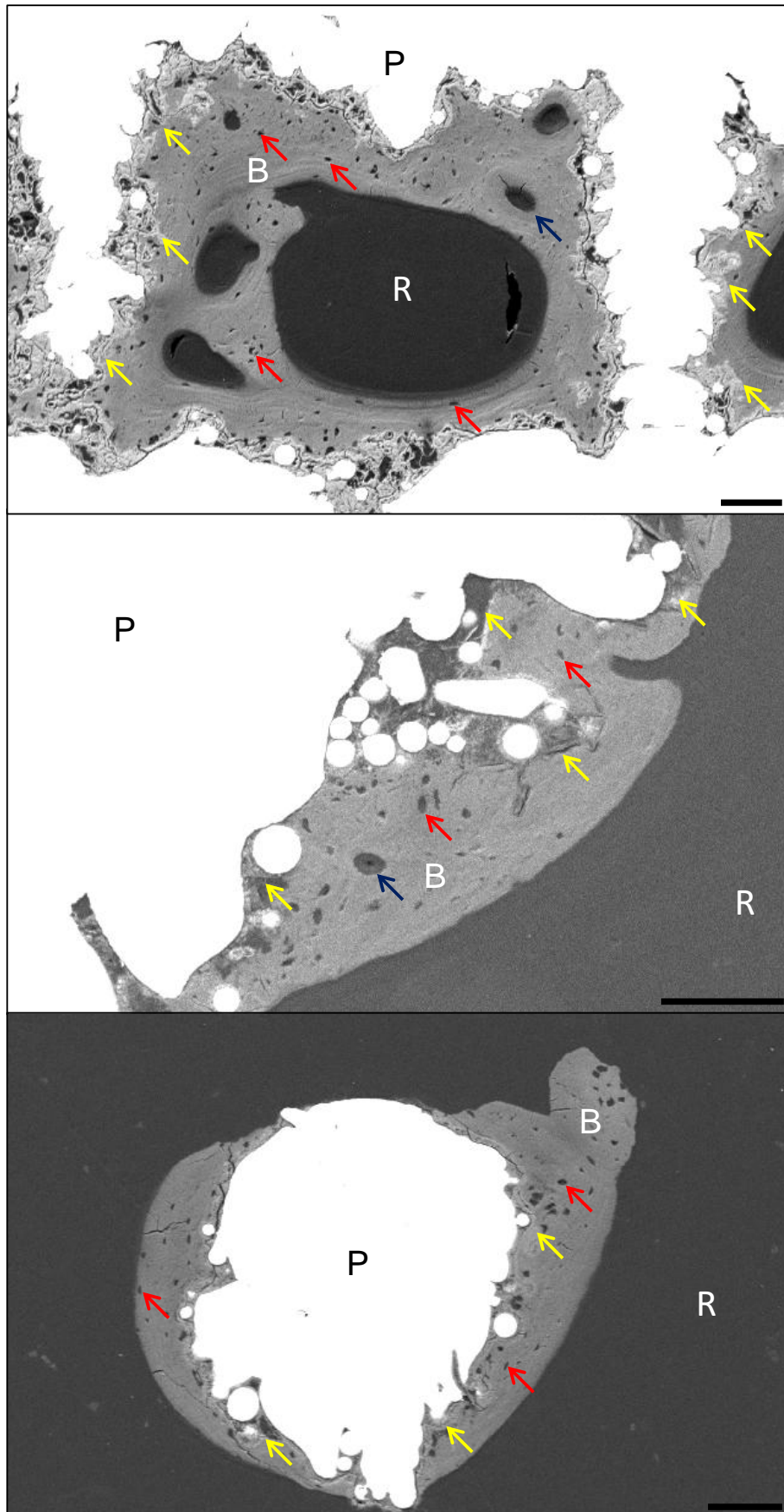


Figure 6-6 Backscattered scanning electron microscopy (SEM) images of plug cross-sections showing direct attachment of bone to EC coatings. Top, EHA (x100). Middle, ESiHAlI (x200). Bottom, ESrHAlI (x120). Scale bars as shown (100 $\mu$ m). Yellow arrows identify coating, blue arrows show Haversian canals, red arrows identify lacuna. P, plug strut. R, resin. B, bone.

### 6.3.2 Histomorphometric analysis of collar surface size and pore content

The surface available for bone contact (mm, IQR) for the SP (151.9, 143.6-157.6) region was significantly greater ( $p<0.001$ ) than that available with the LP (69, 64.1-74.3) region.

No difference ( $p=0.848$ ) was seen in the overall percentage integration (% , IQR) between the different pore size designs with smaller pore regions showing 34.2% (18.7-78.3) compared with the larger pore variety exhibiting 40.3% (20.4-73.1) integration.

A significant difference in percentage integration was seen across the coating groups ( $p<0.001$ ). Implants with EHA (46.1, 30.5-102.2,  $p<0.001$ ), ESiHAlI (34.5, 19.9-49.5,  $p=0.001$ ) and ESrHAlI (50.9, 26.2-78.8,  $p<0.001$ ) coatings showed significantly greater integration compared with uncoated implants (31, 7.5-112.5). Significantly greater ( $p=0.001$ ) integration was also observed in the EHA group when compared with the plasma sprayed (28.4, 15.7-46.7) implants. Analysis did not reveal a significant difference between the percentage integration of implants with differing EC coatings (EHA, ESiHAlI and ESrHAlI).

Subgroup analysis reveals ESrHAlI SP, EHA LP and EHA SP combinations were found to have significantly greater integration than the uncoated controls with EHA SP also showing significantly improved integration compared with the plasma sprayed SP group. The percentage integration (% , IQR) for the scaffolds were 9.9 (6.4-13.4), 9 (7.3-15.7), 18 (10.5-22.8), 66.1 (54-81), 71.9 (69-80) and 77.7 (70-93.3) for U LP, U SP, PS SP, ESrHAlI SP, EHA LP and EHA SP respectively. Figure 6-7 and Table 6-3 summarises the significant comparisons.

The proportion of bone ( $\pm$ SD) to soft tissue within the pores of the different experimental groups varied. Generally the EC coated plugs contained greater amounts of bone within their pores. This only translated statistically in one comparison with EHA SP ( $0.26\pm 0.08$ ) containing a significantly ( $p=0.047$ ) higher proportion of bone within its pores than U LP ( $0.13\pm 0.09$ ). In parallel the amount

of soft tissue found within the pores as a result also showed a significant difference ( $p=0.047$ ) (Figure 6-8).

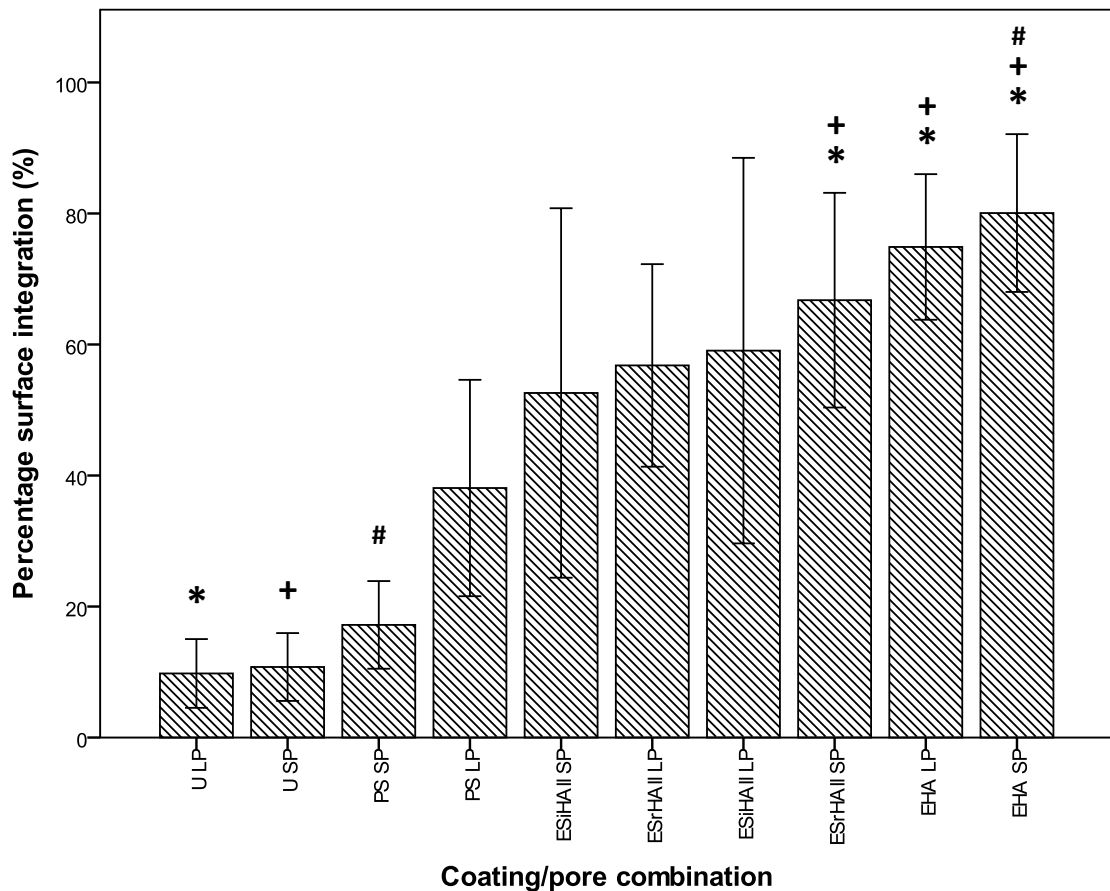


Figure 6-7 Percentage integration of various experimental groups; U, uncoated; PS, plasma sprayed HA; EHA, electrochemical HA; ESHAIL, electrochemical SiHA; ESrHAIL, electrochemical SrHA; SP, small pore; LP, large pore. Error bars represent 95% confidence intervals. \*\*\* $p<0.05$

Scaffold (% integration, IQR)	ESrHAIL SP (66.1, 54-81)	EHA LP (71.9, 69-80)	EHA SP (77.7, 70-93.3)
U LP (9.9, 6.4-13.4)	0.022	0.004	0.001
U SP (9, 7.3-15.7)	0.028	0.006	0.001
PS SP (18, 10.5-22.8)			0.019

Table 6-3 Significant p-values and percentage integration (IQR) for significant findings between various scaffold designs. U, uncoated; PS, plasma sprayed HA; EHA, electrochemical HA; ESHAIL, electrochemical SiHA; ESrHA, electrochemical SrHA; SP, small pore; LP, large pore.

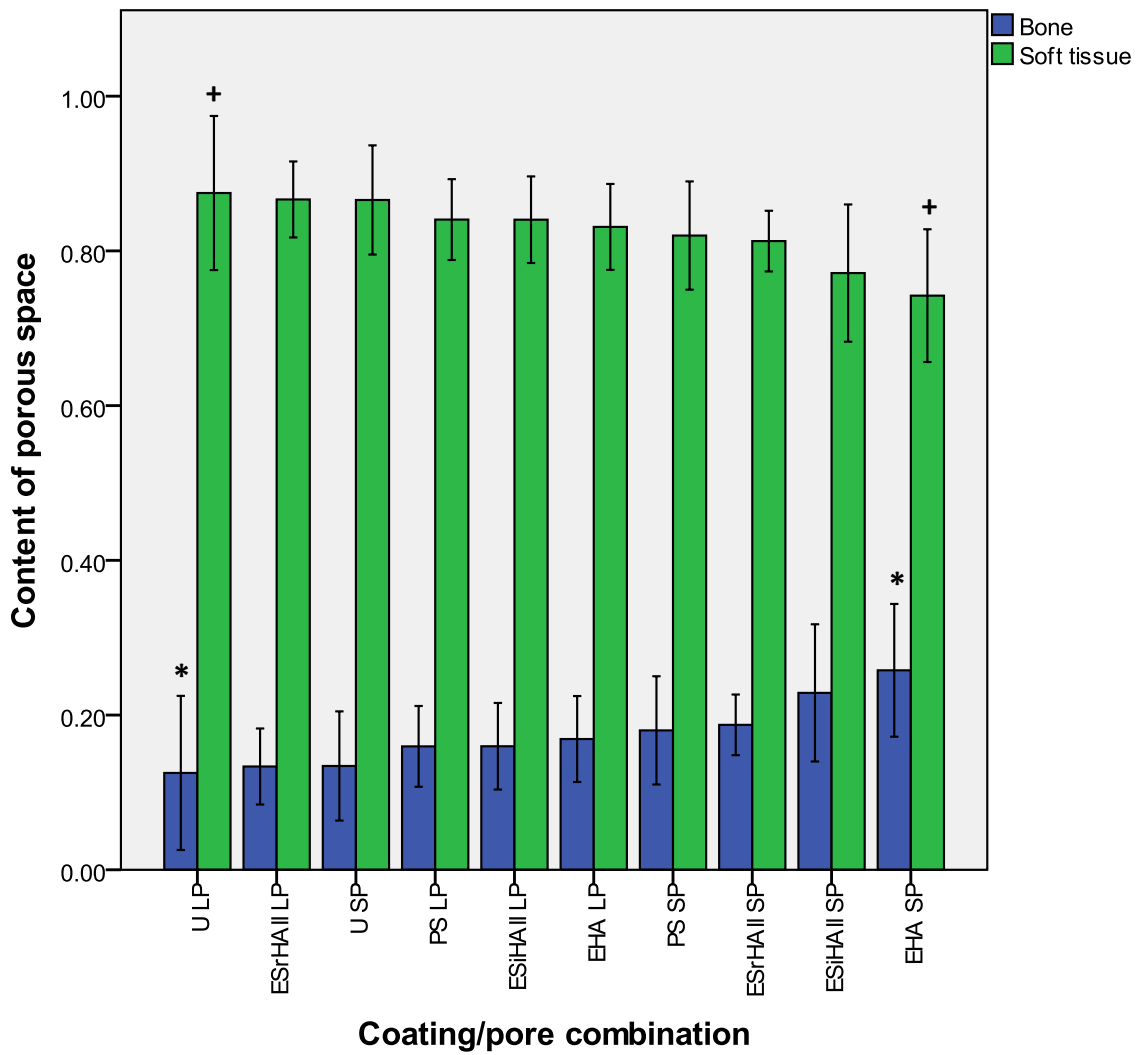


Figure 6-8 Proportion of the porous space with bone and soft tissue growth between different coating/pore size combinations at 6 weeks. Error bars represent 95% confidence intervals. U, uncoated; PS, plasma sprayed HA; EHA, electrochemical HA; ESiHA||, electrochemical SiHA; ESrHA||, electrochemical SrHA; SP, small pore; LP, large pore. \*\*p=0.047

## 6.4 Discussion

This is the first direct *in vivo* comparison of the osseointegrative ability of different EC coatings on identical SLS structures. The ability to investigate this was made possible by designing custom dual-pore selective laser sintered Ti<sub>6</sub>Al<sub>4</sub>V scaffolds. These were of an open pore structure with well-defined concavities, which is generally accepted to be important for bone ingrowth. It is also worth considering that the optimal pore size for open porous structures may be different to that seen for porous coatings on solid metallic surfaces.

This work has shown that bone growth within selective laser sintered porous scaffolds is optimum in a small pore scaffold coated with EHA however no overall significant difference was found between pore sizes. The initial hypothesis cannot be accepted as this study has not shown small pore scaffolds to allow for greater osseointegration. EC coatings overall outperformed control groups significantly in terms of osseointegration and thus the second hypothesis can be accepted. Although in the *in vitro* work, ESrHAII coated discs showed highest levels of cell proliferation and differentiation, this did not translate into the *in vivo* environment and therefore our last hypothesis is rejected.

EC coatings have already been described to allow for improved osseointegration in the *in vivo* environment (Wang et al., 2006, Schmidmaier et al., 2002, Yang et al., 2012b, Liang et al., 2015). The literature describes the use of these coatings on solid structures. One of the many advantages of EC coatings is its ability to be applied to porous structures and it is this characteristic that has been exploited in this experimental chapter. This has not been reported in the current literature at the time of writing this thesis.

EC coatings EHA, ESiHAII and ESrHAII performed significantly better than uncoated groups with EHA also showing greater osseointegration when compared with the plasma sprayed HA group. *In vitro* examination of its structural characteristics show it to have a significantly rougher surface topography than controls with a Ca:P of 1.53, the closest of any of the EC coatings produced when compared with stoichiometric HA. *In vitro* studies in

chapters 4 and 5 show a mixed picture when evaluating cell proliferation and differentiation occurring on the EC coatings compared with control groups.

In the previous chapter I have proposed that the EC coatings are expected to dissolve quicker when compared with the plasma sprayed variety due to their lack of crystallinity. *In vivo* work in this chapter shows that the EC coatings are still present after 6 weeks in situ. Furthermore, the pore surfaces are decorated with bone due to the EC coatings and therefore it is difficult to understand and justify the use of a more crystalline or thicker coating, such as plasma sprayed HA, as the EC coatings have fulfilled their role.

With the results of this chapter, a disparity is seen in the bioactivity of the coatings between the *in vitro* and *in vivo* experiments. This may be due to the presence of additional biological factors in the latter interacting with the various coatings.

CaP biomaterials have a high affinity to proteins, which allow for them to carry bone growth factors. CaP biomaterials are osseoconductive, and more recent studies have shown them to be osseoinductive. It is thought that the geometry of the CaP pores allow for optimal binding of circulating endogenous bone morphogenic protein, which is an important factor in controlling osteogenic differentiation (LeGeros, 2002).

The adsorption of cell-adhesive proteins to the coating also plays an important role. Protein adsorption is a complex process and is dependent upon the physico-chemical characteristics of the CaP coating. The microporous structure of all the EC coatings produced in previous chapters' favours protein adsorption as it allows for a high specific surface area. When compared with plasma spray, the EC coatings exhibit amorphous phases and lower crystallinity and therefore increased solubility. Local changes in pH and ion concentration as a result of this can also positively affect protein adsorption (Samavedi et al., 2013). The EHA and SP combination is thought to have the highest levels of osseointegration as the significantly higher SP surface area in combination with an amorphous coating that closely resembles stoichiometric HA allows for optimal adsorption of cell-adhesive proteins. The EHA and LP combination also

performed well suggesting that a highly bioactive coating can still allow for bone growth regardless of pore size.

Wang et al (Wang et al., 2006) investigated early bone apposition onto EHA coated k-wires in a canine model. They found that at 7 days post surgery the plasma sprayed HA coating exhibited higher bone apposition ratios when compared with their EHA and uncoated groups. Subsequently at 14 days both plasma sprayed and EHA coated groups showed similar bone apposition ratios, much higher than that for uncoated  $Ti_6Al_4V$  k-wires. They explained this result as their plasma sprayed coating exhibited a lower crystallinity and therefore a higher solubility when compared with their EHA coating. Schmidmaier et al (Schmidmaier et al., 2002) used a rat model where EHA coated k-wires were inserted into the rodent femora. Significantly higher implant fixation was achieved with histology confirming improved bone contact and ingrowth in the coated k-wire group.

Bioactivity and degradation behaviour of various CaP substrates differ depending on Ca:P, crystallinity and phase purity, although most are generally stable at physiological pH (7.4) (Bose and Tarafder, 2012). Given that the ESiHAlI and ESrHAlI coatings had a Ca:P that was further from that of HA, it may suggest a degree of instability in the *in vivo* environment.

*In vivo* models similar to the one described in this chapter have been used to evaluate the use of silicate substituted HA. Both Patel et al (Patel et al., 2005) and Hing et al (Hing et al., 2006) showed that the *in vivo* bioactivity of HAs were significantly improved as a result of the Si substitution using ovine and lapine femoral condyle defect models respectively.

The evaluation of the *in vivo* bioactivity of EC deposited strontium-substituted HAs is described by Yang et al (Yang et al., 2012b). They had used a rabbit model with a 10.1 molar % SrHA coating on a non-porous screw. Improved bone-implant contact was observed at 4 and 6 weeks with a significantly greater area of bone seen at 6 weeks within the screw threads. Liang et al (Liang et al., 2014) analysed the osseointegration of a number of EC deposited SrHA coatings with varying molar percentages of Sr. A rat model was used where

coated Ti screws were implanted into proximal tibiae and bone growth was assessed using micro-computed tomography (micro-CT). The 10mol% SrHA coating performed best with the greatest amount of bone formation. Biomechanical testing also found a significantly greater torque was required to remove the screws with 5 and 10mol% compared with the controls and the 20mol% coating. Interestingly the 20mol% SrHA was shown to have the highest cytotoxicity using *in vitro* methods with significantly lower numbers of MC3T3-E1 cells observed compared with the 5 and 10mol% groups. Offermanns et al (Offermanns et al., 2015) used two Sr doped HA coatings of 6.7 and 8.9at%, although these were applied using a magnetron co-sputtering process rather than EC deposition. Ti pins were coated and inserted into the femur of rats. Significantly greater bone contact and new bone formation was seen in the SrHA coated pins when compared with the uncoated group. Liang et al (Liang et al., 2015) again investigated EC coated SrHA Ti screws in ovariectomised rats. A higher rate of bone mineralisation and better osseointegration was observed in ovariectomised rats with a SrHA coated screw compared with those with uncoated screws. The presence of SrHA in this case enhances osseointegration even in an osteopenic *in vivo* model.

The work reported in this chapter of my thesis is not without limitations as the femoral condyle defect model utilised does not fully simulate the same mechanical forces that ingrowth collars are subjected to. Future work can include the use of another validated model such as using mid-diaphyseal implants as used in chapter 3. The mechanical environment associated with the relative structural stiffness of the implant compared to the surrounding bone may be one of the reasons that pores were not completely filled with bone. This may be because the stresses passing through our condyle plugs may be less than the surrounding bone and hence bone growth is not stimulated as dictated by Wolff's law (Chamay and Tschantz, 1972). It would be interesting in longer term studies to see if the coatings were able to maintain the level of bone formation seen after 6 weeks because one would predict that the bone would disappear as it is not loaded. The implants were kept in situ for 6 weeks and considerable differences in rates of osseointegration and bone formation was observed. The complete osseointegration of HA coated implants is achieved at 4 weeks however uncoated surfaces may require a longer period of 12 weeks to

achieve full potential (Lakstein et al., 2009). It is a possibility that if the study length were to be conducted over a longer period of time, the level of osseointegration and bone formation in the uncoated control group may be different to that found at 6 weeks. Keeping the implant in situ for longer may be something to consider in future studies. This is however very much dependant on the model being used as loading forces passing through the implant will vary according to anatomical location and method of fixation, which will ultimately affect bone growth.

## 6.5 Conclusion

In this final experimental chapter it has been shown that EC coatings when combined with an SLS porous implant significantly augments osseointegration *in vivo* when compared with an uncoated or plasma sprayed equivalent regardless of whether the pores are of SP or LP specifications.

## **Chapter 7. General Discussion and Conclusion**

## 7.1 General Discussion

AL is the most common cause of failure of endoprostheses used for limb salvage procedures after the resection of bone and soft tissue sarcomas (Jeys et al., 2008, Batta et al., 2014), particularly in younger patients (Unwin et al., 1996). Potentially, osseointegration at the shoulder of the implant may reduce the risk of AL by improving stress transfer within the cement mantle, reduce mechanical loosening, prevent inappropriate loading of the Ti alloy stem, which may lead to fatigue failure. It may also prevent migration of fluid and wear particles along the bone implant interface by forming a seal and load the bone in a physiological manner reducing bone resorption associated with stress shielding (Chao et al., 2004, Chao and Sim, 1990, Chao and Sim, 1992, Sim and Chao, 1979, Blunn and Wait, 1991, Taylor et al., 1997, Fromme et al., 2017, Ward et al., 1997). HA coated collars have been developed to encourage ECBB onto endoprostheses. Clinical and radiological studies have shown HA collar osseointegration to have a protective effect with improved implant survivorship (Coathup et al., 2013b, Coathup et al., 2015, Myers et al., 2007) with a significant reduction in survivorship seen in those implants that have not osseointegrated.

It is clear that ECBB and osseointegration must be optimised in order to prevent implant failure requiring multiple revision operations associated with high morbidity especially in young patient cohort. AM provides a novel method to produce fully porous ingrowth collars maximising the surface area for osseointegration and allowing for bone to permeate into the scaffold rather than attach to the surface. Traditional line-of-sight methods of HA coating does not allow for the porous scaffold to be coated adequately with HA which is needed to allow for direct bone contact and improved stress transfer (Fromme et al., 2017, Tanzer et al., 2003). EC deposition of coatings is an alternative biomimetic coating technique allowing coverage of the entirety of a complex structure (Redepenning et al., 2003, Redepenning et al., 1996).

The aim of my thesis was to develop a novel EC coated additively manufactured ingrowth collar using selectively laser sintered  $Ti_6Al_4V$  to be used as part of endoprostheses to enhance ECBB and osseointegration. The overall

hypothesis was that SLS manufactured porous ingrowth collars augmented with EC coatings allow for improved osseointegration when compared with the current solid plasma sprayed grooved collar design. This body of work is a culmination of clinical, *in vitro*, and *in vivo* studies that reinforces the need for such a construct, proves the construct works *in vivo*, shows development of EC coatings and finally confirms that the scaffolds perform better than current designs.

In modern orthopaedic oncology, nearly all patients with malignant bone and soft tissue sarcomas requiring endoprosthetic limb reconstruction undergo multidrug chemotherapy after Rosen et al (Rosen et al., 1979) first demonstrated that neoadjuvant chemotherapy was beneficial. The aim of the first study was to delineate whether chemotherapy affects osseointegration and early signs of radiographic loosening of distal femoral replacements using current HA ingrowth collars. The hypotheses for this chapter were that multidrug chemotherapy had a negative effect upon ECBB, osseointegration and loosening of the HA collar as part of distal femoral replacements.

In order to investigate this, a radiographic clinical study was performed comparing ECBB, gap size, osseointegration at the transection site and the overall RLL score (Coathup et al., 2013b) between patients who receive chemotherapy and patients not receiving chemotherapy as part of their treatment. Patients in both groups underwent reconstruction with DFRs, the former group for malignant bone and soft tissue sarcomas and the latter for benign giant cell tumours. Results confirmed significantly increased gap size at the shoulder of the collar abutting the transection site with a significantly increased RLL score in chemotherapy patients. This is thought to be due to osteolysis from increased strain at the shoulder (Perren, 2002) due the lack of osseointegration. No difference in ECBB was found between the groups. The data in this chapter suggests that multidrug chemotherapy affects osseointegration at the molecular level without seeming to influence radiographic bone growth at the transection site. This is also the first time that multidrug chemotherapy has been shown to accelerate radiographic signs of loosening of DFRs in the early years. This can be explained by the reduction in the levels of integrins, in particular fibronectin, as a result of chemotherapy

(Choate and Mosher, 1983, Brodin et al., 1983, Carminati et al., 2010) and therefore reducing osteoblastic attachment. It is also difficult to determine whether the findings in this chapter were due to the chemotherapy or the underlying cancerous process. *In vivo* studies have however shown reduced bone turnover with chemotherapy although osseointegration was not investigated the same way (Burchardt et al., 1983, Friedlaender et al., 1984, Pelker et al., 1985). The hypotheses that multidrug chemotherapy affects osseointegration and RLL score were therefore accepted however the hypothesis outlining the negative effect of chemotherapy on ECBB was rejected. There is a need to change the collar design to improve osseointegration in all patients including those receiving chemotherapy. For this reason, a fully porous SLS collar located at the shoulder of the implant may further improve the level and reliability of osseointegration achieved in this region (Bram et al., 2006).

Scaffolds with pore sizes between 20 $\mu$ m and 1500 $\mu$ m have been investigated for bone tissue engineering applications successfully (Elema et al., 1990, Pilliar, 1987, Engh, 1983, Hungerford and Kenna, 1983, Bucholz, 2002, Laptev et al., 2004, Murphy et al., 2010). EC HA coatings reported by Redepenning et al (Redepenning et al., 1996, Redepenning et al., 2003) allows for complex porous structure to be coated, although this had not been done previously with ingrowth collars. These types of coatings also favor adsorption of cell-adhesive proteins compared with plasma sprayed equivalents due to their microporous structure and increased solubility leading to local changes in pH and ion concentration (Samavedi et al., 2013).

One of the aims of my thesis was to answer whether a SLS ingrowth collar augmented with an EC deposited HA coating is able to be used as an ingrowth region as part of endoprostheses. The hypotheses for this were that an EC deposited HA coating can be applied to a SLS Ti<sub>6</sub>Al<sub>4</sub>V scaffold of which small pore (SP, Ø550 $\mu$ m) and large pore (LP, Ø1125 $\mu$ m) designs were made. It was hypothesised that bone would directly grow within the open cell porous structure with the small pore design allowing for the greatest amount of osseointegration.

This was an *in vivo* study using a validated ovine model where the control and experimental collars were inserted as part of a custom midshaft diaphyseal endoprosthesis over a 6 month period. Plasma sprayed solid grooved collars, plasma sprayed LP collars and EC coated SP collars were investigated. EC deposited coatings were evaluated using SEM, EDS and XRD. Retrieved specimens underwent radiological and histomorphometric analysis to investigate ECBB and osseointegration. Subgroup analysis of the SLS collars was performed to investigate the bone and soft tissue content of the pores. None of the implants or collars failed mechanically during the experimental period. Results showed that a calcium deficient HA coating was deposited onto the porous scaffold with a Ca:P of 1.53. XRD confirmed the presence of HA peaks with both crystalline and amorphous phases and an even coating accurately covering the undulating surface of the SLS implant was observed using SEM. Significantly greater ECBB was evident around the grooved solid collar control when compared with the experimental SLS collars. Histology confirmed that bone grew directly from the transection site into the porous collar regardless of the SP and LP design. Histomorphometric analysis revealed significantly greater surface area is present for bone attachment in the porous designs compared to the current design, with the SP porous design showing a significantly greater surface available compared with the LP collars. Significantly greater osseointegration occurred with the SP design when compared with the grooved collar. Subgroup analysis showed no difference in soft tissue and bone contents of the pores between the SP and LP SLS collars.

The results of this chapter confirm that the concept of a SLS porous collar is a better alternative to the standard collar design by allowing for greater osseointegration and this is achieved by direct bone ingrowth from the transection site rather than the traditional overgrowth seen on radiographs. The SP design as a result of its geometry allows for the largest surface for bone contact and this indeed did occur therefore the hypotheses outlined previously can be accepted. The question remains whether bone ingrowth into the scaffold is due to the pore size and geometry, as AM implants with fine tuned pore sizes can be osseoinductive and osseoconductive in itself (Van Bael et al., 2012, Yang et al., 2014, Wu et al., 2013), or whether it is due to the EC HA coating. This chapter has proven that EC coatings can be used to coat porous scaffolds

successfully and as a result osseointegration is augmented. The coatings were further investigated to ensure the appropriate physical characteristics of the coating were achieved as well as introducing substituted-HA coatings that may further improve bioactivity of the scaffold. This is described in chapters 4 and 5.

HA coatings on metal prostheses allows for osseointegration and improves implant fixation (Cook et al., 1988, Cook et al., 1992, Goodman et al., 2013) as commonly used metals such as Ti and its alloys have poor osseoinductive and osseoconductive properties (Garcia-Gareta et al., 2013). *In vitro* work has shown HA to promote osteogenic differentiation (Oreffo et al., 1998, Garcia-Gareta et al., 2013, Nishio et al., 2000, Ohgushi et al., 1993). Native bone however is not composed of stoichiometric HA as it contains various ionic substitutions (Gadow et al., 2010, Khan et al., 2014). Early work had identified Si as a important element required for mineralisation and connective tissue development (Carlisle, 1970, Schwarz and Milne, 1972). Silicate-substituted HA has been investigated with *in vitro* and *in vivo* studies confirming improved bioactivity (Patel et al., 2002, Patel et al., 2005, Gibson et al., 2009, Botelho et al., 2006, Hing et al., 2006, Coathup et al., 2011). Sr is another element known to improve bone growth and osseointegration. Its action is through a dual mechanism affecting both the OPG and RANKL pathways and in turn promoting osteoblastic activity as well as inhibiting osteoclast action (Brennan et al., 2009, Maimoun et al., 2010). *In vitro* and *in vivo* evidence has observed enhanced osseointegration with the use of Sr substituted HA (Capuccini et al., 2008, Maimoun et al., 2010, Yang et al., 2015, Offermanns et al., 2015, Yang et al., 2012b, Li et al., 2010, Thian et al., 2005). Si- and Sr-substituted HA coatings can be produced by a variety of methods including EC deposition (Liang et al., 2014, Li et al., 2011, Huang et al., 2013).

EC coatings are low cost with a simple set up and have the ability to coat complex geometries (Ducheyne et al., 1990). This method is able to produce uniform, highly pure coatings with adhesive strengths greater than plasma sprayed HA (Zhang et al., 2001). EC deposition also allows for close control of the greatest range of coating thicknesses compared with other processes (Sridhar et al., 2002, Li et al., 2011), which is advantageous as coatings that are too thick are susceptible to shear forces, delamination and failure (Wang et al.,

1993, de Groot et al., 1987). Physical characteristics of the coatings can be controlled by altering current densities and deposition times used (Redepenning et al., 1996, Redepenning et al., 2003).

The aim of chapter 4 was to produce and optimise EHA, ESiHA and ESrHA coatings on roughened Ti<sub>6</sub>Al<sub>4</sub>V surfaces and assess their bioactivity *in vitro*. The hypotheses for this chapter were that by changing coating parameters such as current density and deposition time, the coating can be optimised for use on a porous scaffold. Furthermore, substituted coatings were thought to increase osteogenic differentiation when compared with controls and EHA.

Methods derived from Redepenning et al (Redepenning et al., 1996, Redepenning et al., 2003), Li et al (Li et al., 2011) and Liang et al (Liang et al., 2014) were used to produce EHA, ESiHA and ESrHA coatings. A range of current densities and deposition times were used to ascertain optimal parameters. The surfaces of the coatings were observed under light microscopy and both the surface and thickness of the coatings produced with the combinations of each of these parameters were analysed using SEM. Crystal morphology observed with EHA, ESiHA and ESrHA coatings were in keeping with the original studies. Optimal coating uniformity and thickness out of those produced was observed with 10mA/cm<sup>2</sup>-15mins for EHA, 10mA/cm<sup>2</sup>-10mins for ESiHA and 15mA/cm<sup>2</sup>-20mins for ESrHA with thicknesses of 22.4±2.8µm, 29.6±2.6µm and 202±82.8µm respectively. These coatings were characterised using EDS and XRD, which confirmed a Si 0.29wt% and a Sr 6.4wt% with a Ca:P of 1.53, 1.36 and 1.65 for EHA, ESiHA and ESrHA coatings respectively. EC coatings were found to be less crystalline when compared with plasma sprayed HA.

Meng et al (Meng et al., 2006) and Mondragon-Corez et al (Mondragon-Cortez and Vargas-Gutierrez, 2004) describes electrokinetic phenomena where different sized ions of varying charges travel through solutions of differing saturations at a range of velocities. This explains the ability of varying currents, deposition times and electrolyte solutions to influence the rate of coating deposition and ultimately the coating thickness, and this chapter developed optimal methods to produce coatings of the appropriate chemical composition and thickness.

Adequate coating thicknesses for EHA and ESiHA were achieved to help prevent failure (Wang et al., 1993, de Groot et al., 1987). The ESrHA coating was too thick and therefore theoretically susceptible to failure and hence must be thinner for further work. This coating can also block smaller pore SLS collar designs, which could inhibit bone permeation through the scaffold.

The Ca:P of EHA (1.53) suggests a calcium deficient HA was produced when compared with stoichiometric HA (1.67). 1.53 is however comparable to the Ca:P of EC HA coatings from Garcia-Gareta et al (Garcia-Gareta et al., 2013) who also used EC deposition and falls within the range that describes HA in normal bone (1.37-1.87). The Ca:(P+Si) of the ESiHA coating produced (1.36) is just below the same range explaining why ESiHA possibly the reason why this coating exhibited lower bioactivity than the EHA and control groups during the cell culture experiments. ESrHA resembled stoichiometric HA the closest in terms of Ca:P (1.65) but showed a lack of bioactivity with significantly lower AlamarBlue® and ALP activity.

hMSCs were characterised successfully by demonstrating their multipotency by tridifferentiation. These hMSCs were seeded onto the EHA, ESiHA and ESrHA coatings as well as uncoated and plasma sprayed HA discs as controls over 28 days. AlamarBlue®, ALP, DNA assays as well as SEM analysis was performed at 3, 7 and 14 days timepoints with further SEM analysis at 28 days of culture. Control groups exhibited higher cellular metabolic activity when compared with experimental groups although at day 14 no statistical difference in metabolic activity was observed between the control groups and EHA and ESiHA. ESrHA performed poorly at all timepoints with regards to AlamarBlue® activity. hMSCs seeded onto ESrHA demonstrated the least osteogenic differentiation with EHA in particular performing significantly better. There was no difference in ALP activity observed between EHA, ESiHA and the control groups at 14 days of culture. Cells were observed on all surfaces at all timepoints using SEM with filopodial interaction seen with the varying crystals. An apparent fewer number of cells were observed on the ESrHA surface.

Cells respond to alterations in surface roughness and topography as a result of changes in cytoskeletal tension (McBeath et al., 2004). The roughness of the

uncoated discs (Ra 6711nm) allows for optimal differentiation (Boyan et al., 1999), although Anselme et al (Anselme et al., 2000) had shown increasing roughness to have the opposite effect. Formal quantitative analysis of surface roughness was not performed on the coatings; this may aid in explaining the disparity in bioactivity between each of the coatings. Incorporation of Si into HA is known to increase the dissolution of material in *in vivo* and *in vitro* models (Porter et al., 2004) and therefore a dissolution study of the coatings would have been prudent to complete for both ESiHA and ESrHA as this would affect their bioactivity. The 0.29wt% of Si in ESiHA was below the optimal 0.8wt% (Hing et al., 2006) that would inevitably lead to poorer bioactivity, although 0.33wt% has been reported to have favourable results (Zhang and Zou, 2009). Increasing the Si content of the ESiHA coating would, in theory, improve its bioactivity although this in turn may inhibit crystal size (Li et al., 2011).

The potential causes of ESrHA exhibiting poor bioactivity may lie in its surface topography, dissolution profile and thickness. The ESrHA Ca:P resembled HA the closest out of the other EC coatings and hence unlikely to be the limiting factor. The Sr 1.68at% is lower than the 5at% reported to induce cellular changes (Drevet and Benhayoune, 2013). ESrHA coating is also less crystalline when the levels of Sr incorporated within it are so low. XRD revealed ESrHA to contain amorphous phases and therefore the dissolution of Sr could possibly be too great leading to local cellular toxicity. Sr dissolution can be improved by improving the crystallinity of ESrHA by increasing the Sr content in the coating and annealing the coating post deposition. ESrHA can be optimised further by reducing the thickness and therefore improve possible coating failure when evaluated in an *in vivo* model.

EC coatings are able to be modified by changing coating parameters and therefore this hypothesis is able to be accepted however substituted coatings did not show significantly better bioactivity than EHA and control groups and hence this hypothesis is rejected. From chapter 4 it is evident that there were a number of further refinements that needed to be made to the substituted coatings before evaluating them *in vivo*. These further optimisations were the focus of chapter 5.

Samples for chapter 5 were prepared the same way but with the additional step of acid etching. This has shown to improve interlocking (Mohseni et al., 2014) and nucleation (Lakstein et al., 2009) of HA coatings and therefore reduce the risk of coating failure further. The electrolyte solution used to produce ESiHA was changed to increase Si content in the coating. The new coating (ESiHAll) was based on the methods of Huang et al (Huang et al., 2013) who used nano-silicate as the source for Si. Post-coating annealing was used to improve crystallinity of ESiHAll.

Coating thickness is an indicator of coating volume being deposited. The thickness of ESrHA should be reduced, given the higher risk of mechanical failure and theoretical high dissolution rate. The level of Sr being eluted into the local vicinity will be reduced as a result. Coating parameters used to produce ESrHA in chapter 4 were altered to produce a thinner ESrHAll coating.

Dissolution of ESiHA and ESrHA was not evaluated in chapter 4 and therefore only a comparison in the dissolution profiles between ESiHAll and ESrHAll can be made in chapter 5. Using ICPMS would have allowed dissolution to be analysed appropriately. Unfortunately ICPMS could not be used, whilst these experiments were being performed. As an alternative the coating on the discs at each of the time-points of the cell culture experiment underwent EDS analysis and in order to determine the remaining amount of Si and Sr in the ESiHAll and ESrHAll coatings respectively. This would be an indicator as to how much Si and Sr had eluted locally.

The aims of chapter 5 were to refine and optimise the ESiHA and ESrHA coatings further, assess the bioactivity of the new ESiHAll and ESrHAll coatings together with the EHA and control coatings from chapter 4 as well as perform studies on dissolution and quantify surface roughness. The hypotheses for the chapter were that by increasing Si content in ESiHA and reducing the thickness of the ESrHA will improve bioactivity.

The EHA coating was produced using the same parameters (10mA/cm<sup>2</sup>-15mins) as before on the new acid etched Ti<sub>6</sub>Al<sub>4</sub>V discs. Two variants of the new ESiHAll was produced on acid etched discs using methods based on

Huang et al (Huang et al., 2013) using a current density of  $0.8\text{mA}/\text{cm}^2$  over 30 and 45 minutes. After deposition the coatings underwent annealing. Two variants of the ESrHAlI coating were produced using  $15\text{mA}/\text{cm}^2$  over 2.5 and 5 minute deposition times. In addition to the techniques used in chapter 4, non-contact surface profilometry and EDS were used to characterise the surface roughness and Si/Sr dissolution.

ESiHAlI exhibited a heterogeneous array of clumped needle shaped crystals interspersed with large plate-like crystals similar to those found in EHA. Significantly thicker ESiHAlI coatings were deposited at 45 minutes ( $19.2\mu\text{m}$ ) when compared with 30 minutes ( $9.9\mu\text{m}$ ) and therefore the  $0.8\text{mA}/\text{cm}^2$ -45 minute coating was chosen for further characterisation. The coating contained a higher Si wt% (1.63) albeit with a Ca:P of 1.13 that may be a result of suboptimal annealing treatment. XRD suggested greater crystallinity compared with ESiHA. It is also evident that the ESiHAlI coating is a composite coating of HA and  $\text{CaSiO}_3$  (Huang et al., 2013), which would explain the heterogeneously shaped crystals. ESrHAlI was found to have a very homogenous coating of shorter crystals compared with ESrHA. The  $15\text{mA}/\text{cm}^2$ -5minute ESrHAlI coating was chosen due to its thickness and uniformity, this coating was also thinner ( $14.2\mu\text{m}$ ) than that of ESrHA from the previous chapter ( $202\mu\text{m}$ ). The ESrHAlI coating also exhibited a lower Sr wt% of 4.08 compared with that of ESrHA (6.41) with a Ca:P which was found to be reduced to 1.31.

EDS analysis suggests that a significant proportion of the Si within the ESiHAlI coating eluted into the media within the first 3 days with only 3% of the original Si amount remained in the coating at 28 days. Si elution is known to affect cell proliferation favourably (Shie et al., 2011) however this is dose-dependent (Pietak et al., 2007) and high Si concentrations can have adverse effects (Gibson et al., 2009, Hing et al., 2006, Botelho et al., 2006). By comparison, Sr loss from ESrHAlI was more consistent with 62.8% of the original amount remaining in the coating. Profilometry of the groups revealed ESiHAlI to have the roughest surface with the uncoated being the least. EC coatings were generally significantly rougher than control groups although no difference was found between plasma sprayed HA and ESrHAlI.

Non-contact profilometry confirms that EC coatings have significantly greater surface roughness that increases cell synthetic activity (Boyan et al., 1999). The uncoated roughened disc surface was the smoothest, which allows for high levels of proliferation (Washburn et al., 2004). Both EHA and ESiHAlI were also significantly rougher than that of plasma sprayed HA. Amongst the EC coatings, ESiHAlI was the roughest followed by EHA and finally ESrHAlI.

Ovine MSCs were cultured on these discs to assess coating bioactivity. Cell culture was performed with osteogenic media under standard conditions. The cells cultured on ESrHAlI exhibited significantly greater metabolic activity when compared with EHA and ESiHAlI although no difference was found when compared against the controls at day 3. No difference was found between the groups at the other timepoints. The variability in metabolic activity observed at other timepoints can possibly be due to cell death as a result of cells reaching confluency, furthermore differentiated cells rarely divide compared with immature cells which is reflected by stable or low AlamarBlue® activity.

Cell differentiation was evaluated using ALP assays, which showed no difference between the experimental and control groups at any of the timepoints. SEM analysis revealed filopodial and nanopodial interactions between the cells on the EC coatings but the same was not observed on the control coatings. Peak ALP expression can be seen at 20 days of culture (Stein et al., 1996) and this is important as nanoscale changes in topography can dictate cell phenotype with disordered topographies showing greater cellular adhesion and differentiation (Dalby et al., 2014, Dalby et al., 2007, McMurray et al., 2011). The higher ALP expression of cells seeded onto ESiHAlI and ESrHAlI coatings may be due to their rougher topographical profile when compared with EHA. HA crystal deposition was observed on all the coatings at the later time points although crystal clusters on ESrHAlI were found as early as day 3. This suggested that Sr elution locally may have a greater osteogenic effect leading to earlier mineralisation when compared with other coatings.

Cell culture protocols in this chapter used osteogenic media compared with chapter 4 that did not use osteogenic supplementation. There is an argument that the use of osteogenic media may marginalise the contribution of CaP

coatings on cell behaviour, many studies exist reporting favourable effects on cell behaviour in both their presence and absence. A number of *in vitro* studies have shown increased ALP, osteocalcin and bone sialoprotein on HA (Lee et al., 2010) and  $\beta$ -tricalcium phosphate (Eslaminejad et al., 2007) loaded scaffolds compared with controls in osteogenic media. A range of osseoinductive capabilities have also been shown in the absence of osteogenic media *in vitro* with increased expression of the same markers on scaffolds containing a variety of CaP ceramics (Müller et al., 2008, Polini et al., 2011, Guha et al., 2009).

Overall no statistical difference was observed in the bioactivity of ESiHAII compared with the other coatings as a result of increasing the Si wt%. By reducing the thickness of ESrHA to form ESrHAII, a significant improvement in bioactivity was observed overall when compared with other EC coatings and control groups.

The next step in my thesis was to evaluate these coatings in an *in vivo* environment. The performance of the scaffold *in vivo* is difficult to predict from the *in vitro* data as the cells interacting with the scaffold *in vivo* are unlikely to be mesenchymal in origin and the complex mechanisms involved in bone formation and osseointegration are also difficult to reproduce *in vitro*. The aim of my final experimental chapter was to use a validated femoral condyle defect model to evaluate the osseointegration of SLS Ti<sub>6</sub>Al<sub>4</sub>V porous implants augmented with EHA, ESiHAII and ESrHAII. EC coating enabled complete coverage of the porous scaffold with plasma spraying only allowing for the external surface of the scaffold to be coated. Bone growth on all implants was found at 6 weeks with centripetal bone growth within pores observed only in EC coated implants. SEM analysis confirmed the presence of EC coatings at 6 weeks. Significantly greater absolute osseointegration was found overall in the EC coated implants compared with uncoated implants; with the EHA small pore combination showing the highest proportion of surface osseointegration with 77.7% of its surface having bone contact. This is significantly higher than all uncoated implants and small pore plasma sprayed HA implants. The EHA small pore combination exhibited significantly higher bone and lower soft tissue content within its pores when compared with uncoated large pore implants. No

significant difference in osseointegration was seen between the EC coated groups. EHA large pore and ESrHAII small pore combinations also exhibited significantly greater osseointegration when compared with both small pore and large pore uncoated varieties

The presence of all the EC coatings at 6 weeks together with enhanced osseointegration suggests there is no need for a thicker, more crystalline coating typical of plasma sprayed HA on porous scaffolds as greater osseointegration is achieved with the EC coatings.

The work in this chapter is, at the time of writing this thesis, the first time EC coated SLS implants have been evaluated *in vivo*. EC coatings have been shown to augment osseointegration on solid implants (Wang et al., 2006, Schmidmaier et al., 2002, Yang et al., 2012b, Liang et al., 2015) however this is the first to prove its ability to augment porous structures. Importantly, I have shown in this chapter that EHA coated large pore and small pore implants both showed greater osseointegration than controls and therefore a bioactive coating can enhance bone formation regardless of pore size. ESiHAII and ESrHAII did not show greater bioactivity when compared with EHA, this may be due to their lower Ca:P, which is known to effect the stability of the compound. The benefits of Si and Sr substitution on bone growth can be offset by the inherent instability of the coating *in vivo* (Bose and Tarafder, 2012).

The hypothesis that small pore scaffolds augmented with EC coatings provide the greatest osseointegration can be accepted. ESrHAII did not provide any further osseointegration compared with EHA or ESiHAII and therefore the hypothesis that ESrHAII is the optimal EC coating cannot be accepted.

The model used in this final chapter may limit the amount of bone formed and hence the osseointegration observed. Pores were not completely filled in any of the implants as the loads passing through the implant were not great enough to induce further bone formation. It may be advantageous to use the mid-diaphyseal model used in chapter 3 to more accurately replicate the forces that these scaffolds may be subjected to clinically. Micro-structural characteristics of EC coatings, amorphous phases and lower crystallinity compared with plasma

sprayed HA allow for local dissolution, pH and ion concentration changes which all maximise the adsorption of circulating cell-adhesion proteins (Samavedi et al., 2013). This is clearly of benefit to optimise osseointegration in the aforementioned patient population.

## 7.2 General Conclusions

The work in this thesis identified a clinical rationale for developing a novel ingrowth collar, which would enhance osseointegration. Further *in vitro* and *in vivo* work helped to develop a coated SLS porous collar that improves bone ingrowth and osseointegration.

This work has expanded the evidence base for a number of novel concepts. It is the first study to show accelerated radiographic signs of endoprosthetic loosening in patients receiving chemotherapy. This work has identified a group of patients which must be followed-up with more stringent protocols in order to identify signs of early loosening. Although osseointegration is multifactorial, the collar component can be optimised to provide an improved environment for osseointegration.

This thesis is the first to successfully use selective laser sintered Ti<sub>6</sub>Al<sub>4</sub>V scaffolds for ingrowth collars to enable improved osseointegration. This new application of an additive manufacturing technique has allowed the production of a scaffold with a highly specific geometry and pore size. This porous structure allows for bone to permeate through it allowing for a better mechanism of osseointegration that unlike surface ongrowth is not as susceptible to shear forces. Bioactive electrochemical coatings have been developed that can be applied to porous structures and allow them to be covered completely. This is very different from the current plasma spray method that is used commercially to coat orthopaedic implants. Plasma spraying does not allow coverage of the inner pores as well as potentially blocking pores thus preventing bony ingrowth in an open porous structure.

The augmentation of a porous structure with an electrochemical coating provides a scaffold which has been shown by this work to be highly osseoconductive. This completely novel scaffold has the potential to greatly reduce the issue of aseptic loosening across orthopaedics and thus its impact upon orthopaedic implant technology could be vast. During the time of writing this thesis implant companies have started to release new products, harnessing

porous laser sintered scaffolds, although they have not yet augmented these with electrochemical coatings.

This innovative scaffold technology can be translated across a broad spectrum of orthopaedic subspecialties. Apart from its use in endoprostheses, which is the primary subject of this thesis it is easily applied to joint arthroplasty where aseptic loosening is a problem. This includes both primary and revision arthroplasty of the shoulder, elbow, hip, knee and ankle. With approximately 100,000 hip replacements alone being performed in the UK during 2016, the potential to improve implant longevity and patient outcomes for joint arthroplasty cannot be underestimated.

### 7.3 Future Work

*In vivo* studies evaluating the effect of chemotherapy on bone turnover have been published however there are no publications on the effect of chemotherapy on the osseointegration. Although chapter one helps to address this, the question still remains whether osseointegration is also affected by the impact of an underlying sarcoma on the patients' metabolism and physiology. The next step is to conduct a large animal study using current collar designs as part of a diaphyseal implant with one group receiving chemotherapy and the control not. Chemotherapy similar to the routine used to treat bone cancers in humans have previously been used in animals. Radiological and histological analysis should be completed at 6 months. It will also be beneficial to use bone markers to compare the rate of bone apposition between the groups.

Further coating refinement is required for the ESiHAlI and ESrHAlI coatings. The Si wt% needs be increased to reach the optimal 0.8wt% as well as improving the Ca:P. Although improved bioactivity was observed with the thinner ESrHAlI coating, the at% of Sr is lower than that of the optimal 3-7% needed. These can be achieved by further modification of the electrolyte solutions used to deposit the coatings.

The stability of all coatings could be improved by post-deposition annealing in a vacuum furnace. Dissolution profiles should be more accurately determined with the use of ICPMS. Further *in vitro* assessment in both osteogenic and non-osteogenic media may help to determine bioactivity and osseoinductive nature of these coatings. Results from my thesis suggest that these EC coatings dissolve between 6 weeks and 6 months in the *in vivo* environment. It is important to evaluate the period of time the coatings remain on the scaffold. These can be assessed by inserting coated porous scaffolds into bone defects and retrieving them over regular time points for histological, SEM and elemental analysis. The dissolution of the coatings would probably be different depending on whether they were osseointegrated or if there was a soft tissue interface.

Using a femoral condyle defect model does not replicate the same biomechanical environment ingrowth collars are subjected to clinically.

Therefore it would be sensible to conduct an *in vivo* study, which uses SLS porous EC coated collars as part of a mid-diaphyseal implant.

More interestingly, the small pore SLS scaffold has now been manufactured as part of a proximal femoral replacement (Figure 7-1). This implant will be used in a clinical trial based at the Royal National Orthopaedic Hospital to evaluate whether these novel collars provide improved osseointegration in patients undergoing proximal femoral reconstruction as a result of bone and soft tissue sarcomas and failed total hip replacements due to aseptic and septic loosening.



Figure 7-1 SLS Ti<sub>6</sub>Al<sub>4</sub>V proximal femoral replacement. Assembled (left) and exploded (right) implant views shown with (a) intramedullary stem, (b) ingrowth collar and (c) proximal femur with ingrowth regions for soft tissue attachments.

## **Chapter 8. Bibliography**

2013. *Mayo Clinic: 3D Printer Uses CT Scan to Print Out Model of Hip Joint Before Surgery* [Online]. Mayo Clinic. Available: <http://newsnetwork.mayoclinic.org/discussion/3d-printer-uses-ct-scan-to-print-out-model-of-hip-joint-before-surgery/> [Accessed 6/9/2015].
2017. Arcam and Lima celebrate anniversary. *Metal Powder Report*, 72, 206.
- ABDEL-HADY GEPREEL, M. & NIINOMI, M. 2013. Biocompatibility of Ti-alloys for long-term implantation. *Journal of the Mechanical Behavior of Biomedical Materials*, 20, 407-415.
- AGARWAL, M., GULIA, A., RAVI, B., GHYAR, R. & PURI, A. 2010. Revision of broken knee megaprotheses: new solution to old problems. *Clinical Orthopaedics and Related Research*®, 468, 2904-2913.
- AI-AQL, Z., ALAGL, A. S., GRAVES, D. T., GERSTENFELD, L. C. & EINHORN, T. A. 2008. Molecular mechanisms controlling bone formation during fracture healing and distraction osteogenesis. *Journal of dental research*, 87, 107-118.
- ALBAYRAK, O., EL-ATWANI, O. & ALTINTAS, S. 2008. Hydroxyapatite coating on titanium substrate by electrophoretic deposition method: effects of titanium dioxide inner layer on adhesion strength and hydroxyapatite decomposition. *Surface and coatings Technology*, 202, 2482-2487.
- ALBREKTSSON, T., BRÅNEMARK, P.-I., HANSSON, H.-A. & LINDSTRÖM, J. 1981. Osseointegrated titanium implants: requirements for ensuring a long-lasting, direct bone-to-implant anchorage in man. *Acta Orthopaedica Scandinavica*, 52, 155-170.
- ALBREKTSSON, T. & JOHANSSON, C. 2001. Osteoinduction, osteoconduction and osseointegration. *Eur Spine J*, 10 Suppl 2, S96-101.
- ALLEN, M. R., HOCK, J. M. & BURR, D. B. 2004. Periosteum: biology, regulation, and response to osteoporosis therapies. *Bone*, 35, 1003-12.
- ALLISON, D. C., CARNEY, S. C., AHLMANN, E. R., HENDIFAR, A., CHAWLA, S., FEDENKO, A., ANGELES, C. & MENENDEZ, L. R. 2012. A meta-analysis of osteosarcoma outcomes in the modern medical era. *Sarcoma*, 2012, 704872.
- AMANKWAH, E. K., CONLEY, A. P. & REED, D. R. 2013. Epidemiology and therapies for metastatic sarcoma. *Clin Epidemiol*, 5, 147-162.
- ANDERSON, M. E. 2016. Update on survival in osteosarcoma. *Orthopedic Clinics of North America*, 47, 283-292.
- ANSELME, K., LINEZ, P., BIGERELLE, M., LE MAGUER, D., LE MAGUER, A., HARDOUIN, P., HILDEBRAND, H., IOST, A. & LEROY, J. 2000. The relative influence of the topography and chemistry of TiAl6V4 surfaces on osteoblastic cell behaviour. *Biomaterials*, 21, 1567-1577.
- AVEDIAN, R., GOLDSBY, R., KRAMER, M. & O'DONNELL, R. 2007. Effect of chemotherapy on initial compressive osseointegration of tumor endoprostheses. *Clinical orthopaedics and related research*, 459, 48-53.
- BALAMURUGAN, A., BALOSSIER, G., TORRES, P., MICHEL, J. & FERREIRA, J. 2009. Sol-gel synthesis and spectrometric structural evaluation of strontium substituted hydroxyapatite. *Materials Science and Engineering: C*, 29, 1006-1009.
- BANERJEE, C., MCCABE, L. R., CHOI, J. Y., HIEBERT, S. W., STEIN, J. L., STEIN, G. S. & LIAN, J. B. 1997. Runt homology domain proteins in osteoblast differentiation: AML3/CBFA1 is a major component of a bone-specific complex. *Journal of cellular biochemistry*, 66, 1-8.

- BANERJEE, S., KULESHA, G., KESTER, M. & MONT, M. A. 2014. Emerging technologies in arthroplasty: additive manufacturing. *The journal of knee surgery*, 27, 185-191.
- BAO, Q., CHEN, C., WANG, D., JI, Q. & LEI, T. 2005. Pulsed laser deposition and its current research status in preparing hydroxyapatite thin films. *Applied Surface Science*, 252, 1538-1544.
- BARNES, J. E. 2015. Manufacturing a human heel in titanium via 3D printing. *The Medical journal of Australia*, 202, 118.
- BARRERE, F., VAN BLITTERSWIJK, C. A. & DE GROOT, K. 2006. Bone regeneration: molecular and cellular interactions with calcium phosphate ceramics. *Int J Nanomedicine*, 1, 317-32.
- BATTA, V., COATHUP, M., PARRATT, M., POLLOCK, R., ASTON, W., CANNON, S., SKINNER, J., BRIGGS, T. & BLUNN, G. 2014. Uncemented, custom-made, hydroxyapatite-coated collared distal femoral endoprostheses. *Bone Joint J*, 96, 263-269.
- BELLANOVA, L., PAUL, L. & DOCQUIER, P. L. 2013. Surgical guides (patient-specific instruments) for pediatric tibial bone sarcoma resection and allograft reconstruction. *Sarcoma*, 2013, 787653.
- BIAN, W., LI, D., LIAN, Q., LI, X., ZHANG, W., WANG, K. & JIN, Z. 2012. Fabrication of a bio-inspired beta-Tricalcium phosphate/collagen scaffold based on ceramic stereolithography and gel casting for osteochondral tissue engineering. *Rapid Prototyping Journal*, 18, 68-80.
- BIGI, A., BRACCI, B., CUISINIER, F., ELKAIM, R., FINI, M., MAYER, I., MIHAILESCU, I. N., SOCOL, G., STURBA, L. & TORRICELLI, P. 2005. Human osteoblast response to pulsed laser deposited calcium phosphate coatings. *Biomaterials*, 26, 2381-2389.
- BIZZOTTO, N., TAMI, I., SANTUCCI, A., ADANI, R., POGGI, P., ROMANI, D., CARPEGGIANI, G., FERRARO, F., FESTA, S. & MAGNAN, B. 2016. 3D Printed replica of articular fractures for surgical planning and patient consent: a two years multi-centric experience. *3D Printing in Medicine*, 2, 2.
- BLOEBAUM, R. D., BACHUS, K. N., JENSEN, J. W., SCOTT, D. F. & HOFMANN, A. A. 1998. Porous-coated metal-backed patellar components in total knee replacement. A postmortem retrieval analysis. *J Bone Joint Surg Am*, 80, 518-28.
- BLOEBAUM, R. D., BEEKS, D., DORR, L. D., SAVORY, C. G., DUPONT, J. A. & HOFMANN, A. A. 1994. Complications with hydroxyapatite particulate separation in total hip arthroplasty. *Clin Orthop Relat Res*, 19-26.
- BLUNN, G. W. & WAIT, M. E. 1991. Remodelling of bone around intramedullary stems in growing patients. *J Orthop Res*, 9, 809-19.
- BOANINI, E., TORRICELLI, P., FINI, M., SIMA, F., SERBAN, N., MIHAILESCU, I. N. & BIGI, A. 2012. Magnesium and strontium doped octacalcium phosphate thin films by matrix assisted pulsed laser evaporation. *Journal of inorganic biochemistry*, 107, 65-72.
- BOBYN, J. D., PILLIAR, R. M., CAMERON, H. U. & WEATHERLY, G. C. 1980. The optimum pore size for the fixation of porous-surfaced metal implants by the ingrowth of bone. *Clin Orthop Relat Res*, 263-70.
- BOCCACCINI, A. R., KEIM, S., MA, R., LI, Y. & ZHITOMIRSKY, I. 2010. Electrophoretic deposition of biomaterials. *Journal of The Royal Society Interface*, 7, S581-S613.
- BODEN, S. D. & SUMNER, D. R. 1995. Biologic factors affecting spinal fusion and bone regeneration. *Spine*, 20, 113S.

- BOHNER, M. & BAUMGART, F. 2004. Theoretical model to determine the effects of geometrical factors on the resorption of calcium phosphate bone substitutes. *Biomaterials*, 25, 3569-3582.
- BONEWALD, L. F. 1999. Establishment and characterization of an osteocyte-like cell line, MLO-Y4. *J Bone Miner Metab*, 17, 61-5.
- BOONEN, B., SCHOTANUS, M. G. & KORT, N. P. 2012. Preliminary experience with the patient-specific templating total knee arthroplasty. *Acta Orthop*, 83, 387-93.
- BORGGREVE, J. 1930. Kniegelenkersatz durch das in der Beinlängsachse um 180 gedrehte Fußgelenk. *Arch Orthop Unfallchir*, 28, 175-178.
- BORON, W. F. & BOULPAEP, E. L. 2003. Medical physiology. A cellular and molecular approach. Saunders. Elsevier Science), Philadelphia.
- BORSARI, V., GIAVARESI, G., FINI, M., TORRICELLI, P., SALITO, A., CHIESA, R., CHIUSOLI, L., VOLPERT, A., RIMONDINI, L. & GIARDINO, R. 2005. Physical characterization of different-roughness titanium surfaces, with and without hydroxyapatite coating, and their effect on human osteoblast-like cells. *Journal of Biomedical Materials Research Part B: Applied Biomaterials*, 75B, 359-368.
- BOSCO, R., EDREIRA, E. R. U., WOLKE, J. G. C., LEEUWENBURGH, S. C. G., VAN DEN BEUCKEN, J. J. J. P. & JANSEN, J. A. 2013. Instructive coatings for biological guidance of bone implants. *Surface and Coatings Technology*, 233, 91-98.
- BOSE, S., FIELDING, G., TARAFDER, S. & BANDYOPADHYAY, A. 2013. Understanding of dopant-induced osteogenesis and angiogenesis in calcium phosphate ceramics. *Trends in Biotechnology*, 31, 594-605.
- BOSE, S. & TARAFDER, S. 2012. Calcium phosphate ceramic systems in growth factor and drug delivery for bone tissue engineering: A review. *Acta Biomaterialia*, 8, 1401-1421.
- BOSKEY, A., WRIGHT, T. & BLANK, R. 1999. Collagen and bone strength. *Journal of Bone and Mineral Research*, 14, 330-335.
- BOTELHO, C. M., BROOKS, R. A., BEST, S. M., LOPES, M. A., SANTOS, J. D., RUSHTON, N. & BONFIELD, W. 2006. Human osteoblast response to silicon-substituted hydroxyapatite. *J Biomed Mater Res A*, 79, 723-30.
- BOWERS, G. N. & MCCOMB, R. B. 1966. A continuous spectrophotometric method for measuring the activity of serum alkaline phosphatase. *Clinical Chemistry*, 12, 70-89.
- BOXALL, S. A. J., E 2012. Markers for Characterization of Bone Marrow Multipotential Stromal Cells. *Stem Cells International*, 2012, 12.
- BOYAN, B. D., SYLVIA, V. L., LIU, Y., SAGUN, R., COCHRAN, D. L., H. LOHMANN, C., DEAN, D. D. & SCHWARTZ, Z. 1999. Surface roughness mediates its effects on osteoblasts via protein kinase A and phospholipase A2. *Biomaterials*, 20, 2305-2310.
- BRAM, M., SCHIEFER, H., BOGDANSKI, D., KÖLLER, M., BUCHKREMER, H. P. & STÖVER, D. 2006. Implant surgery: How bone bonds to PM titanium. *Metal Powder Report*, 61, 26-31.
- BRANEMARK, P.-I. 1977. Osseointegrated implants in the treatment of the edentulous jaw. Experience from a 10-year period. *Scand J. Plast. Reconstr Surg.*, 11, 1-32.
- BRAV, E. A., MC, F. J. & MILLER, J. A. 1958. The replacement of shaft defects of long bones by metallic prostheses. *Am J Surg*, 95, 752-60.

- BRENNAN, T., RYBCHYN, M., GREEN, W., ATWA, S., CONIGRAVE, A. & MASON, R. 2009. Osteoblasts play key roles in the mechanisms of action of strontium ranelate. *British journal of pharmacology*, 157, 1291-1300.
- BRODIN, B., LIEDEN, G., MALM, C. & VIKROT, O. 1983. Plasma fibronectin deficiency during chemotherapy of acute myeloid leukaemia. *Scand J Haematol*, 30, 247-9.
- BRODSKY, B. & PERSIKOV, A. V. 2005. Molecular structure of the collagen triple helix. *Adv Protein Chem*, 70, 301-39.
- BUCHOLZ, R. W. 2002. Nonallograft osteoconductive bone graft substitutes. *Clin Orthop Relat Res*, 44-52.
- BURCHARDT, H., GLOWCZEWSKIE, F. & ENNEKING, W. 1983. The effect of Adriamycin and methotrexate on the repair of segmental cortical autografts in dogs. *J Bone Joint Surg Am*, 65, 103-108.
- BURDER, S. P., FINK, D. J. & CAPLAN, A. I. 1994. Mesenchymal stem cells in bone development, Bone repair, and skeletal regeneration therapy. *Journal of Cellular Biochemistry*, 56, 283 - 294.
- CAETANO-LOPES, J., CANHAO, H. & FONSECA, J. E. 2007. Osteoblasts and bone formation. *Acta Reumatol Port*, 32, 103-10.
- CANNON, S. R. 2015. The use of megaprosthesis in the treatment of periprosthetic knee fractures. *International orthopaedics*, 39, 1945-1950.
- CAPUCCINI, C., TORRICELLI, P., SIMA, F., BOANINI, E., RISTOSCU, C., BRACCI, B., SOCOL, G., FINI, M., MIHAILESCU, I. & BIGI, A. 2008. Strontium-substituted hydroxyapatite coatings synthesized by pulsed-laser deposition: in vitro osteoblast and osteoclast response. *Acta Biomaterialia*, 4, 1885-1893.
- CARLISLE, E. M. 1970. Silicon: a possible factor in bone calcification. *Science*, 167, 279-80.
- CARMINATI, P. O., MELLO, S. S., FACHIN, A. L., JUNTA, C. M., SANDRIN-GARCIA, P., CARLOTTI, C. G., DONADI, E. A., PASSOS, G. A. & SAKAMOTO-HOJO, E. T. 2010. Alterations in gene expression profiles correlated with cisplatin cytotoxicity in the glioma U343 cell line. *Genet Mol Biol*, 33, 159-68.
- CHAE, M. P., HUNTER-SMITH, D. J., SPYCHAL, R. T. & ROZEN, W. M. 2014. 3D volumetric analysis for planning breast reconstructive surgery. *Breast Cancer Research and Treatment*, 146, 457-460.
- CHAMAY, A. & TSCHANTZ, P. 1972. Mechanical influences in bone remodeling. Experimental research on Wolff's law. *Journal of biomechanics*, 5, 173-180.
- CHAO, E. Y., FUCHS, B., ROWLAND, C. M., ILSTRUP, D. M., PRITCHARD, D. J. & SIM, F. H. 2004. Long-term results of segmental prosthesis fixation by extracortical bone-bridging and ingrowth. *J Bone Joint Surg Am*, 86-a, 948-55.
- CHAO, E. Y. & SIM, F. H. 1990. Composite fixation of segmental bone/joint defect replacement (SDR) prostheses. Biological and biomechanical justifications. *Chir Organi Mov*, 75, 171-3.
- CHAO, E. Y. & SIM, F. H. 1992. Composite fixation of salvage prostheses for the hip and knee. *Clin Orthop Relat Res*, 91-101.
- CHARNLEY, J. 1970. Total hip replacement by low-friction arthroplasty. *Clin Orthop Relat Res*, 72, 7-21.
- CHEN, Y.-L., LIN, T., LIU, A., SHI, M.-M., HU, B., SHI, Z.-L. & YAN, S.-G. 2015. Does hydroxyapatite coating have no advantage over porous coating in primary total hip arthroplasty? A meta-analysis. *Journal of orthopaedic surgery and research*, 10, 1.

- CHEN, Y. X., ZHANG, K., HAO, Y. N. & HU, Y. C. 2012. Research status and application prospects of digital technology in orthopaedics. *Orthopaedic surgery*, 4, 131-138.
- CHEUNG, J. T. 1994. History and fundamentals of pulsed laser deposition. *Pulsed laser deposition of thin films*, 1.
- CHOATE, J. J. & MOSHER, D. F. 1983. Fibronectin concentration in plasma of patients with breast cancer, colon cancer, and acute leukemia. *Cancer*, 51, 1142-7.
- CIOCCA, L., DE CRESCENZIO, F., FANTINI, M. & SCOTTI, R. 2010. Rehabilitation of the nose using CAD/CAM and rapid prototyping technology after ablative surgery of squamous cell carcinoma: a pilot clinical report. *The International journal of oral & maxillofacial implants*, 25, 808-812.
- CLARKE, B. 2008. Normal bone anatomy and physiology. *Clin J Am Soc Nephrol*, 3 Suppl 3, S131-9.
- COATHUP, M., KALIA, P., KONAN, S., MIRZA, K. & BLUNN, G. 2013a. A comparison of allogeneic and autologous mesenchymal stromal cells and osteoprogenitor cells in augmenting bone formation around massive bone tumor prostheses. *Journal of biomedical materials research. Part A*, 101, 2210-8.
- COATHUP, M. J., BATTI, V., POLLOCK, R. C., ASTON, W. J., CANNON, S. R., SKINNER, J. A., BRIGGS, T. W., UNWIN, P. S. & BLUNN, G. W. 2013b. Long-term survival of cemented distal femoral endoprostheses with a hydroxyapatite-coated collar: a histological study and a radiographic follow-up. *J Bone Joint Surg Am*, 95, 1569-75.
- COATHUP, M. J., BLUNN, G. W., FLYNN, N., WILLIAMS, C. & THOMAS, N. P. 2001. A comparison of bone remodelling around hydroxyapatite-coated, porous-coated and grit-blasted hip replacements retrieved at post-mortem. *J Bone Joint Surg Br*, 83, 118-23.
- COATHUP, M. J., SAMIZADEH, S., FANG, Y. S., BUCKLAND, T., HING, K. A. & BLUNN, G. W. 2011. The osteoinductivity of silicate-substituted calcium phosphate. *J Bone Joint Surg Am*, 93, 2219-2226.
- COATHUP, M. J., SANGHRAJKA, A., ASTON, W. J., GIKAS, P. D., POLLOCK, R. C., CANNON, S. R., SKINNER, J. A., BRIGGS, T. W. & BLUNN, G. W. 2015. Hydroxyapatite-coated collars reduce radiolucent line progression in cemented distal femoral bone tumor implants. *Clin Orthop Relat Res*, 473, 1505-14.
- COLLINS, S. F. 2014. Bioprinting is changing regenerative medicine forever. *Stem cells and development*, 23, 79-82.
- COOK, S. D., THOMAS, K. A., DALTON, J. E., VOLKMAN, T. K., WHITECLOUD, T. S., 3RD & KAY, J. F. 1992. Hydroxylapatite coating of porous implants improves bone ingrowth and interface attachment strength. *J Biomed Mater Res*, 26, 989-1001.
- COOK, S. D., THOMAS, K. A., KAY, J. F. & JARCHO, M. 1988. Hydroxyapatite-coated titanium for orthopedic implant applications. *Clin Orthop Relat Res*, 225-43.
- DA CRUZ, M. J. & FRANCIS, H. W. 2015. Face and content validation of a novel three-dimensional printed temporal bone for surgical skills development. *Journal of Laryngology and Otology*, 129, S23-S29.
- DALBY, M. J., GADEGAARD, N. & OREFFO, R. O. C. 2014. Harnessing nanotopography and integrin-matrix interactions to influence stem cell fate. *Nat Mater*, 13, 558-569.

- DALBY, M. J., GADEGAARD, N., TARE, R., ANDAR, A., RIEHLE, M. O., HERZYK, P., WILKINSON, C. D. W. & OREFFO, R. O. C. 2007. The control of human mesenchymal cell differentiation using nanoscale symmetry and disorder. *Nat Mater*, 6, 997-1003.
- DAVIS, W., MATTHEWS, J., MARTIN, J., KENNEDY III, J. & TALMAGE, R. 1975. The endosteum as a functional membrane. *Calcium regulating hormones (Talmage, RV, Owen, M., Parsons, JA, eds.)*, 275-283.
- DE GROOT, K., GEESINK, R., KLEIN, C. P. & SEREKIAN, P. 1987. Plasma sprayed coatings of hydroxylapatite. *J Biomed Mater Res*, 21, 1375-81.
- DEBARRE, E., HIVART, P., BARANSKI, D. & DEPREZ, P. 2012. Speedy skeletal prototype production to help diagnosis in orthopaedic and trauma surgery. Methodology and examples of clinical applications. *Orthopaedics and Traumatology: Surgery and Research*, 98, 597-602.
- DELIGIANNI, D. D., KATSALA, N., LADAS, S., SOTIROPOULOU, D., AMEDEE, J. & MISSIRLIS, Y. 2001. Effect of surface roughness of the titanium alloy Ti-6Al-4V on human bone marrow cell response and on protein adsorption. *Biomaterials*, 22, 1241-1251.
- DEMOL, J., LENAERTS, B., LEURIDAN, S. & DELPORT, H. 2012. Bone loss management with 3d printed metal augments: In vivo evaluation of bone ingrowth and fixation. *HIP International*, 22 (4), 427.
- DESHMUKH, T. R., KUTHE, A. M., CHAWARE, S. M., BAGARIA, V. & INGOLE, D. S. 2012. A novel rapid prototyping and finite element method-based development of the patient-specific temporomandibular joint implant. *Computer methods in biomechanics and biomedical engineering*, 15, 363-370.
- DIAZ LANTADA, A., VALLE-FERNANDEZ, R. D., MORGADO, P. L., MUNOZ-GARCIA, J., MUNOZ SANZ, J. L., MUNOZ-GUIJOSA, J. M. & OTERO, J. E. 2010. Development of personalized annuloplasty rings: combination of CT images and CAD-CAM tools. *Annals of biomedical engineering*, 38, 280-290.
- DOMINICI, M., LE BLANC, K., MUELLER, I., SLAPER-CORTENBACH, I., MARINI, F., KRAUSE, D., DEANS, R., KEATING, A., PROCKOP, D. & HORWITZ, E. 2006. Minimal criteria for defining multipotent mesenchymal stromal cells. The International Society for Cellular Therapy position statement. *Cytotherapy*, 8, 315-317.
- DREVET, R. & BENHAYOUNE, H. 2013. Pulsed electrodeposition for the synthesis of strontium-substituted calcium phosphate coatings with improved dissolution properties. *Materials Science and Engineering: C*, 33, 4260-4265.
- DU, Y., LIU, H., SHUANG, J., WANG, J., MA, J. & ZHANG, S. 2015. Microsphere-based selective laser sintering for building macroporous bone scaffolds with controlled microstructure and excellent biocompatibility. *Colloids Surf B Biointerfaces*, 135.
- DUCHAMP, S. 2013. *GE Asks Maker Community to Push the Boundaries of What is 3D Printable, Launching Open Engineering Quests (MarketWatch 2013)* [Online]. Business Wire 2013. Available: <http://www.marketwatch.com/story/ge-asks-maker-community-to-push-the-boundaries-of-what-is-3d-printable-launching-open-engineering-quests-2013-06-11> [Accessed 09/07/2017].
- DUCHEYNE, P. & CUCKLER, J. M. 1992. Bioactive ceramic prosthetic coatings. *Clinical Orthopaedics and Related Research*, 102-114.
- DUCHEYNE, P., RADIN, S., HEUGHEBAERT, M. & HEUGHEBAERT, J. 1990. Calcium phosphate ceramic coatings on porous titanium: effect of structure and

- composition on electrophoretic deposition, vacuum sintering and in vitro dissolution. *Biomaterials*, 11, 244-254.
- DUCY, P., SCHINKE, T. & KARSENTY, G. 2000. The osteoblast: a sophisticated fibroblast under central surveillance. *Science*, 289, 1501-1504.
- DWEK, J. R. 2010. The periosteum: what is it, where is it, and what mimics it in its absence? *Skeletal Radiol*, 39, 319-23.
- EILBER, F., GIULIANO, A., ECKARDT, J., PATTERSON, K., MOSELEY, S. & GOODNIGHT, J. 1987. Adjuvant chemotherapy for osteosarcoma: a randomized prospective trial. *J Clin Oncol*, 5, 21-6.
- ELEMA, H., DE GROOT, J. H., NIJENHUIS, A. J., PENNING, A. J., VETH, R. P. H., KLOMPMAKER, J. & JANSEN, H. W. B. 1990. Use of porous biodegradable polymer implants in meniscus reconstruction. 2) Biological evaluation of porous biodegradable polymer implants in menisci. *Colloid and Polymer Science*, 268, 1082-1088.
- ELIAZ, N., RITMAN-HERTZ, O., ARONOV, D., WEINBERG, E., SHENHAR, Y., ROSENMAN, G., WEINREB, M. & RON, E. 2011. The effect of surface treatments on the adhesion of electrochemically deposited hydroxyapatite coating to titanium and on its interaction with cells and bacteria. *Journal of Materials Science: Materials in Medicine*, 22, 1741-1752.
- ELLIES, L., NELSON, D. & FEATHERSTONE, J. 1992. Crystallographic changes in calcium phosphates during plasma-spraying. *Biomaterials*, 13, 313-316.
- ENGH, C. A. 1983. Hip arthroplasty with a Moore prosthesis with porous coating. A five-year study. *Clin Orthop Relat Res*, 52-66.
- ERIKSEN, E. F. 1986. Normal and pathological remodeling of human trabecular bone: three dimensional reconstruction of the remodeling sequence in normals and in metabolic bone disease. *Endocr Rev*, 7, 379-408.
- ESLAMINEJAD, M. B., MIRZADEH, H., MOHAMADI, Y. & NICKMAHZAR, A. 2007. Bone differentiation of marrow-derived mesenchymal stem cells using  $\beta$ -tricalcium phosphate–alginate–gelatin hybrid scaffolds. *Journal of tissue engineering and regenerative medicine*, 1, 417-424.
- FARFALLI, G. L., BOLAND, P. J., MORRIS, C. D., ATHANASIAN, E. A. & HEALEY, J. H. 2009. Early Equivalence of Uncemented Press-fit and Compress® Femoral Fixation. *Clinical Orthopaedics and Related Research*®, 467, 2792-2799.
- FAUR, C., CRAINIC, N., STICLARU, C. & OANCEA, C. 2013. Rapid prototyping technique in the preoperative planning for total hip arthroplasty with custom femoral components. *Wiener Klinische Wochenschrift*, 125, 144-149.
- FENG, J. 2016. *Liu Zhongjun: 3D Printing Reshapes Orthopedic Surgery* [Online]. Available: [http://en.chinagate.cn/2016-10/13/content\\_39481323.htm](http://en.chinagate.cn/2016-10/13/content_39481323.htm) [Accessed 22/1/2017].
- FERRARI, B., SANCHEZ-HERENCIA, A. & MORENO, R. 1998. Aqueous electrophoretic deposition of Al<sub>2</sub>O<sub>3</sub>/ZrO<sub>2</sub> layered ceramics. *Materials Letters*, 35, 370-374.
- FIELDING, G. A., ROY, M., BANDYOPADHYAY, A. & BOSE, S. 2012. Antibacterial and biological characteristics of silver containing and strontium doped plasma sprayed hydroxyapatite coatings. *Acta biomaterialia*, 8, 3144-3152.
- FLETCHER, C. D., UNNI, K. K. & MERTENS, F. 2002. *Pathology and genetics of tumours of soft tissue and bone*, Iarc.

- FLORENCIO-SILVA, R., SASSO, G. R. D. S., SASSO-CERRI, E., SIMÕES, M. J. & CERRI, P. S. 2015. Biology of bone tissue: structure, function, and factors that influence bone cells. *BioMed research international*, 2015.
- FOX, J. M., CHAMBERLAIN, G., ASHTON, B. A. & MIDDLETON, J. 2007. Recent advances into the understanding of mesenchymal stem cell trafficking. *British Journal of Haematology*, 137, 491-502.
- FRIEDENSTEIN, A., CHAILAKHJAN, R. & LALYKINA, K. 1970. The development of fibroblast colonies in monolayer cultures of guinea-pig bone marrow and spleen cells. *Cell Proliferation*, 3, 393-403.
- FRIEDLAENDER, G. E., TROSS, R., DOGANIS, A., KIRKWOOD, J. & BARON, R. 1984. Effects of chemotherapeutic agents on bone. I. Short-term methotrexate and doxorubicin (adriamycin) treatment in a rat model. *J Bone Joint Surg Am*, 66, 602-607.
- FROMME, P., BLUNN, G. W., ASTON, W. J., ABDOOLA, T., KORIS, J. & COATHUP, M. J. 2017. The effect of bone growth onto massive prostheses collars in protecting the implant from fracture. *Medical Engineering & Physics*.
- FUKUDA, A., TAKEMOTO, M., SAITO, T., FUJIBAYASHI, S., NEO, M., PATTANAYAK, D. K., MATSUSHITA, T., SASAKI, K., NISHIDA, N., KOKUBO, T. & NAKAMURA, T. 2011. Osteoinduction of porous Ti implants with a channel structure fabricated by selective laser melting. *Acta Biomater*, 7, 2327-36.
- GADOW, R., KILLINGER, A. & STIEGLER, N. 2010. Hydroxyapatite coatings for biomedical applications deposited by different thermal spray techniques. *Surface and Coatings Technology*, 205, 1157-1164.
- GARBUZ, D. S., HU, Y., KIM, W. Y., DUAN, K., MASRI, B. A., OXLAND, T. R., BURT, H., WANG, R. & DUNCAN, C. P. 2008. Enhanced gap filling and osteoconduction associated with alendronate-calcium phosphate-coated porous tantalum. *J Bone Joint Surg Am*, 90, 1090-100.
- GARCIA-GARETA, E., HUA, J., KNOWLES, J. C. & BLUNN, G. W. 2013. Comparison of mesenchymal stem cell proliferation and differentiation between biomimetic and electrochemical coatings on different topographic surfaces. *J Mater Sci Mater Med*, 24, 199-210.
- GEETHA, M., SINGH, A. K., ASOKAMANI, R. & GOGIA, A. K. 2009. Ti based biomaterials, the ultimate choice for orthopaedic implants – A review. *Progress in Materials Science*, 54, 397-425.
- GENG, Z., CUI, Z., LI, Z., ZHU, S., LIANG, Y., LU, W. W. & YANG, X. 2015. Synthesis, characterization and the formation mechanism of magnesium-and strontium-substituted hydroxyapatite. *Journal of Materials Chemistry B*, 3, 3738-3746.
- GHANI, Y., COATHUP, M. J., HING, K. A. & BLUNN, G. W. 2012. Development of a hydroxyapatite coating containing silver for the prevention of peri-prosthetic infection. *J Orthop Res*, 30, 356-63.
- GIBBS, D. M. R., VAEZI, M., YANG, S. & OREFFO, R. O. C. 2014. Hope versus hype: What can additive manufacturing realistically offer trauma and orthopedic surgery? *Regenerative Medicine*, 9, 535-549.
- GIBSON, I., HUANG, J., BEST, S. & BONFIELD, W. 2009. Enhanced in vitro cell activity and surface apatite layer formation on novel silicon-substituted hydroxyapatites.
- GILBERT, S. 2000. *Developmental Biology*, Sunderland, MA: Sinauer Assoc. Inc.
- GOLISH, S. R. & MIHALKO, W. M. 2011. Principles of biomechanics and biomaterials in orthopaedic surgery. *J Bone Joint Surg Am*, 93, 207-12.

- GONG, X. & YU, Q. 2012. Correction of maxillary deformity in infants with bilateral cleft lip and palate using computer-assisted design. *Oral Surgery, Oral Medicine, Oral Pathology and Oral Radiology*, 114, S74-S78.
- GOODMAN, S., TOKSVIG-LARSEN, S. & ASPENBERG, P. 1993. Ingrowth of bone into pores in titanium chambers implanted in rabbits: effect of pore cross-sectional shape in the presence of dynamic shear. *J Biomed Mater Res*, 27, 247-53.
- GOODMAN, S. B., YAO, Z., KEENEY, M. & YANG, F. 2013. The future of biologic coatings for orthopaedic implants. *Biomaterials*, 34, 3174-83.
- GOUIN, F., PAUL, L., ODRI, G. A. & CARTIAUX, O. 2014. Computer-Assisted Planning and Patient-Specific Instruments for Bone Tumor Resection within the Pelvis: A Series of 11 Patients. *Sarcoma*, 2014, 842709.
- GRIMER, R. J., TAMINIAU, A. M. & CANNON, S. R. 2002. Surgical outcomes in osteosarcoma. *J Bone Joint Surg Br*, 84, 395-400.
- GRUBL, A., CHIARI, C., GRUBER, M., KAIDER, A. & GOTTSÄUNER-WOLF, F. 2002. Cementless total hip arthroplasty with a tapered, rectangular titanium stem and a threaded cup: a minimum ten-year follow-up. *J Bone Joint Surg Am*, 84-A, 425-31.
- GU, B. K., CHOI, D. J., PARK, S. J., KIM, M. S., KANG, C. M. & KIM, C.-H. 2016. 3-dimensional bioprinting for tissue engineering applications. *Biomaterials Research*, 20, 12.
- GUHA, A. K., SINGH, S., KUMARESAN, R., NAYAR, S. & SINHA, A. 2009. Mesenchymal cell response to nanosized biphasic calcium phosphate composites. *Colloids and Surfaces B: Biointerfaces*, 73, 146-151.
- HABIBOVIC, P., GBURECK, U., DOILLON, C. J., BASSETT, D. C., VAN BLITTERSWIJK, C. A. & BARRALET, J. E. 2008. Osteoconduction and osteoinduction of low-temperature 3D printed bioceramic implants. *Biomaterials*, 29, 944-953.
- HALLAB, N. J., ANDERSON, S., STAFFORD, T., GLANT, T. & JACOBS, J. J. 2005. Lymphocyte responses in patients with total hip arthroplasty. *Journal of Orthopaedic Research*, 23, 384-391.
- HAMDI, M., HAKAMATA, S. & EKTESSABI, A. 2000. Coating of hydroxyapatite thin film by simultaneous vapor deposition. *Thin Solid Films*, 377, 484-489.
- HANYALOGLU, C., AKSAKAL, B. & BOLTON, J. 2001. Production and indentation analysis of WC/Fe-Mn as an alternative to cobalt-bonded hardmetals. *Materials Characterization*, 47, 315-322.
- HARADA, S. & RODAN, G. A. 2003. Control of osteoblast function and regulation of bone mass. *Nature*, 423, 349-55.
- HAZENBERG, J. G., LEE, T. C. & TAYLOR, D. 2006. The role of osteocytes in functional bone adaptation. *IBMS BoneKEy*, 3, 10-16.
- HENDERSON, E. R., GROUNDLAND, J. S., PALA, E., DENNIS, J. A., WOOTEN, R., CHEONG, D., WINDHAGER, R., KOTZ, R. I., MERCURI, M., FUNOVICS, P. T., HORNICEK, F. J., TEMPLE, H. T., RUGGIERI, P. & LETSON, G. D. 2011. Failure mode classification for tumor endoprostheses: retrospective review of five institutions and a literature review. *J Bone Joint Surg Am*, 93, 418-29.
- HERMAN, H. 1988. Plasma spray deposition processes. *MRS Bulletin*, 13, 60-67.
- HERØ, H., WIE, H., JØRGENSEN, R. B. & RUYTER, I. 1994. Hydroxyapatite coatings on Ti produced by hot isostatic pressing. *Journal of biomedical materials research*, 28, 343-348.

- HING, K. A., REVELL, P. A., SMITH, N. & BUCKLAND, T. 2006. Effect of silicon level on rate, quality and progression of bone healing within silicate-substituted porous hydroxyapatite scaffolds. *Biomaterials*, 27, 5014-26.
- HORWITZ, E., LE BLANC, K., DOMINICI, M., MUELLER, I., SLAPER-CORTENBACH, I., MARINI, F. C., DEANS, R., KRAUSE, D. & KEATING, A. 2005. Clarification of the nomenclature for MSC: The International Society for Cellular Therapy position statement. *Cytotherapy*, 7, 393-395.
- HORWITZ, T. 1955. Use of a shaft prosthesis in the treatment of surgically resistant nonunion of the humerus. *Bull Hosp Joint Dis*, 16, 37-44.
- HOWLADER, N., NOONE, A., KRAPCHO, M., MILLER, D., BISHOP, K., ALTEKRUSE, S., KOSARY, C., YU, M., RUHL, J., TATALOVICH, Z., MARIOTTO, A., LEWIS, D., CHEN, H., FEUER, E. & CRONIN, K. 1975-2013. *SEER Cancer Statistics Review* [Online]. Bethesda, MD: National Cancer Institute. Available: [http://seer.cancer.gov/csr/1975\\_2013/](http://seer.cancer.gov/csr/1975_2013/) [Accessed based on November 2015 SEER data submission].
- HUANG, Y., HAN, S., PANG, X., DING, Q. & YAN, Y. 2013. Electrodeposition of porous hydroxyapatite/calcium silicate composite coating on titanium for biomedical applications. *Applied Surface Science*, 271, 299-302.
- HUGHES, A., SODEN, P., O'DONNCHADHA, B., TANSEY, A., ABDULKARIM, A., MCMAHON, C. & HURSON, C. 2014. A 'Hip' approach to revision hip surgery-3D printing in complex acetabular reconstruction. *Irish Journal of Medical Science*, 1), S47.
- HUNGERFORD, D. S. & KENNA, R. V. 1983. Preliminary experience with a total knee prosthesis with porous coating used without cement. *Clin Orthop Relat Res*, 95-107.
- HUVOS, A. G., ROSEN, G. & MARCOVE, R. C. 1977. Primary osteogenic sarcoma: pathologic aspects in 20 patients after treatment with chemotherapy en bloc resection, and prosthetic bone replacement. *Arch Pathol Lab Med*, 101, 14-8.
- IJIMA, T., HOMMA, S., SEKINE, H., SASAKI, H., YAJIMA, Y. & YOSHINARI, M. 2013. Influence of surface treatment of yttria-stabilized tetragonal zirconia polycrystal with hot isostatic pressing on cyclic fatigue strength. *Dent Mater J*, 32, 274-80.
- IMANISHI, J. & CHOONG, P. F. M. 2015. Three-dimensional printed calcaneal prosthesis following total calcanectomy. *International Journal of Surgery Case Reports*, 10, 83-87.
- ISO, B. 2000. 13779-2: 2000: Implants for surgery—Hydroxyapatite—Part 2: coatings of hydroxyapatite. *British Standards Institution, London, UK*.
- JAFFE, W. L. & SCOTT, D. F. 1996. Total hip arthroplasty with hydroxyapatite-coated prostheses. *Journal of Bone and Joint Surgery - Series A*, 78, 1918-1934.
- JARCHO, M., BOLEN, C., THOMAS, M., BOBICK, J., KAY, J. & DOREMUS, R. H. 1976. Hydroxylapatite synthesis and characterization in dense polycrystalline form. *Journal of Materials Science*, 11, 2027-2035.
- JASTY, M., KIENAPFEL, H. & GRISS, P. 2007. Fixation by Ingrowth. In: RUBASH, H. E. (ed.) *The Adult Hip*. Philadelphia: Lippincott Williams and Wilkins.
- JEYS, L. M., KULKARNI, A., GRIMER, R. J., CARTER, S. R., TILLMAN, R. M. & ABUDU, A. 2008. Endoprosthetic reconstruction for the treatment of musculoskeletal tumors of the appendicular skeleton and pelvis. *J Bone Joint Surg Am*, 90, 1265-71.
- KALIA, P., BLUNN, G. W., MILLER, J., BHALLA, A., WISEMAN, M. & COATHUP, M. J. 2006. Do autologous mesenchymal stem cells augment bone growth and contact to massive bone tumor implants? *Tissue Eng*, 12, 1617-26.

- KAMIOKA, H., HONJO, T. & TAKANO-YAMAMOTO, T. 2001. A three-dimensional distribution of osteocyte processes revealed by the combination of confocal laser scanning microscopy and differential interference contrast microscopy. *Bone*, 28, 145-9.
- KANCZLER, J. M. & OREFFO, R. O. 2008. Osteogenesis and angiogenesis: the potential for engineering bone. *Eur Cell Mater*, 15, 100-14.
- KARAGEORGIU, V. & KAPLAN, D. 2005. Porosity of 3D biomaterial scaffolds and osteogenesis. *Biomaterials*, 26, 5474-5491.
- KASSAB, S. & PIETRZAK, W. S. 2014. Patient-specific positioning guides versus manual instrumentation for total knee arthroplasty: an intraoperative comparison. *J Surg Orthop Adv*, 23, 140-6.
- KHAN, A. F., SALEEM, M., AFZAL, A., ALI, A., KHAN, A. & KHAN, A. R. 2014. Bioactive behavior of silicon substituted calcium phosphate based bioceramics for bone regeneration. *Mater Sci Eng C Mater Biol Appl*, 35, 245-52.
- KIM, Y. H., PARK, J. W., PATEL, C. & KIM, D. Y. 2013. Polyethylene wear and osteolysis after cementless total hip arthroplasty with alumina-on-highly cross-linked polyethylene bearings in patients younger than thirty years of age. *J Bone Joint Surg Am*, 95, 1088-93.
- KLAWITTER, J., BAGWELL, J., WEINSTEIN, A., SAUER, B. & PRUITT, J. 1976. An evaluation of bone growth into porous high density polyethylene. *Journal of Biomedical Materials Research Part A*, 10, 311-323.
- KNOTHE TATE, M. L., ADAMSON, J. R., TAMI, A. E. & BAUER, T. W. 2004. The osteocyte. *Int J Biochem Cell Biol*, 36, 1-8.
- KOCH, C., JOHNSON, S., KUMAR, D., JELINEK, M., CHRISEY, D., DORAISWAMY, A., JIN, C., NARAYAN, R. & MIHAILESCU, I. 2007. Pulsed laser deposition of hydroxyapatite thin films. *Materials Science and Engineering: C*, 27, 484-494.
- KOROLEVA, A., DEIWICK, A., NGUYEN, A., SCHLIE-WOLTER, S., NARAYAN, R., TIMASHEV, P., POPOV, V., BAGRATASHVILI, V. & CHICHKOV, B. 2015. Osteogenic Differentiation of Human Mesenchymal Stem Cells in 3-D Zr-Si Organic-Inorganic Scaffolds Produced by Two-Photon Polymerization Technique. *PLoS One*, 10.
- KRAMER, M. J., TANNER, B. J., HORVAI, A. E. & O'DONNELL, R. J. 2008. Compressive osseointegration promotes viable bone at the endoprosthetic interface: retrieval study of Compress implants. *Int Orthop*, 32, 567-71.
- KRAUSE, D. S. 2002. Plasticity of marrow-derived stem cells. *Gene Therapy*, 9, 754-758.
- LAKSTEIN, D., KOPELOVITCH, W., BARKAY, Z., BAHAA, M., HENDEL, D. & ELIAZ, N. 2009. Enhanced osseointegration of grit-blasted, NaOH-treated and electrochemically hydroxyapatite-coated Ti-6Al-4V implants in rabbits. *Acta Biomaterialia*, 5, 2258-2269.
- LAPTEV, A., BRAM, M., BUCHKREMER, H. P. & STÖVER, D. 2004. Study of production route for titanium parts combining very high porosity and complex shape. *Powder Metallurgy*, 47, 85-92.
- LARKER, H. T. & LARKER, R. 1991. Hot isostatic pressing. *Materials Science and Technology*.
- LEE, J. H., RIM, N. G., JUNG, H. S. & SHIN, H. 2010. Control of Osteogenic Differentiation and Mineralization of Human Mesenchymal Stem Cells on Composite Nanofibers Containing Poly [lactic-co-(glycolic acid)] and Hydroxyapatite. *Macromolecular bioscience*, 10, 173-182.

- LEGEROS, R. Z. 2002. Properties of osteoconductive biomaterials: calcium phosphates. *Clinical orthopaedics and related research*, 395, 81-98.
- LEGOSTAEVA, E. V., KULYASHOVA, K. S., KOMAROVA, E. G., EPPLE, M., SHARKEEV, Y. P. & KHLUSOV, I. A. 2013. Physical, chemical and biological properties of micro-arc deposited calcium phosphate coatings on titanium and zirconium-niobium alloy
- Physikalische, chemische und biologische Eigenschaften von Calciumphosphatbeschichtungen auf Titan und Zirkonium, hergestellt durch Mikro-Lichtbogenabscheidung. *Materialwissenschaft und Werkstofftechnik*, 44, 188-197.
- LEUDERS, S., THÖNE, M., RIEMER, A., NIENDORF, T., TRÖSTER, T., RICHARD, H. A. & MAIER, H. J. 2013. On the mechanical behaviour of titanium alloy TiAl6V4 manufactured by selective laser melting: Fatigue resistance and crack growth performance. *International Journal of Fatigue*, 48, 300-307.
- LEVIN, A. S., ARKADER, A. & MORRIS, C. D. 2017. Reconstruction Following Tumor Resections in Skeletally Immature Patients. *Journal of the American Academy of Orthopaedic Surgeons*, 25, 204-213.
- LI, D. H., LIN, J., LIN, D. Y. & WANG, X. X. 2011. Synthesized silicon-substituted hydroxyapatite coating on titanium substrate by electrochemical deposition. *J Mater Sci Mater Med*, 22, 1205-11.
- LI, H., OPPENHEIMER, S. M., STUPP, S. I., DUNAND, D. C. & BRINSON, L. C. 2004. Effects of pore morphology and bone ingrowth on mechanical properties of microporous titanium as an orthopaedic implant material. *Materials Transactions*, 45, 1124-1131.
- LI, T., LEE, J., KOBAYASHI, T. & AOKI, H. 1996. Hydroxyapatite coating by dipping method, and bone bonding strength. *Journal of Materials Science: Materials in Medicine*, 7, 355-357.
- LI, Y., FENG, G., GAO, Y., LUO, E., LIU, X. & HU, J. 2010. Strontium ranelate treatment enhances hydroxyapatite-coated titanium screws fixation in osteoporotic rats. *Journal of Orthopaedic Research*, 28, 578-582.
- LIANG, H., JI, T., ZHANG, Y., WANG, Y. & GUO, W. 2017. Reconstruction with 3D-printed pelvic endoprostheses after resection of a pelvic tumour. *Bone Joint J*, 99-b, 267-275.
- LIANG, Y., LI, H., XU, J., LI, X., LI, X., YAN, Y., QI, M. & HU, M. 2015. Strontium coating by electrochemical deposition improves implant osseointegration in osteopenic models. *Experimental and therapeutic medicine*, 9, 172-176.
- LIANG, Y., LI, H., XU, J., LI, X., QI, M. & HU, M. 2014. Morphology, composition, and bioactivity of strontium-doped brushite coatings deposited on titanium implants via electrochemical deposition. *Int J Mol Sci*, 15, 9952-62.
- LINK, M. P., GOORIN, A. M., MISER, A. W., GREEN, A. A., PRATT, C. B., BELASCO, J. B., PRITCHARD, J., MALPAS, J. S., BAKER, A. R., KIRKPATRICK, J. A. & ET AL. 1986. The effect of adjuvant chemotherapy on relapse-free survival in patients with osteosarcoma of the extremity. *N Engl J Med*, 314, 1600-6.
- LIU, D.-M. Influence of porous microarchitecture on the in-vitro dissolution and biological behaviour of porous calcium phosphate ceramics. *Materials Science Forum*, 1997. Trans Tech Publ, 183-208.

- LIU, X., CHU, P. & DING, C. 2004. Surface modification of titanium, titanium alloys, and related materials for biomedical applications. *Materials Science and Engineering R47*, 49–121.
- LOGAN, C. Y. & NUSSE, R. 2004. The Wnt signaling pathway in development and disease. *Annu Rev Cell Dev Biol*, 20, 781-810.
- LOMBARDI, A. V. & FRYE, B. M. 2012. Customization of cutting blocks: Can this address the problem. *Current Reviews in Musculoskeletal Medicine*, 5, 309-314.
- LOOMIS, L. K. 1950. Internal prosthesis for upper portion of femur; a case report. *J Bone Joint Surg Am*, 32 a, 944-6.
- LU, S., XU, Y.-Q. & ZHANG, Y.-Z. 2011a. Application of a novel patient-specific rapid prototyping template in orthopedics surgery. *Advanced applications of rapid prototyping technology in modern engineering*. InTech.
- LU, S., XU, Y. Q., CHEN, G. P., ZHANG, Y. Z., LU, D., CHEN, Y. B., SHI, J. H. & XU, X. M. 2011b. Efficacy and accuracy of a novel rapid prototyping drill template for cervical pedicle screw placement. *Computer Aided Surgery*, 16, 240-248.
- MA, J., LIANG, C., KONG, L. & WANG, C. 2003. Colloidal characterization and electrophoretic deposition of hydroxyapatite on titanium substrate. *Journal of materials science: materials in medicine*, 14, 797-801.
- MACAUSLAND, W. R. 1954. Replacement of the lower end of the humerus with a prosthesis; a report of four cases. *West J Surg Obstet Gynecol*, 62, 557-66.
- MACKIE, E. J. 2003. Osteoblasts: novel roles in orchestration of skeletal architecture. *The International Journal of Biochemistry & Cell Biology*, 35, 1301-1305.
- MACKIE, E. J., AHMED, Y. A., TATARCZUCH, L., CHEN, K. S. & MIRAMS, M. 2008. Endochondral ossification: How cartilage is converted into bone in the developing skeleton. *The International Journal of Biochemistry & Cell Biology*, 40, 46-62.
- MAÏMOUN, L., BRENNAN, T. C., BADOUD, I., DUBOIS-FERRIERE, V., RIZZOLI, R. & AMMANN, P. 2010. Strontium ranelate improves implant osseointegration. *Bone*, 46, 1436-1441.
- MALAVAL, L., LIU, F., ROCHE, P. & AUBIN, J. E. 1999. Kinetics of osteoprogenitor proliferation and osteoblast differentiation in vitro. *Journal of cellular biochemistry*, 74, 616-627.
- MANDRACCI, P., MUSSANO, F., RIVOLO, P. & CAROSSA, S. 2016. Surface treatments and functional coatings for biocompatibility improvement and bacterial adhesion reduction in dental implantology. *Coatings*, 6, 7.
- MANLEY, M. T., D'ANTONIO, J. A., CAPELLO, W. N. & EDIDIN, A. A. 2002. Osteolysis: a disease of access to fixation interfaces. *Clin Orthop Relat Res*, 129-37.
- MANOLAGAS, S. C. 2000. Birth and death of bone cells: basic regulatory mechanisms and implications for the pathogenesis and treatment of osteoporosis. *Endocr Rev*, 21, 115-37.
- MARUO, S. & IKUTA, K. 2002. Submicron stereolithography for the production of freely movable mechanisms by using single-photon polymerization. *Sensors and Actuators A: Physical*, 100, 70-76.
- MAVIS, B. & TAŞ, A. C. 2000. Dip Coating of Calcium Hydroxyapatite on Ti-6Al-4V Substrates. *Journal of the American Ceramic Society*, 83, 989-991.
- MCBEATH, R., PIRONE, D. M., NELSON, C. M., BHADRIRAJU, K. & CHEN, C. S. 2004. Cell shape, cytoskeletal tension, and RhoA regulate stem cell lineage commitment. *Developmental cell*, 6, 483-495.

- MCMURRAY, R. J., GADEGAARD, N., TSIMBOURI, P. M., BURGESS, K. V., MCNAMARA, L. E., TARE, R., MURAWSKI, K., KINGHAM, E., OREFFO, R. O. C. & DALBY, M. J. 2011. Nanoscale surfaces for the long-term maintenance of mesenchymal stem cell phenotype and multipotency. *Nat Mater*, 10, 637-644.
- MELCHELS, F. P. W., FEIJEN, J. & GRIJPMAN, D. W. 2010. A review on stereolithography and its applications in biomedical engineering. *Biomaterials*, 31, 6121-6130.
- MÉNDEZ-FERRER, S., MICHURINA, T. V., FERRARO, F., MAZLOOM, A. R., MACARTHUR, B. D., LIRA, S. A., SCADDEN, D. T., MA'AYAN, A., ENIKOLOPOV, G. N. & FRENETTE, P. S. 2010. Mesenchymal and haematopoietic stem cells form a unique bone marrow niche. *nature*, 466, 829-834.
- MENG, X., KWON, T.-Y., YANG, Y., ONG, J. L. & KIM, K.-H. 2006. Effects of applied voltages on hydroxyapatite coating of titanium by electrophoretic deposition. *Journal of Biomedical Materials Research Part B: Applied Biomaterials*, 78B, 373-377.
- MERC, M., DRSTVENSEK, I., VOGRIN, M., BRAJLIH, T. & RECNIK, G. 2013. A multi-level rapid prototyping drill guide template reduces the perforation risk of pedicle screw placement in the lumbar and sacral spine. *Archives of orthopaedic and trauma surgery*, 133, 893-899.
- MERCERON, T., LEE, J., KENGLA, C., KANG, H., KIM, H., LEE, S., YOO, J. J. & ATALA, A. 2014. 3-D bioprinting for muscle-tendon unit regeneration. *Tissue Engineering - Part A*, 20, S-97.
- MEYERS, P. A., HELLER, G., HEALEY, J. H., HUVOS, A., APPLEWHITE, A., SUN, M. & LAQUAGLIA, M. 1993. Osteogenic sarcoma with clinically detectable metastasis at initial presentation. *Journal of Clinical Oncology*, 11, 449-453.
- MILLER, P. & HOLLADAY, J. 1958. Friction and wear properties of titanium. *Wear*, 2, 133-140.
- MINNS, R. J., BIBB, R., BANKS, R. & SUTTON, R. A. 2003. The use of a reconstructed three-dimensional solid model from CT to aid the surgical management of a total knee arthroplasty: A case study. *Medical Engineering and Physics*, 25, 523-526.
- MIRON, R. J. & ZHANG, Y. F. 2012. Osteoinduction. *Journal of Dental Research*, 91, 736-744.
- MOE, D., GARBARSCHEK, C. & KIRKEBY, S. 1994. The protein effect on determination of DNA with Hoechst 33258. *Journal of Biochemical and Biophysical Methods*, 28, 263-276.
- MOHSENI, E., ZALNEZHAD, E. & BUSHROA, A. 2014. Comparative investigation on the adhesion of hydroxyapatite coating on Ti-6Al-4V implant: A review paper. *International Journal of Adhesion and Adhesives*, 48, 238-257.
- MONDRAGON-CORTEZ, P. & VARGAS-GUTIERREZ, G. 2004. Electrophoretic deposition of hydroxyapatite submicron particles at high voltages. *Materials Letters*, 58, 1336-1339.
- MONDRAGÓN-CORTEZ, P. & VARGAS-GUTIÉRREZ, G. 2003. Selective deposition of hydroxyapatite nanoparticles by electrophoretic deposition. *Advanced Engineering Materials*, 5, 812-815.
- MOORE, A. T. 1952. Metal hip joint; a new self-locking vitallium prosthesis. *Southern medical journal*, 45, 1015.

- MOORE, A. T. 1957. The self-locking metal hip prosthesis. *J Bone Joint Surg Am*, 39-a, 811-27.
- MORRISON, R. J., KASHLAN, K. N., FLANANGAN, C. L., WRIGHT, J. K., GREEN, G. E., HOLLISTER, S. J. & WEATHERWAX, K. J. 2015. Regulatory Considerations in the Design and Manufacturing of Implantable 3D-Printed Medical Devices. *Clin Transl Sci*, 8, 594-600.
- MÜLLER, P., BULNHEIM, U., DIENER, A., LÜTHEN, F., TELLER, M., KLINKENBERG, E. D., NEUMANN, H. G., NEBE, B., LIEBOLD, A. & STEINHOFF, G. 2008. Calcium phosphate surfaces promote osteogenic differentiation of mesenchymal stem cells. *Journal of cellular and molecular medicine*, 12, 281-291.
- MURPHY, C. M., HAUGH, M. G. & O'BRIEN, F. J. 2010. The effect of mean pore size on cell attachment, proliferation and migration in collagen-glycosaminoglycan scaffolds for bone tissue engineering. *Biomaterials*, 31, 461-466.
- MURPHY, S. V. & ATALA, A. 2014. 3D bioprinting of tissues and organs. *Nat Biotechnol*, 32.
- MURR, L. E., GAYTAN, S. M., MARTINEZ, E., MEDINA, F. & WICKER, R. B. 2012. Next generation orthopaedic implants by additive manufacturing using electron beam melting. *International journal of biomaterials*, 2012.
- MURR, L. E., GAYTAN, S. M., MEDINA, F., LOPEZ, H., MARTINEZ, E., MACHADO, B. I., HERNANDEZ, D. H., MARTINEZ, L., LOPEZ, M. I., WICKER, R. B. & BRACKE, J. 2010. Next-generation biomedical implants using additive manufacturing of complex, cellular and functional mesh arrays. *Philosophical Transactions of the Royal Society A: Mathematical, Physical and Engineering Sciences*, 368, 1999-2032.
- MUSCOLO, D. L., AYERZA, M. A., APONTE-TINAO, L. A. & RANALLETTA, M. 2005. Use of distal femoral osteoarticular allografts in limb salvage surgery. *J Bone Joint Surg Am*, 87, 2449-2455.
- MUSCOLO, D. L., AYERZA, M. A., FARFALLI, G. & APONTE-TINAO, L. A. 2010. Proximal Tibia Osteoarticular Allografts in Tumor Limb Salvage Surgery. *Clinical Orthopaedics and Related Research*, 468, 1396-1404.
- MYERS, G. J., ABUDU, A. T., CARTER, S. R., TILLMAN, R. M. & GRIMER, R. J. 2007. Endoprosthetic replacement of the distal femur for bone tumours: long-term results. *J Bone Joint Surg Br*, 89, 521-6.
- NAHLER, G. & NAHLER, G. 2009. computer assisted product licensing application review. *Dictionary of Pharmaceutical Medicine*, 35-35.
- NAKASHIMA, K., ZHOU, X., KUNKEL, G., ZHANG, Z., DENG, J. M., BEHRINGER, R. R. & DE CROMBRUGGHE, B. 2002. The novel zinc finger-containing transcription factor osterix is required for osteoblast differentiation and bone formation. *Cell*, 108, 17-29.
- NISHIO, K., NEO, M., AKIYAMA, H., NISHIGUCHI, S., KIM, H. M., KOKUBO, T. & NAKAMURA, T. 2000. The effect of alkali- and heat-treated titanium and apatite-formed titanium on osteoblastic differentiation of bone marrow cells. *J Biomed Mater Res*, 52, 652-61.
- NOBLE, J. W., JR., MOORE, C. A. & LIU, N. 2012. The value of patient-matched instrumentation in total knee arthroplasty. *J Arthroplasty*, 27, 153-5.
- OFFERMANN, V., ANDERSEN, O. Z., FALKENSAMMER, G., ANDERSEN, I. H., ALMTOFT, K. P., SØRENSEN, S., SILLASSEN, M., JEPPESEN, C. S., RASSE, M. & FOSS, M. 2015. Enhanced osseointegration of endosseous

- implants by predictable sustained release properties of strontium. *Journal of Biomedical Materials Research Part B: Applied Biomaterials*, 103, 1099-1106.
- OHGUSHI, H., DOHI, Y., TAMAI, S. & TABATA, S. 1993. Osteogenic differentiation of marrow stromal stem cells in porous hydroxyapatite ceramics. *J Biomed Mater Res*, 27, 1401-7.
- OHTSUKA, Y., MATSUURA, M., CHIDA, N., YOSHINARI, M., SUMII, T. & DÉRAND, T. 1994. Formation of hydroxyapatite coating on pure titanium substrates by ion beam dynamic mixing. *Surface and Coatings Technology*, 65, 224-230.
- OKAZAKI, Y. & GOTOH, E. 2005. Comparison of metal release from various metallic biomaterials in vitro. *Biomaterials*, 26, 11-21.
- OLDAKOWSKI, M., OLDAKOWSKA, I., KIRK, T. B., FORD, C. T., SERCOMBE, T. B., HARDCASTLE, P. & DAY, R. E. 2016. Pull-out strength comparison of a novel expanding fastener against an orthopaedic screw in an ovine vertebral body: an ex-vivo study. *J Med Eng Technol*, 40, 43-51.
- ONG, J. L. & CHAN, D. C. 2000. Hydroxyapatite and their use as coatings in dental implants: a review. *Critical Reviews™ in Biomedical Engineering*, 28.
- OREFFO, R. O., DRIESSENS, F. C., PLANELL, J. A. & TRIFFITT, J. T. 1998. Growth and differentiation of human bone marrow osteoprogenitors on novel calcium phosphate cements. *Biomaterials*, 19, 1845-1854.
- ORIMO, H. 2010. The mechanism of mineralization and the role of alkaline phosphatase in health and disease. *J Nippon Med Sch*, 77, 4-12.
- OZEKI, K., HOSHINO, T., AOKI, H. & MASUZAWA, T. 2013. Phase composition of sputtered film from a mixture target of hydroxyapatite and strontium-apatite. *Journal Of Materials Science & Technology*, 29, 1-6.
- PALUMBO, B. T., HENDERSON, E. R., GROUNDLAND, J. S., CHEONG, D., PALA, E., LETSON, G. D. & RUGGIERI, P. 2011. Advances in segmental endoprosthetic reconstruction for extremity tumors: a review of contemporary designs and techniques. *Cancer Control*, 18, 160-70.
- PALUMBO, C., PALAZZINI, S., ZAFFE, D. & MAROTTI, G. 1990. Osteocyte differentiation in the tibia of newborn rabbit: an ultrastructural study of the formation of cytoplasmic processes. *Acta Anat (Basel)*, 137, 350-8.
- PATEL, N., BEST, S. M., BONFIELD, W., GIBSON, I. R., HING, K. A., DAMIEN, E. & REVELL, P. A. 2002. A comparative study on the in vivo behavior of hydroxyapatite and silicon substituted hydroxyapatite granules. *J Mater Sci Mater Med*, 13, 1199-206.
- PATEL, N., BROOKS, R. A., CLARKE, M. T., LEE, P. M., RUSHTON, N., GIBSON, I. R., BEST, S. M. & BONFIELD, W. 2005. In vivo assessment of hydroxyapatite and silicate-substituted hydroxyapatite granules using an ovine defect model. *J Mater Sci Mater Med*, 16, 429-40.
- PEDTKE, A. C., WUSTRACK, R. L., FANG, A. S., GRIMER, R. J. & O'DONNELL, R. J. 2012. Aseptic failure: how does the Compress((R)) implant compare to cemented stems? *Clin Orthop Relat Res*, 470, 735-42.
- PELKER, R. R., FRIEDLAENDER, G. E., PANJABI, M. M., MARKHAM, T., HAUSMAN, M., DOGANIS, A. C. & MCKAY, J. 1985. Chemotherapy-induced alterations in the biomechanics of rat bone. *Journal of orthopaedic research*, 3, 91-95.
- PEREZ-MANANES, R., BURRO, J. A., MANAUTE, J. R., RODRIGUEZ, F. C. & MARTIN, J. V. 2016. 3D Surgical Printing Cutting Guides for Open-Wedge High Tibial Osteotomy: Do It Yourself. *J Knee Surg*, 29, 690-695.

- PERREN, S. M. 2002. Evolution of the internal fixation of long bone fractures. *Bone & Joint Journal*, 84, 1093-1110.
- PHAN, K., SGRO, A., MAHARAJ, M. M., D'URSO, P. & MOBBS, R. J. 2016. Application of a 3D custom printed patient specific spinal implant for C1/2 arthrodesis. *J Spine Surg*, 2, 314-8.
- PIETAK, A. M., REID, J. W., STOTT, M. J. & SAYER, M. 2007. Silicon substitution in the calcium phosphate bioceramics. *Biomaterials*, 28, 4023-4032.
- PILLIAR, R. M. 1987. Porous-surfaced metallic implants for orthopedic applications. *J Biomed Mater Res*, 21, 1-33.
- PITTENGER, M. F., MACKAY, A. M., BECK, S. C., JAISWAL, R. K., DOUGLAS, R., MOSCA, J. D., MOORMAN, M. A., SIMONETTI, D. W., CRAIG, S. & MARSHAK, D. R. 1999. Multilineage potential of adult human mesenchymal stem cells. *science*, 284, 143-147.
- PLOTKIN, L. I., MANOLAGAS, S. C. & BELLIDO, T. 2002. Transduction of cell survival signals by connexin-43 hemichannels. *J Biol Chem*, 277, 8648-57.
- POLINI, A., PISIGNANO, D., PARODI, M., QUARTO, R. & SCAGLIONE, S. 2011. Osteoinduction of human mesenchymal stem cells by bioactive composite scaffolds without supplemental osteogenic growth factors. *PloS one*, 6, e26211.
- POPESCU, D. & LAPTOIU, D. 2016. Rapid prototyping for patient-specific surgical orthopaedics guides: A systematic literature review. *Proceedings of the Institution of Mechanical Engineers, Part H: Journal of Engineering in Medicine*, 230, 495-515.
- PORTER, A. E., BOTELHO, C. M., LOPES, M. A., SANTOS, J. D., BEST, S. M. & BONFIELD, W. 2004. Ultrastructural comparison of dissolution and apatite precipitation on hydroxyapatite and silicon-substituted hydroxyapatite in vitro and in vivo. *Journal of Biomedical Materials Research Part A*, 69, 670-679.
- QIAO, F., LI, D., JIN, Z., GAO, Y., ZHOU, T., HE, J. & CHENG, L. 2015. Application of 3D printed customized external fixator in fracture reduction. *Injury*, 46, 1150-1155.
- QIU, D., YANG, L., YIN, Y. & WANG, A. 2011. Preparation and characterization of hydroxyapatite/titania composite coating on NiTi alloy by electrochemical deposition. *Surface and Coatings Technology*, 205, 3280-3284.
- QUARLES, L. D. 2008. Endocrine functions of bone in mineral metabolism regulation. *The Journal of Clinical Investigation*, 118, 3820-3828.
- RALSTON, S. H. 2005. Structure and metabolism of bone. *Medicine*, 33, 58-60.
- RALSTON, S. H. 2013. Bone structure and metabolism. *Medicine*, 41, 581-585.
- REDEPENNING, J., SCHLESSINGER, T., BURNHAM, S., LIPPIELLO, L. & MIYANO, J. 1996. Characterization of electrolytically prepared brushite and hydroxyapatite coatings on orthopedic alloys. *J Biomed Mater Res*, 30, 287-94.
- REDEPENNING, J., VENKATARAMAN, G., CHEN, J. & STAFFORD, N. 2003. Electrochemical preparation of chitosan/hydroxyapatite composite coatings on titanium substrates. *J Biomed Mater Res A*, 66, 411-6.
- REGINSTER, J.-Y., SEEMAN, E., DE VERNEJOU, M., ADAMI, S., COMPSTON, J., PHENEKOS, C., DEVOGELAER, J.-P., CURIEL, M. D., SAWICKI, A. & GOEMAERE, S. 2005. Strontium ranelate reduces the risk of nonvertebral fractures in postmenopausal women with osteoporosis: Treatment of Peripheral Osteoporosis (TROPOS) study. *The journal of clinical endocrinology & metabolism*, 90, 2816-2822.
- RENSON, L., POILVACHE, P. & VAN DEN WYNGAERT, H. 2014. Improved alignment and operating room efficiency with patient-specific instrumentation for TKA. *Knee*, 21, 1216-20.

- RICHARD, D., DUMELIÉ, N., BENHAYOUNE, H., BOUTHORS, S., GUILLAUME, C., LALUN, N., BALOSSIER, G. & LAURENT-MAQUIN, D. 2006. Behavior of human osteoblast-like cells in contact with electrodeposited calcium phosphate coatings. *Journal of Biomedical Materials Research Part B: Applied Biomaterials*, 79, 108-115.
- RODAN, G. A. 1992. Introduction to bone biology. *Bone*, 13, Supplement 1, S3-S6.
- RONCA, A., AMBROSIO, L. & GRIJPMAN, D. W. 2012. Design of porous three-dimensional PDLA/nano-hap composite scaffolds using stereolithography. *Journal of Applied Biomaterials and Functional Materials*, 10, 249-258.
- ROSEN, G., MARCOVE, R. C., CAPARROS, B., NIRENBERG, A., KOSLOFF, C. & HUVOS, A. G. 1979. Primary osteogenic sarcoma: the rationale for preoperative chemotherapy and delayed surgery. *Cancer*, 43, 2163-77.
- ROSEN, G., MURPHY, M. L., HUVOS, A. G., GUTIERREZ, M. & MARCOVE, R. C. 1976. Chemotherapy, en bloc resection, and prosthetic bone replacement in the treatment of osteogenic sarcoma. *Cancer*, 37, 1-11.
- RUYS, A. 1993. Silicon-doped hydroxyapatite. *J. Australas. Ceram. Soc.(Switzerland)*, 29, 71-80.
- RYAN, G., PANDIT, A. & APATSIDIS, D. P. 2006. Fabrication methods of porous metals for use in orthopaedic applications. *Biomaterials*, 27, 2651-2670.
- SAMAVEDI, S., WHITTINGTON, A. R. & GOLDSTEIN, A. S. 2013. Calcium phosphate ceramics in bone tissue engineering: A review of properties and their influence on cell behavior. *Acta Biomaterialia*, 9, 8037-8045.
- SANGHERA, B., NAIQUE, S., PAPA HARILAOU, Y. & AMIS, A. 2001. Preliminary study of rapid prototype medical models. *Rapid Prototyping Journal*, 7, 275-284.
- SARAN, N., ZHANG, R. & TURCOTTE, R. E. 2011. Osteogenic protein-1 delivered by hydroxyapatite-coated implants improves bone ingrowth in extracortical bone bridging. *Clin Orthop Relat Res*, 469, 1470-8.
- SARGEANT, A. & GOSWAMI, T. 2006. Hip implants: paper V. Physiological effects. *Materials & design*, 27, 287-307.
- SARKAR, P. & NICHOLSON, P. S. 1996. Electrophoretic deposition (EPD): mechanisms, kinetics, and application to ceramics. *Journal of the American Ceramic Society*, 79, 1987-2002.
- SCHMID, M., AMADO, A. & WEGENER, K. 2014. Materials perspective of polymers for additive manufacturing with selective laser sintering. *Journal of Materials Research*, 29, 1824-1832.
- SCHMIDMAIER, G., WILDEMANN, B., SCHWABE, P., STANGE, R., HOFFMANN, J., SÜDKAMP, N. P., HAAS, N. P. & RASCHKE, M. 2002. A new electrochemically graded hydroxyapatite coating for osteosynthetic implants promotes implant osteointegration in a rat model. *Journal of Biomedical Materials Research*, 63, 168-172.
- SCHWARTZ, A., MONEY, K., SPANGHEHL, M., HATTRUP, S., CLARIDGE, R. J. & BEAUCHAMP, C. 2015. Office-based rapid prototyping in orthopedic surgery: a novel planning technique and review of the literature. *American journal of orthopedics (Belle Mead, N.J.)*, 44, 19-25.
- SCHWARZ, K. & MILNE, D. B. 1972. Growth-promoting effects of silicon in rats. *Nature*, 333-4.
- SCHWARZ, K., RICCI, B., PUNSAR, S. & KARVONEN, M. 1977. Inverse relation of silicon in drinking water and atherosclerosis in Finland. *The Lancet*, 309, 538-539.

- SEDDON, H. J. & SCALES, J. T. 1949. A polythene substitute for the upper two-thirds of the shaft of the femur. *Lancet*, 2, 795.
- SHEPHERD, J. H., SHEPHERD, D. V. & BEST, S. M. 2012. Substituted hydroxyapatites for bone repair. *Journal of Materials Science: Materials in Medicine*, 23, 2335-2347.
- SHIE, M.-Y., DING, S.-J. & CHANG, H.-C. 2011. The role of silicon in osteoblast-like cell proliferation and apoptosis. *Acta Biomaterialia*, 7, 2604-2614.
- SHIMAZAKI, T., MIYAMOTO, H., ANDO, Y., NODA, I., YONEKURA, Y., KAWANO, S., MIYAZAKI, M., MAWATARI, M. & HOTOKEBUCHI, T. 2010. In vivo antibacterial and silver-releasing properties of novel thermal sprayed silver-containing hydroxyapatite coating. *Journal of Biomedical Materials Research Part B: Applied Biomaterials*, 92, 386-389.
- SHU, R., MCMULLEN, R., BAUMANN, M. J. & MCCABE, L. R. 2003. Hydroxyapatite accelerates differentiation and suppresses growth of MC3T3-E1 osteoblasts. *J Biomed Mater Res A*, 67, 1196-204.
- SIM, F. H. & CHAO, E. Y. 1979. Prosthetic replacement of the knee and a large segment of the femur or tibia. *J Bone Joint Surg Am*, 61, 887-92.
- SINKS, L. F. & MINDELL, E. R. 1975. Chemotherapy of osteosarcoma. *Clin Orthop Relat Res*, 101-4.
- SOBALLE, K. 1993. Hydroxyapatite ceramic coating for bone implant fixation. Mechanical and histological studies in dogs. *Acta Orthop Scand Suppl*, 255, 1-58.
- SOBALLE, K., TOKSVIG-LARSEN, S., GELINECK, J., FRUENSGAARD, S., HANSEN, E. S., RYD, L., LUCHT, U. & BUNGER, C. 1993. Migration of hydroxyapatite coated femoral prostheses. A Roentgen Stereophotogrammetric study. *J Bone Joint Surg Br*, 75, 681-7.
- SODIAN, R., HAEBERLE, S., WEBER, S., LUETH, T., BEIRAS-FERNANDEZ, A., SCHMITZ, C. & REICHAERT, B. 2011. Medical rapid prototyping (MRP) in adult-and paediatric cardiac surgery. *Thoracic and Cardiovascular Surgeon*, 59.
- SOMMERFELDT, D. & RUBIN, C. 2001. Biology of bone and how it orchestrates the form and function of the skeleton. *European Spine Journal*, 10, 86-95.
- SRIDHAR, T., ELIAZ, N., MUDALI, U. K. & RAJ, B. 2002. Electrophoretic deposition of hydroxyapatite coatings and corrosion aspects of metallic implants. *Corrosion reviews*, 20, 255-294.
- STEIN, G. S., LIAN, J. B., STEIN, J. L., VAN WIJNEN, A. J. & MONTECINO, M. 1996. Transcriptional control of osteoblast growth and differentiation. *Physiological reviews*, 76, 593-629.
- STOFFELEN, D. V. C., ERALY, K. & DEBEER, P. 2015. The use of 3D printing technology in reconstruction of a severe glenoid defect: A case report with 2.5 years of follow-up. *Journal of Shoulder and Elbow Surgery*, 24, e218-e222.
- STONE, J., CANDELA, B., ALLELUIA, V., FAZILI, A., RICHARDS, M., FENG, C., PEYRE, S., JOSEPH, J. & GHAZI, A. 2015. A novel technique for simulated surgical procedures using 3D printing technology. *Journal of Urology*, 1), e270.
- SUMNER, D. R., TURNER, T. M., PURCHIO, A. F., GOMBOTZ, W. R., URBAN, R. M. & GALANTE, J. O. 1995. Enhancement of bone ingrowth by transforming growth factor-beta. *J Bone Joint Surg Am*, 77, 1135-47.
- SURMENEV, R. A., SURMENEVA, M. A. & IVANOVA, A. A. 2014. Significance of calcium phosphate coatings for the enhancement of new bone osteogenesis – A review. *Acta Biomaterialia*, 10, 557-579.

- TACK, P., VICTOR, J., GEMMEL, P. & ANNEMANS, L. 2016. 3D-printing techniques in a medical setting: a systematic literature review. *BioMedical Engineering OnLine*, 15, 115.
- TADIC, D., PETERS, F. & EPPLE, M. 2002. Continuous synthesis of amorphous carbonated apatites. *Biomaterials*, 23, 2553-2559.
- TAICHMAN, R. S. 2005. Blood and bone: two tissues whose fates are intertwined to create the hematopoietic stem-cell niche. *Blood*, 105, 2631-9.
- TANIGUCHI, N., FUJIBAYASHI, S., TAKEMOTO, M., SASAKI, K., OTSUKI, B., NAKAMURA, T., MATSUSHITA, T., KOKUBO, T. & MATSUDA, S. 2016. Effect of pore size on bone ingrowth into porous titanium implants fabricated by additive manufacturing: An in vivo experiment. *Materials Science and Engineering: C*, 59, 690-701.
- TANIZAWA, Y. & SUZUKI, T. 1994. X-Ray Photoelectron Spectroscopy Study on Silicate-Containing Apatite. *Phosphorus Research Bulletin*, 4, 83-88.
- TANZER, M., TURCOTTE, R., HARVEY, E. & BOBYN, J. D. 2003. Extracortical bone bridging in tumor endoprostheses. Radiographic and histologic analysis. *J Bone Joint Surg Am*, 85-a, 2365-70.
- TAYLOR, S. J., PERRY, J. S., MESWANIA, J. M., DONALDSON, N., WALKER, P. S. & CANNON, S. R. 1997. Telemetry of forces from proximal femoral replacements and relevance to fixation. *J Biomech*, 30, 225-34.
- TEITELBAUM, S. L. 2000. Bone Resorption by Osteoclasts. *Science*, 289, 1504-1508.
- TENENBAUM, H. 1987. Levamisole and inorganic pyrophosphate inhibit beta-glycerophosphate induced mineralization of bone formed in vitro. *Bone and mineral*, 3, 13-26.
- THEOBALD, S. *Custom surgery creates normal hips for 30-year-old* [Online]. Available: <http://sharing.mayoclinic.org/discussion/custom-surgery-creates-normal-hips-for-30-year-old> [Accessed 22/1/2017].
- THIAN, E., CHANG, L., LIM, P., GURUCHARAN, B., SUN, J., FUH, J., HO, B., TAY, B., TEO, E. & WANG, W. 2013. Chemically-modified calcium phosphate coatings via drop-on-demand micro-dispensing technique. *Surface and Coatings Technology*, 231, 29-33.
- THIAN, E., HUANG, J., BEST, S., BARBER, Z. & BONFIELD, W. 2005. Magnetron co-sputtered silicon-containing hydroxyapatite thin films—an in vitro study. *Biomaterials*, 26, 2947-2956.
- THOMAS, D. S., GILBERT, S.W. 2014. Costs and Cost Effectiveness of Additive Manufacturing. National Institute of Standards and Technology, U.S. Department of Commerce.
- THOMAS, K. A. 1994. Hydroxyapatite coatings. *Orthopedics*, 17, 267-278.
- TISDEL, C. L., GOLDBERG, V. M., PARR, J. A., BENSUSAN, J. S., STAIKOFF, L. S. & STEVENSON, S. 1994. The influence of a hydroxyapatite and tricalcium-phosphate coating on bone growth into titanium fiber-metal implants. *J Bone Joint Surg Am*, 76, 159-71.
- TRIPPEL, S. B., COUTTS, R. D., EINHORN, T. A., MUNDY, G. R. & ROSENFELD, R. G. 1996. Instructional Course Lectures, The American Academy of Orthopaedic Surgeons-Growth Factors as Therapeutic Agents\*. *J Bone Joint Surg Am*, 78, 1272-86.
- TUCHINSKIY, L. & LOUTFY, R. 2004. Titanium foams for medical applications. In: SHRIVASTAVA, S., ed. *Materials & Processes for Medical Devices Conference, 2003 Anaheim, California*. ASM International, 377-381.

- TYE, C. E., HUNTER, G. K. & GOLDBERG, H. A. 2005. Identification of the type I collagen-binding domain of bone sialoprotein and characterization of the mechanism of interaction. *Journal of Biological Chemistry*, 280, 13487-13492.
- UNWIN, P. S., CANNON, S. R., GRIMER, R. J., KEMP, H. B., SNEATH, R. S. & WALKER, P. S. 1996. Aseptic loosening in cemented custom-made prosthetic replacements for bone tumours of the lower limb. *J Bone Joint Surg Br*, 78, 5-13.
- URIST, M. R., SILVERMAN, B. F., DÜRING, K., DUBUC, F. L. & ROSENBERG, J. M. 1967. 24 The Bone Induction Principle. *Clinical orthopaedics and related research*, 53, 243-284.
- VAEZI, M., BLACK, C., GIBBS, D. M., OREFFO, R. O., BRADY, M., MOSHREFI-TORBATI, M. & YANG, S. 2016. Characterization of new PEEK/HA composites with 3D HA network fabricated by extrusion freeforming. *Molecules*, 21, 687.
- VAN BAEL, S., CHAI, Y. C., TRUSCELLO, S., MOESEN, M., KERCKHOFS, G., VAN OOSTERWYCK, H., KRUTH, J.-P. & SCHROOTEN, J. 2012. The effect of pore geometry on the in vitro biological behavior of human periosteum-derived cells seeded on selective laser-melted Ti6Al4V bone scaffolds. *Acta biomaterialia*, 8, 2824-2834.
- VAN DER STOK, J., VAN DER JAGT, O. P., AMIN YAVARI, S., DE HAAS, M. F., WAARSING, J. H., JAHR, H., VAN LIESHOUT, E. M., PATKA, P., VERHAAR, J. A. & ZADPOOR, A. A. 2013. Selective laser melting-produced porous titanium scaffolds regenerate bone in critical size cortical bone defects. *Journal of Orthopaedic Research*, 31, 792-799.
- VAN DER VIS, H., ASPENBERG, P., DE KLEINE, R., TIGCHELAAR, W. & VAN NOORDEN, C. J. 1998a. Short periods of oscillating fluid pressure directed at a titanium-bone interface in rabbits lead to bone lysis. *Acta Orthop Scand*, 69, 5-10.
- VAN DER VIS, H. M., ASPENBERG, P., MARTI, R. K., TIGCHELAAR, W. & VAN NOORDEN, C. J. 1998b. Fluid pressure causes bone resorption in a rabbit model of prosthetic loosening. *Clin Orthop Relat Res*, 201-8.
- VAN DER WINDT, D. A., PIETERSON, I., VAN DER EIJKEN, J. W., HOLLANDER, A. P., DAHMEN, R. & DE JONG, B. A. 1992. Energy expenditure during walking in subjects with tibial rotationplasty, above-knee amputation, or hip disarticulation. *Archives of physical medicine and rehabilitation*, 73, 1174-1180.
- VAN HAVER, A., DE ROO, K., DE BEULE, M., VAN CAUTER, S., LABEY, L., DE BAETS, P., CLAESSENS, T. & VERDONK, P. 2014. The use of rapid prototyped implants to simulate knee joint abnormalities for in vitro testing: a validation study with replica implants of the native trochlea. *Proceedings of the Institution of Mechanical Engineers, Part H, Journal of engineering in medicine*. 228, 833-842.
- VENABLE, C. S. 1952. An elbow and an elbow prosthesis; case of complete loss of the lower third of the humerus. *Am J Surg*, 83, 271-5.
- VENTOLA, C. L. 2014. Medical Applications for 3D Printing: Current and Projected Uses. *P T*, 39, 704-11.
- VICTOR, J. & PREMANATHAN, A. 2013. Virtual 3D planning and patient specific surgical guides for osteotomies around the knee. *Bone Joint J*, 95, 153-158.
- VIROLAINEN, P., INOUE, N., NAGAO, M., FRASSICA, F. J. & CHAO, E. 2005. The effect of multidrug chemotherapy on bone graft augmented prosthesis fixation. *Journal of orthopaedic research*, 23, 795-801.

- WANG, B., LEE, T., CHANG, E. & YANG, C. 1993. The shear strength and the failure mode of plasma-sprayed hydroxyapatite coating to bone: The effect of coating thickness. *Journal of biomedical materials research*, 27, 1315-1327.
- WANG, H., ELIAZ, N., XIANG, Z., HSU, H.-P., SPECTOR, M. & HOBBS, L. W. 2006. Early bone apposition in vivo on plasma-sprayed and electrochemically deposited hydroxyapatite coatings on titanium alloy. *Biomaterials*, 27, 4192-4203.
- WAPNER, K. L. 1991. Implications of metallic corrosion in total knee arthroplasty. *Clinical orthopaedics and related research*, 271, 12-20.
- WARD, W. G., JOHNSTON, K. S., DOREY, F. J. & ECKARDT, J. J. 1993. Extramedullary porous coating to prevent diaphyseal osteolysis and radiolucent lines around proximal tibial replacements. A preliminary report. *J Bone Joint Surg Am*, 75, 976-87.
- WARD, W. G., JOHNSTON, K. S., DOREY, F. J. & ECKARDT, J. J. 1997. Loosening of massive proximal femoral cemented endoprostheses. Radiographic evidence of loosening mechanism. *J Arthroplasty*, 12, 741-50.
- WASHBURN, N. R., YAMADA, K. M., SIMON, C. G., KENNEDY, S. B. & AMIS, E. J. 2004. High-throughput investigation of osteoblast response to polymer crystallinity: influence of nanometer-scale roughness on proliferation. *Biomaterials*, 25, 1215-1224.
- WATSON, R. A. 2014. A low-cost surgical application of additive fabrication. *Journal of Surgical Education*, 71, 14-17.
- WAZEN, R. M., LEFEBVRE, L. P., BARIL, E. & NANCI, A. 2010. Initial evaluation of bone ingrowth into a novel porous titanium coating. *J Biomed Mater Res B Appl Biomater*, 94, 64-71.
- WEI, C.-N., HUI-YUN BOR, AND LI CHANG. 2008. Effect of hot isostatic pressing on microstructure and mechanical properties of CM-681LC nickel-base superalloy using microcast. *Materials Transactions* 49, 193-201.
- WEI, M., RUYS, A., SWAIN, M., KIM, S., MILTHORPE, B. & SORRELL, C. 1999. Interfacial bond strength of electrophoretically deposited hydroxyapatite coatings on metals. *Journal of Materials Science: Materials in Medicine*, 10, 401-409.
- WIE, H., HERO, H. & SOLHEIM, T. 1998. Hot isostatic pressing-processed hydroxyapatite-coated titanium implants: light microscopic and scanning electron microscopy investigations. *International Journal of Oral and Maxillofacial Implants*, 13, 837-844.
- WILLIAMS, D. F. 2008. On the mechanisms of biocompatibility. *Biomaterials*, 29, 2941-2953.
- WIRGANOWICZ, P. Z., ECKARDT, J. J., DOREY, F. J., EILBER, F. R. & KABO, J. M. 1999. Etiology and results of tumor endoprosthesis revision surgery in 64 patients. *Clin Orthop Relat Res*, 64-74.
- WOHLERS, T. 2014. Wohlers Report 2014: Global Reports. *Wohlers Associates, Belgium*.
- WU, S. H., LI, Y., ZHANG, Y. Q., LI, X. K., YUAN, C. F., HAO, Y. L., ZHANG, Z. Y. & GUO, Z. 2013. Porous Titanium-6 Aluminum-4 Vanadium Cage Has Better Osseointegration and Less Micromotion Than a Poly-Ether-Ether-Ketone Cage in Sheep Vertebral Fusion. *Artificial organs*, 37, E191-E201.
- WU, X. B., WANG, J. Q., ZHAO, C. P., SUN, X., SHI, Y., ZHANG, Z. A., LI, Y. N. & WANG, M. Y. 2015. Printed three-dimensional anatomic templates for virtual preoperative planning before reconstruction of old pelvic injuries: Initial results. *Chinese Medical Journal*, 128, 477-482.

- XU, Y., FAN, F., KANG, N., WANG, S., YOU, J., WANG, H. & ZHANG, B. 2015. Tissue engineering of human nasal alar cartilage precisely by using three-dimensional printing. *Plastic and reconstructive surgery*, 135, 451-458.
- XUE, W., TAO, S., LIU, X., ZHENG, X. & DING, C. 2004. In vivo evaluation of plasma sprayed hydroxyapatite coatings having different crystallinity. *Biomaterials*, 25, 415-421.
- YAMASHITA, K., MATSUDA, M., INDA, Y., UMEGAKI, T., ITO, M. & OKURA, T. 1997. Dielectric depression and dispersion in electrophoretically fabricated BaTiO<sub>3</sub> Ceramic films. *Journal of the American Ceramic Society*, 80, 1907-1909.
- YANG, F., DONG, W.-J., HE, F.-M., WANG, X.-X., ZHAO, S.-F. & YANG, G.-L. 2012a. Osteoblast response to porous titanium surfaces coated with zinc-substituted hydroxyapatite. *Oral Surgery, Oral Medicine, Oral Pathology and Oral Radiology*, 113, 313-318.
- YANG, G. L., SONG, L. N., JIANG, Q. H., WANG, X. X., ZHAO, S. F. & HE, F. M. 2012b. Effect of strontium-substituted nanohydroxyapatite coating of porous implant surfaces on implant osseointegration in a rabbit model. *Int J Oral Maxillofac Implants*, 27, 1332-9.
- YANG, H. W., LIN, M. H., XU, Y. Z., SHANG, G. W., WANG, R. R. & CHEN, K. 2015. Osteogenesis of bone marrow mesenchymal stem cells on strontium-substituted nano-hydroxyapatite coated roughened titanium surfaces. *Int J Clin Exp Med*, 8, 257-64.
- YANG, J., CAI, H., LV, J., ZHANG, K., LENG, H., SUN, C., WANG, Z. & LIU, Z. 2014. In vivo study of a self-stabilizing artificial vertebral body fabricated by electron beam melting. *Spine*, 39, E486-E492.
- YANG, W., HAN, W., HE, W., LI, J., WANG, J., FENG, H. & QIAN, Y. 2016. Surface topography of hydroxyapatite promotes osteogenic differentiation of human bone marrow mesenchymal stem cells. *Materials Science and Engineering: C*, 60, 45-53.
- YANG, Y., KIM, K.-H. & ONG, J. L. 2005. A review on calcium phosphate coatings produced using a sputtering process—an alternative to plasma spraying. *Biomaterials*, 26, 327-337.
- YOSHIOKA, T., ONOMOTO, H., KASHIWAZAKI, H., INOUE, N., KOYAMA, Y., TAKAKUDA, K. & TANAKA, J. 2009. Improvement of Biocompatibility of Chitosan Fiber Modified by Ca-Phosphate Deposition through an Alternate Soaking Process. *MATERIALS TRANSACTIONS*, 50, 1269-1272.
- ZARB, G. & ALBREKTSSON, T. 1991. Osseointegration: a requiem for the periodontal ligament. *Int J Periodont Rest Dent*, 11, 88-91.
- ZARDIACKAS, L. D., PARSELL, D. E., DILLON, L. D., MITCHELL, D. W., NUNNERY, L. A. & POGGIE, R. 2001. Structure, metallurgy, and mechanical properties of a porous tantalum foam. *J Biomed Mater Res*, 58, 180-7.
- ZHAI, Y., LADOS, D. A. & LAGOY, J. L. 2014. Additive Manufacturing: Making Imagination the Major Limitation. *JOM*, 66, 808-816.
- ZHANG, E. & ZOU, C. 2009. Porous titanium and silicon-substituted hydroxyapatite biomodification prepared by a biomimetic process: characterization and in vivo evaluation. *Acta Biomaterialia*, 5, 1732-1741.
- ZHANG, J. X., GUAN, R. F. & ZHANG, X. P. 2011a. Synthesis and characterization of sol-gel hydroxyapatite coatings deposited on porous NiTi alloys. *Journal of Alloys and Compounds*, 509, 4643-4648.
- ZHANG, Y. Z., CHEN, B., LU, S., YANG, Y., ZHAO, J. M., LIU, R., LI, Y. B. & PEI, G. X. 2011b. Preliminary application of computer-assisted patient-specific

- acetabular navigational template for total hip arthroplasty in adult single development dysplasia of the hip. *Int J Med Robot*, 7, 469-74.
- ZHANG, Z., DUNN, M. F., XIAO, T., TOMSIA, A. P. & SAIZ, E. Nanostructured hydroxyapatite coatings for improved adhesion and corrosion resistance for medical implants. MRS Proceedings, 2001. Cambridge Univ Press, V7. 5.
- ZHAO, J., XIAO, S., LU, X., WANG, J. & WENG, J. 2006. A study on improving mechanical properties of porous HA tissue engineering scaffolds by hot isostatic pressing. *Biomed Mater*, 1, 188-92.
- ZHENG, X., HUANG, M. & DING, C. 2000. Bond strength of plasma-sprayed hydroxyapatite/Ti composite coatings. *Biomaterials*, 21, 841-849.
- ZHITOMIRSKY , I. & GAL-OR , L. 1997. Electrophoretic deposition of hydroxyapatite. *Journal of Materials Science: Materials in Medicine*, 8, 213-219.
- ZIEGLER, U. & GROSCURTH, P. 2004. Morphological Features of Cell Death. *Physiology*, 19, 124-128.
- ZUKAS, V. & ZUKAS, J. A. 2015. *An Introduction to 3D Printing*, First Edition Design eBook Publishing.
- ZYMAN, Z., WENG, J., LIU, X., LI, X. & ZHANG, X. 1994. Phase and structural changes in hydroxyapatite coatings under heat treatment. *Biomaterials*, 15, 151-155.